PHYSIK-DEPARTMENT

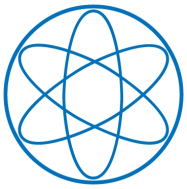

# First Measurement of the Cross Section for the Production of Hadrons with High Transverse Momenta at COMPASS, and Developments for Particle Tracking in High-Rate Experiments

Dissertation von Christian Höppner

TECHNISCHE UNIVERSITÄT
MÜNCHEN

TECHNISCHE UNIVERSITÄT MÜNCHEN
Physik-Department E18

# First Measurement of the Cross Section for the Production of Hadrons with High Transverse Momenta at COMPASS, and Developments for Particle Tracking in High-Rate Experiments

Christian C. Höppner

Vollständiger Abdruck der von der Fakultät für Physik der Technischen Universität München zur Erlangung des akademischen Grades eines

Doktors der Naturwissenschaften

genehmigten Dissertation.

Vorsitzender: Univ.-Prof. Dr. Wolfram Weise

Prüfer der Dissertation:

1. Univ.-Prof. Dr. Stephan Paul
2. Hon.-Prof. Allen C. Caldwell, Ph.D.

Die Dissertation wurde am 12.12.2011 bei der Technischen Universität München eingereicht und durch die Fakultät für Physik am 31.01.2012 angenommen.

# Abstract

In this dissertation, the first measurement of the luminosity for data from the COMPASS experiment is presented. The result is obtained by the direct measurement of the beam flux and the correction of all inefficiencies and dead times of the measurement. The normalized data set consists of about 30% of the COMPASS data recorded in 2004 and the effective integrated luminosity is $142.4\,\mathrm{pb}^{-1}$ $\pm 10\%$, which is verified by the determination of the structure function $F_2$ of the nucleon and its comparison to literature. Based on this result, the cross section for the quasi-real photoproduction of charged hadrons with high transverse momenta in muon-deuteron scattering at a center-of-mass energy of $\sqrt{s} = 17.4\,\mathrm{GeV}$ is determined. The measurement of a hadron-production cross section in a thick solid-state target is quite challenging in comparison to collider measurements of such processes. The issue of secondary hadronic interactions in the target material is carefully studied and taken into account. The cross section is presented in bins of the pseudo-rapidity of the hadrons and separated by hadron charge. The results are discussed and compared to recent calculations of next-to-leading order perturbative Quantum Chromodynamics. This comparison serves as a test of the applicability of such calculations to the production of hadrons with high transverse momenta at COMPASS energies.

The second part of this dissertation describes new developments for charged-particle tracking in high-rate experiments. The design of a new type of Time Projection Chamber (TPC), which employs GEM foils instead of proportional wires for gas amplification, is discussed. This technology opens up the possibility of using TPCs in experiments with trigger rates beyond about 1 kHz. Several important contributions to the GEM-TPC project are presented. Furthermore, a generic framework for track fitting in high-energy physics, called GENFIT, is introduced. This novel software is being used in the $\overline{\mathrm{P}}$ANDA, Belle-II, and GEM-TPC projects.

# Zusammenfassung

In dieser Dissertation wird die erste Messung der Luminosität für Daten des COMPASS Experiments präsentiert. Dieses Ergebnis wird durch die direkte Messung des Strahlflusses und der Korrektur aller auftretenden Ineffizienzen und Totzeiten erreicht. Der so normierte Datensatz umfasst ungefähr 30% der im Jahre 2004 von COMPASS aufgenommenen Daten und entspricht einer effektiven integrierten Luminosität von $142.4\,\mathrm{pb}^{-1}$ $\pm 10\%$. Dieser Luminositätswert wird über die Bestimmung der Strukturfunktion $F_2$ des Nukleons und deren Vergleich zu Literaturwerten verfiziert. Dieses Ergebnis dient als Basis für die Bestimmung des Wirkungsquerschnitts für die quasireelle Photoproduktion von geladenen Hadronen mit hohem Transversalimpuls in der Muon-Deuteron Streuung bei einer Schwerpunktsenergie von $\sqrt{s} = 17.4\,\mathrm{GeV}$. Die Messung eines Wirkungsquerschnitts für Hadronenproduktion in einem dicken Festkörper-Target stellt im Vergleich zu Collider-Messungen solcher Prozesse eine größere Herausforderung dar. Sekundäre hadronische Wechselwirkungen im Targetmaterial werden genau untersucht und im Ergebnis berücksichtigt. Der Wirkungsquerschnitt wird in mehreren Bereichen der Pseudo-Rapidität der Hadronen und separiert nach Hadronenladungen präsentiert. Die Ergebnisse werden diskutiert und mit Rechnungen der perturbativen Quantenchromodynamik in nächstführender Ordnung verglichen. Dieser Vergleich dient als Test für die Anwendbarkeit solcher Rechnungen auf die Produktion von Hadronen mit hohem Transversalimpuls bei COMPASS-Energien.

Der zweite Teil dieser Dissertation beschäftigt sich mit der Entwicklung neuer Technologien für die Spurrekonstruktion von geladenen Teilchen in Hochraten-Experimenten. Eine neue Art der Zeitprojektionskammer (TPC), die GEM-Folien anstelle von Proportionaldrähten zur Gasverstärkung einsetzt, wird vorgestellt. Diese Technologie ermöglicht die Benutzung von Zeitprojektionskammern in Experimenten mit Trigger-Raten von mehr als ungefähr 1 kHz. Mehrere wichtige Beiträge zu dieser Entwicklung werden in dieser Arbeit vorgestellt. Außerdem wird eine neuartige generische Software für die Anpassung von Spurparametern in Hochenergiephysik-Experimenten präsentiert. Dieses Programm heißt GENFIT und wird in den $\overline{\mathrm{P}}$ANDA, Belle-II und GEM-TPC Experimenten eingesetzt.

# Contents

# Chapter 1

# Introduction

The year 2011 marks the centennial anniversary of the discovery of the atomic nucleus by E. Rutherford [1]. He showed that the large-angle scattering of $\alpha$ particles from a radioactive source off a thin gold foil can only be explained if the positive charge carriers, which balance out the charge of the spread-out electrons, are concentrated at the center of the atom. Experiments in which particles are scattered off targets to learn about their inner structure have been a very successful tool ever since. The length scale that can be resolved in an elastic scattering experiment is given by the reduced de Broglie wave length $\lambda\!\!\!^{-} = \hbar/|\mathbf{q}|$, with the reduced Planck constant $\hbar = 197\,\mathrm{fm\,MeV}/c$ and the momentum transfer $|\mathbf{q}|$. Particle accelerators deliver projectiles with momenta much greater than those from radioactive sources, which are needed to investigate structures smaller than the size of atomic nuclei and their constituents.
The atomic nuclei consist of protons and neutrons, which are collectively referred to as nucleons. The nucleons are composite systems themselves which are made up of elementary particles called quarks. Quarks interact with each other via the strong interaction, which is one of the four fundamental forces of nature. The other three are the electromagnetic force, the weak interaction, and gravity. With the exception of gravity, physicists have developed quantum field theories that successfully describe the interactions in terms of the exchange of quanta of the corresponding fields. Quantum Electrodynamics (QED) describes the electromagnetic interaction between particles carrying electrical charge by the exchange of photons. QED processes can be calculated in perturbation theory with great accuracy, which is owed to the fact that the electromagnetic coupling constant is sufficiently small.
The strong interaction between quarks is described by the exchange of gluons in the theory of Quantum Chromodynamics (QCD). The equivalent to the electrical charge in QCD is the so-called color charge. The term color has nothing to do with the visible colors, but just expresses the analogy that the color charge comes in three different kinds which neutralize each other, just like the colors red, green, and blue. The main difference between QCD and QED is that the gluons carry color charge themselves, while the photons are electrically neutral. This enables gluon-gluon coupling, which leads to a diverging increase of the coupling strength with increasing distances between the quarks. At very short distances, i.e. at large momentum transfers, the coupling constant is small, which allows a perturbative treatment of QCD. The small coupling at large momentum transfers is referred to as the asymptotic freedom of QCD. The very large coupling at higher distances disallows the observation of free quarks and leads to the confinement of quarks

in color-neutral particles collectively called hadrons. It is an astounding fact that the masses of the elementary quarks, which are believed to be generated by the coupling to the Higgs field in the standard model of particle physics, account only for about one percent of the masses of protons and neutrons. The rest of the mass is generated by the force field of the strong interaction, which is hence responsible for about 99 percent of the mass of all matter we know.

The inner structure of matter is investigated in scattering experiments that are conducted at particle-accelerator laboratories. A high-energy beam of particles is shot onto a stationary nuclear target or collided with another particle beam. The structure of the beam particles, the target particles, or of other short-lived particles that are produced in the process is imprinted in the distribution of the particles that constitute the final state of the scattering process. Particle spectrometers are used to identify the 4-momenta and vertices of these particles. Besides calorimetric and particle-identification measurements, this is achieved by measuring the 3-momenta of charged particles by tracking them in magnetic fields with position-sensitive detectors. The experiments proceed in the following main steps:

(I) Design, construction, and operation of particle detectors which electronically record information about the passage of particles.

(II) Reconstruction of the recorded raw data, to identify the 4-momenta and vertices of particles. One of the main aspects of this step is the reconstruction of particle trajectories in the magnetic field arrangements.

(III) Analysis of the distributions of particle vertices and 4-momenta to extract the sought-after information about the structure of the particles and their interactions.

Three projects from this spectrum of tasks in experimental high-energy physics have been realized in the course of the presented PhD project: (I) Prototyping of a Time Projection Chamber with Gas Electron Multiplier amplification for high-rate experiments, (II) development of a generic software for track fitting in nuclear and particle physics experiments, and (III) the analysis of reconstructed data from the COMPASS experiment for the first measurement of the cross section for the production of hadrons with high transverse momenta at COMPASS.

The first part of this thesis describes the first measurement of the cross section for the production of hadrons with high transverse momenta (high $p_T$) at the COMPASS experiment [2] at CERN and its theoretical and experimental background. The structure and spin structure of nucleons is introduced in chapter 2. The measurement of the polarization of gluons in the nucleon is one of the main goals of the COMPASS experiment. A sizable polarization of the gluons in the nucleon would be a possible solution of the "spin puzzle of the nucleon", which describes the fact that the nucleon spin of $\hbar/2$ can not be fully explained by the polarization of the quark spins. One possibility to constrain the gluon polarization is the comparison of the double-spin asymmetry of the cross section for the quasi-real photoproduction of high-$p_T$ hadrons measured in COMPASS with a next-to-leading order perturbative QCD (NLO pQCD) calculation [3]. But before this analysis can be trusted it must first be established that the pQCD framework can correctly predict the unpolarized cross section for the same process to evaluate the importance of higher-order corrections that are missing in the calculation. The calculation of high-$p_T$ hadron production in pQCD is introduced in chapter 3. The measurement of the unpolarized cross section for the quasi-real

photoproduction of high-$p_T$ hadrons that allows the discussed evaluation of the applicability of pQCD is the main result of the presented dissertation.
The COMPASS experiment and its physics program are discussed in chapter 4. Thus far, COMPASS has not published any absolutely normalized measurements of cross sections from its muon-scattering program, because the experiment does not have a dedicated luminosity monitoring system. It was specifically designed for direct measurements of double-spin asymmetries of cross sections. The first determination of the luminosity for COMPASS data by the direct measurement of the beam flux and the application of corrections for all dead times and inefficiencies is presented in chapter 5. The result is checked by the determination of the well-known structure function $F_2$ and its comparison to literature. This is followed by the determination of the cross section for the quasi-real photoproduction of high-$p_T$ hadrons at the center-of-mass energy of $\sqrt{s} = 17.4\,\mathrm{GeV}$ in chapter 6. The measurement of a hadron-production cross section in the thick solid-state target of COMPASS is challenging. The issue of a possible background to the yield of high-$p_T$ hadrons produced in the muon-scattering vertices from hadrons produced in secondary reactions in the target material is thoroughly investigated and taken into account in the systematic error. The results presented here have recently been approved for publication by the COMPASS collaboration. The discussion of the results and their comparison to the pQCD calculations concludes the first part of this dissertation.

The second part of this thesis describes the development of a new type of Time Projection Chamber (TPC) for high-rate experiments and of an experiment-independent software for track-fitting. These projects were born in the framework of the $\overline{\mathrm{P}}$ANDA experiment at the future FAIR facility, which will be an extension of the present site of GSI at Darmstadt. The $\overline{\mathrm{P}}$ANDA experiment will investigate numerous aspects of the strong interaction in the non-perturbative regime by measurements such as precision charmonium spectroscopy, searches for hybrids or glueballs, Drell-Yan measurements, or the measurement of the time-like electromagnetic form factors of the proton. The experiment and its physics program are introduced in chapter 7. The development of a TPC which uses GEM (Gas Electron Multiplier) foils for gas amplification instead of the traditional proportional wires is presented in chapter 8. A TPC which uses proportional wires needs to be equipped with a gating grid, which is used to evacuate the large number of ions that are created in the avalanche amplification from the chamber. The necessity of employing a gating grid, however, limits the usability of TPCs to experiments with trigger rates below about 1 kHz. The intrinsic suppression of the backflow of ions in GEM-amplification stages is a possible solution for operating a TPC without a gating grid and hence for using it in high-rate experiments. A small GEM-TPC test chamber, which had been built at TUM before, has been upgraded and tested with particle beams at the ELSA facility in Bonn and at the COMPASS experiment. This development was essential for the construction of a large GEM-TPC prototype with $\sim 10,000$ electronic readout channels, a drift length of 728 mm, and an outer diameter of 308 mm, which has been successfully operated in the FOPI spectrometer at GSI, by the GEM-TPC collaboration.
The final part of this thesis introduces GENFIT, which is a track-fitting software that is designed in a completely modular way to allow its use in different nuclear and particle physics experiments with a minimal amount of interfacing. It is independent of the concrete choice of tracking detectors and their arrangement as well as of the magnetic field geometry of the experiment. The development of GENFIT and its implementation have been done together with S. Neubert at TUM.

The software is up to now being used in the $\overline{\text{P}}$ANDA, Belle-II, and FOPI experiments. It has been written in the C++ programming language and is available as free software. The project is briefly introduced in chapter 9. A detailed description of the GENFIT concept has been published in a dedicated paper [4], which is considered an important part of this dissertation and is hence attached in appendix H.

Chapter 10 concludes this thesis with a summary and gives an outlook on the future prospects of the presented projects.

# Chapter 2

# Measurements of the Structure of the Nucleon

The structure of nucleons can be studied in experiments in which highly-energetic electrons or muons are scattered off protons or deuterons. The kinematical variables which are used to describe the scattering cross sections of such processes are introduced in Sec. 2.1. The fact that nucleons have a substructure of point-like particles was first revealed in the deep inelastic scattering (DIS) experiments conducted at the Stanford Linear Accelerator Center (SLAC) in the late 1960s. The technique of DIS and basic results on the nucleon structure are described in Sec. 2.2. When the DIS experiments are carried out with polarized beams and polarized targets they allow access to the spin structure of the nucleon, which is discussed in Sec. 2.3. The polarization of the gluons in the nucleon plays an important role for understanding the spin structure of nucleons. Measurements of the gluon polarization are discussed in Sec. 2.4.

## 2.1 Kinematical Variables

The kinematical variables which are used to describe the *inclusive scattering* of leptons[1] off nucleons are introduced first. The term *inclusive* denotes that only the scattered beam particle is analyzed in the final state of the scattering process. The reaction is:

$$lN \rightarrow l'X \quad , \tag{2.1}$$

where $N$ is the target nucleon, $l$ is the incoming lepton, $l'$ is the scattered lepton, and $X$ is an undetected rest of particles. The 4-momentum of the incoming lepton is $k = [E/c, \mathbf{k}]$ and that of the scattered muon is $k' = [E'/c, \mathbf{k}']$. The target nucleon is at rest and has the 4-momentum $P = [Mc, \mathbf{0}]$. The process is usually described in the one-photon exchange picture, which is depicted in Fig. 2.1. The virtual photon, which is exchanged between the lepton and the nucleon, has the 4-momentum $q = k - k'$.
The negative 4-momentum squared transfer of the reaction, which is also referred to as the photon

[1] in the scope of this discussion the term *leptons* just refers to electrons or muons. Neutrino scattering is not discussed in this thesis.

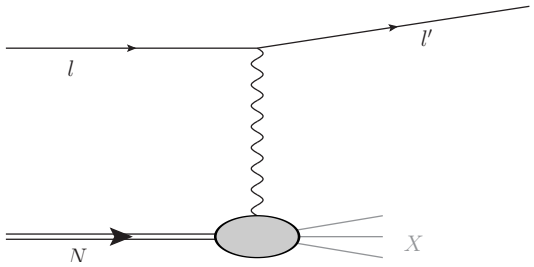


**Figure 2.1:** Fully inclusive lepton-nucleon scattering in the one-photon exchange picture: $lN \rightarrow l'X$, where $X$ is the undetected rest of particles.

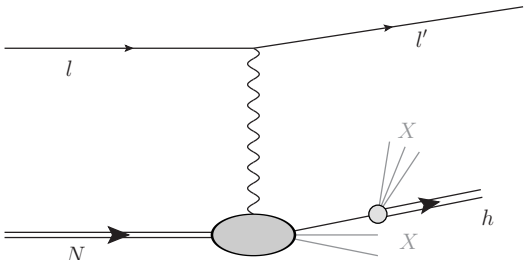


**Figure 2.2:** Semi-inclusive lepton-nucleon scattering, where an inclusive hadron, $h$, is observed in addition to the scattered lepton: $lN \rightarrow l'hX$.

virtuality, is

$$Q^2 = -q^2 = -2m^2c^2 + 2\left(\frac{EE'}{c^2} - |\mathbf{k}||\mathbf{k}'|\cos\vartheta\right) \overset{|\mathbf{k}'|\gg mc}{\approx} -2m^2c^2 + \frac{4EE'}{c^2}\sin^2\frac{\vartheta}{2} \quad , \tag{2.2}$$

where $m$ is the lepton mass and $\vartheta$ is the angle between the incoming lepton and the outgoing lepton. In the laboratory system, which is used for the definition of all variables from now on, the Lorentz-invariant variable $\nu = \frac{P\cdot q}{M}$ is equal to the energy loss of the muon

$$\nu = E - E' \quad . \tag{2.3}$$

Often, it is more convenient to use the dimension-less variable

$$y = \frac{\nu}{E} \quad , \tag{2.4}$$

which is the relative energy loss of the muon. Another Lorentz-invariant variable which is of great importance for deep inelastic scattering, which is discussed in the next section, is the Bjorken scaling variable

$$x_{\mathrm{Bj}} = \frac{Q^2}{2M\nu} \quad . \tag{2.5}$$

The Bjorken scaling variable is a measure for the inelasticity of the scattering process. The elastic scattering off nucleons proceeds at $x_{\mathrm{Bj}} = 1$, and all inelastic scattering at $x_{\mathrm{Bj}} \in [0, 1[$.
The invariant mass, $W$, of the undetected hadronic final state is given by the center of mass energy of the photon-nucleon system

$$W^2c^2 = (P+q)^2 = M^2c^2 - Q^2 + 2M\nu = M^2c^2 + Q^2\cdot\left(\frac{1-x_{\mathrm{Bj}}}{x_{\mathrm{Bj}}}\right) \quad . \tag{2.6}$$

In *semi-inclusive scattering* reactions, an inclusive hadron, $h$, is detected in the final state in addition to the scattered lepton:

$$lN \rightarrow l'hX \quad . \tag{2.7}$$

Such a reaction is shown in Fig. 2.2. The energy of the hadron, $E_h$, is expressed in units of the virtual photon energy with the variable

$$z = \frac{E_h}{\nu} \quad . \tag{2.8}$$

Another useful variable is the angle $\theta$ between the 3-momenta of the virtual photon and the hadron. A more commonly used variable is the pseudo-rapidity, which in the laboratory system is

$$\eta_{\text{lab}} = -\ln\tan\frac{\theta}{2} \quad . \tag{2.9}$$

It is transformed into lepton-nucleon center-of-mass system as follows:

$$\eta_{\text{c.m.s.}} = \eta_{\text{lab}} - \frac{1}{2}\ln\frac{2E}{M} \quad . \tag{2.10}$$

## 2.2 Deep Inelastic Scattering – Nucleon Structure

The inelastic scattering of leptons off nucleons can excite various resonances in the nucleon in the invariant mass region $W \lesssim 2\,\text{GeV}/c^2$. Scattering reactions beyond this resonance regime which feature a large momentum transfer are called deep inelastic scattering (DIS). In the case of inclusive scattering the large momentum transfer is ensured by a large photon virtuality (the selection $Q^2 > 1\,(\text{GeV}/c)^2$ is typical).
The one-photon exchange picture of Fig. 2.1 which is used to describe DIS processes implies that the scattering cross section must factorize into a tensor which describes the lepton vertex, $L_{\mu\nu}$, contracted with a tensor, $W^{\mu\nu}$, which describes the hadron vertex. The experimental cross sections of DIS are usually corrected for higher-order QED effects beyond one-photon exchange (radiative corrections) before they are used for interpretations in regard to the nucleon structure.
The unpolarized cross section [2] for the inclusive scattering of a lepton into the solid angle element $\mathrm{d}\Omega$ about $\mathbf{k}'$ with a final-state energy in the range $[E', E' + dE']$ is

$$\frac{\mathrm{d}^2\sigma}{\mathrm{d}\Omega\mathrm{d}E'} = \frac{\alpha_{\text{em}}^2(\hbar c)^2}{Q^4}\frac{E'}{E}\cdot L_{\mu\nu}W^{\mu\nu} \quad , \tag{2.11}$$

where $\alpha_{\text{em}}$ is the fine-structure constant and $\hbar$ is the reduced Planck constant. Experiments usually do not analyze events with $|\mathbf{k}'| \to 0$; the selection of events with $y < 0.9$ is common practice. For beam momenta which are very large compared to the lepton mass, e.g. the $20\,\text{GeV}/c$ electron beam of SLAC or the $160\,\text{GeV}/c$ muon beam of the COMPASS experiment, this implies $E/c \approx |\mathbf{k}|$ and $E'/c \approx |\mathbf{k}'|$. In this limit the cross section can be transformed to:

$$\frac{\mathrm{d}^2\sigma}{\mathrm{d}x_{\text{Bj}}\mathrm{d}Q^2} = \frac{\alpha_{\text{em}}^2\pi(\hbar c)^2}{E^2Q^4}\frac{\nu}{x_{\text{Bj}}}\cdot L_{\mu\nu}W^{\mu\nu} \quad . \tag{2.12}$$

The tensors, $L_{\mu\nu}$ and $W^{\mu\nu}$, can both be split into a part that is symmetrical under the exchange of $\mu$ and $\nu$ and a part that is anti-symmetrical under the index exchange:

$$L_{\mu\nu} = L_{\mu\nu}^{(\text{S})} + L_{\mu\nu}^{(\text{A})}, \qquad W^{\mu\nu} = W^{\mu\nu(\,\text{S})} + W^{\mu\nu\,(\text{A})}. \tag{2.13}$$

[2] there are many text books (e.g. [5] or [6]) and review articles (e.g. [7]) on the structure of nucleons. The derivations and discussions presented in this section and the next can be found in more mathematical detail in such texts.

For the unpolarized cross section, in which all lepton and nucleon spins are summed over, only the symmetrical parts of the tensors have to be considered. The symmetrical lepton tensor is

$$L_{\mu\nu}^{(\mathrm{S})} = 2 \cdot \left[ k'_\mu k_\nu + k_\mu k'_\nu - g_{\mu\nu}(k \cdot k' - m^2c^2) \right] \quad . \tag{2.14}$$

The most general form of the symmetrical hadron tensor is constructed from $g^{\mu\nu}$ and combinations of the two independent 4-momenta $q^\mu$ and $P^\mu$ ($q^\mu q^\nu$, $P^\mu P^\nu$, and $q^\mu q^\nu + P^\mu P^\nu$) each multiplied with a structure function. The structure functions parameterize the unknown structure of the nucleon. Current conservation implies that there are only two independent structure functions $W_1$ and $W_2$ and leads to the form

$$W^{\mu\nu\,(\mathrm{S})} = W_1 \left( -g^{\mu\nu} + \frac{q^\mu q^\nu}{q^2} \right) + \frac{1}{M^2c^2} W_2 \left( P^\mu - \frac{P \cdot q}{q^2} q^\mu \right) \left( P^\nu - \frac{P \cdot q}{q^2} q^\nu \right) \quad . \tag{2.15}$$

The contraction of the tensors is:

$$\begin{aligned} L_{\mu\nu}^{(\mathrm{S})} W^{\mu\nu\,(\mathrm{S})} = \; & 2W_1 \left( 2k \cdot k' - 4m^2c^2 \right) + 2\frac{W_2}{M^2c^2} \left( 2(k' \cdot P)(k \cdot P) - (k \cdot k' - m^2c^2)M^2c^2 \right) \\ \overset{\text{lab}}{=} \; & 2W_1 Q^2 \left( 1 - \frac{2m^2c^2}{Q^2} \right) + W_2 \left( \frac{4EE'}{c^2} - Q^2 \right) \\ \overset{m^2c^2 \ll Q^2}{\approx} \; & \frac{4EE'}{c^2} \left( 2W_1 \sin^2 \frac{\vartheta}{2} + W_2 \cos^2 \frac{\vartheta}{2} \right) \end{aligned} \tag{2.16}$$

The approximation in the last line is usually applied for electron scattering. It is, however, not adopted for this work, because the COMPASS experiment uses a muon beam for which the mass terms are not negligible for low values of $Q^2$.
The cross section for unpolarized inclusive lepton scattering is:

$$\frac{\mathrm{d}^2\sigma_{\mathrm{unpol}}}{\mathrm{d}x_{\mathrm{Bj}}\mathrm{d}Q^2} = \frac{\alpha_{\mathrm{em}}^2 \pi (\hbar c)^2}{E^2 Q^4} \frac{\nu}{x_{\mathrm{Bj}}} \cdot \left[ 2W_1 Q^2 \left( 1 - \frac{2m^2c^2}{Q^2} \right) + W_2 \left( \frac{4EE'}{c^2} - Q^2 \right) \right]. \tag{2.17}$$

The first measurements of the inclusive DIS cross section were conducted at SLAC in the late 1960s. Somewhat surprisingly, they showed that the cross section beyond $W > 2\,\mathrm{GeV}/c^2$ depends only very weakly on $Q^2$ [8, 9], much less than what would have been expected if the nucleon would be a soft, uniform distribution of charge. This was the first indication that the nucleons consist of charged, point-like scattering centers. This result is a great analogy to Rutherford's discovery of atomic nuclei, which he concluded from the higher count rates for particle scattering at high angles than what would have been expected for evenly distributed charge carriers in the atoms. In about ten years following the first SLAC measurements, the charged scattering centers in the nucleon were identified with the quarks which had been introduced before to explain the observation of the multiplets of mesons and baryons [10].
The structure functions of the nucleon exhibit a characteristic known as *scaling*, which had been predicted by Bjorken and was confirmed by the early SLAC experiments. Scaling means that the structure functions $W_1$ and $\nu W_2$ depend on the ratio of $Q^2$ and $\nu$, given by $x_{\mathrm{Bj}} = Q^2/2M\nu$, but not on the individual values of $Q^2$ or $\nu$. This behavior directly implies that the deep inelastic scattering of leptons off nucleons is really the elastic scattering of leptons off point-like constituents of the nucleons, which are called partons. A strict relation between $Q^2$ and $\nu$ generally implies elastic scattering. In a reference frame in which the nucleon is moving with infinite momentum, $x_{\mathrm{Bj}}$ is the

fraction of the 4-momentum of the nucleon that is carried by the struck parton. A photon with a particular value of $x_{\mathrm{Bj}}$ can only be absorbed by a parton with the correct momentum fraction $x_{\mathrm{Bj}}$ in an elastic scattering process. The leptons are incoherently scattered off single partons, which are treated as free particles in the scattering process. This is justified because the strong interaction is rather weak at the short length scales which are probed in scattering with large momentum transfer (asymptotic freedom). Also, a scattering process in which a large amount of energy $\nu$ is transferred to the parton happens on a very short time scale, while the parton-parton interaction is slowed down by the time dilatation in the fast moving nucleon.
It is customary to replace the structure functions $W_1(Q^2, \nu)$ and $W_2(Q^2, \nu)$ with the dimension-less functions

$$\begin{aligned} F_1(x_{\mathrm{Bj}}) &= Mc^2 W_1(Q^2, \nu) \\ F_2(x_{\mathrm{Bj}}) &= \nu W_2(Q^2, \nu) \quad . \end{aligned} \tag{2.18}$$

The new structure functions are related to each other by the Callan-Gross relation

$$F_2(x_{\mathrm{Bj}}) = 2x_{\mathrm{Bj}} F_1(x_{\mathrm{Bj}}) \quad , \tag{2.19}$$

which can be derived from the assumption that the partons are point-like spin $\hbar/2$ particles. The experimental confirmation of the relation (2.19) was a major step in the identification of the charged partons with the spin $\hbar/2$ quarks.
The quark parton model is completed by the introduction of the parton distribution functions (PDFs), $q_f(x_{\mathrm{Bj}})$, which are related to the structure functions as follows:

$$\begin{aligned} F_2(x_{\mathrm{Bj}}) = 2x_{\mathrm{Bj}} F_1(x_{\mathrm{Bj}}) &= x_{\mathrm{Bj}} \sum_f e_f^2 q_f(x_{\mathrm{Bj}}) \\ &= x_{\mathrm{Bj}} \cdot \left[ \frac{4}{9} u(x_{\mathrm{Bj}}) + \frac{4}{9} \bar{u}(x_{\mathrm{Bj}}) + \frac{1}{9} d(x_{\mathrm{Bj}}) + \frac{1}{9} \bar{d}(x_{\mathrm{Bj}}) + \frac{1}{9} s(x_{\mathrm{Bj}}) + \frac{1}{9} \bar{s}(x_{\mathrm{Bj}}) \right] \quad . \end{aligned} \tag{2.20}$$

The PDF $q_f(x_{\mathrm{Bj}})$ is the number density for finding a quark of flavor $f$ with a momentum fraction $x_{\mathrm{Bj}}$ in the nucleon. Only the quark distributions contribute directly to the structure functions, because the gluons are electrically neutral. The total fraction of the momentum of the nucleon that is carried by the quarks and antiquarks can be estimated from the structure function of the deuteron which is (disregarding small corrections) the mean value of the structure functions of the proton and the neutron:

$$F_2^d(x_{\mathrm{Bj}}) \approx \frac{F_2^p(x_{\mathrm{Bj}}) + F_2^n(x_{\mathrm{Bj}})}{2} = \frac{5}{18} \sum_{f=u,d,\bar{u},\bar{d}} q_f^d(x_{\mathrm{Bj}}) + \frac{1}{9} \left( s^d(x_{\mathrm{Bj}}) + \bar{s}^d(x_{\mathrm{Bj}}) \right) \quad , \tag{2.21}$$

where isospin symmetry has been used, and 5/18 is the mean squared charge of $u$ and $d$ quarks. Neglecting the rather small contributions of the strange quarks, the total fraction of the nucleon momentum carried by the quarks and antiquarks can be estimated as:

$$\int_0^1 \sum_f x_{\mathrm{Bj}} q_f^d(x_{\mathrm{Bj}}) \, \mathrm{d}x_{\mathrm{Bj}} \approx \frac{18}{5} \int_0^1 F_2^d(x_{\mathrm{Bj}}) \, \mathrm{d}x_{\mathrm{Bj}} \approx 0.5 \quad . \tag{2.22}$$

The rest of nucleon momentum is carried by the electrically neutral gluons, whose role in the nucleon can be understood in a much more quantitative way in the phenomenon of *scaling violation*: When $F_2$ is probed over a much wider kinematical range than was available at SLAC, the scaling of the structure function is found to be violated:

$$F_2(x_{\mathrm{Bj}}) \rightarrow F_2(x_{\mathrm{Bj}}, Q^2) \quad . \tag{2.23}$$

The structure function $F_2$ is found to logarithmically depend on $Q^2$ at constant values of $x_{\mathrm{Bj}}$. The structure function at high $x_{\mathrm{Bj}}$ decreases with increasing $Q^2$, while the structure function at low $x_{\mathrm{Bj}}$ increases with increasing $Q^2$. In other words, with increasing $Q^2$ one can find less and less quarks with a high momentum fraction $x_{\mathrm{Bj}}$. The momentum values of the quarks are shifted towards smaller values, if the nucleon is probed at shorter and shorter length scales. This effect is well understood and calculable in QCD: Quarks can emit gluons. When a quark emits a gluon, it loses part of its momentum to the gluon. Gluons can, in turn, generate quark-antiquark pairs, which is how the sea quarks are generated. Effectively, a quark of a given value of $x_{\mathrm{Bj}}$ has a substructure of gluons, quarks, and antiquarks which each have lower values of $x_{\mathrm{Bj}}$. While the quark is seen as a point-like particle which does not have a substructure at one scale $Q_a^2$, the partonic substructure of the quark can be resolved at a scale $Q_b^2 > Q_a^2$, i.e. at smaller distance scales. If the nucleon is probed at $Q_b^2$, the photon can interact with one of the low-$x_{\mathrm{Bj}}$ quarks that are generated by the gluon emission of the high-$x_{\mathrm{Bj}}$ quark.
The scaling violations can be calculated with a very high accuracy in perturbative QCD with the DGLAP[3] *evolution* equations. They relate the $Q^2$ dependence of a quark PDF at a given value of $x_{\mathrm{Bj},0}$ to the quark PDFs and gluon PDF, $G(x_{\mathrm{Bj}})$, over the range $x_{\mathrm{Bj}} > x_{\mathrm{Bj},0}$, because the quark can be generated by the higher-$x_{\mathrm{Bj}}$ quark distribution via gluon emission, or by a higher-$x_{\mathrm{Bj}}$ gluon that has generated a quark-antiquark pair. Equivalently, the $Q^2$ dependence of the gluon PDF at $x_{\mathrm{Bj},0}$ is related to the higher $x_{\mathrm{Bj}}$ quark and gluon distributions. While the gluon PDF is quite small at large $x_{\mathrm{Bj}}$ it diverges towards $x_{\mathrm{Bj}} \rightarrow 0$. There are, so to speak, infinitely many gluons in a nucleon. The fact that the scaling violation are calculable with a very high accuracy provides a lot of confidence in the fact that QCD is indeed the correct theory to describe the interaction between the quarks and gluons in the nucleon.
The introduced PDFs of the quarks, antiquarks, and gluons are universal objects, which parameterize information on the nucleon structure in a process-independent way. PDFs which are constrained by DIS measurements for instance enable good perturbative QCD calculations of cross sections for instance in proton-proton scattering. PDFs that are constrained by measurements at fixed-target kinematics at $Q^2$ values of a few $(\mathrm{GeV}/c)^2$ can be evolved to much higher scales accessible in collider experiments, where they still provide valid information on the nucleon structure and enable perturbative QCD calculations of cross sections.
Finally, the DIS cross section of Eq. (2.17) is expressed in terms of $F_2$ and $R$, which is the ratio of the cross section of nucleons for the absorption of virtual photons of helicity 0 (also called longitudinally polarized photons) and the cross section for the absorption of virtual photons of helicity

[3] please be referred to a text book on theoretical high energy physics (e.g. [5]) for a further explanation of the DGLAP equations and for the references to the original papers.

$\pm 1$ (also called transversely polarized photons):

$$R(x_{\mathrm{Bj}}, Q^2) = \frac{\sigma_{\mathrm{L}}}{\sigma_{\mathrm{T}}} = \frac{\left(1 + \frac{\nu^2}{Q^2 c^2}\right) \cdot W_2(Q^2, \nu) - W_1(Q^2, \nu)}{W_1(Q^2, \nu)} = \left(1 + \gamma^2\right) \cdot \frac{F_2(x_{\mathrm{Bj}}, Q^2)}{2 x_{\mathrm{Bj}} F_1(x_{\mathrm{Bj}}, Q^2)} - 1 \quad , \tag{2.24}$$

where

$$\gamma^2 = \frac{4 M^2 c^2 x_{\mathrm{Bj}}^2}{Q^2} \quad . \tag{2.25}$$

The form of the cross section which is used to extract $F_2$ from the inclusive muon-scattering cross section measured in COMPASS in chapter 5 is,

$$\frac{\mathrm{d}^2\sigma_{\mathrm{unpol}}}{\mathrm{d}x_{\mathrm{Bj}}\mathrm{d}Q^2} = \frac{4\alpha_{\mathrm{em}}^2 \pi \hbar^2}{Q^4 x_{\mathrm{Bj}}} \cdot F_2(x_{\mathrm{Bj}}, Q^2) \cdot \left\{ 1 - y - \frac{x_{\mathrm{Bj}}^2 y^2 M^2 c^2}{Q^2} + \frac{y^2 + \frac{Q^2 c^2}{E^2}}{2 \cdot [1 + R(x_{\mathrm{Bj}}, Q^2)]} \left(1 - \frac{2 m^2 c^2}{Q^2}\right) \right\}. \tag{2.26}$$

## 2.3 Spin Structure of Nucleons

It is of fundamental interest to understand how the nucleon spin of $\hbar/2$ is made up from its constituents. The nucleon-spin sum rule is

$$\frac{1}{2} = \frac{1}{2}\Delta\Sigma(Q^2) + \Delta G(Q^2) + L_q(Q^2) + L_g(Q^2), \tag{2.27}$$

where $\Delta\Sigma$ quantifies the quark and antiquark spin polarization, $\Delta G$ is the gluon polarization, $L_q$ is the total orbital angular momentum of the quarks and antiquarks, and $L_g$ is the orbital angular momentum of the gluons. The form in which the quark polarization is written, speaks for the expectation that the nucleon spin could be entirely due to the quark polarization, which would mean $\Delta\Sigma = 1$ and all other terms equal to zero. More realistic, relativistic models of the nucleon show that even if the quark-spin polarization was entirely responsible for the nucleon spin, one would expect a value of $\Delta\Sigma \approx 0.6$ (see e.g. [11]). This somewhat naive expectation is found to be in disagreement with the experimental data, which shall be explained in more detail in this section. The investigation of the spin structure of nucleons remains a very active field of research that tries to quantify the individual contributions of all terms in the nucleon-spin sum rule of Eq. (2.27).

The spin structure of nucleons can be accessed experimentally by measuring double-spin asymmetries in the DIS cross section of Eq. (2.11). The longitudinal lepton-nucleon double-spin asymmetry

$$A_{\parallel} = \frac{\frac{\mathrm{d}^2\sigma^{\rightarrow\Leftarrow}}{\mathrm{d}x_{\mathrm{Bj}}\mathrm{d}Q^2} - \frac{\mathrm{d}^2\sigma^{\rightarrow\Rightarrow}}{\mathrm{d}x_{\mathrm{Bj}}\mathrm{d}Q^2}}{2\frac{\mathrm{d}^2\sigma_{\mathrm{unpol}}}{\mathrm{d}x_{\mathrm{Bj}}\mathrm{d}Q^2}} \tag{2.28}$$

is measured with a longitudinally polarized lepton beam, which is indicated by the superscript "$\rightarrow$", and a longitudinally polarized target with polarization orientations which are parallel to the

beam polarization, "⇒", and anti-parallel to the beam polarization, "⇐". The quantity $A_{\parallel}$ can be directly measured by comparing the count rates for DIS on targets with different polarizations that are exposed to an equal beam flux.
The numerator of $A_{\parallel}$ can be derived in analogy to Eqs. (2.11)-(2.16) from the anti-symmetric parts of the lepton and hadron tensors:

$$L_{\mu\nu}^{(\mathrm{A})} = 2im\epsilon_{\mu\nu\alpha\beta}s^{\alpha}q^{\beta} \tag{2.29}$$

$$W^{\mu\nu\,(\mathrm{A})} = \frac{i}{P\cdot q}\epsilon_{\mu\nu\alpha\beta}q^{\alpha}\left[S^{\beta}g_1(x_{\mathrm{Bj}}) + \left(S^{\beta} - \frac{S\cdot q}{P\cdot q}P^{\beta}\right)g_2(x_{\mathrm{Bj}})\right] \quad , \tag{2.30}$$

where $s$ is the spin of the incoming lepton, $S$ is the spin of the target nucleon, and $\epsilon_{\mu\nu\alpha\beta}$ is the totally anti-symmetric Levi-Civita tensor[4]. The hadronic tensor has been directly expressed in the polarized structure functions $g_1$ and $g_2$, which exhibit Bjorken scaling. The numerator of $A_{\parallel}$ is:

$$\frac{\mathrm{d}^2\sigma^{\rightarrow\Leftarrow}}{\mathrm{d}x_{\mathrm{Bj}}\mathrm{d}Q^2} - \frac{\mathrm{d}^2\sigma^{\rightarrow\Rightarrow}}{\mathrm{d}x_{\mathrm{Bj}}\mathrm{d}Q^2} = \frac{16\alpha_{\mathrm{em}}^2\pi\hbar^2 y}{Q^4}\cdot\left[\left(1 - \frac{y}{2} - \frac{y^2\left(M^2x_{\mathrm{Bj}}^2 + m^2\right)c^2}{Q^2}\right)g_1 + x_{\mathrm{Bj}}\frac{Mc^2}{E}g_2\right]. \tag{2.31}$$

One can see immediately that the contribution of $g_2$ is very small at high lepton energies, as it is suppressed with $Mc^2/E$. It is customary to introduce the photon-nucleon asymmetries, which are directly related to $g_1$ and $g_2$:

$$A_2 = \gamma\left(\frac{g_1 + g_2}{F_1}\right) \tag{2.32}$$

$$A_1 = \frac{g_1 - \gamma^2 g_2}{F_1} = (1+\gamma^2)\frac{g_1}{F_1} - \gamma A_2 \quad . \tag{2.33}$$

The lepton-nucleon asymmetry $A_{\parallel}$ is related to the photon-nucleon asymmetries like

$$\frac{A_{\parallel}}{D} = A_1 + \eta A_2 = (1+\gamma^2)\frac{g_1}{F_1} + (\eta - \gamma)A_2 \quad , \tag{2.34}$$

where the new kinematical factors[5] are,

$$D = \frac{y\left[(1+\gamma^2 y/2)(2-y) - 2y^2m^2c^2/Q^2\right]}{y^2(1-2m^2c^2/Q^2)(1+\gamma^2) + 2(1+R)(1-y-\gamma^2y^2/4)} \tag{2.35}$$

$$\eta = \gamma\frac{\left[1 - y - y^2(\gamma^2/4 + m^2c^2/Q^2)\right]}{(1-y/2)(1+\gamma^2y/2) - y^2m^2c^2/Q^2} \quad . \tag{2.36}$$

Since the factor $(\eta - \gamma)$ and the asymmetry $A_2$ are small, it is a good approximation to extract $g_1$ directly from $A_{\parallel}$ (sometimes absorbing the uncertainty due to $A_2$ into the systematic errors) [7, 12, 13]:

$$g_1 \approx \frac{A_{\parallel}}{D}\frac{F_1}{1+\gamma^2} = \frac{A_{\parallel}}{D}\frac{F_2}{2x_{\mathrm{Bj}}(1+R)} \quad . \tag{2.37}$$

$A_{\parallel}$ is directly measured in polarized DIS experiments, while $F_2$ and $R$ are taken from parameterizations of the world data on unpolarized DIS.

[4] the tensor is $\epsilon_{0123} = 1$ and changes sign if any two indices are interchanged.

[5] $D$ is called the depolarization factor and quantifies the spin transfer of the polarized lepton to the virtual photon.

The polarized structure function $g_1$ is related to polarized PDFs, which are also called helicity distributions, as follows:

$$g_1(x_{\mathrm{Bj}}) = \frac{1}{2}\sum_f e_f^2 \Delta q_f(x_{\mathrm{Bj}}) \tag{2.38}$$
$$= \left[\frac{4}{18}\Delta u(x_{\mathrm{Bj}}) + \frac{4}{18}\Delta\bar{u}(x_{\mathrm{Bj}}) + \frac{1}{18}\Delta d(x_{\mathrm{Bj}}) + \frac{1}{18}\Delta\bar{d}(x_{\mathrm{Bj}}) + \frac{1}{18}\Delta s(x_{\mathrm{Bj}}) + \frac{1}{18}\Delta\bar{s}(x_{\mathrm{Bj}})\right] \quad ,$$

where the helicity distribution is defined as

$$\Delta q_f = q_f^+ - q_f^- \quad , \tag{2.39}$$

i.e. the number density of quarks with helicty "+" in a nucleon with positive helicity, minus the number density of quarks with helicity "−" in a nucleon with positive helicity. For the further discussion, three linear combinations of the $\Delta q_f$ are defined:

$$\Delta q_3(x_{\mathrm{Bj}}) = \left[\Delta u(x_{\mathrm{Bj}}) + \Delta\bar{u}(x_{\mathrm{Bj}})\right] - \left[\Delta d(x_{\mathrm{Bj}}) + \Delta\bar{d}(x_{\mathrm{Bj}})\right] \tag{2.40}$$
$$\Delta q_8(x_{\mathrm{Bj}}) = \left[\Delta u(x_{\mathrm{Bj}}) + \Delta\bar{u}(x_{\mathrm{Bj}})\right] + \left[\Delta d(x_{\mathrm{Bj}}) + \bar{d}(x_{\mathrm{Bj}})\right] - 2\left[\Delta s(x_{\mathrm{Bj}}) + \Delta\bar{s}(x_{\mathrm{Bj}})\right] \tag{2.41}$$
$$\Delta q_0(x_{\mathrm{Bj}}) = \left[\Delta u(x_{\mathrm{Bj}}) + \Delta\bar{u}(x_{\mathrm{Bj}})\right] + \left[\Delta d(x_{\mathrm{Bj}}) + \bar{d}(x_{\mathrm{Bj}})\right] + \left[\Delta s(x_{\mathrm{Bj}}) + \Delta\bar{s}(x_{\mathrm{Bj}})\right], \tag{2.42}$$

which transform like the third component of an isospin triplet, the eighth component of an *SU(3)* flavor octet, and a flavor singlet, respectively. With these definitions:

$$g_1(x_{\mathrm{Bj}}) = \frac{\Delta q_3(x_{\mathrm{Bj}})}{12} + \frac{\Delta q_8(x_{\mathrm{Bj}})}{36} + \frac{\Delta q_0(x_{\mathrm{Bj}})}{9} \quad . \tag{2.43}$$

The first moment of $g_1$ is

$$\Gamma_1 = \int_0^1 g_1(x_{\mathrm{Bj}})\,\mathrm{d}x_{\mathrm{Bj}} = \frac{a_3}{12} + \frac{a_8}{36} + \frac{a_0}{9} \quad , \tag{2.44}$$

where

$$a_3 = \int_0^1 \Delta q_3(x_{\mathrm{Bj}})\,\mathrm{d}x_{\mathrm{Bj}} \tag{2.45}$$
$$a_8 = \int_0^1 \Delta q_8(x_{\mathrm{Bj}})\,\mathrm{d}x_{\mathrm{Bj}} \tag{2.46}$$
$$a_0 = \int_0^1 \Delta q_0(x_{\mathrm{Bj}})\,\mathrm{d}x_{\mathrm{Bj}} \quad . \tag{2.47}$$

The values of $a_3$ and $a_8$ are known from the $\beta$ decay of neutrons and hyperons. So, a measurement of the first moment of $g_1$ yields a result for $a_0$. A recent measurement [12] of the COMPASS experiment yields a value of:

$$a_0 = 0.35 \pm 0.03(\mathrm{stat.}) \pm 0.05(\mathrm{syst.}) \quad (Q_0^2 = 3\,(\mathrm{GeV}/c)^2) \quad . \tag{2.48}$$

Other analyses which use all world data on $g_1$ result in similar or slightly smaller values for $a_0$ (e.g. [14]).
The contribution of the quark-spin polarization to the total angular momentum of the nucleon is:

$$\frac{1}{2}\Delta\Sigma = \sum_f \int_0^1 \left[\left(\frac{1}{2}\right) q_f^+(x_{\mathrm{Bj}}) + \left(-\frac{1}{2}\right) q_f^-(x_{\mathrm{Bj}})\right] \mathrm{d}x_{\mathrm{Bj}} = \left(\frac{1}{2}\right) \sum_f \int_0^1 \Delta q_f(x_{\mathrm{Bj}})\, \mathrm{d}x_{\mathrm{Bj}} = \frac{1}{2} a_0 \quad . \tag{2.49}$$

The result $a_0 = \Delta\Sigma$ means that the measurements of $g_1$ and its first moment indicate that the spin of the nucleon of $\hbar/2$ can not be entirely explained by the polarization of quarks. This fact is often called the "spin puzzle of the nucleon".
The result $a_0 = \Delta\Sigma$ holds true in leading-order QCD analyses. In the calculation of the next-to-leading order QCD corrections there is a dependence on the renormalization scheme: In the $\overline{MS}$ scheme [15, 16], the result $\Delta\Sigma = a_0$ remains untouched in the next-to-leading order. In this scheme, however, $\Delta\Sigma$ depends on $Q^2$ and its interpretation as the spin contribution of the quarks is a little problematic. In the *AB* [17] and *JET* [18] schemes on the other hand, $\Delta\Sigma$ is independent of $Q^2$. In these schemes there is a correction to $a_0$ from the polarization of gluons which is due to the axial anomaly of QCD (see e.g. [7]):

$$a_0 \overset{AB/JET\ \text{scheme}}{=} \Delta\Sigma - 3\frac{\alpha_s}{2\pi}\Delta G \quad , \tag{2.50}$$

where $\Delta G$ is first moment of the gluon helicity distribution

$$\Delta G(x_g) = G^+(x_g) - G^-(x_g) \quad , \tag{2.51}$$

where $x_g$ is the momentum fraction of the nucleon that is carried by the gluon, $G^+$ is the number density of gluons with helicity "+" in a positive-helicity nucleon, and $G^-$ is the number density of gluons with helicity "−" in a positive-helicity nucleon. It is an interesting fact that the $Q^2$ evolution of $\Delta G$ makes it increase logarithmically with $Q^2$. So, even if $\alpha_s$ logarithmically goes to zero for $Q^2 \to \infty$ (which usually makes next-to-leading order corrections disappear), the product $\alpha_s \Delta G$ is finite in the limit $Q^2 \to \infty$.
A large value of $\Delta G$ could explain the small measured value of $a_0$, even if $\Delta\Sigma$ was close to 0.6. The price to pay for such a large $\Delta G$ is that it would have to be balanced out by a considerable orbital angular momentum in the spin sum rule of Eq. (2.27). Either way, direct measurements of $\Delta G$, which are discussed in the next section, are of great importance for the understanding of the nucleon spin. Measurements of orbital angular momentum of quarks might become possible for the first time via the formalism of Generalized Parton Distributions, which is discussed in Sec. 4.1.3 on the future physics program of the COMPASS-II experiment.

## 2.4 Gluon Polarization

In order to measure the polarization of gluons in lepton-nucleon scattering, processes must be selected in which a photon from lepton scattering interacts with a gluon in the nucleon, which can only proceed via a quark line. This process is called photon-gluon fusion (PGF) and its Feynman graph is shown in Fig. 2.3. If the quark-antiquark pair that appears in the graph is a charm

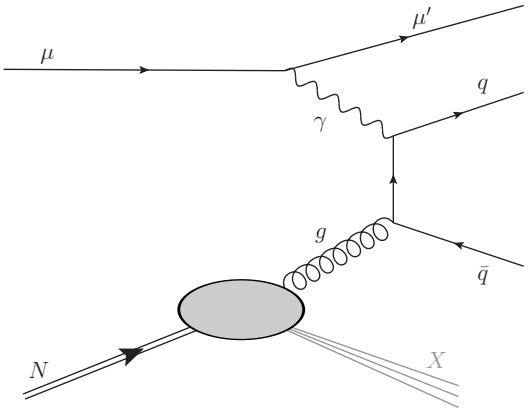


**Figure 2.3:** Feynman graph of photon-gluon fusion in lepton-nucleon scattering.

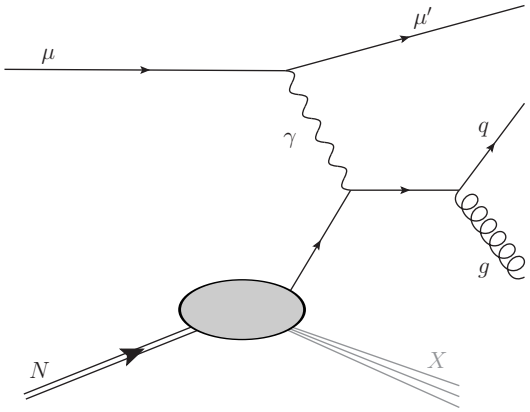


**Figure 2.4:** Feynman graph of lepton-quark scattering with the emission of a hard gluon.

quark and an anticharm quark, the PGF will yield a pair of charmed mesons. Under the reasonable assumption that there is no, or very little, intrinsic charm in the nucleon, the PGF completely dominates the open-charm production cross section. The PGF also has a considerable contribution to the cross section for the production of light hadrons with high transverse momenta. The longitudinal double-spin asymmetries of the open-charm and the high-$p_T$ cross sections are hence sensitive to the polarization of gluons in the nucleon.

Interestingly, the open-charm production as well as the high-$p_T$ hadron production can be treated in perturbative QCD, even at low $Q^2$, close to zero. In the discussion so far, it was always a high photon virtuality that ensured that there was a high momentum transfer in the reaction and that the cross section would hence factorize into non-perturbative parton distributions and a hard scattering of the photon with a quasi-free quark. But the high value of the charm-quark mass ($m_c \approx 1.5\,\mathrm{GeV}/c^2$) or the high transverse momenta of the light hadrons can also provide the *hard scale* that ensures the presence of a large momentum transfer in the reaction and consequently the factorization of the cross section into non-perturbative, soft parton distributions and a hard scattering on the parton level. The inclusion of data with $Q^2 < 1\,(\mathrm{GeV}/c)^2$ vastly improves the statistical accuracy of any lepton-scattering experiment, because the cross sections fall steeply with increasing $Q^2$. The regime of low $Q^2$ is referred to as quasi-real photoproduction.

Results for $\Delta G/G(x_g)$ obtained in lepton-nucleon scattering are shown in Fig. 2.5. The plot also contains curves from the DSSV [14] and LSS [19] collaborations which are constrained by the $Q^2$ evolution of quark-helicity distributions. Although the statistical accuracy of the data is not very high, they can already exclude scenarios of a very large gluon polarization.

The open-charm result from COMPASS is systematically very clean, as there is no physical background for this final state. The fact that $\Delta G/G(x_g)$ was extracted in leading-order, however, could be considered problematic. There is a preliminary result by the COMPASS experiment, for which $\Delta G/G$ and the average $x_g$ have been extracted in next-to-leading order perturbative QCD. While $\Delta G/G$ remains almost identical to the leading-order result, the new result is shifted towards higher values of $x_g$ [20]. The statistical error bars for the open-charm result are quite large, which is due to a very small cross section for this process as well as an acceptance for the reconstruction of events with $D$ mesons in COMPASS of 1-5%.

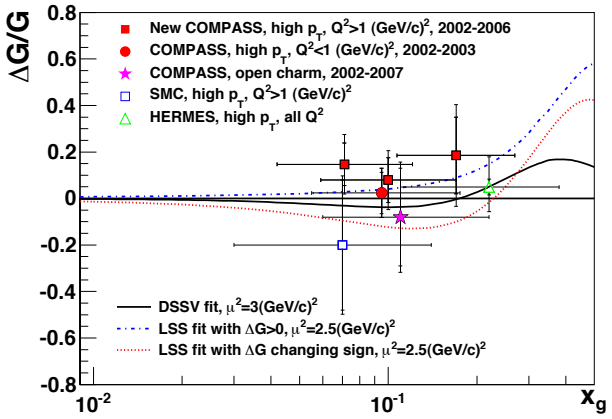


**Figure 2.5:** Direct measurements of the gluon polarization in the nucleon from fixed-target lepton-nucleon scattering. The results have been extracted in leading-order QCD analyses (see text). The plot is taken from Ref. [21].

The analysis of $\Delta G/G$ from the production of hadron pairs with high $p_T$ suffers from the complication that there are background processes which also contribute to the cross section. The most important background process is the scattering of the photon off a quark in the nucleon with the emission of a hard gluon from the quark line (QCD Compton scattering), which is shown in Fig. 2.4. Such background processes are not sensitive to the polarization of gluons, but instead can introduce spin asymmetries due to quark polarization. The extraction of $\Delta G/G$ from high-$p_T$ hadron production in COMPASS so far relies on Monte Carlo generators to quantify the contributions of PGF and the background processes to the double-spin asymmetries. In the regime $Q^2 < 1\,(\mathrm{GeV}/c)^2$, this is done with PYTHIA [22] and for $Q^2 > 1\,(\mathrm{GeV}/c)^2$ COMPASS uses the LEPTO generator [23]. As these programs function in leading-order of perturbative QCD, the $\Delta G/G$ results from high-$p_T$ hadrons in COMPASS are leading-order QCD results. Especially at the low momentum-transfer scales of fixed-target experiments this seems somewhat tenuous.

The final state with the largest cross section and a high reconstruction efficiency that is sensitive to the gluon polarization is the production of single hadrons with high-$p_T$ at low $Q^2$. In this channel, the double-spin asymmetries can be calculated in a full next-to-leading order perturbative QCD calculation [3], which includes the mixing of the different subprocesses that produce high $p_T$ at full next-to-leading order accuracy. Different input $\Delta G/G$ distributions can be used in the calculation and the results can be compared to the experimentally measured asymmetries. This concept is described in detail in the next chapter.

The latter analysis method is very similar to the extractions of the gluon polarization from the polarized proton-proton scattering experiments at RHIC. The STAR and PHENIX experiments have published results on the gluon polarization in the nucleon from longitudinal double-spin asymmetries of high-$p_T$ hadron production [24, 25, 26]. The results of RHIC so far also support small gluon polarizations in the nucleon. Due to the higher center-of-mass energy of 200 GeV at RHIC as compared to 17.4 GeV at COMPASS, the probed $x_g$ is smaller in the RHIC measurements. They can in principle also reach the expected sensitivity range of COMPASS high-$p_T$ hadron production of $x_g \in [0.1, 0.3]$, but this regime corresponds to very high $p_T$ values at RHIC. The COMPASS

data should be statistically superior in this regime. The direct comparison of the COMPASS high-$p_T$ hadron results with RHIC data in an overlapping range of $x_g$ would also be very interesting to test the $Q^2$ scaling of $\Delta G/G$. RHIC operates at $Q^2$ scales which are more than one order of magnitude higher than at COMPASS.

# Chapter 3

# High-$p_T$ Hadron Production in Perturbative QCD

This chapter discusses the single-inclusive cross section of the process

$$lN \to l' h_{\text{high-}p_T} X \quad , \tag{3.1}$$

where the hadron $h$ has a high transverse momentum ($p_T$) with respect to the direction of the virtual photon. The term *single-inclusive* means that all high-$p_T$ hadrons are counted, explicitly allowing the counting of several hadrons per lepton-scattering event. The longitudinal double-spin asymmetry of the cross section of process (3.1) is sensitive to the polarization of gluons in the nucleon, as explained in the previous chapter. The double-spin asymmetry is defined as

$$A_{LL} = \frac{\mathrm{d}\Delta\sigma}{\mathrm{d}\sigma_{\text{unpol}}} \quad , \tag{3.2}$$

where $\mathrm{d}\Delta\sigma$ is the *polarized* cross section, and $\mathrm{d}\sigma_{\text{unpol}}$ is the *unpolarized* cross section. The polarized cross section is defined as

$$\mathrm{d}\Delta\sigma = \frac{1}{2}\left(\mathrm{d}\sigma^{\rightarrow\Leftarrow} - \mathrm{d}\sigma^{\rightarrow\Rightarrow}\right) \quad , \tag{3.3}$$

where $\mathrm{d}\sigma^{\rightarrow\Leftarrow}$ ($\mathrm{d}\sigma^{\rightarrow\Rightarrow}$) denotes the spin-dependent cross section for anti-parallel (parallel) orientations of the longitudinal beam and target polarizations. The unpolarized cross section is the mean value of the spin-dependent cross sections:

$$\mathrm{d}\sigma_{\text{unpol}} = \frac{1}{2}\left(\mathrm{d}\sigma^{\rightarrow\Leftarrow} + \mathrm{d}\sigma^{\rightarrow\Rightarrow}\right) \quad . \tag{3.4}$$

The unpolarized and polarized cross sections for high-$p_T$ hadron production can be calculated in perturbative QCD. Perturbative QCD (pQCD) calculations of inclusive hadron production rely on the fact that in the presence of a *hard scale*, which ensures a high momentum transfer in the reaction, the cross section factorizes into a convolution of

- non-perturbative parton distribution functions, which parameterize the quark and gluon structure of the nucleon in a process-independent way,

- hard partonic cross sections, which are calculable in pQCD,

- and non-perturbative fragmentation functions, which describe the probability that a hadron of a particular type is produced in the hadronization of a particular type of parton.

In the process discussed here, the hard scale is provided by the high $p_T$ of the final state hadrons. In the regime of quasi-real photoproduction, i.e. at low photon virtualities $Q^2$, next-to-leading order (NLO) pQCD calculations of the unpolarized and polarized cross sections for high-$p_T$ hadron production have been calculated for COMPASS kinematics [3]. To constrain the polarization of gluons in the nucleon, the double-spin asymmetry can be calculated with different inputs for the $\Delta G(x_g)$ distribution (see Eq. (2.51)) and the results can be compared to the measured $A_{LL}$. But before the extraction of the gluon polarization with the NLO pQCD calculations can be trusted, the applicability of the theory framework needs to be tested by comparing the measured unpolarized cross section to the calculated unpolarized cross section. This is necessary to ensure that the cross section properly factorizes into short-distance and long-distance components and that all significant contributions to the scattering amplitude are taken into account. The measurement of the unpolarized cross section for the quasi-real photoproduction of hadrons with high $p_T$ is presented in chapter 6. This chapter describes the pQCD calculations of the cross section to set the stage for the comparison of the experimental results with the theory results at the end of chapter 6.
Before the pQCD calculation of the cross section of Ref. [3] is explained in detail in Sec. 3.2, the issue of resolved-photon processes is adressed in Sec. 3.1. These are processes in which the photon, which is emitted from the beam lepton, fluctuates into a hadron-like state that can partake in the hard interaction with the target nucleon instead of the photon itself. In the quasi-real photoproduction regime these virtual hadron-like states have high propagation lengths, which enhances their significance.

## 3.1 Resolved Photon Processes

Photons have a hadronic substructure [27, 28] that can contribute significantly to the amplitudes of lepton-nucleon scattering. The photon can be thought of as consisting of virtual quark-antiquark pairs with the same spin-parity quantum numbers as the photon ($J^{PC} = 1^{--}$), which means that it can fluctuate into an off-shell $\rho$, $\omega$, $\phi$, ... meson. The fluctuation into a quark-antiquark pair is suppressed by $\alpha_{\text{em}}$ in the calculation of the amplitude of a scattering process. But once the fluctuation has happened, these hadron-like states have very high propagation lengths in the limit of high photon energies and low photon virtualities. According to the uncertainty principle, energy conservation can be violated by the amount $\Delta E$ for a period of time $\Delta t \sim \hbar/|\Delta E|$. A photon with energy $\nu$ and virtuality $Q^2$ carries the 3-momentum $\sqrt{\nu^2/c^2 + Q^2}$. Respecting 3-momentum conservation, it can fluctuate into a quark-antiquark pair of mass $M_{q\bar{q}}$, which violates energy conservation by the

amount:

$$\Delta E = \nu - E_{q\bar{q}} = \nu - \sqrt{M_{q\bar{q}}^2 c^4 + \nu^2 + Q^2 c^2} = \nu \left( 1 - \sqrt{1 - \frac{M_{q\bar{q}}^2 c^4 + Q^2 c^2}{\nu^2}} \right)$$
$$\approx \frac{M_{q\bar{q}}^2 c^4 + Q^2 c^2}{2\nu} \qquad \text{(Taylor expansion for } \frac{M_{q\bar{q}}^2 c^4 + Q^2 c^2}{\nu^2} \ll 1\text{).} \tag{3.5}$$

Hence, the propagation length of the virtual quark-antiquark pair is

$$\Delta x = c\Delta t \approx \hbar c \frac{2\nu}{M_{q\bar{q}}^2 c^4 + Q^2 c^2} \quad . \tag{3.6}$$

To make a numerical example, in typical kinematics of quasi-real photoproduction at COMPASS, e.g. $\nu = 50\,\text{GeV}$ and $Q^2 = 0.1\,(\text{GeV}/c)^2$, a $\rho$ meson emerging from a photon has a large propagation length of 28 fm. Resolved photon processes are thus expected to have a considerable contribution to the overall hadron-production cross section in the quasi-real photoproduction regime. The hard partonic interaction can either involve the photon directly, or it can involve a quark, antiquark, or gluon that carries a fraction $x_\gamma$ of the momentum of the photon.
The partonic content of quasi-real photons is described by the structure function of the photon $F_2^\gamma$, which has been, for instance, measured in the reaction [$e^+e^- \rightarrow e^+e^-$ + hadrons] at LEP (e.g. [29]). In the discussed pQCD calculations, the partonic structure of photons is taken into account by using the GRV parton distribution functions of the photon [30]. The GRV model is based on vector-meson dominance (VMD) valence-like structure at a low resolution scale of $Q_0^2 \equiv \mu_0^2 = 0.3\,(\text{GeV/c})^2$. The scale evolutions to the higher scales which are probed in the discussed process are performed at NLO. The photon PDF $f_a^\gamma(x_\gamma, \mu)$ is the number density of partons of type $a$ (quark, antiquark, gluon) in the photon at the scale $\mu$, where the parton carries the momentum fraction $x_\gamma$ of the photon. For the calculation of the polarized cross section in pQCD, the polarized parton distributions (helicity distributions) of the photon $\Delta f_a^\gamma(x_\gamma, \mu)$ are required. The polarized parton structure of the photon is completely unknown experimentally. The cross-section calculations are performed with two extreme assumptions on the polarized photon structure; in the scenario of *minimal* polarization, it is assumed that the photon is completely unpolarized at the scale $\mu_0$, $\Delta f_{a,\text{min}}^\gamma(x_\gamma, \mu_0) = 0$; in the scenario of *maximal* polarization, the polarized parton content of the photon at the scale $\mu_0$ is given by $\Delta f_{a,\text{max}}^\gamma(x_\gamma, \mu_0) = f_a^\gamma(x_\gamma, \mu_0)$. The functions $\Delta f_{a,\text{min}}^\gamma$ and $\Delta f_{a,\text{max}}^\gamma$ are then evolved to the higher scales which are probed in the discussed process with NLO accuracy [31]. The calculations for $A_{LL}$ are carried out with both scenarios and the difference between them can be regarded as a systematic error band due to the unknown polarized parton structure of the photon.
For the direct photon contribution, the photon PDF and helicity distribution have the trivial form:

$$(\Delta) f_{a=\gamma}^\gamma = \delta(1 - x_\gamma) \quad . \tag{3.7}$$

## 3.2 Calculation of the Cross Section

The factorization of the cross section for high-$p_T$ hadron production at low $Q^2$ is depicted in Fig. 3.1 for the direct-photon and resolved-photon components. The polarized and unpolarized cross

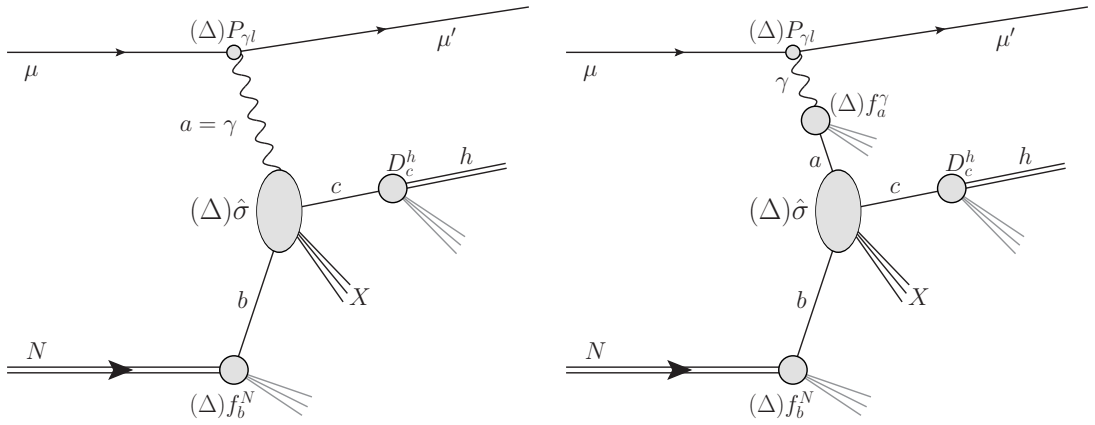


**(a)** Direct-photon contribution.

**(b)** Resolved-photon contribution.

**Figure 3.1:** Generic Feynman graph for the pQCD calculation of the cross section of quasi-real photoproduction of hadrons in muon-nucleon scattering for (a) direct-photon contribution and (b) resolved-photon contribution. To obtain the unpolarized cross sections, the unpolarized quantities $P_{\gamma l}$, $f_a^\gamma$, $\hat{\sigma}$, and $f_b^N$ have to be used. The polarized cross section is obtained by using the polarized quantities $\Delta P_{\gamma l}$, $\Delta f_a^\gamma$, $\Delta\hat{\sigma}$, and $\Delta f_b^N$.

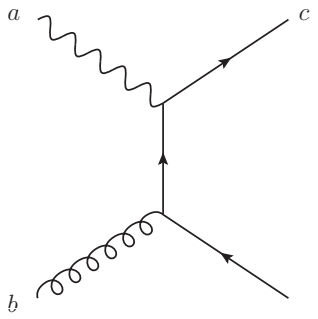


**(a)** One of the two graphs for the photon-gluon fusion: $\gamma g \to q\bar{q}$.

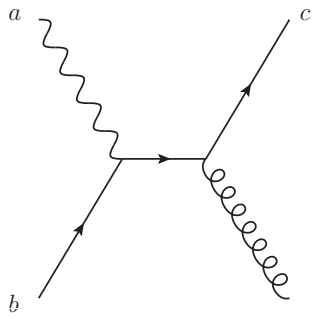


**(b)** One of the two graphs for the QCD Compton process: $\gamma q \to qg$.

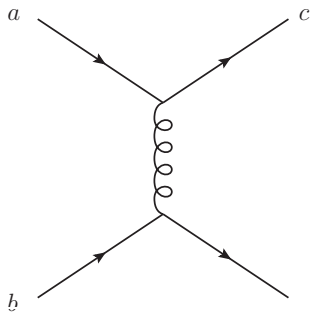


**(c)** One of the two graphs for the resolved-photon process: $qq \to qq$.

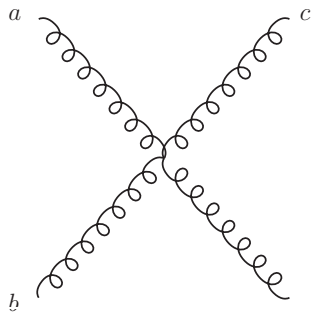


**(d)** One of the four graphs for the resolved-photon process: $gg \to gg$.

**Figure 3.2:** Examples of the leading-order Feynman graphs of the partonic cross sections, $\hat{\sigma}_{ab\to cX}$, for high-$p_T$ scattering of Fig. 3.1.

sections are [3]:

$$\mathrm{d}\Delta\sigma = \sum_{a,b,c} \int \mathrm{d}x_a\, \mathrm{d}x_b\, \mathrm{d}z_c\, \Delta f_a^l(x_a,\mu_f)\, \Delta f_b^N(x_b,\mu_f) \times \mathrm{d}\Delta\hat{\sigma}_{ab\to cX}(\sqrt{s}, x_a, x_b, E_h/z_c, \mu_r, \mu_f, \mu_f')\, D_c^h(z_c,\mu_f') \quad , \tag{3.8}$$

$$\mathrm{d}\sigma_{\mathrm{unpol}} = \sum_{a,b,c} \int \mathrm{d}x_a\, \mathrm{d}x_b\, \mathrm{d}z_c\, f_a^l(x_a,\mu_f)\, f_b^N(x_b,\mu_f) \times \mathrm{d}\hat{\sigma}_{ab\to cX}(\sqrt{s}, x_a, x_b, E_h/z_c, \mu_r, \mu_f, \mu_f')\, D_c^h(z_c,\mu_f') \quad , \tag{3.9}$$

where $\sqrt{s}$ is the muon-nucleon center-of-mass energy. The sums run over all possible partonic channels $ab \to cX$, where $a$ can either be a direct photon or a parton. $f_a^l(x_a,\mu_f)$ is the PDF for finding a parton of type $a$ with a momentum fraction $x_a$ in the beam lepton (i.e. the beam muon) at momentum scale $\mu_f$ (factorization scale), and $\Delta f_a^l(x_a,\mu_f)$ is the helicity distribution of parton type $a$ with momentum fraction $x_a$ in the beam lepton. These objects are defined as:

$$\Delta f_a^l(x_a,\mu_f) = \int_{x_a}^1 \frac{\mathrm{d}y}{y}\, \Delta P_{\gamma l}(y)\, \Delta f_a^\gamma(x_\gamma = \frac{x_a}{y}, \mu_f), \tag{3.10}$$

$$f_a^l(x_a,\mu_f) = \int_{x_a}^1 \frac{\mathrm{d}y}{y}\, P_{\gamma l}(y)\, f_a^\gamma(x_\gamma = \frac{x_a}{y}, \mu_f), \tag{3.11}$$

where $y$ is the energy of the photon emitted from the lepton in units of the lepton energy (as defined in Eq. (2.4)), $f_a^\gamma$ and $\Delta f_a^\gamma$ are the PDF and the helicity distribution of the photon as defined in the previous section, respectively, and $\Delta P_{\gamma l}$ and $P_{\gamma l}$ are the spin-dependent [32] and spin-independent [33] Weizsäcker-Williams equivalent-photon spectra, respectively:

$$\Delta P_{\gamma l}(y) = \frac{\alpha_{\mathrm{em}}}{2\pi}\left[2m^2y^2\left(\frac{1}{Q^2_{\max}} - \frac{1-y}{m^2y^2}\right) + \frac{1-(1-y)^2}{y}\ln\frac{Q^2_{\max}(1-y)}{m^2y^2}\right], \tag{3.12}$$

$$P_{\gamma l}(y) = \frac{\alpha_{\mathrm{em}}}{2\pi}\left[2m^2y\left(\frac{1}{Q^2_{\max}} - \frac{1-y}{m^2y^2}\right) + \frac{1+(1-y)^2}{y}\ln\frac{Q^2_{\max}(1-y)}{m^2y^2}\right], \tag{3.13}$$

where $m$ is the lepton mass and $Q^2_{\max}$ is the maximal value of the photon virtuality that is allowed in the measurement. The direct-photon contributions are taken into account in this general formulation of the cross section by using the definition of Eq. (3.7), which leads to the identification of the lepton helicity distribution (PDF) with the spin-dependent (spin-independent) Weizsäcker-Williams equivalent-photon spectrum.

$f_b^N(x_b,\mu_f)$ and $\Delta f_b^N(x_b,\mu_f)$ are the usual PDF and helicity distribution for partons of type $b$ with a momentum fraction $x_b$ in the nucleon at the momentum scale $\mu_f$, respectively. For the unpolarized case, the PDFs of the CTEQ set [34] are used, while the helicity distributions are taken from the GRSV set [35].

$D_c^h(z_c,\mu_f')$ is the fragmentation function at the factorization scale $\mu_f'$, which is the probability for a hadron $h$ to emerge from the hadronization of a parton of type $c$, where the hadron has the energy $E_h$, which is the fraction $z_c$ of the energy of the parton (i.e. the parton has the energy $E_h/z_c$).

Finally, the partonic cross sections $\mathrm{d}\hat{\sigma}_{ab\to cX}$ and $\mathrm{d}\Delta\hat{\sigma}_{ab\to cX}$ can be calculated in pQCD. They are

defined in analogy to the lepton-nucleon cross sections of Eqs. (3.3, 3.4):

$$\mathrm{d}\Delta\hat{\sigma}_{ab\to cX} = \frac{1}{2}\left(\mathrm{d}\hat{\sigma}_{a^+b^+\to cX} - \mathrm{d}\hat{\sigma}_{a^+b^-\to cX}\right), \tag{3.14}$$

$$\mathrm{d}\hat{\sigma}_{ab\to cX} = \frac{1}{2}\left(\mathrm{d}\hat{\sigma}_{a^+b^+\to cX} + \mathrm{d}\hat{\sigma}_{a^+b^-\to cX}\right), \tag{3.15}$$

where the indices $a^+$ and $b^\pm$ indicate the helicities of the partons in the initial state[1]. $\mu_r$ is the renormalization scale at which the strong coupling constant $\alpha_s(\mu_r)$ is evaluated. Figure 3.2 shows four examples of lowest-order graphs that contribute to the cross section in the direct photon channel, where $a$ is a photon, as well as in the resolved channel, where $a$ is either a quark, an antiquark, or a gluon. The partonic cross sections are known up to NLO in pQCD.
The hard scales in the factorized cross section $\mu_f$, $\mu'_f$, and $\mu_r$ are usually all set to the same value $\mu$. The default choice in such kinds of calculations is $\mu = p_T$. The systematic uncertainty called *scale uncertainty* is defined by the variation of the cross section that is caused by varying the scale between the somewhat arbitrary values $\mu = 2p_T$ and $\mu = p_T/2$. The scale uncertainty is a measure for the significance of higher-order corrections that are missing in the calculation. The scale uncertainty is hence expected to decrease order by order.

## 3.3 Results of the NLO pQCD Calculation

The calculated unpolarized and polarized cross sections for high-$p_T$ $\pi^0$ production in muon-deuteron scattering for COMPASS kinematics and their scale uncertainties are shown in Fig. 3.3. While the scale uncertainty for the polarized cross section is significantly reduced when going from LO to NLO, this is not really the case for the unpolarized cross section. For the original publication [3], where the plot was taken from, the cross section calculations for COMPASS kinematics were performed in the range $Q^2_{\mathrm{max}} = 0.5\,(\mathrm{GeV}/c)^2$, $y \in [0.2, 0.9]$, and $\theta < 70\,\mathrm{mrad}$, where $\theta$ is the angle between the photon direction and the hadron momentum. In the COMPASS experiment, the measurement of the cross section for the production of unidentified charged hadrons is much simpler than the measurement of the cross section for $\pi^0$ production and has hence been chosen for this work. Also, the definition of the kinematical range for the unpolarized hadron-production cross section has been refined in the course of the data analysis. The pQCD curves which are shown in comparison to the measured cross section in chapter 6 use the updated definition of the kinematical range and the fragmentation functions for the observation of unidentified charged hadrons instead of neutral pions.
Figure 3.4 shows the results of the calculation of the longitudinal double-spin asymmetry of the cross section for charged-hadron production in COMPASS from Ref. [3]. The plot features curves for different gluon-polarization scenarios. Besides the "standard" $\Delta G(x_g)$ distribution[2] of the GRSV set, there are three extreme scenarios, $\Delta G(x_g, \mu_0) = G(x_g, \mu_0)$, $\Delta G(x_g, \mu_0) = 0$, and $\Delta G(x_g, \mu_0) = -G(x_g, \mu_0)$ at the input scale of GRSV of $\mu_0^2 = 0.4\,(\mathrm{GeV}/c)^2$. Two curves are shown for each $\Delta G$ scenario, which use the *maximal* and *minimal* polarization scenarios for the polarized parton structure of the photon, $\Delta f^\gamma_{a,\mathrm{max}}$ and $\Delta f^\gamma_{a,\mathrm{min}}$ (see Sec. 3.1). It is clearly visible that for

[1] parity conservation implies $\hat{\sigma}_{a^+b^+\to cX} = \hat{\sigma}_{a^-b^-\to cX}$ and $\hat{\sigma}_{a^+b^-\to cX} = \hat{\sigma}_{a^-b^+\to cX}$.

[2] the different symbol for the gluon polarization in Fig. 3.4 "$\Delta g$" instead of the otherwise used $\Delta G(x_g)$ is just due to a different nomenclature in this work and Ref. [3].

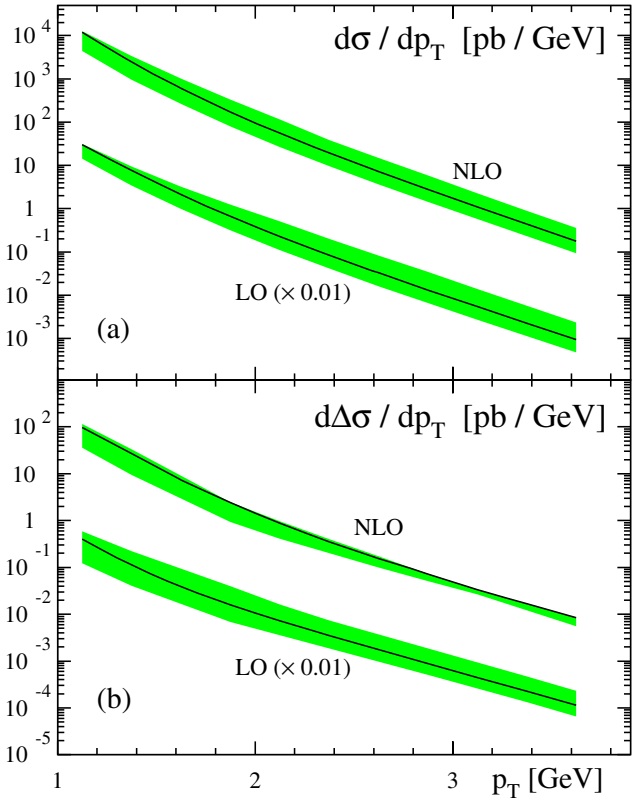


**Figure 3.3:** Unpolarized (a) and polarized (b) cross sections for $\mu d \rightarrow \mu' \pi^0 X$ in COMPASS kinematics in LO and NLO accuracy. The colored bands indicate the scale uncertainty, varying the scale in the range $2p_T \geq \mu \geq p_T/2$, and the solid lines correspond to $\mu = p_T$. The $\pi^0$ fragmentation functions were taken from the KKP set [36]. The plot is taken from Ref. [3].

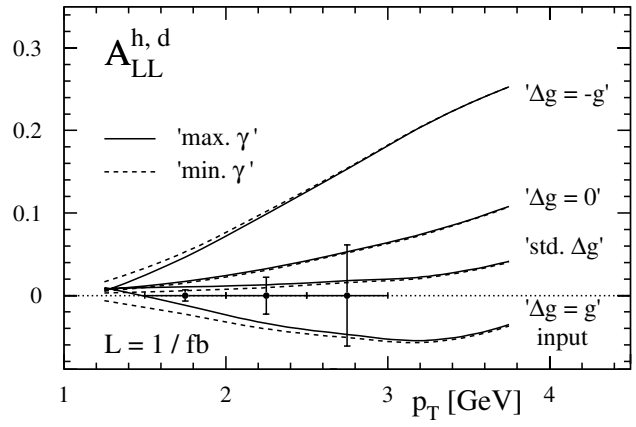


**Figure 3.4:** $A_{LL}$ for the process $\mu d \rightarrow \mu' h^{\pm} X$ in COMPASS kinematics for different gluon-polarization scenarios (see text) and minimal and maximal polarizations of the parton content of the photon (see text), where the $h^{\pm}$ fragmentation functions were taken from the KKP set [36]. Also shown are the projected statistical errors of the COMPASS measurement of $A_{LL}$. The plot is taken from Ref. [3].

$p_T$ values below $\sim 1.75\,\mathrm{GeV}/c$ the uncertainty due to the unknown polarized-photon structure is larger than the separation between the different gluon-polarization scenarios. For larger $p_T$ values, however, there is a clear separation of the different gluon-polarization scenarios beyond the uncertainty of the photon structure. The uncertainty due to the photon structure decreases with increasing $p_T$ because the contribution of the resolved-photon processes decreases with increasing $p_T$. Also shown in Fig. 3.4 are the projected error bars of a COMPASS measurement of $A_{LL}$, which is based on the assumption of an integrated luminosity of $1\,\mathrm{fb}^{-1}$ and a detection efficiency of 100%. The error bars show that there should indeed be some potential to distinguish between different gluon-polarization scenarios in the $p_T$ region $\sim 1.75\,\mathrm{GeV}/c$ to $\sim 2.5\,\mathrm{GeV}/c$. Please note that the integrated luminosity of the COMPASS data set with the polarized deuteron target is actually around $2\,\mathrm{fb}^{-1}$. But since the detection efficiency is only around 40% (see Sec. 6.3), the value of $L = 1\,\mathrm{fb}^{-1}$ used for Fig. 3.4 is quite reasonable.

## 3.4 Discussion

### The Role of $Q^2$

In fact, the equivalent-photon spectra of Eqs. (3.12, 3.13) are integrations over the $Q^2$-dependent photon spectra with the bounds $Q^2_{\mathrm{min}} = m^2y^2/(1-y)$ (from kinematics) and the parameter $Q^2_{\mathrm{max}}$ [32, 33]. In the discussed calculations, all photons of these energy spectra are assumed to be on-mass-shell, i.e. to have $Q^2 = 0$. This should be a good approximation as long as the neglected $Q^2 \leq Q^2_{\mathrm{max}}$ is much smaller than the scales of the hard process $\mu_f^2$, $\mu_f'^2$, and $\mu_r^2$ [37]. The accuracy of the presented description of quasi-real photoproduction can be tested to some extent by comparing the $Q^2_{\mathrm{max}}$ dependence of the calculated cross section and the measured cross section, which is presented in Sec. 6.5.

### Unpolarized Cross Section as a Benchmark for Applicability of NLO pQCD

As mentioned earlier, it is very important to benchmark the applicability of NLO pQCD to the quasi-real photoproduction of hadrons with high $p_T$ at the COMPASS center-of-mass energy, before one can have confidence in the $\Delta G$ extraction with the NLO pQCD framework. This approach has been successfully employed for high-$p_T$ $\pi^0$ production in proton-proton collisions at $\sqrt{s} = 200\,\mathrm{GeV}$ at RHIC [38, 39, 40]. The measured cross sections are in good agreement with the NLO pQCD calculations, allowing the analysis of the double-spin asymmetries in terms of $\Delta G$ [24, 25, 26]. So, while NLO pQCD calculations of high-$p_T$ hadron production work well at collider energies, it is known that they tend to increasingly underestimate the cross section for high-$p_T$ hadron production in proton-proton collisions with decreasing center-of-mass energies [41]. At center-of-mass energies close to the COMPASS value, the measured cross section in proton-proton scattering is a factor three to five larger than the corresponding NLO pQCD result. The all-order *resummation* of large logarithmic pQCD corrections, which are associated with the emission of soft gluons, have been shown to reconcile this discrepancy with the experimental data at fixed-target energies in proton-proton collisions [42]. The pQCD calculation of the single-inclusive high-$p_T$ hadron production cross section in proton-proton scattering proceeds identically

to the lepto-production process discussed in Sec. 3.2, when the PDF of the lepton, $f_a^l$, is replaced with the PDF of the proton, $f_a^p$, in Eq. (3.8). The partonic cross sections $\mathrm{d}\hat{\sigma}_{ab\to cX}$ are completely identical to the ones involved in the resolved photon processes of the lepto-production. At the lowest order, one has the $2 \to 2$ process $ab \to cd$. The corrections arise when the parton $c$ recoils against several partons $d, e, ...$ due to higher-order corrections, which together have a squared invariant mass[3] of $M_X^2 = (\sum_{i=d,e,...} p_i)^2$. When the incoming partons have a squared center-of-mass energy $\hat{s} = (p_a + p_b)^2$ that is greater than $(p_c + \sum_{i=d,e,...} p_i)^2$, the energy balance can be established by gluon emissions. If $\hat{s}$ is near the *threshold* to produce $p_c$, which is equivalent to $M_x \to 0$, the phase space which is available for the gluon radiation is inhibited, meaning that the energy of the gluons approaches zero. This leads to the large logarithms which are the remainders of the cancellation of the infrared singularities of the real gluon emission with virtual corrections. The threshold corrections can be summed up to all orders in $\alpha_s$. Typically, nowadays this is achieved to next-to-leading logarithmic order.
The partonic center-of-mass energy $\sqrt{\hat{s}}$ is not an observable variable. In the case of proton-proton collisions, the partonic center-of-mass energy and the proton-proton center-of-mass energy, $\sqrt{s_{pp}}$, are related as follows:

$$\frac{\sqrt{\hat{s}}}{\sqrt{s_{pp}}} \approx \sqrt{x_a x_b} \quad , \tag{3.16}$$

where terms of the order $\sqrt{M/E_{\mathrm{beam}}}$ have been neglected, $x_a$ and $x_b$ are the momentum fractions of the protons taken by the colliding partons $a$ and $b$, $M$ is the proton mass, and $E_{\mathrm{beam}}$ is the beam energy. In the case of the lepton-nucleon scattering discussed in this work, the relation reads:

$$\frac{\sqrt{\hat{s}}}{\sqrt{s_{lN}}} \approx \sqrt{y x_\gamma x_b} \quad , \tag{3.17}$$

where $x_\gamma = 1$ for direct-photon processes and $x_\gamma < 1$ for resolved-photon processes. The variable $y$ is observed in each scattering event, which makes the connection between the beam-target center-of-mass energy and the partonic center-of-mass energy more direct as in the case of proton-proton scattering.
When observing hadrons at central center-of-mass rapidity, $\eta_{\mathrm{c.m.s.}} = 0$, at a fixed transverse momentum $p_T$ at COMPASS ( $\sqrt{s_{lN}} = 17.4\,\mathrm{GeV}$), the partonic center-of-mass energy can take values in the range

$$\sqrt{\hat{s}} \in \left[ \frac{2p_T}{z_c},\ \sqrt{y x_\gamma x_b} \cdot 17.4\,\mathrm{GeV} \right] \quad , \tag{3.18}$$

where $\sqrt{\hat{s}} = 2p_T/z_c$ is the discussed partonic threshold near which the large logarithmic corrections arise. It is quite obvious that when observing the cross section at low $y$, the available energy range is limited. Choosing for instance $p_T = 3\,\mathrm{GeV}$ and $y = 0.25$, the relation reads

$$\sqrt{\hat{s}} \in \left[ \frac{6\,\mathrm{GeV}}{z_c},\ \sqrt{x_\gamma x_b} \cdot 8.7\,\mathrm{GeV} \right] \quad . \tag{3.19}$$

[3] natural units with $c = 1$ are used just for the discussion of the resummations.

If, on the other hand, one observes the production of $p_T = 3\,\mathrm{GeV}$ hadrons at high $y$, e.g. $y = 0.75$, the allowed energy range is larger,

$$\sqrt{\hat{s}} \in \left[ \frac{6\,\mathrm{GeV}}{z_c},\ \sqrt{x_\gamma x_b} \cdot 15.1\,\mathrm{GeV} \right] \quad . \tag{3.20}$$

One can see clearly that observing the high-$p_T$ hadron production at low $y$ has two consequences: 1) The kinematically allowed ranges of $x_\gamma$, $x_b$, and $z_c$ are limited, which might be very useful information, and 2) the reactions happen closer to the partonic threshold than at high $y$. The magnitude of the correction due to the all-order resummation of the large logarithms on the double-differential cross section

$$\frac{\mathrm{d}^2\sigma}{\mathrm{d}p_T \mathrm{d}y} \tag{3.21}$$

could hence be expected to increase with decreasing $y$.
The resummations for the quasi-real photoproduction in lepton-nucleon scattering are not yet available, but they are expected to be published soon [37]. For the time being, the double-differential cross section (3.21) calculated in *fixed-order* NLO pQCD is compared to the experimental cross section in Sec. 6.5.

# Chapter 4

# The COMPASS Experiment at CERN

COMPASS (COmmon Muon and Proton Apparatus for Structure and Spectroscopy) is a fixed-target experiment at the Super Proton Synchrotron (SPS) at CERN, Geneva. It is a 60 m long two-stage magnet spectrometer, which is equipped with hundreds of planes of tracking detectors, hadronic and electromagnetic calorimeters, and a Cherenkov particle-identification detector. COMPASS is located at the M2 beam line of the SPS which can deliver high-intensity hadron beams as well as naturally polarized muon beams in the momentum range 50-280 GeV/$c$.

## 4.1 Physics Programs

The COMPASS experiment is a merger of two proposed experiments, namely HMC [43] which was meant to follow up on the muon-scattering experiment SMC, and CHEOPS [44] which was meant to be the successor of the WA89 experiment for the spectroscopy of a large variety of hadrons. The two proposals were merged [2] for the mutual benefit of both communities, because they require similar detector setups. The physics program of COMPASS is hence twofold:

1. The spin structure of protons and neutrons is investigated with measurements of double-spin asymmetries of inclusive and semi-inclusive cross sections of muon-scattering reactions.

2. The hadron program utilizes various hadron beams for studying the spectra of light mesons and baryons for the search of hadrons with exotic spin-parity quantum numbers, and for the investigation of the polarizabilities of pions and kaons.

COMPASS has been taking physics data since 2002 and just concluded its final beam time in 2011. A wealth of results has been published already, and further data analyses are ongoing. Phase II of the experiment has recently been approved. The physics program of COMPASS-II [45] covers the subjects of Deeply Virtual Compton Scattering with muon beams for the investigation of Generalized Parton Distributions, the investigation of the transverse spin structure of nucleons by analyzing polarized Drell-Yan reactions in pion scattering, and further measurements of the polarizabilities of pions and kaons. Data taking for COMPASS-II will begin in 2012.

### 4.1.1 Investigation of the Spin and Structure of the Nucleon with Muon Beams

Muon-scattering reactions with large values of the negative 4-momentum transfer $Q^2 > 1\,(\mathrm{GeV/c})^2$ resolve the partonic substructure of nucleons, which is parameterized in the frameworks of the structure function $F_2$ and the related parton distribution functions (PDFs) of the individual quark flavors. When the measurements of such reactions are carried out with a longitudinally polarized beam and a longitudinally polarized target, they are sensitive to the longitudinal spin polarizations of the partons. A $^6$LiD target is used for experiments with polarized deuterons, while experiments with polarized protons are carried out with an $NH_3$ target. The production of the polarized muon beam is described in Sec. 4.2.1 and the polarized target system is described in Sec. 4.2.2. The polarized structure of nucleons is measured via double-spin asymmetries of the scattering cross sections (see Sec. 2.3). The longitudinal spin structure of nucleons is described in the frameworks of the polarized structure function $g_1$ and the related helicity distributions of the individual quark species, which can be extracted from the $A_{LL}$ of different final states. The measurement of the polarization of gluons in the nucleon is the main physics topic of the muon-scattering program of COMPASS. It has been described in the previous chapter. This section shall provide a very brief overview of the other COMPASS results on the nucleon spin structure besides gluon polarization.
The COMPASS experiment has published measurements of the inclusive[1] spin asymmetries and resulting polarized structure functions $g_1$ of deuteron and proton targets. Both measurements have significantly improved the statistics of the world data set on $g_1$, especially in the low-$x_{\mathrm{Bj}}$ region, which is very important for the calculation of the first moments[2] of the distributions. The deuteron measurement [13] yielded an improved value of the first moment of $g_1^d$, which is closely related to the contribution of the quark polarization to the nucleon spin. In combination with the deuteron results, the measurement of the polarized structure function of the proton $g_1^p$ [46] has allowed a test of the Bjorken sum rule with unprecedented accuracy.
The COMPASS experiment has also performed new measurements of the double-spin asymmetries of semi-inclusive final states with a proton target [47], where an identified inclusive hadron is observed in addition to the scattered muon. The measurement of the double-spin asymmetry of $\mu p \rightarrow \mu' \pi^+ X$ (with an unidentified rest $X$) for instance allows access to the polarization of $u$ quarks, because they favorably fragment into $\pi^+$ in the hadronization. The measurement of kaon asymmetries is naturally sensitive to the polarization of $s$ and $\bar{s}$ quarks. The new COMPASS measurements contribute significantly to a more complete picture of the helicity structure of the individual parton species in the nucleon.
When the semi-inclusive spin-asymmetries are measured with a transversely polarized target, they are sensitive to transverse momentum dependent parton distributions (TMDs), which are described in more detail in Sec. 4.1.3. COMPASS has measured the Sivers and Collins asymmetries with a deuteron target [48, 49] and a proton target [50].
The polarized muon-scattering program of COMPASS covers more subjects which are not described here, such as the longitudinal spin transfer to $\Lambda$ and $\overline{\Lambda}$ hyperons, spin asymmetries of exclusive $\rho^0$-meson production, and azimuthal asymmetries of hadron production with longitudinal target polarization.

[1] meaning that only the scattered muon is analyzed, ignoring any other particles in the final state.
[2] the first moment of a parton distribution is the integral over $x_{\mathrm{Bj}}$ from 0 to1.

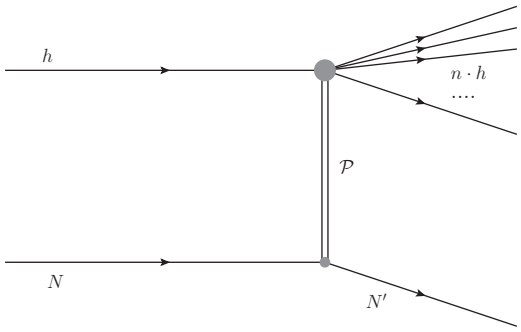


**Figure 4.1:** Diffractive dissociation of a hadron beam into $n$ hadrons via Pomeron exchange with a nucleus.

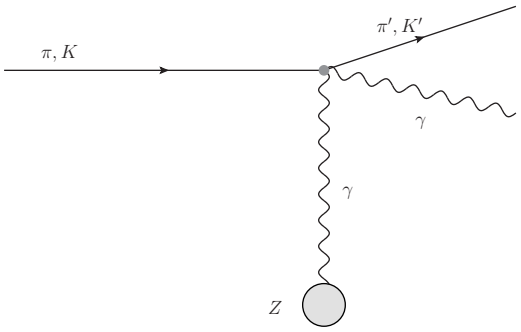


**Figure 4.2:** Primakoff scattering to measure the polarizabilities of pions or kaons.

### 4.1.2 Physics with Hadron Beams

In the constituent quark model baryons consist of three valence quarks, while mesons consist of a valence quark and a valence antiquark. There are of course gluons and more quarks and antiquarks generated in the field of the strong interaction, but it is the valence quarks that define the external quantum numbers of the baryons and mesons. However, in QCD other color-neutral configurations of valence partons are allowed. In a so-called hybrid meson a color-octet quark-antiquark pair is color-neutralized by a gluon. Other allowed configurations are objects called glueballs, whose valence partons are just gluons in color-neutral configurations. Mesons are classified in terms of the following quantum numbers: The total angular momentum $J$, the parity $P = (-1)^{L+1}$, and the particle-antiparticle conjugation parity $C = (-1)^{L+S}$, where $L$ is the relative orbital angular momentum of the quark and the antiquark, and $S$ is total spin of the quark-antiquark pair. There are certain sets of "exotic" $J^{PC}$ quantum numbers which are not possible to make with a pair of fermions, for instance $0^{--}$, $0^{+-}$, $1^{-+}$, etc. The observation of objects with exotic quantum numbers would be a clear signature of the existence of QCD states beyond the simple quark model.
The most prominent production channel for exotic states in COMPASS is thought to be diffractive dissociation with one-Pomeron exchange [51], which is depicted in Fig. 4.1. An incoming hadron is excited by a Pomeron into the state under investigation, which then decays immediately into $n$ hadrons with the same charge sum as the beam particle. The beam track, and the momenta of the $n$ hadrons are measured in the spectrometer.
The first step in the analysis is the choice of the final state which is investigated, i.e. events with a certain number ($n$) of neutral or charged pions or kaons in the final state. The spin-parity quantum numbers of the diffractively produced states are analyzed with the technique of Partial Wave Analysis (PWA). The quantum numbers govern the angular distributions of the produced mesons. In the PWA, statistical methods are used to determine which fraction of the sample of $n$-meson final states comes from the decay of states with particular $J^{PC}$ quantum numbers. A large number of complex-valued amplitudes for the production of particles are fitted in the procedure. The acceptance of the spectrometer for the measurement of the particle momenta plays a crucial role in such analyses. COMPASS has a very high and very uniform acceptance over the complete phase space of the reactions which makes it an ideal environment for such measurements.
COMPASS had a pilot run for the hadron-beam program in 2004 where a few days of data were

recorded with a 190 GeV/$c$ $\pi^-$ beam and lead targets. A resonance with exotic quantum number $J^{PC} = 1^{-+}$ was observed in the analysis of $\pi^-\pi^-\pi^+$ final states, which decays into $\rho\pi$ [52, 53]. The resonance has a mass of 1660 MeV/$c^2$ and a width of 269 MeV/$c^2$. The observed state is consistent with the previously reported $\pi_1(1600)$ [54, 55, 56]. A PWA of the events with five charged pions in the final state has also been performed [57].
Much larger data sets with $\pi^-$ beam have been recorded in 2008 with a liquid-hydrogen target and in 2009 with lead, nickel, and tungsten targets. The analysis of the $\pi^-\pi^-\pi^+$ channel is still ongoing [58]. Many other final states, also those including neutral pions, are under investigation in numerous PhD projects in COMPASS. In 2009, COMPASS also recorded a large data set with a positively charged hadron beam (72% protons) and a liquid hydrogen target. PWA studies for the spectroscopy of baryons with this data set are currently underway [59].

The second cornerstone of the hadron-beam program of COMPASS is the measurement of the polarizabilities of pions and kaons. The electric polarizability $\alpha_{\pi/K}$ is the response of the quark and gluon structure of the meson to an external electric field, while the magnetic polarizability $\beta_{\pi/K}$ is the response to an external magnetic field. They influence the cross sections for the Compton-scattering reactions $\pi\gamma \to \pi\gamma$ and $K\gamma \to K\gamma$ on the 10% level. This is realized in COMPASS with the measurement of Primakoff scattering [60] of the hadron beam, which is depicted in Fig. 4.2. Primakoff reactions are interactions of hadrons with quasi-real photons of the electromagnetic field surrounding medium- to highly-charged nuclei such as nickel or lead (coupling scales with $Z^2$). Primakoff reactions are isolated by selecting events with a very low momentum transfer $\lesssim 0.001\,(\mathrm{GeV}/c)^2$, which correspond to very peripheral interactions. In this regime the electromagnetic interaction with the target nucleus dominates over the strong interaction. There are firm predictions from chiral perturbation theory for $\alpha_\pi$ and $\beta_\pi$ [61]. Almost all previous measurements are in strong disagreement with these predictions and also with each other. A new precise measurement of this quantity by COMPASS is eagerly anticipated.
The 2004 pilot run with a $\pi^-$ beam was used to study the potential of the pion-polarizability measurement in COMPASS. The most important detector in this measurement is the electromagnetic calorimeter in the very forward region (ECAL2) for the detection of the high-energy photons that are produced in the Compton-like scattering. The quality of the readout and the calibration of the calorimeter in 2004 was not sufficient for a reliable extraction of the polarizability. Substantial improvements in the electromagnetic calorimetry were made before the hadron-beam runs of 2008 and 2009 with the introduction of new electronics, new calibration systems, and even an additional calorimeter for the detection of photons at higher scattering angles (ECAL1). In 2009 there was another Primakoff run of $\sim$ 2 weeks duration with a novel, fully digital high-energy photon trigger. The analysis of this data is ongoing [62] and shall yield a reliable result for $\alpha_\pi - \beta_\pi$. The production of other final states besides $\pi\gamma$ in Primakoff scattering, for instance the $3\pi$ final state at very low momentum transfers, provides very interesting opportunities to test chiral perturbation theory as the correct description of QCD at low energies [63].

### 4.1.3 Future Physics Program of COMPASS-II

The physics program of COMPASS-II is detailed in the proposal [45]. This chapter summarizes some of the most important aspects of this very interesting program.

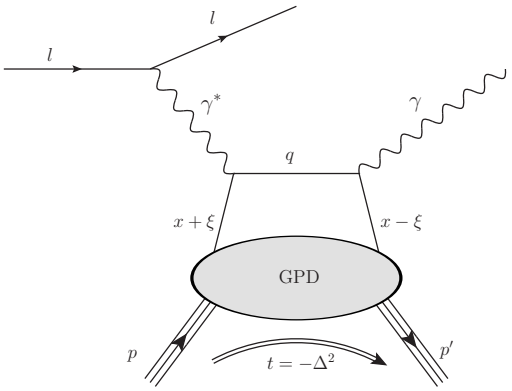


**Figure 4.3:** Diagram of Deeply Virtual Compton Scattering to measure Generalized Parton Distributions of the proton.

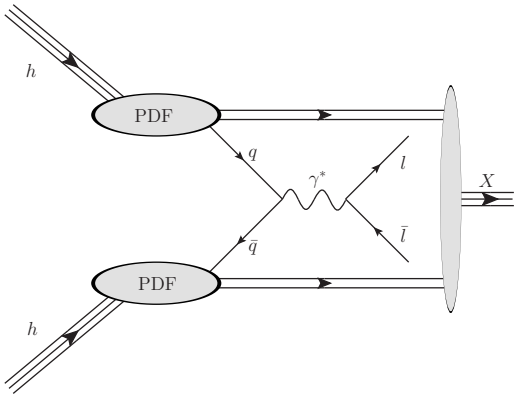


**Figure 4.4:** Drell-Yan process for the measurement of parton distributions.

### Pion Polarizability

A measurement of the polarizability of charged pions in the Primakoff reaction, which has been studied in the 2004 and 2009 runs, will be performed for a duration of 18 weeks in 2012. This will allow independent determinations of the dipole polarizabilities of the pion, $\alpha_\pi$ and $\beta_\pi$. Other goals are the measurement of quadrupole polarizabilities of the pion, and the first measurement of the dipole polarizability of charged kaons, which constitute a fraction of 2.4% of the negatively charged hadron beam of COMPASS.

### Generalized Parton Distributions

The measurement of Generalized Parton Distributions (GPDs) is of great interest for the understanding of the structure of nucleons. GPDs are complex-valued functions that contain information about the unpolarized and polarized nucleon structure in terms of the correlations between the longitudinal momentum fraction of the nucleon carried by the quarks and their transverse displacement with respect to the center of the nucleon. This implies that they contain information about the orbital angular momentum of quarks in the nucleon. They provide a description of the nucleon as an extended 3-dimensional object. GPDs are believed to be universal objects (like the PDFs) that describe the structure of nucleons in a process-independent way.
The most straightforward way to access GPDs experimentally is the process of Deeply Virtual Compton Scattering (DVCS), which is illustrated in Fig. 4.3. A quark is kicked out of the proton by the virtual photon from muon scattering, $\gamma^*$, and is then put back into the proton under the emission of a photon, $\gamma$. The variable $x$ denotes the average longitudinal momentum fraction of the quark in the initial and final state, $\xi$ is half of the difference in longitudinal momentum fraction between the quark in the initial and the final state, and $t = (P_p - P_{p'})^2$ is the 4-momentum squared which is transferred from the initial state proton $P_p$ to the final state proton $P_{p'}$. The information about the GPDs is mostly imprinted in the distribution of the angle between the lepton scattering plane and the plane spanned by the recoil proton and the outgoing photon. Another process that can be exploited to access the GPDs is Deeply Virtual Meson Production (DVMP) where the final-

state photon in Fig. 4.3 is replaced with a neutral meson.
There are two GPDs which conserve the helicity of the nucleon, $H(x,\xi,t)$ and $\tilde{H}(x,\xi,t)$, and two more GPDs that involve a flip of the nucleon helicity $E(x,\xi,t)$ and $\tilde{E}(x,\xi,t)$. The GPDs have straightforward connections to some well-known objects:

- $H_q(x,0,0) = q(x)$, where $q(x)$ is the standard PDF for the quark flavor $q$.
- $\tilde{H}_q(x,0,0) = \Delta q(x)$, where $\Delta q(x)$ is the standard polarized PDF or helicity distribution.
- $F_1^q(t) = \int \mathrm{d}x\, H_q(x,\xi,t)$ and $F_2^q(t) = \int \mathrm{d}x\, E_q(x,\xi,t)$ are the elastic Dirac and Pauli form factors of the nucleon, respectively.
- In the limit $\xi \to 0$, the momentum transfer $t$ is purely transversal. Without the integration over $x$ the GPD $H$ has a very fascinating meaning. It is an electromagnetic form factor that, besides the transverse spatial structure, also depends on the longitudinal momentum fraction of the quarks. Its Fourier transform is an impact-parameter dependent PDF [64]. This is often referred to as "nucleon tomography" because it can reveal the spatial distribution of e.g. the valence quarks or the quark sea in the nucleon.

The GPDs have very interesting properties and meanings also outside of these limits. One of the most important features is expressed by the Ji relation [65]

$$J_q = \frac{1}{2} \lim_{t\to 0} \int \mathrm{d}x\, x\, [H_q(x,\xi,t) + E_q(x,\xi,t)] \quad , \tag{4.1}$$

where $J_q$ is the total angular momentum carried by the quarks of flavor $q$, which includes spin polarization as well as orbital angular momentum. Such a measurement of the orbital angular momenta of partons would be a very important step towards a better understanding of the spin structure of the proton.
In the first phase of the experiment, the measurement will be carried out with an unpolarized liquid hydrogen target. The GPD $E$ is strongly suppressed in measurements with an unpolarized target. In measurements with a transversely polarized target, $E$ will contribute with a comparable strength as $H$ [45]. The measurement with a polarized $NH_3$ target will be pursued after the completion of the first phase of COMPASS-II.
The exclusive measurement of the DVCS process requires a recoil-proton detector which will be built around the target to analyze the momentum of the final state proton and to ensure exclusivity. The acceptance for electromagnetic calorimetry at large angles will be guaranteed by a new calorimeter, ECAL0, which is important to increase the phase space for the exclusive photon measurement and also to further suppress background from exclusive $\pi^0$ production.
The Bethe-Heitler (BH) process (Bremsstrahlung) constitutes a significant source of background for the measurement of the DVCS cross section. This background can be calculated with high accuracy in QED. COMPASS is the only facility in the world which can provide lepton beams of both charges. The $\mu^{+\leftarrow}$ and the $\mu^{-\rightarrow}$ beams of COMPASS are naturally polarized in opposite directions. So, besides subtracting the calculated BH background, one can make use of the fact that the BH process is not spin dependent, while DVCS is spin dependent. By measuring the beam spin and charge cross-section difference $\mathrm{d}\sigma^{+\leftarrow} - \mathrm{d}\sigma^{-\rightarrow}$ the BH contribution can be canceled out. However, the $\mu^{-\rightarrow}$ beam of COMPASS has only about one third of the $\mu^{+\leftarrow}$-beam intensity. The

integrated luminosities for both beams must be measured with an accuracy of a few percent to achieve a good measurement of DVCS with this technique. The luminosity determination which is presented in chapter 5 has been an important step in demonstrating that COMPASS is capable of achieving this goal.

**Transverse Momentum Dependent Parton Distributions**

The parton distributions and polarized parton distributions that were discussed in the previous chapter only take into account the longitudinal momentum and the longitudinal spin polarization of the partons in the nucleon. When additionally taking into account the intrinsic transverse momentum of quarks and their transverse spin polarization, one arrives at a total of eight transverse momentum dependent parton distribution functions (TMDs) to describe the structure of nucleons at leading twist (see e.g. [66]). Nucleons are complex, 3-dimensional objects which consist of partons that can carry orbital angular momentum and can be polarized in various ways. The TMDs contain some information on these aspects of the nucleon dynamics and structure. It should, however, be clearly stated that their interpretation in terms of these physical properties is not all that clear.
In semi-inclusive deep inelastic scattering (SIDIS) TMDs are measured via azimuthal modulations of the hadron production in the scattering of (longitudinally polarized) leptons off longitudinally or transversely polarized targets. In this channel, the factorized cross sections involve fragmentation functions (FFs) which are number densities to produce a certain hadron species from a specific parton flavor. The FFs themselves depend on the transverse momentum of the produced hadron with respect to the quark momentum and the transverse spin of the quark and introduce further angular modulations, which complicates the extraction of the distribution functions considerably.
An alternative process which does not involve FFs to access TMDs is the Drell-Yan (DY) process, which is shown in Fig. 4.4. In this process a quark from a hadron annihilates with an antiquark from another hadron to form a lepton-antilepton pair. The DY experiments in COMPASS-II will be carried out with a $\pi^-$ beam and a transversely polarized $NH_3$ target. The TMDs are encoded in the target-spin asymmetries of the modulations of two angles: 1) The azimuthal angle between the virtual photon direction and the target polarization, and 2) the angle between the plane which is spanned by the direction of the virtual photon and the lepton pair, and the plane spanned by the beam and target hadrons in the rest frame of the virtual photon. A total of four parton distribution functions contribute to the spin asymmetries: a) The Boer-Mulders function, which describes the correlation of the intrinsic transverse momentum and the transverse spin of a quark in an unpolarized nucleon, b) the Sivers function, which describes the correlation between the transverse nucleon spin and the intrinsic transverse momentum of quarks, c) the so-called Pretzelosity distribution, which describes the transverse momentum dependent correlation of the transverse polarization of the nucleon and the transverse spin of the quarks, where the transverse polarizations of the nucleons and the quarks point in different directions, and d) the transversity function, which is the number density for finding a transversely polarized quark in a transversely polarized nucleon (the transverse momentum of the quarks is integrated over). One of the most important results that is anticipated is the confirmation of the predicted change of signs of the Sivers and Boer-Mulders functions in the DY process with respect to SIDIS [67].
The measurement would ideally be performed with an antiproton beam to have access to valence

antiquarks, which follow the same TMDs as the quarks in the target protons. A simpler solution, which is feasible in COMPASS, is the use of a $\pi^-$ beam. The valence $\bar{u}$ antiquarks of the pions can annihilate with valence $u$ quarks in the protons in the target. This, however, adds a complication to the measurement because the unknown Boer-Mulders function of the pion enters in the process. The experiment will be performed with a high-intensity pion beam and a long solid-sate target with oppositely transversely polarized cells. This results in a very high flux of produced particles, which would overload the tracking detectors in the usual COMPASS setup and make the measurement of the DY lepton pairs impossible. The solution to this problem is the introduction of a hadron absorber downstream of the target with a thickness of 55 radiation lengths with a tungsten beam plug in the center (another option with 35 radiation lengths is under consideration). This excludes the measurement of $e^+$-$e^-$ pairs from DY production, while muon pairs pass through the absorber and can be analyzed. The large amount of material, however, causes multiple scattering of the order of centimeters, which makes the event-by-event reconstruction of the invariant mass of the muon pair, the direction of the virtual photon, and most importantly the vertex position quite challenging. It is of utmost importance for the measurement of the spin asymmetry of the cross section to detect which target cell the muon pair was produced in.

## 4.2 Experimental Setup

The COMPASS collaboration has published a paper which contains detailed descriptions of all aspects of the experiment [68]. This chapter summarizes the basic features of the COMPASS experiment and goes into more detail in the aspects that are most relevant for the measurements presented in the chapters 5 and 6. The setups for the experiments with muon beams and hadron beams are almost identical in terms of the used particle detectors, but the target system, the trigger system, and of course the beam itself are completely different. This chapter only describes the muon-beam setup as it was used in the 2004 beam time, because the data analyses described in this thesis are based on the data set recorded then. This choice is motivated by the introduction of the electromagnetic calorimeter ECAL1 after the 2004 beam time, which compromised the efficiency of the triggers for the quasi-real photoproduction regime.

### 4.2.1 High-Intensity Muon Beam

The COMPASS experiment is located at the M2 beam line of the SPS. The production of the beam of polarized, positively charged muons for COMPASS begins with 400 GeV/$c$ protons from the SPS impinging on a 500 mm long beryllium target, called T6. In the 2004 beam time, when the presented data set was recorded, the SPS delivered spills of $1.2 \cdot 10^{13}$ protons during a period of 4.8 s, followed by breaks of 12 s. This beam was well debunched after the first few hundred milliseconds, i.e. it had a uniform time structure. After T6, beam optics consisting of dipole and quadrupole magnets selects a hadron beam of a specific momentum, which has a high $\pi^+$-meson content. The pion beam is guided to a 600 m long decay tunnel in which a fraction of the pions undergoes the parity-violating weak decay $\pi^+ \to \mu^+\nu_\mu$. Since the helicity of the neutrino is fixed to $-1/2$, the muons must also have helicity $-1/2$ in the pion center-of-mass system, because the pion is a spin 0 particle. Muons that are emitted in the flight direction of the pions have the highest

momenta and are polarized 100% against the flight direction, while the muons emitted against the flight direction of the pion have minimal momenta and are polarized 100% in the flight direction. But selecting only the muons with the highest possible momenta for a 100% polarized beam would yield a rather small intensity. Instead, a broader range of muon momenta close to the maximum is selected for an increased intensity. The optimal compromise between polarization and intensity is reached at a pion momentum of 172 GeV/$c$, and a muon momentum of 160 GeV/c, resulting in a polarization of 80%. The muon beam is then transported to the surface via a tunnel equipped with beam optics elements and finally bent into the horizontal direction where it impinges on the COMPASS target. Since the momentum spread of the selected beam is quite large ($\sigma_p = 6\,\mathrm{GeV}/c$), the momenta of the individual beam particles are measured with a set of scintillator hodoscopes surrounding three beam-line dipole magnets $\sim$ 100 m upstream of the target. This system is called the Beam Momentum Station (BMS).

### 4.2.2 Target System

Since the achievable intensities of muon beams are much lower than those of electron beams, muon-scattering experiments require the use of solid-state targets instead of gas targets to reach high luminosities. Besides the increased multiple scattering, which leads to a poor vertex resolution, the thick target increases the possibility of secondary interactions of particles in the target material before they cross the particle detectors. The latter issue is quite important for the hadron-production cross section which is presented in chapter 6.
The investigation of the spin structure of protons and neutrons requires experiments with polarized protons and deuterons. The target material is kept at a very low temperature of $\sim$ 200 mK in a 2.5 T magnetic field. Under these conditions the electrons in the target material are fully polarized. The nucleons on the other hand are not directly polarized beyond the percent level, because the Zeeman splitting is too low due to the higher mass of the nucleons. The technique of "dynamic nuclear polarization" (DNP) [69] is employed to transfer a part of the electron polarization to the nucleons. The target material is exposed to microwave radiation which induces double-spin flips of the electrons together with the nucleons. While the electron spins relax to the ground state instantly, the nucleon polarization can be maintained with decay times of days in the high magnetic field and at the low temperatures. The irradiation of the microwave frequency $\omega_e + \omega_N$ enriches nucleon spins antiparallel to the magnetic field direction, whereas the frequency $\omega_e - \omega_N$ is used to polarize the nucleons parallel to the magnetic field direction. $\omega_e$ and $\omega_N$ are the Larmor frequencies of the electrons and the nucleons.
The presented picture is oversimplified. The DNP process in the real target material requires some amount of paramagnetic centers, which can be introduced to certain materials by irradiation. The actual materials used for the polarized target are hence not just liquid hydrogen or deuterium, but specially prepared LiD for the deuteron experiments and $NH_3$ for the proton experiments.
The target is arranged in two oppositely polarized cells of 60 cm length each, which are separated by a gap of 10 cm. The cells are cylinders of 3 cm diameter, which are not completely filled all the way to the top. The fiducial target which is used in the data analysis is a cylinder of radius 1.4 cm, where the top 0.4 cm are cut off. The target cells are situated in a bath of liquid helium inside a very complex refrigerator system. The packing factor of the solid granulate of LiD or $NH_3$ is about 50%.

The solenoid magnet which was used for the polarized target up to the 2004 run of COMPASS was taken over from the SMC experiment [70]. The new COMPASS solenoid magnet which has a much larger aperture was installed only after the 2004 beam time.
The polarizations of the target are averaged over for the determination of the unpolarized cross section for inclusive muon scattering in chapter 5 and the unpolarized cross section for hadron production with high $p_T$ in chapter 6.

### 4.2.3 Particle Spectrometer

The COMPASS spectrometer is equipped with > 300 planes of tracking detectors of very different spatial resolutions, time resolutions, and active areas, with a RICH particle identification detector, and electromagnetic and hadronic calorimeters. This section shall provide an overview over the most important features of the tracking system. For more detailed descriptions of the detectors please be referred to the COMPASS spectrometer paper [68] and the references therein.
Figure 4.5 shows a schematic view of the COMPASS spectrometer. It is composed of three parts, which are described in the following sections.

#### Beam Telescope

The tracks of the beam particles are measured before they impinge on the target. This is done with three stations of silicon microstrip detectors [72]. Each station consists of two silicon detectors, which have a double-sided readout with orthogonal strips of pitch $\sim 50\,\mu$m. The two detectors of each station are tilted against each other by 5°. The detectors have an active area of $5 \times 7\,\text{cm}^2$ and reach a spatial resolution of 8-11 $\mu$m and a time resolution of 2.5 ns. The silicon telescope has a length of $\sim$ 3 m. The beam tracking is supplemented with 2 stations of scintillating fiber detectors [73, 74], each consisting of 2 orthogonal planes (size $3.9 \times 3.9\,\text{cm}^2$). The scintillating fiber detectors have an excellent time resolution of 400 ps, which is needed for the association of the tracks to the BMS measurements. The BMS consists of scintillator-strip detectors that have been used already in previous experiments [75] and new detectors which are very similar to the scintillating fiber detectors used in the beam telescope. The BMS is located $\sim$ 100 m upstream of the beam tracking detectors. It measures the momentum of the individual beam particles by analyzing their bending in three dipole magnets of the beam line.

#### Large Angle Spectrometer (LAS)

The dipole magnet SM1 is the central component of this part of the COMPASS spectrometer. This magnet has a length of 110 cm and a very large aperture of 229 cm in the horizontal direction and 152 cm in the vertical direction. The field integral of SM1 is 1 Tm, and the acceptance in terms of the angle between the tracks from the target and the beam direction is 180 mrad. The magnetic field lines are vertical, leading to a trajectory bending in the horizontal plane. Positively (negatively) charged particles are deflected towards the so-called Jura (Salève) side of the spectrometer (see Fig. 4.5). The particle tracking upstream of the magnet is performed with six planes of Micromegas detectors [76], which have an active area of $40 \times 40\,\text{cm}^2$ each with a circular, central dead zone of 5 cm diameter. Each detector is equipped with an orthogonal strip readout and reaches a

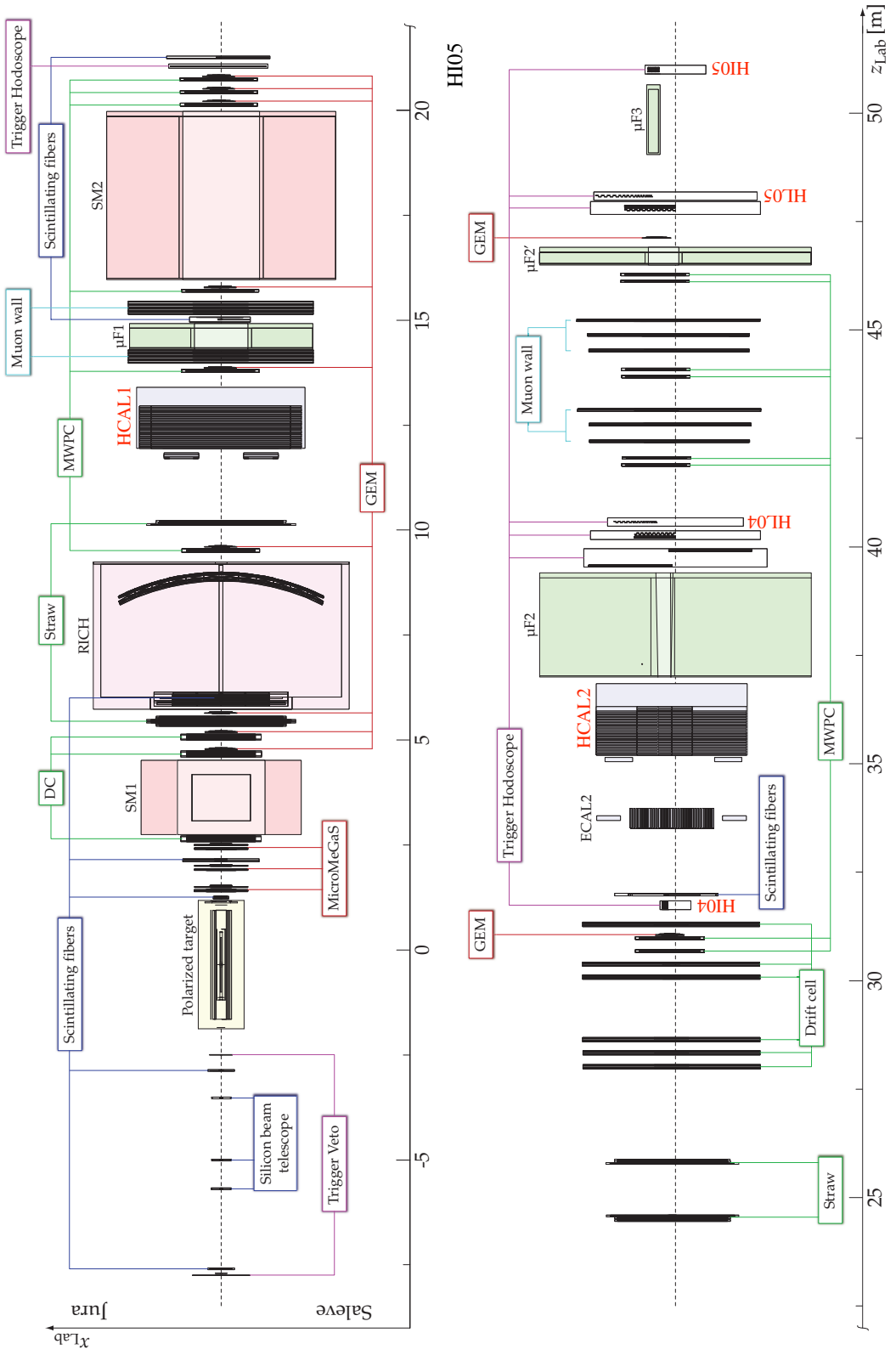


**Figure 4.5:** Schematic view of the COMPASS spectrometer (2004 muon run, taken from Ref. [71]).

spatial resolution of 90 $\mu$m and a time resolution of 9 ns. These parameters are essential for unambiguous particle tracking in this high-rate environment. The dead zones of the MicroMeGas are covered by two stations of scintillating fibres with an active area of $5.3 \times 5.3\,\mathrm{cm}^2$. A large drift chamber with an active area of $180 \times 127\,\mathrm{cm}^2$, which takes eight one-dimensional measurements of the track in four azimuthal orientations with a resolution of 190 $\mu$m each, completes the tracking system upstream of the magnet.
The tracking system continues downstream of SM1 with two more of the afore described drift chambers. Downstream of the drift chambers there are nine planes (arranged in four projections) of straw-tube detectors [77] which reach the same resolution as the drift chambers and have active areas of $323 \times 280\,\mathrm{cm}^2$. Further downstream, multi-wire proportional chambers (MWPCs) with an area of $178 \times 120\,\mathrm{cm}^2$ and a resolution of 1.6 mm contribute four more one-dimensional measurements. All of these detectors have dead zones in the vicinity of the beam to protect them from excessive hit rates. This area is covered with four stations of GEM[3] detectors [78], each of which consists of two detectors with double-strip readout. The detectors have an active area of $31 \times 31\,\mathrm{cm}^2$ and a central dead zone of diameter 5 cm. Each GEM detector reaches a spatial resolution of 70 $\mu$m and a time resolution of 12 ns. The tracking system is completed by one more scintillating fiber detector with an active area of $8.4 \times 8.4\,\mathrm{cm}^2$, which is centered at the beam position.
The LAS is equipped with the large-area hadronic calorimeter HCAL1. This calorimeter consists of 480 blocks, each of which consists of 40 layers of iron plates (20 mm) and scintillator plates (5 mm), amounting to a total of 4.8 hadronic interaction lengths. Each block has a front face of $14.6 \times 14.2\,\mathrm{cm}^2$. The blocks are arranged in a $28 \times 20$ matrix, where 12 blocks are removed from each corner. There is a central hole of $8 \times 4$ blocks which matches the acceptance of the second spectrometer magnet which is located further downstream. The energy resolution of HCAL1 is $\sigma_E/E = (59.4/\sqrt{E/(\mathrm{GeV})} \oplus 7.6)\%$.
Muon identification is performed with particle detectors which are shielded by hadron absorbers. Tracks which are detected downstream of the absorbers in these detectors are positively identified as muons. In the COMPASS LAS this is done with two stations of drift tubes (active area $473 \times 405\,\mathrm{cm}^2$) which are separated by a 60 cm thick iron wall ($\mu$F1), which has a central hole that matches the acceptance of the second stage of the spectrometer. This detector is called "muon wall 1".
A Ring Imaging Cherenkov Detector (RICH) [79] measures the velocity of particles in the LAS, which can be used for particle identification if combined with the momentum measurement. Since the RICH detector is not used in the data analyses presented in this thesis it is not further described here.

### Small Angle Spectrometer (SAS)

Particles which are emitted from the target with small polar angles $< 30$ mrad and large momenta $> 5\,\mathrm{GeV}/c$ are analyzed in the SAS. This spectrometer is built around the magnet SM2, which is located downstream of the muon identification system of the LAS, 18 m downstream of the target. It is a 4 m long dipole magnet with an gap of $2 \times 1\,\mathrm{m}^2$ and a bending power of 4.4 Tm. The field

[3] The GEM technology is also used for the readout of the high-rate TPC which is described in chapter 8.

orientation is the same as for SM1. Listing the tracking detectors from the smallest to the largest active areas, the tracking system of the SAS starts with one scintillating fiber detector (active area: $10 \times 10\,\mathrm{cm}^2$) upstream of SM2 and two scintillating fiber detectors downstream of SM2 (active areas: $10 \times 10\,\mathrm{cm}^2$ and $12.3 \times 12.3\,\mathrm{cm}^2$). There are two more stations of GEM detectors upstream of SM2 and five more GEM stations downstream of SM2. The large area tracking downstream of SM2, but upstream of the muon filter of the SAS ($\mu$F2), is performed with six more MWPC detectors with two projections each and six more planes of straw-tube detectors with the same sizes and resolutions as in the LAS. Additionally, there are six very large drift chambers with active areas of $500 \times 250\,\mathrm{cm}^2$, which measure two projections each with a resolution of 0.5 mm (labeled as "Drift cell" in Fig. 4.5).
The charged tracking system is followed by the electromagnetic calorimeter ECAL2. This calorimeter has a thickness of 16 radiation lengths and has a central hole for the unscattered beam particles. ECAL2 is used to measure the energy of high-energy photons, electrons, and positrons. Since the response of ECAL2 is not used in the analyses presented in this thesis, the detector is not described in more detail. The SAS is also equipped with a hadronic calorimeter, which is located just downstream of ECAL2. This detector is called HCAL2 and consists of cells of area $20 \times 20\,\mathrm{cm}^2$. The cells are arranged in a $22 \times 10$ matrix with a central hole for the passage of the beam of $2 \times 2$ blocks. Most of the blocks consist of 36 layers of 25 mm thick iron plates, interspersed with 5 mm thick scintillator plates. The $8 \times 6$ central cells are a bit thicker; they consist of 40 layers. The energy resolution of HCAL2 is $\sigma_E/E = (66/\sqrt{E/(\mathrm{GeV})} \oplus 5)\%$.
The muon filter $\mu$F2 is a 2.4 m thick concrete wall, which is located downstream of HCAL2. The muon tracking downstream of $\mu$F2 is performed with six MWPC detectors which measure two projections each and have an active area of $178 \times 90\,\mathrm{cm}^2$. Two drift-cell detectors of area $447 \times 202\,\mathrm{cm}^2$ complete the muon tracking system of COMPASS ("muon wall 2"). Each detector has six layers of drift cells with 0.6-0.9 mm resolution, which are arranged as double layers in three different projections.
The scintillator hodoscopes of the trigger system are distributed over a distance of $\sim 30$ m downstream of SM2. The last element of COMPASS is the hodoscope HI05, which is located 51 m downstream of the target and is shielded by a 1.6 m long block of iron ($\mu$F3).

### 4.2.4 Trigger System

The basic principle for triggering the readout of the frontend electronics of the detectors in COMPASS is the detection of the scattered muon with pairs of scintillator hodoscopes which are shielded by iron and concrete absorbers downstream of the second spectrometer magnet SM2. The trigger system employs coincidence matrices between the different channels of the hodoscopes to select events with certain muon kinematics [80].
The $y$-$Q^2$ phase-space coverage of the different muon triggers of COMPASS is shown in Fig. 4.6 (for the definition of the kinematical variables of lepton scattering, please see Sec. 2.1). The Inner Trigger (IT) and the Ladder Trigger (LT) are sensitive to low-$Q^2$ events, i.e. events in the quasi-real photoproduction regime. The coincidence matrices of these triggers select scattered-muon tracks that (roughly) point into the center of SM2 to select events with low scattering angles ($Q^2 \approx 0$) in the target but with an energy loss $y > 0$, which leads to a higher deflection of the muons in the SM2 magnet as compared to unscattered beam particles. The hodoscopes HI04 and HI05 (see Fig.

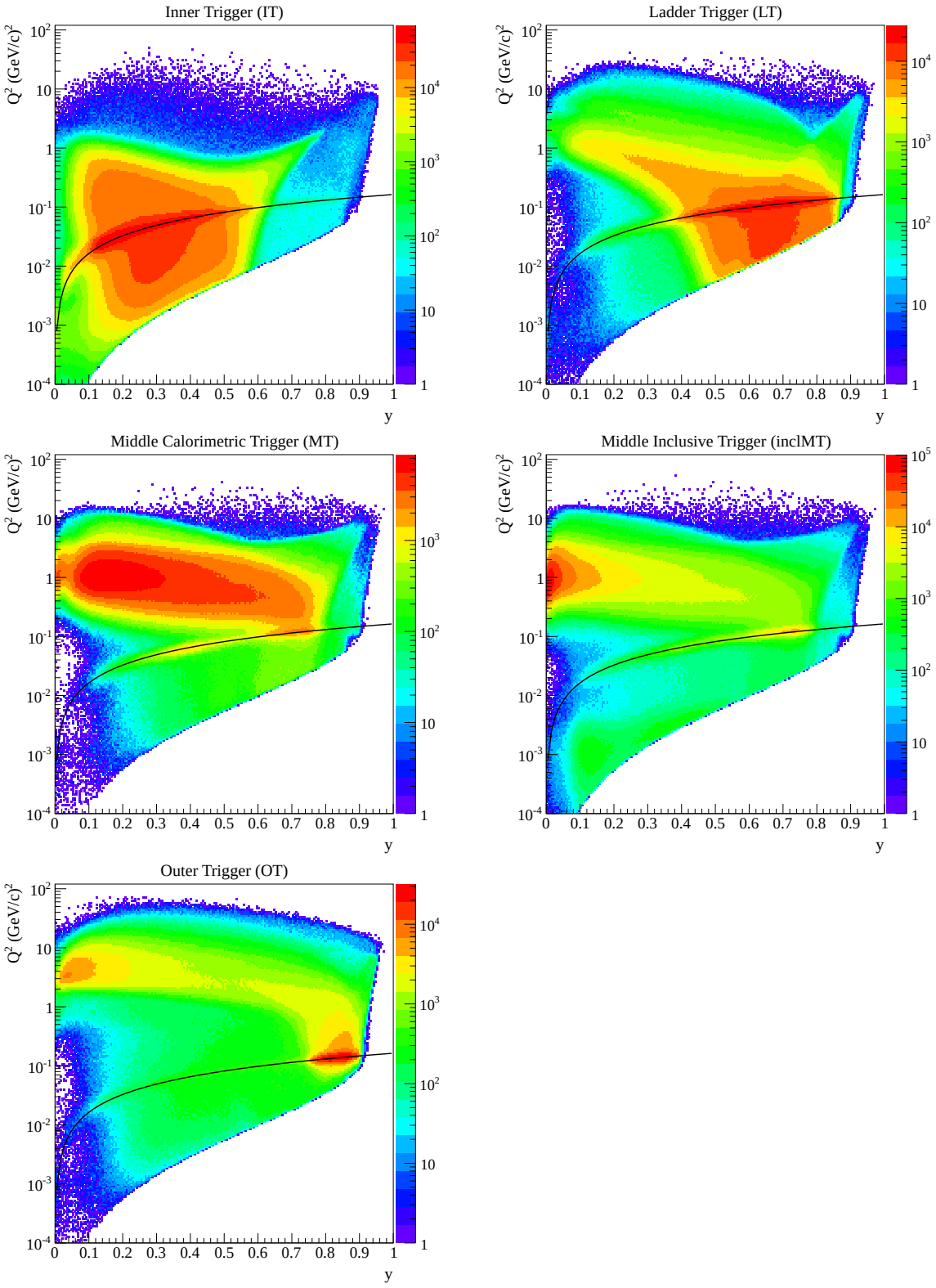


**Figure 4.6:** Phase-space coverage of the muon-trigger systems of COMPASS. The black lines indicate the kinematics for elastic muon-electron scattering at $x_{\mathrm{Bj}} = m_e/m_N$.

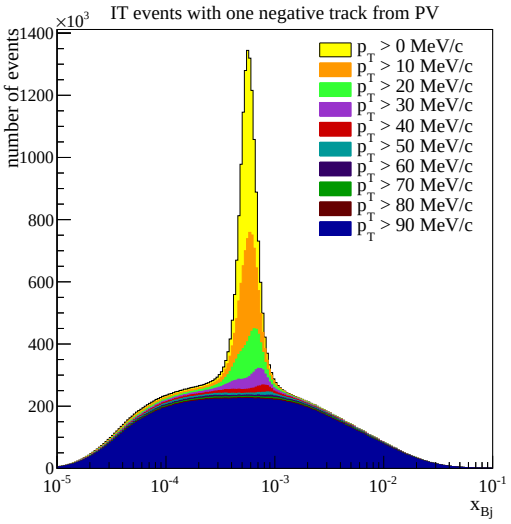


**Figure 4.7:** Spectrum of $x_{\mathrm{Bj}}$ of IT events with exactly one negative track in addition to the scattered-muon track. The peak is due to elastic muon-electron scattering. Cuts on $p_T$ of the negative track remove the peak.

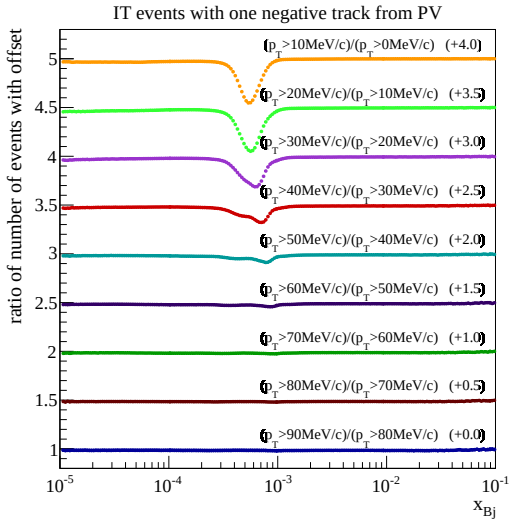


**Figure 4.8:** Ratios of pairs of histograms with neighboring cut values of Fig. 4.7 (offset by multiples of 0.5). Beyond $p_T \gtrsim 70\,\mathrm{MeV}/c$, the cuts remove events uniformly in $x_{\mathrm{Bj}}$, meaning that no more elastic events are left.

4.5), which constitute the IT, are located close to the beam axis. They detect events in which the muons which have lost only little energy in the scattering ($y \in [0.1, 0.6]$). The hodoscopes HL04 and HL05 (see Fig. 4.5), which make up the LT, are further away from the beam axis which results in a sensitivity to events with higher values of $y(\in [0.5, 0.9])$. The determination of the efficiencies of the hodoscopes HI04, HI05, HL04, and HL05 is discussed in Sec. 6.2.1, because it is essential for the absolutely normalized measurement of the hadron production cross section at low $Q^2$.

The elastic scattering of muons off electrons in the target proceeds at a fixed value of $x_{\mathrm{Bj}} = m_e/m_N$ (with the electron mass $m_e$), which is right in the middle of the acceptance of the low-$Q^2$ triggers (see the black lines in the plots of Fig. 4.6). Another background process which falls within the acceptance of the low-$Q^2$ triggers is the radiative tail of the elastic scattering off target nucleons. Since no forward hadrons are produced in these processes, they can be suppressed by requiring an energy deposit in one of the hadronic calorimeters HCAL1 or HCAL2 ("low" threshold $\sim 7\,\mathrm{GeV}$) in addition to the scattered-muon detection in the IT and LT. It is, however, visible in Fig. 4.6 that the suppression does not work perfectly, because there is still an enhancement of events around the $x_{\mathrm{Bj}} = m_e/m_N$ lines. The recoil electrons of the elastic $\mu$-$e$ scattering process hit the electromagnetic calorimeter ECAL2 which is located just upstream of HCAL2. Apparently the ECAL2 is not quite thick enough to contain the energy of all of the highly-energetic electrons. But fortunately the presence of the elastic scattering events does not spoil the measurement of the high-$p_T$ hadron production cross section, because the electrons have a very small transverse momentum $p_T$ with respect to the virtual photon direction $\mathbf{q}$ (definition in Sec. 2.1). Figures 4.7 and 4.8 show that the selection of events with very $p_T \gtrsim 70\,\mathrm{MeV/c}$ effectively removes all of the elastic background.

COMPASS has other triggers for recording events with higher $Q^2$, namely the Middle Trigger (MT) and the Outer Trigger (OT). The MT is a semi-inclusive trigger as well, which means that

it requires an energy deposit in one of the HCALs. But it also exists as a purely inclusive version (inclMT), which is recorded with a pre-scaling factor of two[4]. The inclMT is utilized for the measurement of the inclusive muon-scattering cross section, which is used to validate the measurement of luminosity which is presented in chapter 5. The fraction of inclMT events which have also fired the MT is used in chapter 6.2.2 to determine the efficiency of the HCAL component of the semi-inclusive triggers.
The OT is a purely inclusive trigger for recording very high-$Q^2$ events, which is not used at all in the presented work. COMPASS also has a purely calorimetric trigger (CT), which does not analyze the scattered muons, but just requires a large energy deposit of more than $\sim 20\,\text{GeV}$ ("high" threshold) in one of the HCALs. Events recorded in the CT are used in chapter 6.2.1 to determine the efficiencies of the hodoscopes of the IT and the LT without any bias from the muon detection of the trigger system.

**Veto System**

The muon beam of COMPASS has a very intense halo, which extends up to several meters away from the beam axis and has a very large angular divergence. There is a high number of inclined halo tracks which fulfill the trigger conditions of the coincidence matrices of the scattered-muon triggers at the downstream end of the spectrometer. The triggers that would be caused by these tracks are suppressed by anti-coincidences of the triggers with veto counters that surround the beam upstream of the target. There are several veto counters at different positions and distances from the target. They are combined with a logical OR to form the veto signal called $V_{\text{tot}}$. There is another veto signal called $V'$ which does not include the near-beam veto systems $V_{\text{i1}}$ and $V_{\text{i2}}$. The veto signal $V_{\text{tot}}$ is used to increase the purity of the triggers MT, inclMT, OT, and CT, while the signal $V'$ is used for the LT. The IT is not in anti-coincidence with any veto signal.
Because of the high flux of the beam halo, the veto system generates a considerable dead time of up to $\sim 20\%$ for the trigger system, meaning that active veto signals are present for $\sim 20\%$ of the data-taking time. This dead time is corrected for in the cross section analyses (see Sec. 5.5).

### 4.2.5 Frontend Electronics and Data Acquisition (DAQ)

The COMPASS detectors have a total of $\sim 250000$ electronic channels. In the 2004 muon-beam data taking, the readout of these channels was triggered by the muon-scattering triggers described in the previous section at an average rate of 11 kHz.
The TCS (Trigger Control System) [71] is the central component of the COMPASS DAQ. It broadcasts the common reference clock of the experiment of 38.88 MHz and it receives the trigger signals to distribute them together with an event number to the further DAQ modules in a star-like scheme. The TCS system also generates the dead times which are needed for a stable operation by suppressing triggers under certain conditions (numbers are for the 2004 data taking): If a trigger arrives within a time window of 5 $\mu$s after a previous trigger, if more than 3 triggers arrive within a time window of 75 $\mu$s, or if more than 10 triggers arrive within a time window of 250 $\mu$s. The first condition is needed for some readout electronics that do not have a pipelined structure (electronics for the RICH detector and the calorimeters in 2004), and the latter two requirements are needed because of limitations of the pipelines of some other equipment. At the nominal intensity of the

[4] meaning that only every second trigger is accepted by the data acquisition system.

2004 run, these settings led to an average DAQ dead time of 9%, meaning that 9% of the triggers that were received by the TCS system were not distributed to the other DAQ equipment. The DAQ dead time is corrected for in the absolutely normalized measurements of cross sections (see Sec. 5.5).
All detector signals are digitized very close to the front ends. There are several classes of readout electronics in COMPASS:

- ADC (analog to digital converter) readout of the silicon and GEM detectors (SGADC):
  Both kinds of detectors are read out with the APV25 chip [81]. Three consecutive samples of the shaped and amplified charge pulse from the detectors are read out in each event with a sampling rate of 38.88 MHz to achieve a good time resolution with the ADC readout. The SGADC system performs a correction of baseline fluctuations and a zero-suppression to reduce the data rates.

- Fast Integration ADC (FIADC) readout of the calorimeters:
  These modules are used to read out the signals from the photo-multiplier tubes of the calorimeters in COMPASS. Each channel is a gated charge-integrator circuit, whose output is digitized with an ADC. The signals are zero-suppressed with programmable thresholds. Please note that the readout systems of the calorimeters have been upgraded to a fully pipelined architecture over the past years.

- GASSIPLEX readout of the RICH:
  Up to the 2004 beam time the RICH detector was read out with electronics based on the GASSIPLEX chip [82] and ADCs. This equipment was not pipelined and required a fixed dead time between consecutive events of 5 $\mu$s.

- F1-TDC chips (time to digital converter) for all other detectors:
  The F1-TDC chip [83] has been developed for the readout of a large range of detectors in COMPASS. The requirements range from a time resolution of 100 ps at rates of 10 MHz for the scintillating fiber detectors in the beam to 10 ns time resolution with much lower rates but a very large number of channels for the MWPCs or the muon-wall detectors. Each chip can serve 4, 8, or 32 channels with digitization widths of 65 ps, 130 ps, or 4.2 ps, respectively. The gaseous detectors are equipped with different kinds of charge amplifiers. The signals are discriminated before reaching the inputs of the F1 chips.

- Scalers:
  Some of the discriminated signals which are digitized with TDCs are also counted in scaler modules, which are read out in every event. This is used to monitor rates of different systems such as the the individual trigger counters, the coincidence triggers, the veto counters, the rate of triggers accepted by the DAQ, and many others.

After all data has been digitized with zero suppression very close to the detectors, it is collected and concentrated in two different kinds of dedicated VME modules, which are called GeSiCA (GEM and Silicon Control and Acquisition) and CATCH (COMPASS Accumulate, Transfer, and Control Hardware). Both kinds of modules are configured via Linux VME computers, which communicate with the modules via the VME bus. This interface is also used to configure the frontend electronics

attached to the GeSiCA and the CATCH modules. The modules receive the reference clock, the triggers, and the event numbers from the TCS system via optical fibres. They trigger the readout of the frontend electronics and collect the digitized data. The GeSiCA modules handle the SGADC readout, while the CATCH modules handle all other equipment. The concentrated event data from several detectors which are attached to one GeSiCA or CATCH module are sent to so-called spill buffer cards via optical links. Some of the CATCH modules that serve equipments with low data rates can be multiplexed with other low-rate CATCH modules into one optical link to a spill buffer. The spill buffers are PCI cards which each have a memory of 512MB. The cards are hosted in Linux PCs (readout buffer computers) which can read the data from the spill buffer memory via the PCI bus. Since data is written to the spill buffers only during the 4.8 s on-beam period, while it can be read during the full spill cycle of 16.8 s, the required data bandwidth in the further processing is effectively reduced by a factor of three. During the 2004 beam time COMPASS used 19 readout buffer computers, each of which hosted four spill buffer cards. The final stage in the DAQ are 13 event building computers, which are connected to the readout buffers via a Gigabit network connection. The data from one particular event, which is distributed over many spill buffer cards is sent to one of the event building computers for the final event formatting. The data is saved on hard disks on the event building computer. The recorded data is continuously transferred from the cluster of event building computers to the central tape storage system of CERN.
The data taking in the COMPASS experiment is structured in different entities (the quoted numbers are valid for the 2004 run): The beam is delivered in spills of 4.8 s, which are separated by breaks of 12 s. The spill is the smallest entity in which the data taking is organized. A series of 200 spills defines the entity of a so-called run. Every recorded event can be uniquely identified by its run number, the spill number in the run (1 to 200), and the event number, which is assigned by the DAQ hardware during data taking. The event numbers that are distributed by the TCS system are reset before every spill.

### 4.2.6 Software

#### Event Reconstruction

The reconstruction software of the COMPASS experiment is called CORAL, which is written in the C++ programming language. It reads the raw data files that have been recorded by the event building computers, and produces so-called mDST files (mini Data Summary Table), which are written in the file format of the ROOT data analysis framework [84].
The event processing in CORAL begins with the *decoding* of the data, i.e. the creation of individual objects of raw detector information from the binary data files. The information consists of channel numbers, amplitude information, and time information. The next step is the *mapping* of the channel numbers to geometrical positions of the hits. In some detectors, where a single traversing particle leaves responses in several neighboring channels of the detector (e.g. silicon or GEM detectors), hits can be combined into *clusters* to increase the accuracy of the measurement. The next step in the event reconstruction is the *pattern recognition* of straight-line tracks in five zones of the spectrometer, which are separated by the target, the SM1 magnet, the SM2 magnet, and the second muon filter $\mu$F2. The straight-line finding is performed in separate projections first, meaning that only the detector planes with the same orientation of strips are combined with each

other. The algorithm starts with all combinations of straight lines made up by the hits in the first two planes. It then tries to collect more hits in the other planes of tracking detectors if they lie within a certain "road width" of the line. The road width is defined by the spatial resolution of the hits. The physical tracks are identified by the application of certain track-quality criteria. After completion of this step, the straight lines in the single projections can be combined with each other to form three-dimensional tracks. So-called ghost tracks that are created by random combinations of hits from different tracks are strongly suppressed in this step where the tracks from usually more than two projections are combined with each other. The next step of the event processing is called *bridging*, in which the straight-line track segments from neighboring zones are merged together, for instance by extrapolating the straight lines into the middle of the magnet and checking whether they are continuous. The final step of the particle tracking is the determination of the *best estimates of the track parameters* and their covariance matrix, which is done with the Kalman filter algorithm [85, 86]. The final step in the event processing is the step of *vertex finding and fitting*. A vertex is a point in space where a particle was scattered and possibly created additional particles, or the point where a longer lived particle decayed. The vertex fit is also implemented with the Kalman filter algorithm. The output of the vertex fit is the vertex point itself, but also refined track parameters and covariances that use the information of the vertex point and its uncertainty as an additional constraint for the trajectories. The track parameters from the vertex fit are used for the calculation of the kinematics of the scattering events in the physics analyses, i.e. the calculation of momentum transfers, invariant masses in decays, angles between tracks, and many others.
For each event, the mDST files contain the fitted tracks and vertices with their respective covariance matrices. The clusters of the calorimeters and information about their track association are also written to the mDST files. The hits in the tracking detectors are usually not written to the mDST files in order to reduce the data volume that needs to be processed in the data analyses.

### Monte Carlo Simulations for Acceptance Corrections

Monte Carlo (MC) simulations are needed to study the acceptance of the COMPASS spectrometer for certain scattering reactions. The acceptance is a combination of the detection efficiency and kinematical smearing. The efficiency is defined by the phase-space coverage of the detectors as well as by their intrinsic efficiency. The acceptance in a certain kinematical region is defined by the number of reconstructed final states in that region divided by the number of generated final states in the same region. More detailed descriptions are given in Secs. 5.7 and 6.3 where acceptance corrections are used to determine the cross sections for inclusive muon scattering and high-$p_T$ hadron production, respectively.
Scattering events are generated with different kinds of event generators depending on the specific scattering process under investigation. The generated events are propagated through the COMPASS experimental setup with COMGEANT[5], which is an MC particle-transport program based on GEANT 3.21. COMGEANT generates an output file that for each event contains the positions of the passage of the simulated particles through the COMPASS detectors, as well as the particle 4-momenta and scattering vertices that were generated by the event generator. This information is referred to as MC truth information. The simulated trigger decision is also saved to the output file.

[5] COMGEANT version 7.02 is used for the analysis of 2004 data.

The output file is then processed with the standard event reconstruction program CORAL. First, it converts the MC truth information on the detector hits to more realistic hits by applying inefficiencies of the detectors (statistically ignoring some hits), and by smearing the hits with the detector resolutions. After this step, the MC data is treated in the same way as the real experimental data. In addition to the reconstructed tracks and vertices, CORAL saves the MC truth information about the 4-momenta and the vertices to the mDST output file. The same version of CORAL[6] that has been used for the reconstruction of the real experimental data has to be used for the acceptance correction. This way, the acceptance factors also correct the data for imperfections in the reconstruction software.

**Event Selection and Histogramming**

The software for event processing in COMPASS is called PHAST (PHysics Analysis Software Tools) [87]. It reads the mDST files and allows the implementation of C++ functions called "user event functions" that have access to all data saved in the events. PHAST can be used for the filtering or skimming of mDST files, to fill data trees or so-called ntuples[7] with reduced event information, or for directly filling histograms.
In the case of the high-$p_T$ hadron analysis of chapter 6, the data volume is reduced by a factor of $\sim$ 100 in the first iteration of event processing by saving only the events that have at least one hadron with a transverse momentum of 1 GeV/$c$ or more. The output files of this procedure are often referred to as $\mu$DST files.
The $\mu$DST files are then reprocessed with PHAST to produce ntuple files containing the 4-momenta of all tracks connected to the primary vertex and some supplementary information needed for the further selection cuts. The final piece of software in the presented data analysis is a C++ program which processes the ntuple files and produces histograms that contain the particle yields and kinematical distributions.

[6] CORAL version 2007-10-5 has been used for the reconstruction of the data set used in the analyses of chapters 5 and 6.

[7] the TTree class of the ROOT framework is used for the implementation of ntuples.

# Chapter 5

# Luminosity Measurement at COMPASS

The COMPASS experiment has published a wealth of results on the spin structure of the nucleon, which have been obtained from measurements of double-spin asymmetries of cross sections. The polarized target of COMPASS consists of oppositely polarized cells, which allows the direct measurement of spin asymmetries. A knowledge of the luminosity is not required because it cancels out if an equal beam flux through both target cells is ensured. Systematic effects due to different acceptances for events from the different target cells are cancelled by reversals of the cell polarizations.
Measurements of absolute, unpolarized cross sections of scattering processes provide important benchmarks for theoretical models that describe these processes. Examples in the case of COMPASS are the cross section for open-charm production in muon-nucleon scattering, where the effective charm quark mass and contributions of processes beyond photon-gluon fusion can be probed (see Sec. 2.4), or the cross section for high-$p_T$ particle production, where the applicability of NLO pQCD calculations can be investigated (see chapter 3). Such measurements require a good knowledge of the luminosity of the experiment. In many experiments, luminosity monitors measure the event rate for a reference process with a well-known cross section, such as elastic scattering. Since this is not feasible in the COMPASS kinematics, cross-section measurements were not foreseen in the design of COMPASS and the collaboration, to this date, has not published any such results from the muon-scattering program.
This chapter presents the first determination of the luminosity for the COMPASS data via the direct measurement of the beam flux and the correction of all dead times and inefficiencies. The determined luminosity is validated via the measurement of the well-known unpolarized structure function of the nucleon $F_2$ and its comparison to literature.
The terminology of cross-section and luminosity measurements in the context of COMPASS is introduced in Sec. 5.1. The used data set is described in Sec. 5.2, followed by the data selection criteria in Sec. 5.3. Section 5.4 describes the measurement of the beam flux and is followed by Sec. 5.5 which explains the sources of dead times in the measurement and their corrections. The resulting luminosity and its systematic uncertainty are presented in Sec. 5.6 . Section 5.7 discusses the determination of the structure function $F_2$ from the normalized data set. The comparison of the results to a parametrization obtained from measurements of $F_2$ by the NMC experiment [88] confirms that the COMPASS luminosity has been correctly determined within a systematic uncertainty of 10%. It can hence be used for the measurement of unknown cross sections, for instance

the high-$p_T$ hadron-production cross section of chapter 6.
A previous attempt to determine the luminosity for the COMPASS data [89] did not lead to any publications of cross sections by the COMPASS collaboration because a cross check of the analysis was missing. The analysis presented in this chapter started out as a cross check of the previous analysis, but it soon became clear that the previous analysis contained a number of non-recoverable errors and oversimplifications. It was hence discarded for the purpose of the high-$p_T$ cross section measurement. Nevertheless, some of the procedures presented here were inspired by the previous analysis.

## 5.1 Luminosity Definition

The cross section for the observation of a particular final state is defined as

$$\sigma = \frac{\dot{N}}{\mathcal{L}} = \frac{N}{L} \quad , \tag{5.1}$$

with the rate of occurrence of the final state $\dot{N}$ and the instantaneous luminosity $\mathcal{L}$ (and their respective time integrals $N$ and $L$). For fixed target experiments, the instantaneous luminosity is defined as

$$\mathcal{L} = \Phi_{\text{beam}} \cdot N_{\text{target}} = \frac{R_{\text{beam}}}{A_{\text{target}}} \cdot N_{\text{target}} \quad , \tag{5.2}$$

where $\Phi_{\text{beam}}$ ($R_{\text{beam}}$ ) is the beam flux (rate) through the fiducial target volume, $A_{\text{target}}$ is the area of the fiducial target perpendicular to the beam, and $N_{\text{target}}$ is the number of target nucleons in the fiducial target volume. The fiducial target volume is defined as the part of the target which is retained after the geometrical cuts on the positions of the primary scattering vertices. Only events with beam tracks which cross the full length of the fiducial target volume are considered in the analysis.
The observation of final states can be affected by the misreconstruction of kinematical variables, by detection inefficiencies, and by dead times during which the experiment can not record events. The kinematical smearing and the detection inefficiencies, which are mostly due to incomplete geometrical coverage of the phase space by the detectors and trigger elements, are summarized in the acceptance correction factor $\epsilon$. The cross section is then given by

$$\sigma = \frac{\tilde{N}/\epsilon}{\tilde{L}} \quad , \tag{5.3}$$

with the number of *observed* final states $\tilde{N}$ and the effective integrated luminosity $\tilde{L}$, which is corrected for the dead times of the experiment.
The COMPASS beam is delivered by the SPS accelerator in so-called spills[1]. In the 2004 beam time, when the discussed data set was taken, COMPASS was supplied with spills of muon beam of length 4.8 s, followed by breaks of 12 s. The dead times in the data taking caused by the data acquisition system (DAQ) and the veto system of the scattered-muon trigger [80] are rate dependent. Since the intensities of different spills differ considerably, the dead times need to be

[1] the term *spill* denotes one extraction cycle from the accelerator.

corrected on a spill-by-spill basis. The acceptance correction factor $\epsilon$, which is obtained from a Monte Carlo simulation of the experiment with a constant beam rate assumption, only includes effects which are not, or only weakly, rate dependent. All rate-dependent effects are absorbed into the definition of the effective integrated luminosity of a spill $i$

$$\tilde{L}_i = \int\limits_{\text{duration of spill } i} [\mathcal{L}_i(1 - d_{i,\text{DAQ}})(1 - d_{i,\text{veto}})]\mathrm{d}t \quad , \tag{5.4}$$

where $d_{i,\text{DAQ}}$ is the DAQ dead time, i.e. the fraction of data taking time during which the DAQ can not accept triggers because it is busy with readout of previously triggered events, and $d_{i,\text{veto}}$ is the dead time of the veto system of the muon trigger (for details see Sec. 5.5). The DAQ dead time and the veto dead time are independent from each other. The total integrated effective luminosity $\tilde{L}$ is the sum over all spills which are used for the extraction of the number of final states $\tilde{N}$.

## 5.2 Data Set

The analyzed data set was recorded in 2004. This particular choice is motivated by the fact that the measurement of the hadron production cross section, which is presented in the next chapter, depends on semi-inclusive trigger systems which include the response of the two hadronic calorimeters of COMPASS. After the introduction of a new electromagnetic calorimeter (ECAL1) after the 2004 beam time, the efficiencies of these triggers have been compromised, which would make an absolutely normalized measurement more difficult. Spin asymmetry measurements are not affected by this problem, because the trigger acceptance is canceled out in these measurements. In the 2004 beam time, COMPASS was supplied with a $\mu^+$-beam of 160 GeV/$c$ with a nominal intensity of $4 \cdot 10^7\ \mathrm{s}^{-1}$. The momenta of the individual beam particles were measured with scintillator hodoscopes surrounding three beam-line dipole magnets (Beam Momentum Station, BMS). About 30% of the 2004 data set were reprocessed with a newer version of the event reconstruction software CORAL, in which a small inefficiency in the reconstruction code of the beam momentum measurement was cured. Only this portion of the data set is considered for the luminosity analysis (periods W28, W29, W30, and W31).
Due to an accelerator problem, COMPASS received only half of its nominal beam intensity for half of the data taking time under consideration (W28 and W29). At first glance, this might seem like an unpleasant problem to deal with; however, it provides a valuable tool to check the consistency of the luminosity result. Although many rate-dependent factors enter in the luminosity determination, cross sections measured with the two different beam intensities have to be identical. It is shown at the end of this chapter that this is in fact the case.

## 5.3 Data Selection

### Beam Flat-Top Selection

The intensity of the COMPASS beam increases over the first second of each spill, after which it reaches a flat top with an intensity which is stable within $\sim$ 10%. As the corrections for the rate-dependent dead times of COMPASS shall be applied as simple scaling factors for each spill,

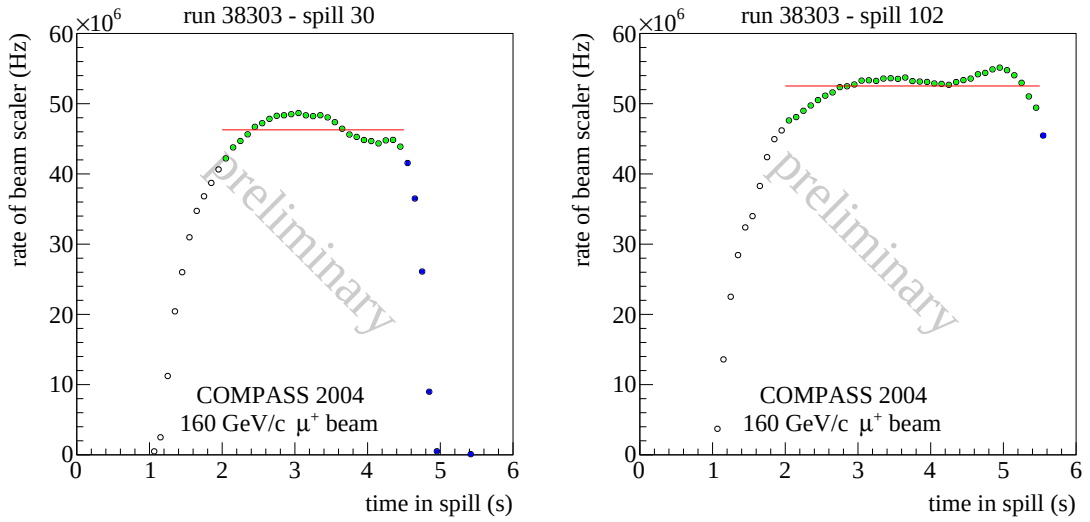


**Figure 5.1:** Time structure of two spills of one data-taking run. The green markers indicate time bins which are used for the analysis starting at $t_1 = 2\,\text{s}$. The blue markers indicate bins which are excluded by the $t_{i,2}$ cut ($t_{30,2} = 4.5\,\text{s}$, $t_{102,2} = 5.5\,\text{s}$). The red lines indicate the average rates.

only the flat top of the beam is selected for the luminosity analysis. Furthermore, it is known that the COMPASS beam from the SPS can be poorly debunched in the first few hundred milliseconds of the spill. This would make the estimation of the dead time of the trigger system very difficult because the beam particles, which fire the trigger, and the halo particles, which are responsible for the trigger-veto signals, would not be independent in their relative timing. This problem is fully avoided by the flat-top selection.

The uniform flat top of spills is defined to start at a value of the *time-in-spill* variable $t_1 = 2\,\text{s}$ after the begin-of-spill signal from the SPS[2]. The length of the flat top varies between different spills. Thus, the *time-in-spill* $t_{i,2}$ after which the data is discarded from the analysis is determined for each of the many thousands of spills individually. $t_{i,2}$ is defined as the time when the instantaneous beam rate has dropped below 90% of the average beam rate in the spill (starting from $t_1$). The analysis of the instantaneous beam rate is performed in time bins of width 0.1 s in each spill by searching the earliest and latest events recorded in each time bin. The integrated rate of incident beam particles is measured by a scaler which counts the number of signals from a scintillating fiber detector which is located just upstream of the target (FI02Y). The instantaneous beam rate in each time bin is given by the difference between the scaler readings of the latest and the earliest event normalized to the time difference between the latest and the earliest event. There are about 500 to 1000 events in the data files for each 0.1 s time bin depending on the beam intensity. Figure 5.1[3] shows two examples of spills with different average intensities and lengths.

The *time-in-spill* information is missing in the data which has been reconstructed with the final version of the event reconstruction software CORAL[4] due to a configuration problem. This is why

[2] please note that there is 1 s time difference between the begin-of-spill signal and the actual delivery of the beam.

[3] all plots which carry a label "preliminary" are approved to be shown in public presentations as official COMPASS results.

[4] PaEvent::TimeInSpill() always returns zero in CORAL-2007-10-5.

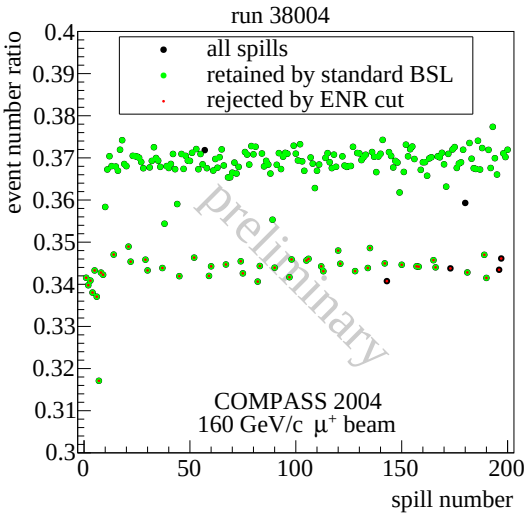


**Figure 5.2:** Event number ratio for the spills of one data-taking run.

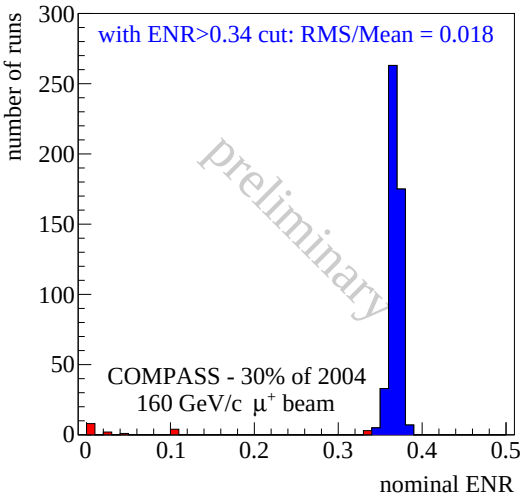


**Figure 5.3:** Distribution of nominal values of ENR for all used runs.

the determination of the average rates of particles counted by the scaler system and the values of $t_{i,2}$ had to be performed on the previous production of the data. The time cut was translated into an event-number cut, which can be used for the physics selection on the latest production. The event numbers are assigned by the DAQ system during data taking. The values $nev_{i,1}$ and $nev_{i,2}$ were determined for each spill which ensure that the event is within the time window $t_1 \leq$ *time-in-spill* $\leq t_{i,2}$ if the condition $nev_{i,1} \leq$ *event number* $\leq nev_{i,2}$ is fulfilled.

### Good Spill Selection

The removal of spills which are affected by detector or data-processing problems is essential for the determination of a correct luminosity for cross section measurements, because such spills contain less reconstructed events for a given incoming beam intensity. Problematic spills are removed from all analyses in the muon program of COMPASS with the use of so-called bad spill lists (BSL) [90, 91]. Spills are selected as bad if they fall below or above their neighboring spills in one of three figures of merit: The number of primary vertices per reconstructed event, the number of tracks per primary vertex, and the number of beam tracks per reconstructed event. Another criterion for spill removal is added for this normalized analysis. The figure of merit *event number ratio* (ENR) is defined per spill as:

$$\text{ENR} = \frac{\text{number of reconstructed events in mDST}}{\text{number of triggered events}} \quad . \tag{5.5}$$

mDST files contain the reconstructed events in which a muon-scattering vertex was detected. Figure 5.2 shows the ENR for each spill of one data-taking run. The nominal value is around 0.37, which is given by the purity of the muon trigger system. As indicated by the green markers, the COMPASS BSL also accepts spills with reduced values of ENR. There are three possibilities how this can happen:

1. Very rarely occurring losses of raw-data files from one of the thirteen event-building computers. The first nine spills of Fig. 5.2 are affected by this problem.

2. Rarely occurring crashes of the reconstruction software on single raw-data files.

3. Spills with detector problems that were not removed by the standard COMPASS BSL.

In the analyzed data set, the latter point mainly concerns the scintillating-fiber detector FI05Y. This detector had a temperature problem with a low voltage power supply which disabled the detector in every other spill in the 2004 beam time. This can be seen in the low-ENR spills in Fig. 5.2. These spills were not removed by the standard BSL in the periods W30 and W31, because the problem affected both periods in the same way, so that the effect cancels out in spin-asymmetry measurements [92]. For normalized cross section measurements, however, the affected spills need to be removed from the data set, which is achieved with a cut on ENR. Spills with an ENR which is more than 0.0125 below the nominal value for the run are removed from the data sample, as indicated by the red symbols in Fig. 5.2. There is an additional hard cut of ENR $\geq$ 0.34 for all spills, which is independent of the nominal value, to remove a few anomalous runs. The nominal ENR value is determined for each spill individually. The distribution of nominal ENR values for all used runs is shown in Fig. 5.3. The fluctuation of 1.8% in the nominal ENR is used in the estimation of the systematic error of the luminosity as an indicator for the stability of the reconstruction efficiency of COMPASS.
After the application of the BSL and the new ENR cut, 54624 of 73591 spills are retained and further used for the luminosity determination and subsequent cross section analyses. Appendix A provides an overview over the number of spills which were removed by the different cuts. A list of all the individual spills which were removed by the different cuts is shown in appendix B of the COMPASS release note about this analysis [93].

## 5.4 Beam Flux Measurement

The rate of particles measured with the scaler on FI02Y, $R_{\mathrm{Sc}}$, does not equal the rate of beam particles, $R_{\mathrm{beam}}$, of Eq. (5.2) because only 65% of all beam particles which cross the beam counter also cross the complete length of the fiducial target volume. Furthermore, the rate measurement with the scaler system and the beam counter can be affected by detection inefficiencies and dead times. A calibration of $R_{\mathrm{Sc}}$ with an unbiased measurement of $R_{\mathrm{beam}}$ is performed on a sub-sample of twelve runs by counting the number of reconstructed beam tracks in random-trigger events[5]. The rate of beam particles measured in random-trigger events is

$$R_{\mathrm{beam}} = \frac{N_{\mathrm{beam\ tracks}}}{\Delta t \cdot N_{\mathrm{random\ triggers}}} \quad , \tag{5.6}$$

where $N_{\mathrm{beam\ tracks}}$ counts the beam particle tracks which are retained after the fiducial target cut and the requirement of a measurement of the track in the BMS. The time window $\Delta t = 3.8$ ns is the interval in which the COMPASS beam telescope can efficiently reconstruct beam tracks (-1.9 ns

[5] random triggers lead to a readout of all detector electronics and are completely uncorrelated to the presence of beam tracks or scattering events.

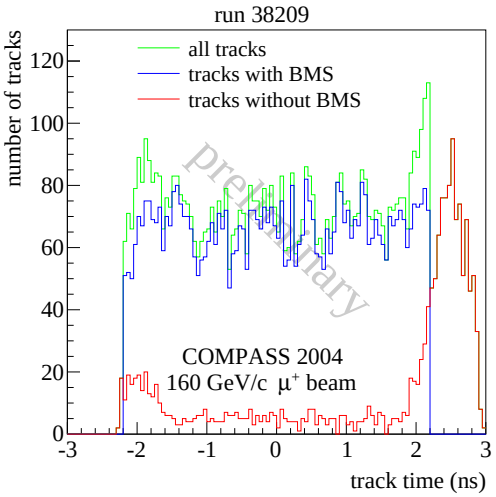


**Figure 5.4:** Time distribution of beam tracks in random-trigger events from one data-taking run. The beam rate estimation uses the blue spectrum from -1.9 ns to 1.9 ns.

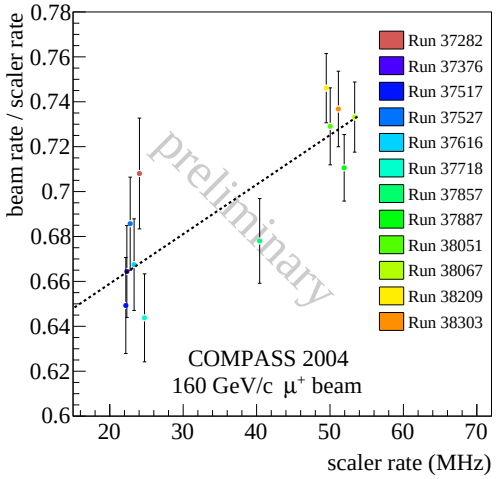


**Figure 5.5:** Calibration factor $R_{\text{beam}}/R_{\text{Sc}}$ as a function of $R_{\text{Sc}}$. The dashed line indicates the function used for the spill-by-spill beam-flux calibration.

before the trigger time to 1.9 ns after the trigger time). Figure 5.4 shows the time distribution of beam tracks w.r.t. the trigger time. In the range where the distributions of beam tracks with and without BMS measurements are flat, the ratio of the integrals can be used to estimate the BMS efficiency which turns out to be 92%. The small inefficiency of 8% is automatically included in the beam rate measurement from random-trigger events so that the resulting luminosity will correctly contain only the portion of the beam which is usable for the measurement of the yield of final states $\tilde{N}$ in Eq. (5.3), where a BMS measurement is of course required. The ratio $R_{\text{beam}}/R_{\text{Sc}}$ is shown in Fig. 5.5 as a function of $R_{\text{Sc}}$. The runs with 50% beam intensity are clearly visible. A linear calibration function has been fitted to the data points and is used in the luminosity analysis to obtain $R_{\text{Beam}}$ from $R_{\text{Sc}}$, which is measured in every spill. The rate dependence of the calibration function is probably due to dead times in the scaler system, but there is currently no clear proof for this possible explanation. The systematic error of the calibration factor is estimated to be 5%, which is given by the standard deviation of the twelve data points. This conservative estimation of the error ignores the rate dependence of the calibration because the reasons for it can not be understood in last detail. The relative difference of the calibration between the half and full intensity runs of more than 10% proves to be correct in the comparison of the inclusive muon scattering cross sections from these data sets in Sec. 5.6.

The rate of recorded random triggers, which was about $100/(t_{i,2} - t_1)$ per spill in the 2004 beam time, will be increased for future measurements for which a good luminosity normalization is required, e.g. the DVCS measurement. If several thousand reconstructed beam tracks per spill are recorded in random-trigger events, the beam rate $R_{\text{Beam}}$ can be estimated directly from the random triggers with a negligible systematic uncertainty.

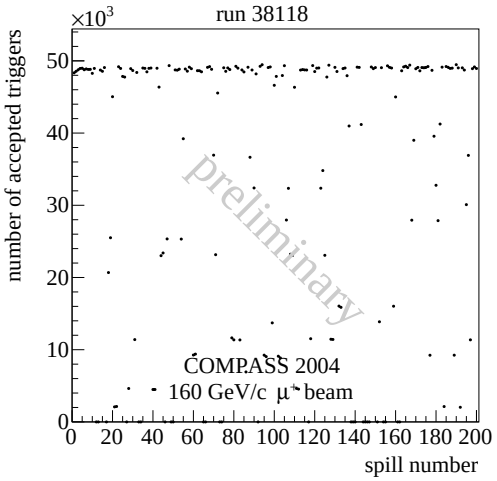


**Figure 5.6:** Number of accepted triggers in each spill of one run.

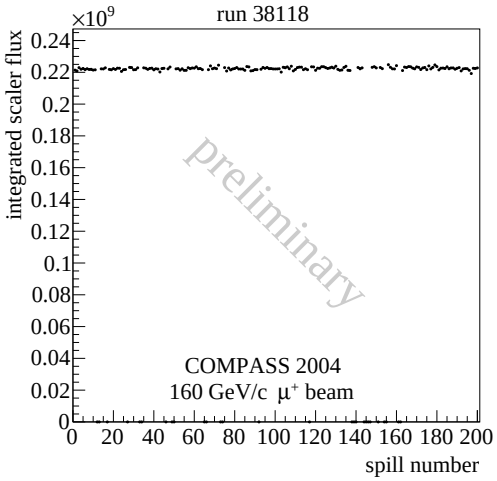


**Figure 5.7:** Flux of beam particles measured in the beam scaler.

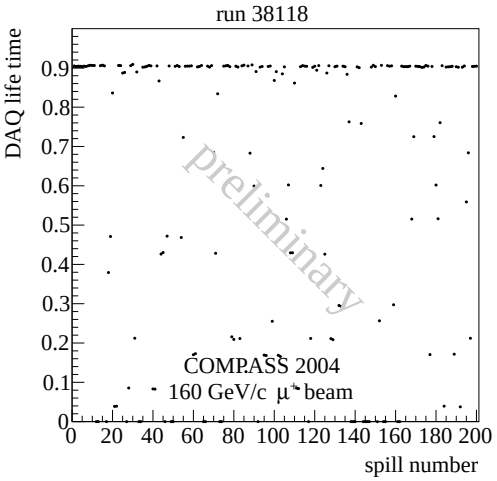


**Figure 5.8:** DAQ life time $1-d_{i,\mathrm{DAQ}}$ as defined in eq. (5.7).

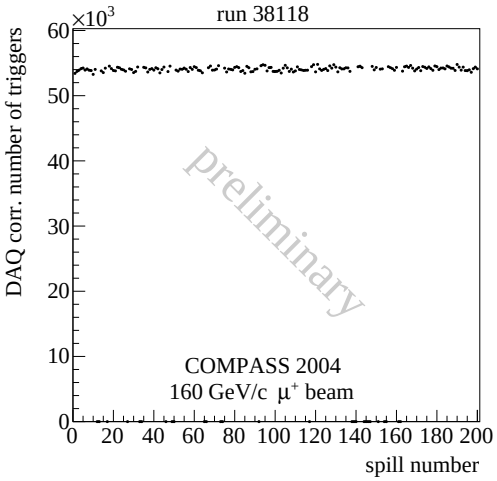


**Figure 5.9:** The number of accepted trigger attempts divided by the DAQ life time.

## 5.5 Corrections for Dead Times

The DAQ dead time, $d_{i,\mathrm{DAQ}}$, of Eq. (5.4) is defined as the fraction of data taking time in which triggers can not be accepted because the DAQ is busy with acquiring and recording previously triggered events. It is measured directly in COMPASS by counting the number of trigger attempts and the number of accepted trigger attempts with scalers that are read out for each recorded event. The DAQ dead time is:

$$d_{i,\mathrm{DAQ}} = 1 - \text{DAQ life time} = 1 - \frac{\#\text{ accepted triggers}}{\#\text{ trigger attempts}} \quad . \tag{5.7}$$

It is determined for each spill in the flat top of the beam (*time-in-spill* $\in [t_1, t_{i,2}]$). The trigger rate during the 2004 run was about 11 kHz at full intensity which resulted in an average DAQ dead time of 9%. The correctness of the DAQ dead-time determination is checked with data from a run

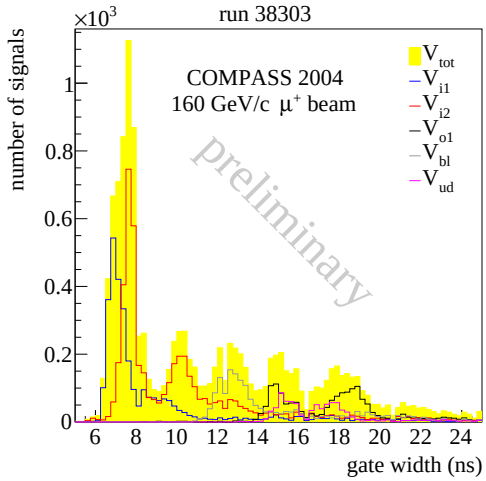


**Figure 5.10:** Gate width distribution of the veto signals. The signal $V_{\text{tot}}$ (yellow filled histogram) is made from a logical OR of the signal of the individual counters $V_{\text{i1}}$ to $V_{\text{ud}}$ (line histograms).

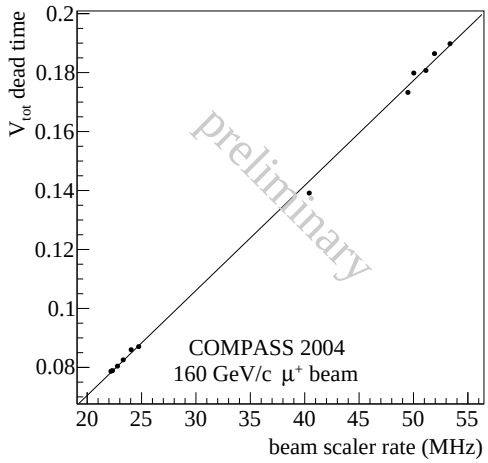


**Figure 5.11:** Veto dead time as a function of the beam-scaler rate. At full intensity, the dead time reaches a maximum of 19%.

with a DAQ problem: Run 38118 was recorded when there was a problem with an event-building computer (EB16) which blocked the DAQ for unusual amounts of time in every other spill ("DAQ throttle"). Figure 5.6 shows the number of accepted triggers for all spills of this run. Figure 5.7 shows that the beam flux is constant, which should lead to a constant number of trigger attempts. The DAQ life time, as defined in Eq. (5.7), is shown in Fig. 5.8. The number of accepted trigger attempts divided by the DAQ life time corresponds to the number of trigger attempts. It is shown in Fig. 5.9 and exhibits the same uniformity as Fig. 5.7 thus proving that the dead time correction works.

The second source of dead times in the COMPASS experiment is the veto system of the muon triggers ($d_{i,\text{veto}}$ of Eq. (5.4)). The triggers consist of coincidences between scintillator-hodoscope pairs with target pointing for different muon-scattering kinematics. The trigger conditions include anti-coincidences with veto counters, which surround the beam region upstream of the target to suppress triggers due to unscattered, inclined halo particles [80]. The veto dead time is defined as the fraction of data taking time during which no triggers can be accepted because active veto signals are present.

In COMPASS, there are veto counter of different sizes, different distances to the beam, and different positions along the beam axis. Larger counters require longer gate widths because of the increased time jitter due to longer light propagation times. The veto signal $V_{\text{tot}}$ is made from a logical OR of the individual signals from the different veto counters. The signals of the individual counters and the $V_{\text{tot}}$ signal are read out with TDCs (time to digital converter). This allows the determination of the gate width distribution of the signals, which is shown in Fig. 5.10. The procedure is described in more detail in Ref. [93].

The number of veto pulses $N_{\text{V},i}$ in the flat top (*time-in-spill* $\in [t_1, t_{i,2}]$) of spill $i$ is counted with a scaler system. The veto dead time in the spill, i.e. the duty cycle of the veto signal, is deter-

mined by summing up $N_{\mathrm{V},i}$ samplings from the gate width distribution and normalizing the sum to $t_{i,2} - t_1$. The average dead times for the same twelve data-taking runs that were used for the beam flux calibration are shown in Fig. 5.11. The linear function which has been fitted to the data is used to calculate the veto dead time for all spills used in the analysis. The absolute systematic error of the veto dead time is conservatively estimated to be 0.03, which arises from the maximal difference with other measurements of the veto dead time during the 2004 data taking [94].

## 5.6 Luminosity Result

The COMPASS target in the 2004 data taking consisted (by number of nucleons) of 42.3% deuterium, 42.5% lithium, and 15.2% helium. The number of nucleons per unit area was $3.44 \cdot 10^{25}\,\mathrm{cm}^{-2}$ which was measured with a relative systematic uncertainty of 2% [95]. The relative systematic uncertainty of the beam flux calibration is 5%. The relative systematic error due to the reconstruction efficiency is 1.8%, and the veto dead time is measured with an absolute uncertainty of 0.03. From these individual contributions, the overall systematic uncertainty is conservatively estimated to be 10%.
The effective integrated luminosity for the discussed data set, corrected for the DAQ dead time, is $\tilde{L} = 142.4\,\mathrm{pb}^{-1}$. The correction for the dead time of the veto system $V_{\mathrm{tot}}$ reduces this number to $122.6\,\mathrm{pb}^{-1}$. Please note that not all triggers in COMPASS include the full veto system. The triggers for the quasi-real photoproduction regime ($Q^2 < 0.5\,(\mathrm{GeV}/c)^2$) are subject to a much lower veto dead time.
In the next section, the structure function $F_2$ is determined from the COMPASS data and compared to a parametrization obtained from previous measurements of $F_2$ by the NMC experiment. The comparison serves as a consistency check for the determined luminosity value.

## 5.7 Determination of the Structure Function $F_2$

### Event Selection

Events which are recorded by the so-called inclusive middle trigger (inclMT) are used for the determination of the cross section for inclusive muon scattering and the subsequent extraction of the structure function $F_2$ in the regime $Q^2 > 1\,(\mathrm{GeV}/c)^2$. The scintillator hodoscopes contributing to this trigger are fully efficient. Only events which pass the good spill selection and the beam flat-top selection of Sec. 5.3 are analyzed. Events are accepted if the beam energy is $E \in [140, 180]\,\mathrm{GeV}$ and the relative energy loss of the muon $y$ is greater than 0.1 and less than 0.9. Furthermore, the extrapolated beam track of each event is required to cross the full length of the fiducial target volume and the muon scattering vertex position must lie in the fiducial target volume (same cuts as in the beam flux determination of Sec. 5.4). The distributions of the kinematical variables $y$ and $Q^2$ of the events which passed all selection criteria are shown in Fig. 5.12.

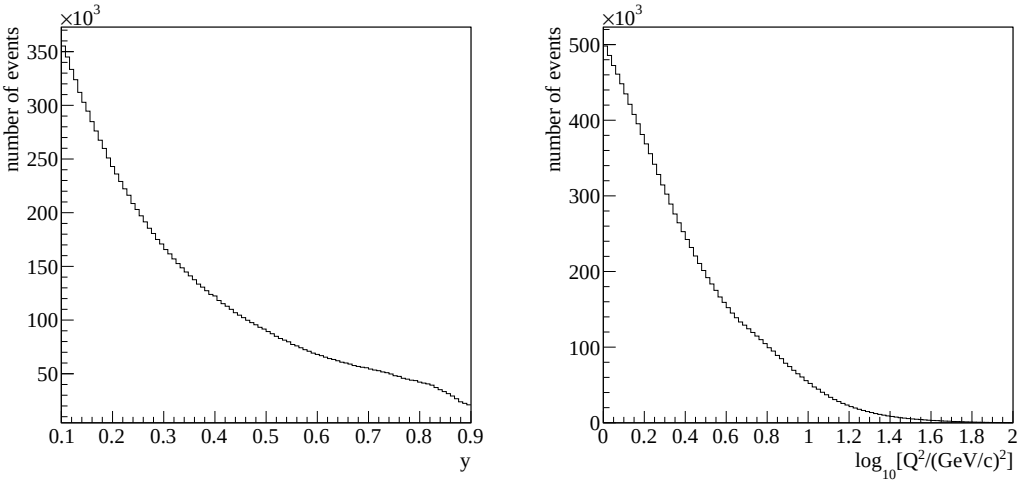


**Figure 5.12:** Distributions of $y$ and $Q^2$ for data set used for the $F_2$ determination.

## Acceptance Correction

The acceptance correction factors $\epsilon$ of Eq. (5.3) are determined with a Monte Carlo (MC) simulation of inclusive muon scattering in the COMPASS experiment. The MC event sample was produced by N. Makke from CEA Saclay for which I am very grateful. The event generator LEPTO [23] was used with the parton distribution functions from MSTW 2008 [96]. The generated events were transported through the spectrometer with COMGEANT and analyzed with the reconstruction software CORAL (for a description of the software, see Sec. 4.2.6).
The acceptance factor for events detected in the kinematical bin $Q^2 \in [Q_1^2, Q_2^2] \wedge y \in [y_1, y_2]$ is defined by the ratio of the number of reconstructed MC events and the number of generated MC events:

$$\epsilon(Q^2, y) = \frac{N_{\mathrm{MC}}^{\mathrm{rec}}(Q_{\mathrm{rec}}^2 \in [Q_1^2, Q_2^2] \wedge y_{\mathrm{rec}} \in [y_1, y_2])}{N_{\mathrm{MC}}^{\mathrm{gen}}(Q_{\mathrm{gen}}^2 \in [Q_1^2, Q_2^2] \wedge y_{\mathrm{gen}} \in [y_1, y_2])} \quad . \tag{5.8}$$

The acceptance for inclusive muon scattering detected in the inclMT is shown in Fig. 5.13. It reaches a maximum of 66%. A simple check has been performed to verify that this acceptance value is reasonable: The middle trigger hodoscopes HM04 and HM05 are pairs of rectangular scintillator planes that leave vertical gaps of $2 \cdot 16$ cm (HM04) and $2 \cdot 20$ cm (HM05), respectively. In the kinematical region of maximal acceptance ($Q^2 = 1.5\,(\mathrm{GeV}/c)^2$ and $y = 0.4$) the $x$-$y$ hit maps in the hodoscopes, which are shown in Fig. 5.14, exhibit clear rings with two missing segments of 47° each. This corresponds to an acceptance of 74%. Assuming a tracking efficiency for the scattered muon of 89%, which is very close to the usual single-track efficiency of COMPASS, this value is in agreement with the COMGEANT result ($0.89 \cdot 0.74 = 0.66$).
A comparison of kinematical distributions of reconstructed Monte Carlo events and real data events is shown in Fig. 5.15. It indicates disagreements of up to 10% in some kinematical regions. This either points towards an incomplete description of the acceptance of the same order of magnitude or to a wrong population of the phase space by LEPTO. Since it is the sole purpose of this analysis to check whether the normalization of the luminosity is correct within the systematic uncertainty of 10%, this disagreement seems tolerable and has not been further investigated.

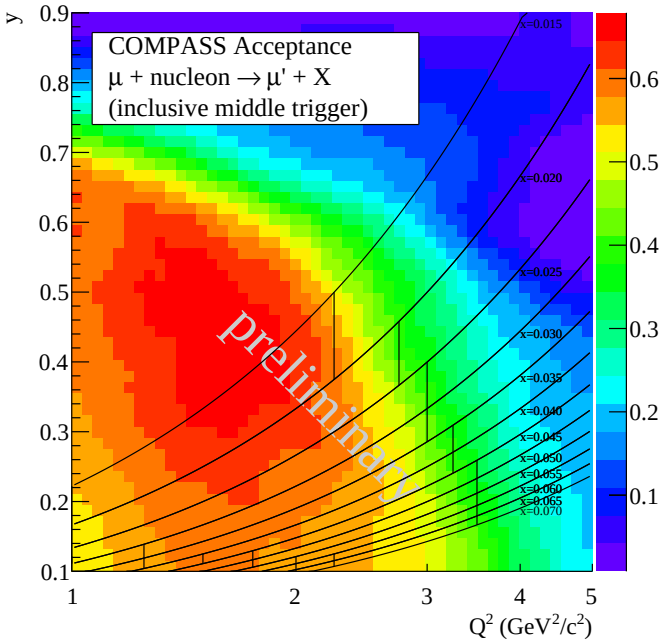


**Figure 5.13:** Acceptance for inclusive muon scattering in the inclMT, as determined with a Monte Carlo simulation. The $x_{\mathrm{Bj}}$-bins which are used in the analysis are the regions between the lines in the plot.

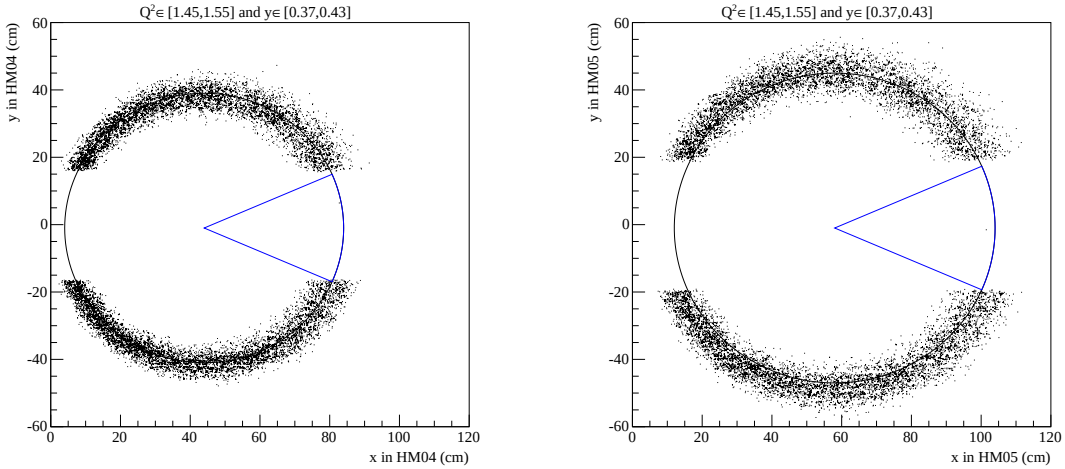


**Figure 5.14:** $x$-$y$ hit map of the extrapolated scattered-muon tracks in inclMT events in HM04 (left plot) and HM05 (right plot) for $Q^2 = 1.5\,(\mathrm{Gev}/c)^2$ and $y = 0.4$, which is the region of maximum acceptance of 66%. The two ring segments without trigger coverage span 47° in both cases which corresponds to 74% acceptance. The circle parameters have been fitted by hand.

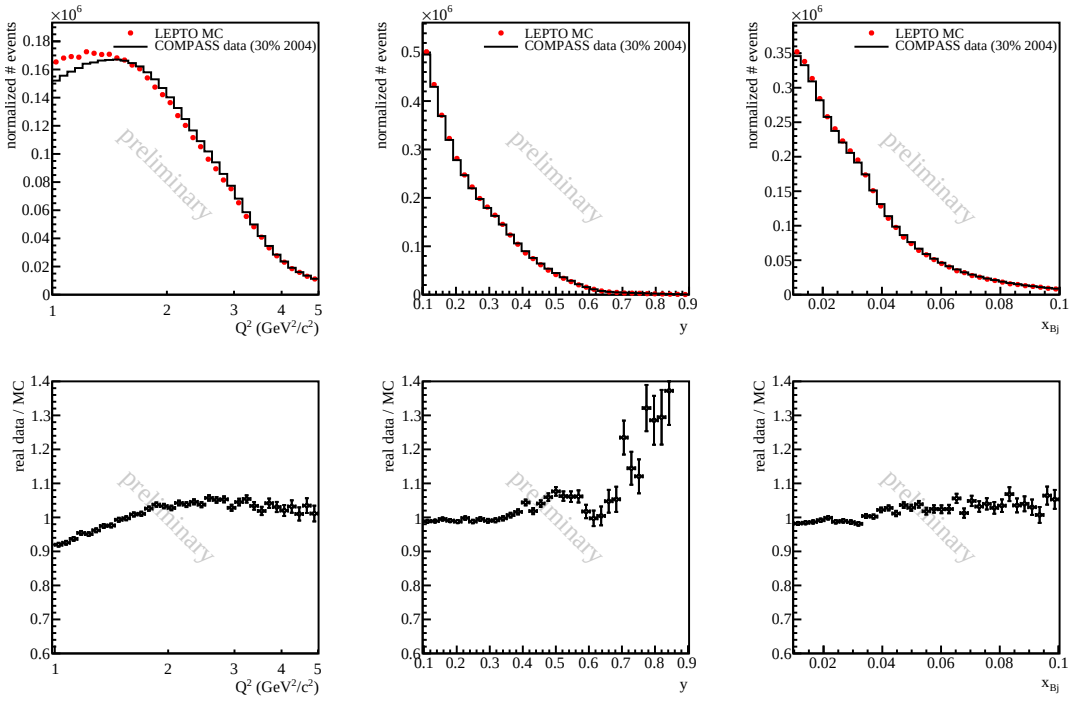


**Figure 5.15:** Comparison of real data (radiative corrections applied) and Monte Carlo simulation in the kinematical variables $Q^2$, $y$, and $x_{\mathrm{Bj}}$.

## Cross Section

The acceptance correction is applied as an event-by-event weighting factor to obtain the differential cross section in the kinematical bin $Q^2 \in [Q_1^2, Q_2^2] \wedge x_{\mathrm{Bj}} \in [x_{\mathrm{Bj},1}, x_{\mathrm{Bj},2}]$:

$$\frac{\mathrm{d}^2\sigma}{\mathrm{d}x_{\mathrm{Bj}}dQ^2} = \frac{1}{\tilde{L}} \cdot \frac{1}{(x_{\mathrm{Bj},2} - x_{\mathrm{Bj},1})(Q_2^2 - Q_1^2)} \cdot \sum_{i=1}^{N} \frac{1}{\epsilon(Q_i^2, y_i)} \quad , \tag{5.9}$$

where the sum runs over all $N$ events in the bin $[Q_1^2, Q_2^2]$, $[x_{\mathrm{Bj},1}, x_{\mathrm{Bj},2}]$.

## $F_2$ Determination

The structure function $F_2$ of the nucleon has been introduced in detail in Sec. 2.2. It is given by the cross section for inclusive muon scattering, by the ratio $R = \sigma_L/\sigma_T$, and by kinematical factors:

$$\begin{aligned} F_2(x_{\mathrm{Bj}}, Q^2) = & \frac{\mathrm{d}^2\sigma_{1\gamma,\,\mathrm{unpol}}}{\mathrm{d}x_{\mathrm{Bj}}\mathrm{d}Q^2} \frac{Q^4 x_{\mathrm{Bj}}}{4\alpha_{\mathrm{em}}^2 \pi \hbar^2} \\ & \cdot \left\{ 1 - y - \frac{x^2 y^2 M^2 c^2}{Q^2} + \frac{y^2 + \frac{Q^2 c^2}{E^2}}{2 \cdot [1 + R(x_{\mathrm{Bj}}, Q^2)]} \left( 1 - \frac{2m^2 c^2}{Q^2} \right) \right\}^{-1} , \end{aligned} \tag{5.10}$$

with the one-photon exchange (Born) cross section $\sigma_{1\gamma}$. The square of the reduced Planck constant has the value $\hbar^2 = 0.3894\,\mathrm{mb}\,(\mathrm{GeV}/c)^2$. For the ratio $R(x_{\mathrm{Bj}}, Q^2)$, the same parametrization which has been used for the NMC $F_2$ extraction [97] is used. Since experiments do not measure the

Born cross section directly, so-called radiative corrections have to be applied to the data [98]. The radiative event weight in a bin $(x_{\mathrm{Bj}}, Q^2)$ is defined as

$$\eta(x_{\mathrm{Bj}}, Q^2) = \frac{\sigma_{1\gamma}(x_{\mathrm{Bj}}, Q^2)}{\sigma_{\mathrm{measured}}(x_{\mathrm{Bj}}, Q^2)} \quad . \tag{5.11}$$

The values are taken from the $F_2$ analysis of the NMC experiment [97]. The corrections are $< 15\%$ in the selected kinematical range ($y < 0.5$). The radiative corrections have not been iterated with the new $F_2$ measurement. Nuclear effects on $F_2$ are negligible in the selected kinematical range and the COMPASS target consists almost entirely of isoscalar nulei (D, $^4$He, and $^6$Li). The measured structure function can thus be directly compared to values of the structure function of the deuteron $F_2^{\mathrm{d}}$ which are taken from a parametrization from the NMC experiment [88] which covers the complete kinematical reach of the presented data. The ratio of the COMPASS result and the NMC parametrization is presented in Fig. 5.16 for eleven bins of $x_{\mathrm{Bj}}$. The gray bands indicate the normalization uncertainty of 10% from the luminosity determination. The ratios lie within the bands thus proving consistency with the NMC result.

Half of the presented data set was taken with 50% of the nominal beam intensity due to an accelerator problem in the 2004 beam time. The comparison of the values of $F_2$, which are independently determined from the two data sets with different beam intensities, is shown in Fig. 5.17. No deviations from unity are visible. This is despite the fact that many rate dependent corrections were applied in the luminosity analysis.

The luminosity value of $\tilde{L} = 142.4\,\mathrm{pb}^{-1}$ for the analyzed data set has been released[6] by the COMPASS collaboration in August 2010 [93] and can now be used for new measurements of unknown cross sections. The release material includes the list of good spills with values for the integrated luminosity (corrected for DAQ dead time), the veto dead times, and the event-number ranges for the flat-top selection for each spill.

[6] I am grateful to Y. Bedfer, N. Makke, A. Morreale, and J.F. Rajotte for the COMPASS-internal cross checks, needed for the release process.

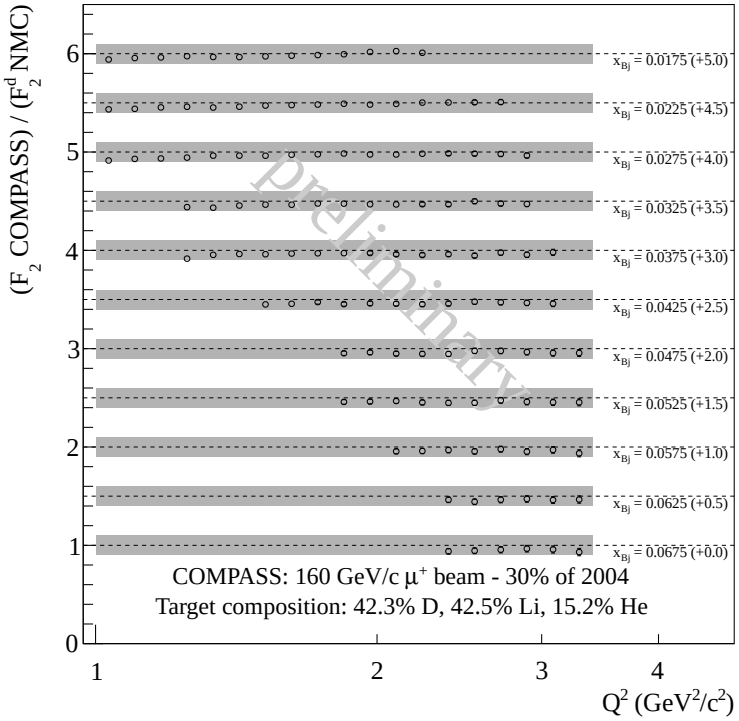


**Figure 5.16:** Comparison of the structure function $F_2$ extracted from COMPASS data with the parametrization from NMC [88]. The ratios for the individual $x_{\mathrm{Bj}}$ bins are offset by constant factors as indicated on the right hand side of the plot. The gray bands indicate the 10% normalization uncertainty arising from the systematic error of the luminosity. All values lie within the bands, thus proving consistency with the NMC result.

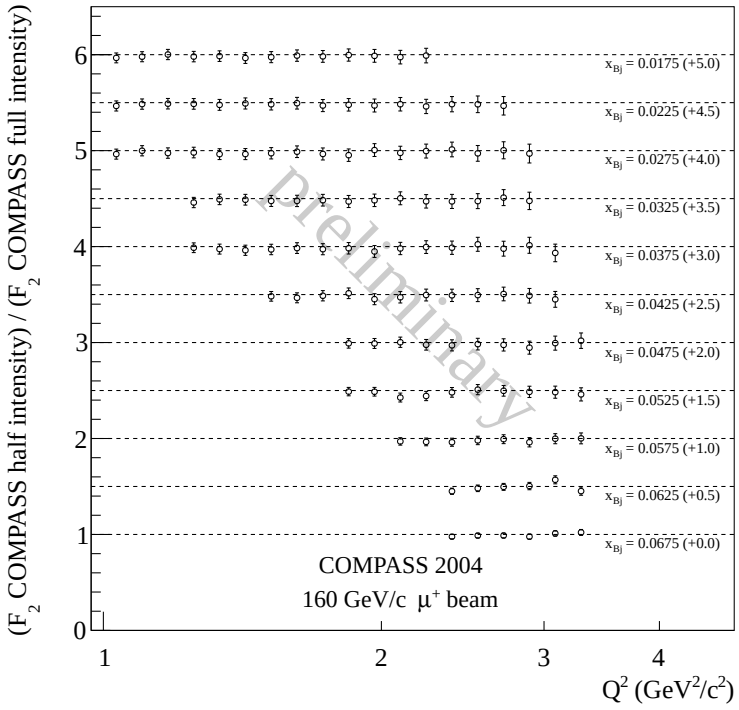


**Figure 5.17:** Comparison of $F_2$ determined from COMPASS with half and full beam intensities. The ratios for the individual $x_{\mathrm{Bj}}$ bins are offset by constant factors as indicated on the right hand side of the plot. The results are fully consistent with each other.

# Chapter 6

# Cross Section for High-$p_T$ Hadron Production at COMPASS

In this chapter, the cross section for the quasi-real photoproduction of charged hadrons with high $p_T$ in muon-deuteron scattering at COMPASS (center-of-mass energy 17.4 GeV) is presented. As explained in chapter 3, the comparison of the measured cross section to the perturbative QCD (pQCD) prediction for the cross section serves as a benchmark for the applicability of pQCD to the quasi-real photoproduction process. If this test is successful, pQCD calculations of the double-spin asymmetry of the cross section can be compared to the double-spin asymmetry measured in COMPASS to constrain the polarization of gluons in the nucleon. This concept has been introduced in more detail in chapter 3.

The cross section for the production of hadrons in the $p_T$ bin $i$, which spans the range $p_T \in [p_{T,i,1}, p_{T,i,2}]$, is:

$$\sigma_i = \frac{1}{\tilde{L}} \cdot \frac{\tilde{N}_i}{\epsilon_i} \quad , \tag{6.1}$$

with the yield of observed hadrons in the bin $\tilde{N}_i$, the acceptance factor $\epsilon_i$, and the effective integrated luminosity $\tilde{L}$, which has been presented in chapter 5. The *single-inclusive* cross section determined here counts the number of observed high-$p_T$ hadrons, and not just the number of events which contain high-$p_T$ hadrons. This allows the counting of several hadrons per scattering event. The data selection cuts and the resulting particle yields $\tilde{N}_i$ are described in Sec. 6.1. The efficiencies of the trigger systems are discussed in Sec. 6.2 as they are crucial for the absolutely normalized cross-section measurement. The determination of the acceptance correction factors $\epsilon_i$ is detailed in Sec. 6.3. This includes an in-depth investigation of secondary interactions of hadrons produced in muon-deuteron scattering in the rather thick solid-state target of COMPASS, which is a challenging effect in this analysis. Section 6.4 describes the conversion of the binned cross section into discrete data points and presents the final results with systematic errors. The cross section results are discussed and compared to recent NLO pQCD calculations in Sec. 6.5.

## 6.1 Data Selection and Resulting Yields

The following selection criteria are applied to the sample of events recorded in the 54624 spills for which the luminosity has been determined:

- Events were recorded by one of the low-$Q^2$ triggers, Inner Trigger (IT) and Ladder Trigger (LT).

- Beam-track and primary-vertex cuts (A): The extrapolated beam tracks are required to fully cross both target cells, and the $z$ positions of the primary vertices are restricted to lie in the target $z \in [-100\,\text{cm}, -40\,\text{cm}]$ or $z \in [-30\,\text{cm}, 30\,\text{cm}]$. These cuts are required to use the luminosity normalization that was presented in the previous chapter[1].

- Beam-track and primary-vertex cuts (B): The $z$ position of the reconstructed primary vertex is reconstructed with an uncertainty of $\sigma_z$. Events are accepted if the whole interval $[z - \sigma_z, z + \sigma_z]$ is situated in the same target cell: $z \pm \sigma_z \in [-100\,\text{cm}, -40\,\text{cm}]$ or $z \pm \sigma_z \in [-30\,\text{cm}, 30\,\text{cm}]$. The beam muons must have momenta between 140 and 180 GeV/$c$.

- $Q^2 < 0.1\,(\text{GeV}/c)^2$, "Quasi-real photoproduction cut" (the kinematical variables used here have been defined in Sec. 2.1): The role of $Q^2$ in the pQCD calculations was discussed in Sec. 3.4. In principle, the calculation should become more accurate with a value of $Q^2_{\text{max}}$ as low as possible. The exact choice of the value $Q^2_{\text{max}} = 0.1\,(\text{GeV}/c)^2$ is motivated by the fact that the acceptance description becomes problematic for larger $Q^2$ values. This is visible in the comparison of the $Q^2$ distribution of the Monte Carlo simulation used for the acceptance correction and the real data at the end of Sec. 6.3. About 67% of the data are retained after this cut.

- $y \in [0.2, 0.8]$: Events with $y < 0.2$ are detected near the inner edges of the hodoscopes HI04 and HI05, while events with $y > 0.8$ are detected in the outer edges of HL04 and HL05 (see Fig. 4.5 for the hodoscope positions). These events are rejected (fiducial detector-area cut). Radiative effects are expected to be largest in the high-$y$ region, which is rejected here.

The hadron candidates in the retained events are subject to the following cuts:

- Tracks must have traversed less than 30 radiation lengths of material before they were last measured in a tracking detector[2], which means that they are not identified as muons.

- The particles must hit the active area of one of the hadronic calorimeters. A margin of 3 cm around the central holes and the outer edges of the HCALs is rejected.

- Hadron candidates must have a reconstructed momentum $p > 15\,\text{GeV}/c$. Together with the previous cut, this ensures full trigger efficiency for the semi-inclusive triggers IT and LT.

[1] the conditions PaAlgo::CrossCells(...,1.4,1.0) and PaAlgo::InTarget(...,1.4,1.0) are applied in the PHAST event processing to select the fiducial target volume. The fiducial target volume is a cylinder of radius 1.4 cm with the top 4 mm cut off.

[2] the value of 30 radiation lengths is the standard cut in COMPASS for muon identification.

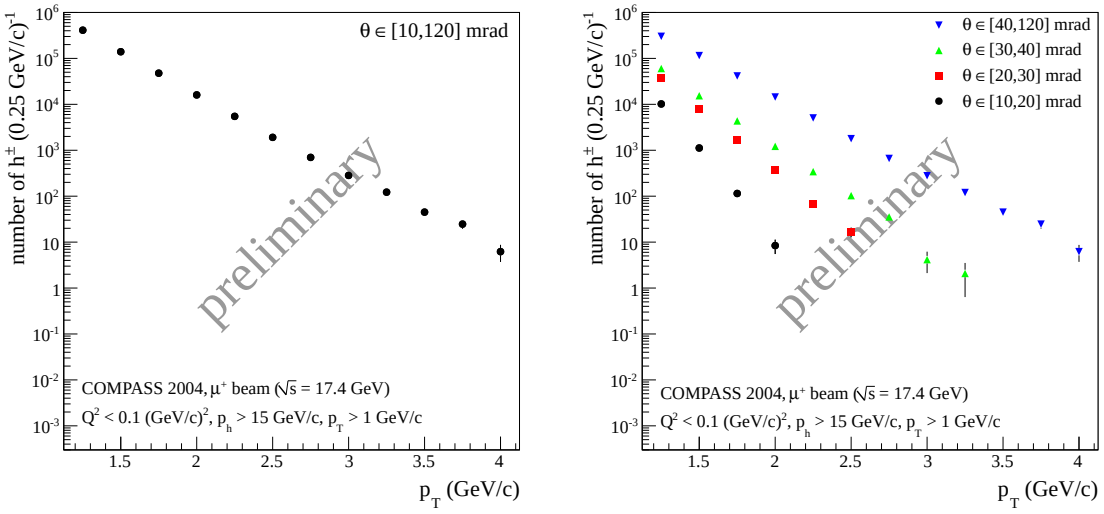


**Figure 6.1:** Yield of charged hadrons $h^{\pm}$ with high $p_T$. The left plot presents the data integrated over the full $\theta$ range, whereas the right plot is binned in $\theta$ (definition of $\theta$ in the text).

- The tracks must not cross the target solenoid magnet. The extrapolated track at the $z$ position of the end flange of the magnet ($z = 118.4\,\text{cm}$) must have a radial distance from the $z$-axis of less than 14 cm.

- $z \in [0.2, 0.8]$: The hadron energy in units of the virtual photon energy must be greater than 0.2 to select the current fragmentation regime (standard SIDIS cut, see e.g. [47, 99]). This ensures that standard factorization and fragmentation functions can be applied in theoretical calculations of the process. Please note that the variable $z$ does not equal the partonic variable $z_c$ used in the pQCD calculations of the process to evaluate the fragmentation functions (see Eq. (3.8)). The energy of the fragmenting parton is smaller than the photon energy, because processes that produce high-$p_T$ hadrons must produce at least two hard partons, which share the photon energy. This means $z_c > z > 0.2$, which is safely in the current fragmentation regime. The requirement $z < 0.8$ guarantees that exclusive production mechanisms do not contribute to the hadron yield.

- The angle $\theta$ between the hadron candidate and the virtual photon direction must be in the range [10 mrad, 120 mrad]. The cross section for lower angles becomes so small that not enough particles can be measured. The acceptance for angles greater than 120 mrad becomes very small due to the target-solenoid cut.

- The transverse momentum of the tracks with respect to the virtual photon direction $p_T = p \cdot \sin\theta$ must be greater than 1 GeV/$c$.

The IT does not include any veto conditions. The LT on the other hand includes an anti-coincidence with the veto signal $V'$. The dead time caused by $V'$ is 28.6% of the $V_{\text{tot}}$ dead time [80], which has been determined on a spill-by-spill basis. The $V'$ dead time is taken into account by weighting hadrons in Eq. (6.1) which stem from events which have been recorded by the LT and have not fired the IT by a factor of one over the $V'$ life time. Hadrons from events which were

| **cut** | **number of events** | **fraction** |
|---|---|---|
| all events | 898,733,361 | 1.0 |
| event has a primary vertex (PV) | 848,940,891 | 0.945 |
| PV has a scattered muon | 462,306,301 | 0.514 |
| PV has $\geq 2$ outgoing tracks | 280,119,680 | 0.312 |
| PV $z$ position is in target | 194,896,373 | 0.217 |
| extrapolated track of beam muon crosses full length of target | 184,625,778 | 0.205 |
| momentum of beam muon $\in [140, 180]\,\mathrm{GeV}/c$ | 183,905,903 | 0.205 |
| $y \in [0.1, 0.9]$ | 175,225,652 | 0.195 |
| [$p_T$(w.r.t. the virtual photon direction) $\geq 1\,\mathrm{GeV}/c$] or [$p_T$(w.r.t. the beam direction) $\geq 1\,\mathrm{GeV}/c$] | 9,046,688 | 0.0101 |
| event was recorded in the flat top of a good spill as described in Sec. 5.3 | 5,677,719 | 0.00632 |
| **cut** | **number of tracks** | **fraction** |
| all charged tracks (after all event cuts) | 16,982,918 | 1.0 |
| IT or LT | 11,816,421 | 0.696 |
| $r_{z=118.4\,\mathrm{cm}} < 14\,\mathrm{cm}$ (target solenoid) | 10,684,219 | 0.629 |
| PV $z \pm \sigma_z$ in target | 10,515,102 | 0.619 |
| $Q^2 \leq 0.1\,(\mathrm{GeV}/c)^2$ | 6,250,939 | 0.368 |
| $y \in [0.2, 0.8]$ | 5,844,256 | 0.344 |
| $z \in [0.2, 0.8]$ | 2,013,815 | 0.119 |
| $p_T$(w.r.t. the virtual photon direction) $\geq 1\,\mathrm{GeV}/c$ | 1,397,643 | 0.0823 |
| $\theta \in [10, 120]$ mrad | 1,383,759 | 0.0815 |
| $p > 15\,\mathrm{GeV}/c$ | 1,192,917 | 0.0702 |
| track geometrically hits HCAL1 or HCAL2 | 1,051,730 | 0.0619 |

**Table 6.1:** Statistics of all selection cuts. The first part of the table describes the event pre-selection, the second part describes the final hadron candidate selection.

accepted in both the IT and the LT do not require scaling, because the IT is free of veto dead times. The statistics of all applied cuts is listed in Tab. 6.1, including pre-selection cuts that are not discussed here. The $p_T$ distributions of this sample, integrated over the full $\theta$ range, and binned in $\theta$, are displayed in Fig. 6.1. The $p_T$ distributions of the hadrons which have been separated by charge are shown in the appendix[3] in Fig. B.1 (p. 149). They exhibit the same shapes as the charge-summed distributions.

The distributions of the hadron sample in the kinematical variables $Q^2$, $y$, $W$, $z$, and $\theta$ are shown in Fig. 6.2. The distributions are not corrected for acceptance. The uneven shape of the $\theta$ distribution is caused by the cut that the tracks must geometrically hit one of the HCALs and is well understood. The uneven shape of the $y$ distribution is due to different acceptances of the IT (low $y$) and the LT (high $y$) in kinematical variables other than $y$. The $p_T$ dependencies of the mean values of these kinematical distributions are shown in the appendix in Fig. B.2 (p. 151).

[3] Appendix B contains supplementary figures for this chapter on the cross section measurement. All of these figures are relevant for the presented work, but not necessary for an understanding of the text and the discussed effects. They have been moved to the appendix to increase the clarity and the readability of the text.

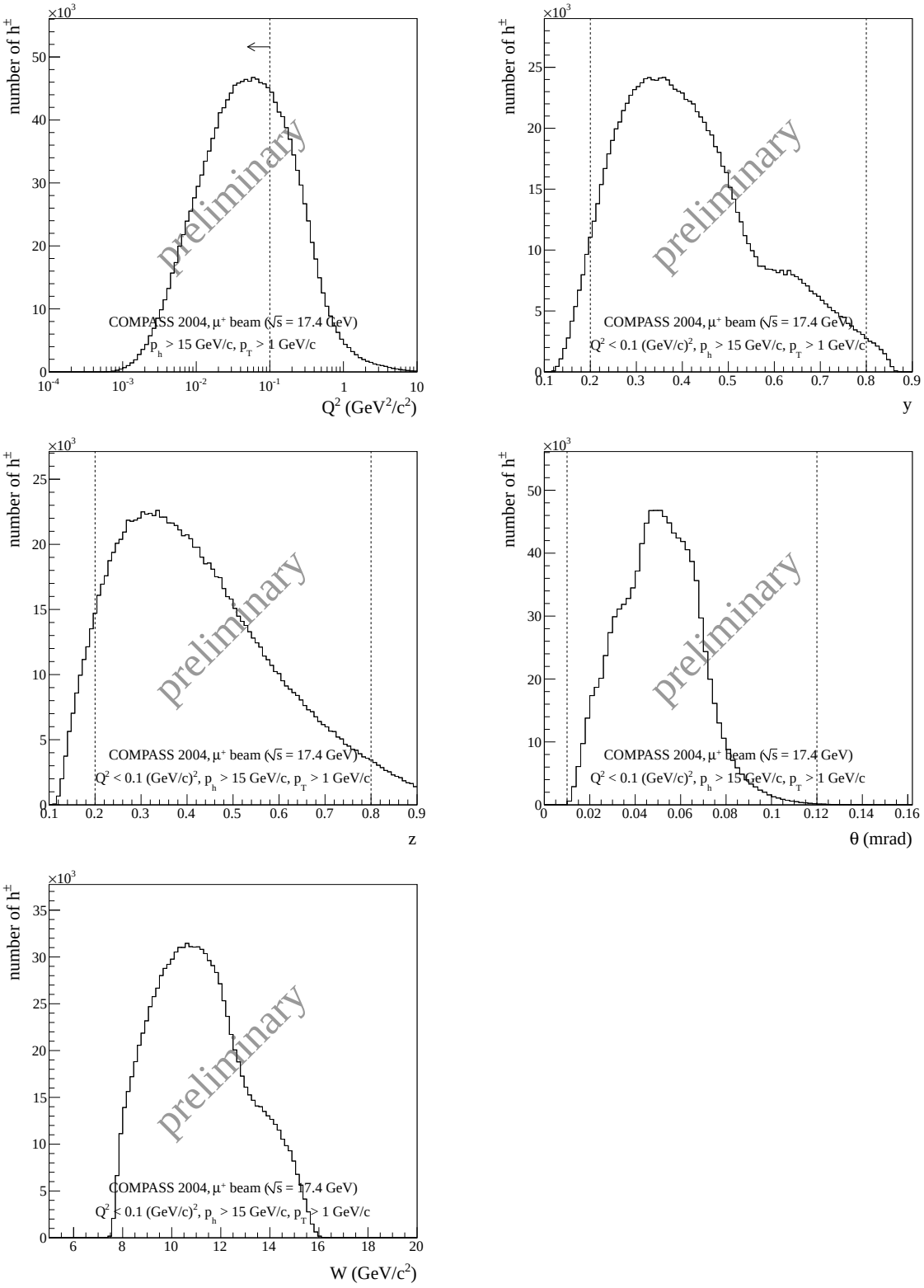


**Figure 6.2:** Kinematical distributions of the high-$p_T$ hadron sample, where all cuts have been applied but the one on the plotted variable. The histograms have one entry per charged hadron.

## 6.2 Efficiency of the Trigger System

The $Q^2$-$y$ coverage of the COMPASS trigger systems is shown in Fig. 4.6. The two low-$Q^2$ triggers IT and LT are used for the cross section measurement. Their functionality has been described in detail in Sec. 4.2.4. They include coincidences with the hadronic calorimeters ("low" threshold $\sim 7\,\mathrm{GeV}$) to suppress elastic scattering processes. The trigger conditions are:

$$\begin{aligned} \mathrm{IT} &= (\mathrm{HI04} \wedge \mathrm{HI05}) \wedge (\mathrm{HCAL1} \vee \mathrm{HCAL2}) \\ \mathrm{LT} &= (\mathrm{HL04} \wedge \mathrm{HL05}) \wedge (\mathrm{HCAL1} \vee \mathrm{HCAL2}) \quad , \end{aligned}$$

with the muon hodoscopes HI04, HI05, HL04, and HL05, and the hadronic calorimeters HCAL1 and HCAL2 (see red labels in Fig. 4.5). The IT covers the range $0.1 \lesssim y \lesssim 0.6$, while the LT covers the range $0.5 \lesssim y \lesssim 0.9$. Any unknown inefficiencies of the scintillator hodoscopes or the hadronic calorimeters would directly lead to a wrong cross section measurement. This chapter discusses the efficiencies of these trigger components.

### 6.2.1 Hodoscope Efficiencies

The efficiencies of the trigger hodoscopes are checked on a sub-sample of three consecutive data taking runs. The hodoscopes under investigation are excluded from the track reconstruction in CORAL and their hits were written to the output data files (mDSTs). The efficiency analysis is performed on events recorded by the purely calorimetric trigger (CT). This trigger ignores the scattered muons, but requires an energy deposit of $\gtrsim 20\,\mathrm{GeV}$ ("high" threshold) in one of the hadronic calorimeters.

The efficiency of a tracking detector is defined as the fraction of detectable tracks which traversed the detector to which a hit can be associated. It is obtained as a function of the track position in the detector plane. Hits can be associated if they lie within a certain "road width" of the track position. A road width of $3\,\sigma$ has been chosen, where $\sigma = P/\sqrt{12}$ with the scintillator pitch[4] $P$. The uncertainty of the track position has been neglected for this study. Usually, the efficiency of a tracking detector is determined by selecting tracks which have been detected upstream as well as downstream of the detector to ensure that the track really traversed the detector. While this principle works well for HI04 and HL04[5], it can not be applied to HI05 and HL05 for the lack of downstream tracking detectors. This problem can easily be circumvented for HL05 by demanding that tracks should have traversed more than 30 radiation lengths of material before their last detection plane (which is still located upstream of HL05). This ensures that the tracks are muons and thus gives a clean sample of tracks which cross HL05. The efficiency of HI05 can not be determined in the COMPASS setup because tracks are neither detected further downstream, nor do they cross enough material before their last detection plane so that a muon sample could be selected. For this detector all tracks pointing to the detector are considered for the calculation of a "quasi-efficiency". This can include hadrons that do not traverse the iron absorber in front of HI05 ($\mu$F3) and will thus lead to an artificial "quasi-inefficiency". If the fraction of hadrons in the track sample is a function of position, the "quasi-inefficiency" will be a function of position as

[4] values of scintillator pitch: $P_{\mathrm{HI04}} = 5.4\,\mathrm{mm}$, $P_{\mathrm{HI05}} = 11\,\mathrm{mm}$, $P_{\mathrm{HL04}} = 21 - 64\,\mathrm{mm}$, $P_{\mathrm{HL05}} = 26 - 84\,\mathrm{mm}$.

[5] at least 4 hits in the detectors PB, MB, or GM11, all of which are downstream of HI04 and HL04, are required.

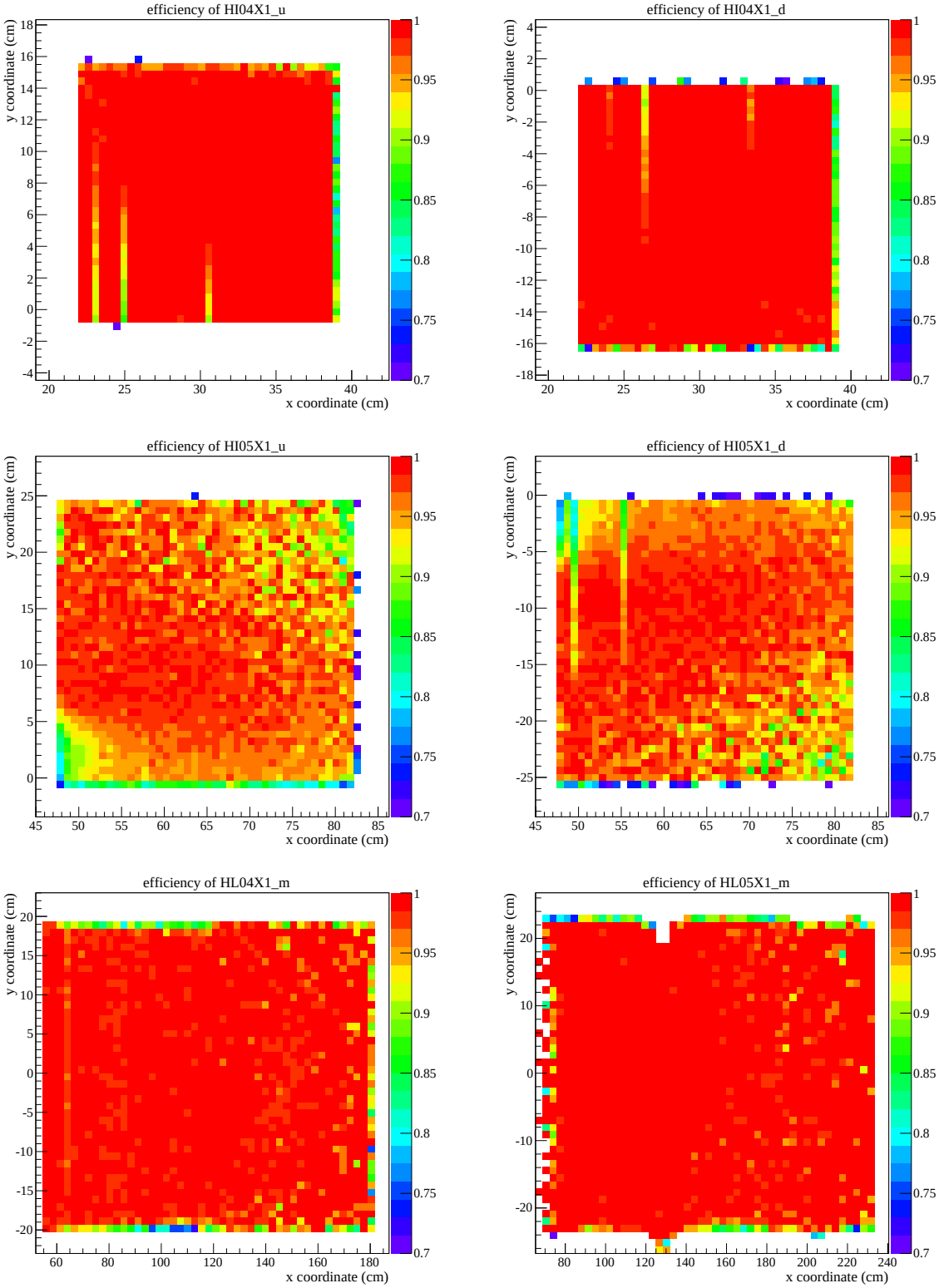


**Figure 6.3:** Efficiencies of the muon hodoscopes of the IT and LT. Please note the special properties of the HI05 efficiency plots, as described in the text. The suffixes "_u" and "_d" denote the upper and lower halves of the hodoscopes HI04 and HI05. The hodoscopes HL04 and HL05 consist of one piece each (denoted by the suffix "_m").

well. It is, however, sufficient to verify that the distributions of the "quasi-efficiency" are smooth to conclude that the hodoscopes are fully efficient. Even if there were some inefficient channels in the scintillator hodoscopes, it is certainly not expected that all channels in a hodoscope exhibit exactly the same inefficiency (which would again lead to smooth "quasi-efficiency" distributions). Figure 6.3 shows the resulting efficiency distributions. The HI04 and HI05 efficiencies show some less efficient strips, but the overall effect on the trigger efficiency, integrated over the complete area, is below the percent level and is thus negligible. The distributions for HI05 are sufficiently smooth. The only visible imperfection is a feature in the distribution for HL05, which looks like a scintillator slab which seems to be shifted downwards by $\sim 4\,\text{cm}$. Integrated over the active area of HL05, the effect is again below the percent level and is thus ignored. For the purpose of the presented cross-section analysis the hodoscopes can be regarded as fully efficient.

### 6.2.2 Efficiency of the Hadronic-Calorimeter Trigger

It is widely known that modeling the energy response of hadronic calorimeters in GEANT detector simulations is very difficult. This makes the simulation of the HCAL trigger efficiency for the acceptance correction unfavorable, especially in the interesting threshold region. The efficiency of the HCAL component of the semi-inclusive triggers is determined from the real data instead, by analyzing events recorded by the so-called Middle Trigger (MT). Like the IT and the LT, the MT is a semi-inclusive trigger which is made from the coincidence between scintillator hodoscopes and the hadronic calorimeters; it just selects higher values of $Q^2$. This trigger also exists as a purely inclusive version which does not include the HCAL response (inclMT). The fraction of inclMT events that have also fired the MT is the efficiency of the calorimetric component of the semi-inclusive triggers. Figure 6.4 shows the efficiency of the trigger as a function of the momentum of the fastest particle hitting the active area of the HCALs. For events in which a particle hits one of the HCALs with $p > 15\,\text{GeV}/c$ the trigger is 96% efficient. The hadron selection cuts discussed in Sec. 6.1 make sure that only hadrons with $p > 15\,\text{GeV}/c$ that hit the active area of one the HCALs are considered for the cross section result. The efficiency of 96% is taken into account directly as a scaling factor in the acceptance correction (see Sec. 6.3.5). The MC simulation which is used for the determination of the acceptance factors is configured to ignore the calorimetric component of the IT and LT, because its acceptance is already taken care of.

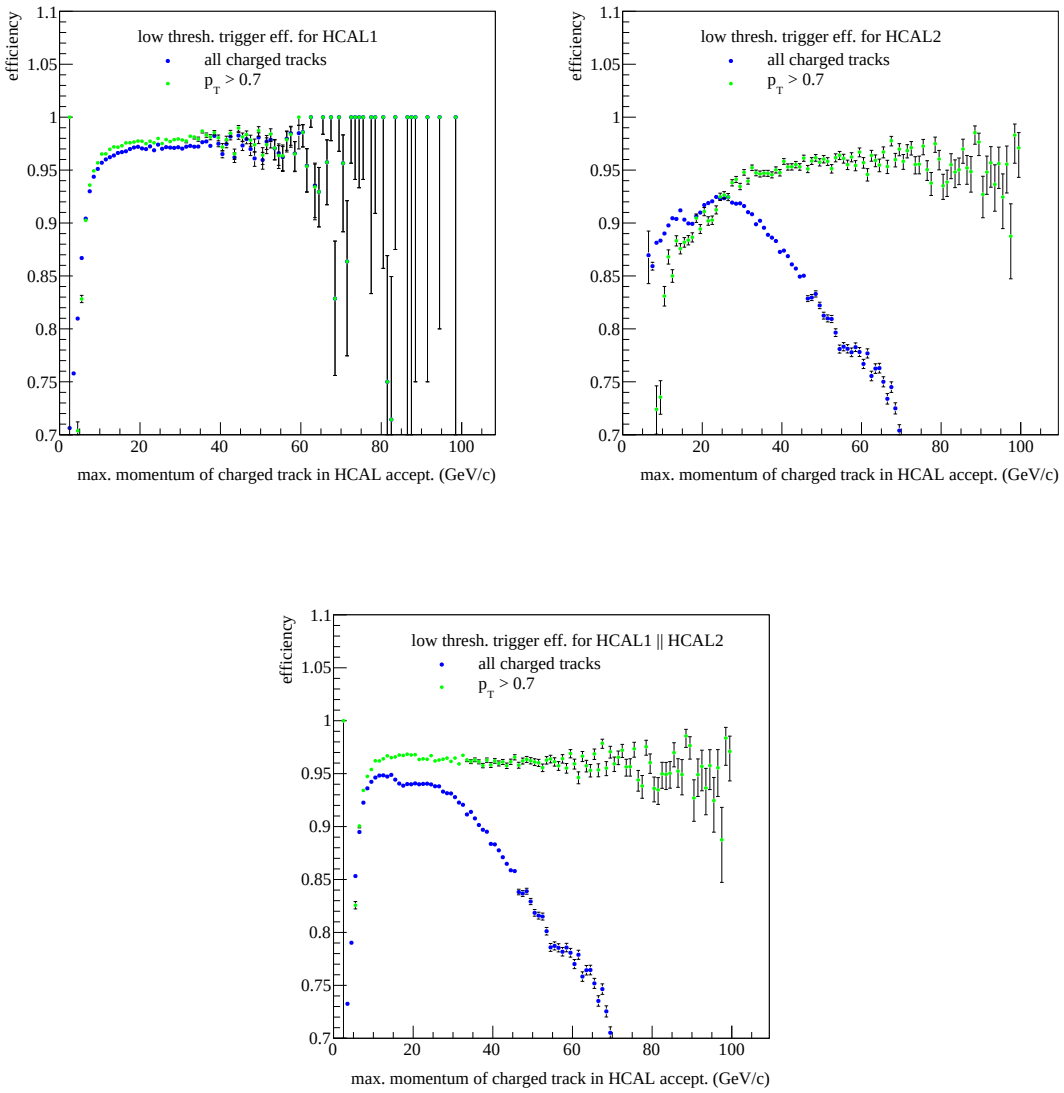


**Figure 6.4:** Efficiency of the HCAL component of the semi-inclusive triggers as a function of the momentum of the fastest track hitting the HCALs. The upper plots show the separate efficiencies for tracks hitting either HCAL1 or HCAL2, and the lower plot shows the efficiency as a function of the momentum of the fastest track hitting either one of the HCALs. The inefficiency of HCAL2 (blue points - all events) is caused by electron tracks which stem from elastic $\mu$-$e$ scattering events. A cut on the transverse momentum (green points) removes them from the sample and shows the efficiency for a hadron sample.

## 6.3 Acceptance Correction

The acceptance correction factors $\epsilon_i$ of Eq. (6.1) are determined with a Monte Carlo (MC) simulation of muon-deuteron scattering events in the COMPASS experiment. Scattering events are generated with PYTHIA 6 [22]. PYTHIA describes high-energy collisions of particles and includes many physics aspects such as parton distributions, hadronization models, parton showers, and many others. The momenta, positions, and directions of the beam muons that were used in the PYTHIA program were sampled from a "beam file" that was produced from real data recorded with a minimum-bias trigger. The PYTHIA tuning parameters[6] are listed in the appendix in Tab. C.1 (p. 161). It should be emphasized that there is no high-$p_T$ preselection on the level of the event generator in the presented MC study. Since the cross section for low-$p_T$ scattering ($p_T < 1\,\mathrm{GeV}/c$) is orders of magnitude higher than that for high-$p_T$ scattering, even very small fractions of low-$p_T$ events which are misreconstructed as high-$p_T$ events can create a significant background for the intrinsic high-$p_T$ events. In more general terms one can say that preselections of the event generator level on any kinematical variables that have a steeply falling or steeply rising spectrum are very dangerous and have to be avoided. A "minimum bias" simulation without a $p_T$ preselection, however, requires the simulation of a very large event sample ($2.3 \cdot 10^9$ events in the presented analysis) to reach a satisfying statistical accuracy in the high-$p_T$ regime.
The generated events are propagated through the COMPASS experimental setup with COMGEANT and analyzed with the standard event reconstruction software CORAL (see Sec. 4.2.6 for a description of the software). The MC sample used for this analysis was generated at the computing center of IN2P3 at Lyon. The paths to the data files and the used configurations and programs are listed in Tab. C.2 (p. 162).

The acceptance correction factor in bin $i$, spanning the range $p_T \in [p_{T,i,1}, p_{T,i,2}]$, is

$$\epsilon_i = \frac{N^{\mathrm{rec}}_{\mathrm{MC}}(p_{T,\mathrm{rec}} \in [p_{T,i,1}, p_{T,i,2}])}{N^{\mathrm{gen}}_{\mathrm{MC}}(p_{T,\mathrm{gen}} \in [p_{T,i,1}, p_{T,i,2}])} \equiv \frac{N^{\mathrm{rec}}_{i,\mathrm{MC}}}{N^{\mathrm{gen}}_{i,\mathrm{MC}}} \quad , \tag{6.2}$$

with the number of generated hadrons $N^{\mathrm{gen}}_{i,\mathrm{MC}}$ in the range of generated $p_{T,\mathrm{gen}} \in [p_{T,i,1}, p_{T,i,2}]$, and the number of reconstructed hadrons $N^{\mathrm{rec}}_{i,\mathrm{MC}}$ in the range of reconstructed $p_{T,\mathrm{rec}} \in [p_{T,i,1}, p_{T,i,2}]$. The numerator is extracted from the reconstructed tracks and vertices in the mDST files, whereas the denominator is extracted from the MC truth 4-momenta and vertices in the mDST files.
The reconstructed MC hadron candidates are subject to the same cuts as the real data as detailed in Sec. 6.1. The number of generated hadrons $N^{\mathrm{gen}}_{\mathrm{MC}}$ is subject to the following cuts:

- Target cuts: The PV has to be in the fiducial target volume, which is defined identically as for the real data, and the extrapolated beam track must cross the full length of the fiducial target.
- GEANT particle ID $\geq 8$. This cut excludes electrons and muons. In combination with the requirement that the charge of the particle has to be 1 or -1 it selects charged hadrons.
- All kinematical cuts: $Q^2 < 0.1\,(\mathrm{GeV}/c)^2$, $y \in [0.2, 0.8]$, $p > 15\,\mathrm{GeV}/c$, $z \in [0.2, 0.8]$, and $\theta \in [10, 120]\,\mathrm{mrad}$. The $\theta$ cut is of course adjusted to $[10, 20]\,\mathrm{mrad}$, $[20, 30]\,\mathrm{mrad}$,

[6] the tuning of the PYTHIA parameters was done by S. Procureur and C. Bernet (CEA Saclay) for their analysis of high-$p_T$ hadron pairs at low $Q^2$ which led to a COMPASS publication on $\Delta g/g$ [100].

[30, 40] mrad, or [40, 120] mrad to calculate the acceptances for the cross sections in $\theta$ bins. These kinematical cuts also have to be applied to any theoretical calculations the data shall be compared to.

The geometrical selection cuts, namely the HCAL geometry cut and the target solenoid cut, are not applied. This means that the losses of real-data particles due to these cuts are recovered in the acceptance correction.
The acceptance factors are used to correct the experimental yields of hadrons for the following effects:

- Imperfections in the reconstruction software that lead to inefficiencies in the track and vertex reconstructions.
- Inefficiencies of the charged-particle tracking system of COMPASS.
- Limited phase-space coverage of the muon-trigger system.
- Secondary interactions of the hadrons produced in muon-deuteron scattering, especially in the target material. The target has a length of about one hadronic interaction length. On the one hand, the secondary interactions lead to a sizable inefficiency for the hadron production measurement due to particle losses. On the other hand, new hadrons are produced in the secondary interactions, which could create a background for the hadrons produced in the muon-scattering vertex. GEANT3 has two interchangeable packages for the creation of hadron showers, namely GHEISHA and FLUKA[7], which are known to behave quite differently from each other [101, 102, 103].

### 6.3.1 Hadron Showers in the Target Material

The measurement of the high-$p_T$ hadron production cross section in a thick solid-state target is very challenging in comparison to collider measurements of such processes. The hadrons which are produced in the primary vertex (PV) can interact inelastically with nuclei in the target material before they are detected. Such interactions can create a shower of secondary hadrons. The position of the secondary interaction is referred to as the secondary vertex (SV) in the following. If the PV and the SV can not be separated in the vertex reconstruction, the secondary hadrons will seem to stem from the muon-scattering vertex. The misidentified secondary hadrons constitute a background to the hadron production in the muon-scattering vertex one wants to measure. The GEANT3 simulation unfortunately suggests that such a background can be sizable in the case of the high-$p_T$ charged-hadron production at low $Q^2$, which is investigated here.

[7] the FLUKA model inside GEANT3 is not identical to the full MC transport program FLUKA. It just corresponds to a port of some FLUKA functionality in 1992, but is nevertheless just referred to as FLUKA here.

Figure 6.5a shows an example of a simulated event topology than can lead to the misreconstruction of the PV and a consequential spurious high-$p_T$ hadron signal. The colored lines indicate differently charged tracks: Red for positively charged particles, blue for negatively charged particles, and green for neutral particles. One of the hadrons that was produced in the PV with a low $p_T$ causes a hadron shower in which more charged hadrons are produced. The $p_T$ spectra of hadron showers are steeply falling functions, but in rare cases the secondary hadrons can have a large $p_T$ with respect to the hadron which produced the shower.

Figure 6.5b shows which of the generated tracks can be reconstructed (solid lines). In this example, no tracks from the primary vertex are reconstructed in the charged-particle tracking system. The positive track which was generated at the primary vertex escapes detection, because it has a low momentum ($\lesssim 1\,\mathrm{GeV}/c$). The position of the real PV can be estimated by extrapolating the tracks (dashed lines) of the incoming muon track $\mu^+$ and the scattered muon track $\mu^{+\prime}$ to their point of closest approach PCA$[\mu, \mu']$. However, the scattering angle of the muon is very close to zero in the low-$Q^2$ regime, and the resolution of such a reconstruction of the "muon-only vertex" is only 16 cm in the beam direction. The resolution of the primary vertex reconstruction would improve down to the level of centimeters if other tracks which stem from the PV could be reconstructed.

Due to the poor "muon-only vertex" resolution and the fact that there are many reconstructed tracks from the SV, the vertex reconstruction can fail in such cases and lead to the reconstructed event topology shown in Fig. 6.5c. The PV has been *misreconstructed* near the position of the SV of the generated event. The hadrons which were really produced in a secondary hadron shower now seem to stem from the muon-scattering reaction. If the shower produces hadrons with high $p_T$, this effect can create a background to the high-$p_T$ hadron production cross section. The fact that this background can be created from muon-scattering events in which only low-$p_T$ hadrons were produced is potentially very dangerous, because low-$p_T$ scattering events are orders of magnitude more abundant than the real, intrinsic high-$p_T$ events.

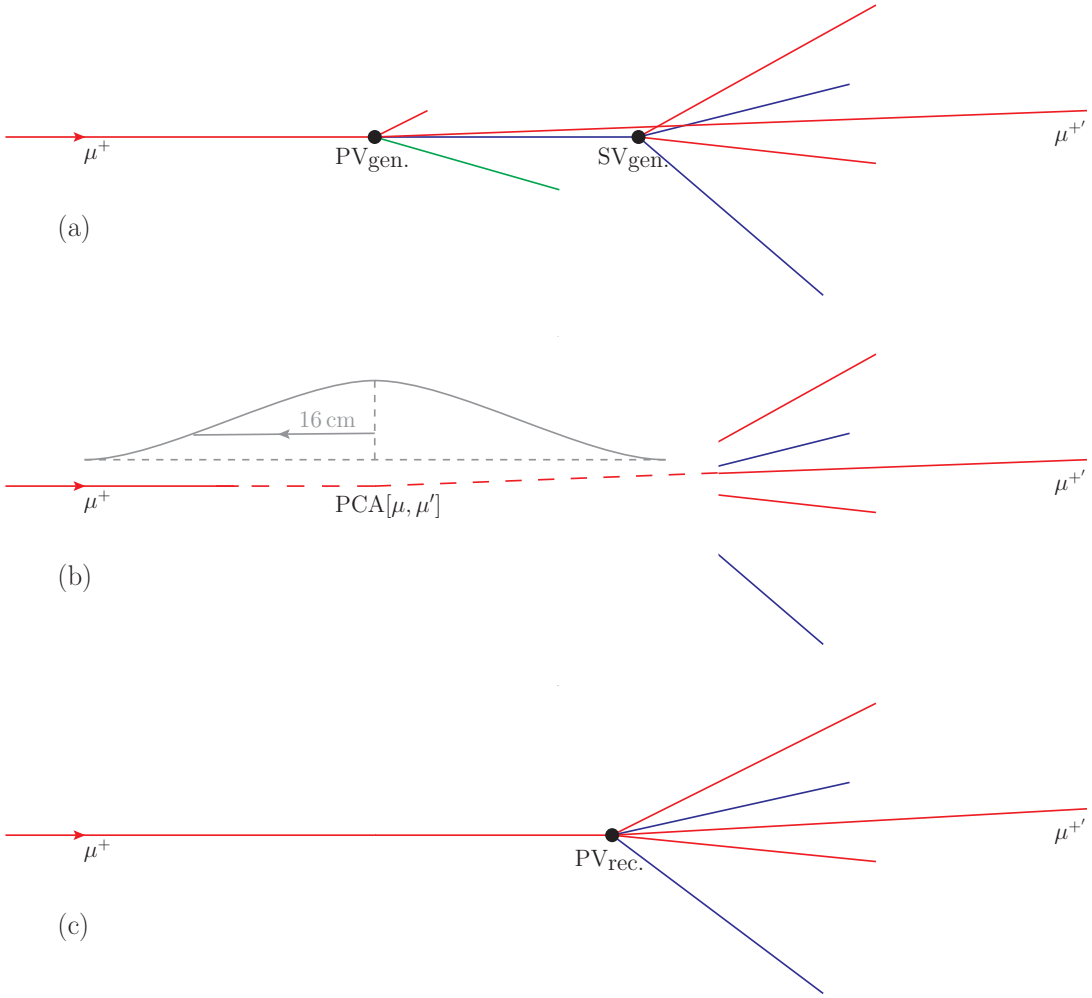


**Figure 6.5:** Illustration of the misreconstruction of the PV in a low-$p_T$ event with a hadron shower. For details, see text.

### 6.3.2 Quantification of the Background due to Hadron Showers

The contribution of hadrons originating from low-$p_T$ events which suffer from PV misreconstruction to the high-$p_T$ hadron yield has been studied using the GHEISHA and FLUKA models for the creation of hadron showers. Figure 6.6 shows the contributions of these background hadrons to the high-$p_T$ particle yields in GEANT3 simulations based on the different shower models. The GHEISHA simulation shows a clear dominance of the background from low-$p_T$ over the spectrum of signal hadrons which originate from the muon-scattering vertex at the highest $p_T$ values. If this prediction were realistic, it would mean that the measurement of high-$p_T$ hadron production in COMPASS would be almost impossible. A correction of a background effect of the order of 90%, which is the contribution of the background hadrons to the overall hadron spectrum at the highest $p_T$ values in the GHEISHA simulation, would not be sensible. The FLUKA simulation on the other hand draws a more optimistic picture by predicting a non-zero, but moderate contribution of the background to the high-$p_T$ hadron yield. The fact that the GHEISHA and FLUKA models completely contradict each other in this very important aspect calls for an independent method of quantifying the background content in the real data without relying on simulations.
The information whether a particle which was reconstructed at the PV really originates from a secondary interaction is obviously not available in the real experimental data. But even if the vertex reconstruction fails to separate the positions of the PV and the SV for the background events, their displacement is still imprinted in the distance variable

$$D = z_{\mathrm{PCA}[\mu,\mu']} - z_{\mathrm{PCA}[h,\mu]} \quad , \tag{6.3}$$

with the $z$ coordinate of the point of closest approach of the beam-muon and scattered-muon tracks $z_{\mathrm{PCA}[\mu,\mu']}$, and of the point of closest approach of the extrapolated beam-muon track and the hadron track $z_{\mathrm{PCA}[h,\mu]}$, as illustrated in Fig. 6.7. The background-quantification method described in the following is applied to real data at the end; however, it is developed and tested on simulation data, where its performance can be evaluated because the amount of background hadrons in the $p_T$ spectrum is known from the MC truth information.
If the hadron under investigation is a signal hadron that originates from the PV, the displacement between PCA$[\mu,\mu']$ and PCA$[h,\mu]$ is zero. The $D$ distribution for signal hadrons hence has a mean value of zero and a width which is defined by the experimental resolutions of the measurements of the PCAs. Since the resolution of $z_{\mathrm{PCA}[h,\mu]}$ is much better than the resolution of $z_{\mathrm{PCA}[\mu,\mu']}$, because of the larger angle between the tracks, it does not contribute significantly to the width of the $D$ distribution.

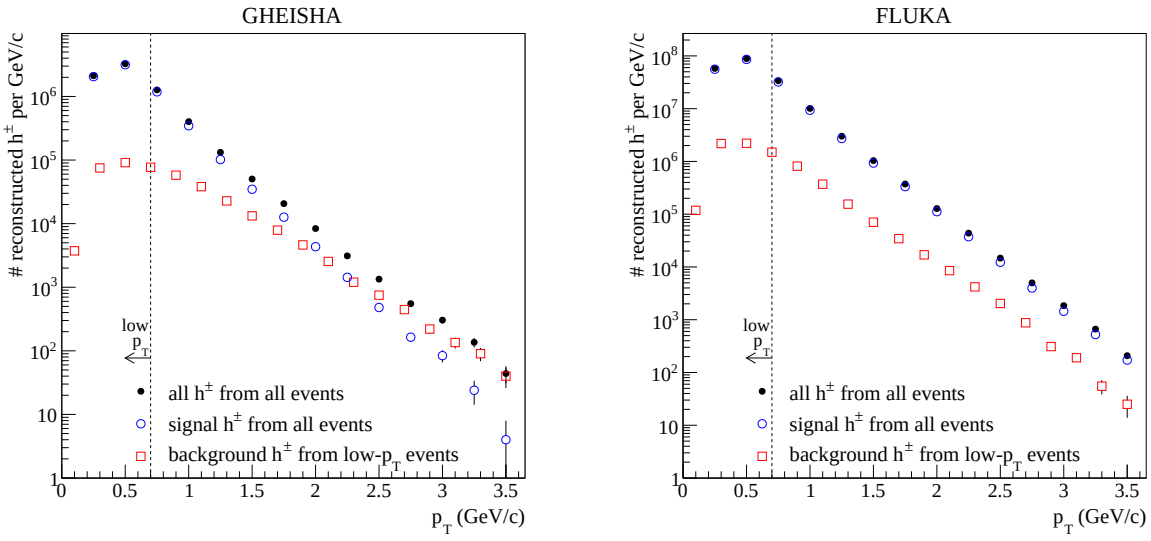


**Figure 6.6:** Contributions of primary hadrons (signal, blue circles) and misreconstructed secondary hadrons from low-$p_T$ events (background, red squares) to the overall hadron yield (black filled circles) in simulations based on GHEISHA (left plot) and FLUKA (right plot). Low-$p_T$ events are defined as events that do not have any charged hadrons with $p_{T,\mathrm{gen}} > 0.7\,\mathrm{GeV}/c$.

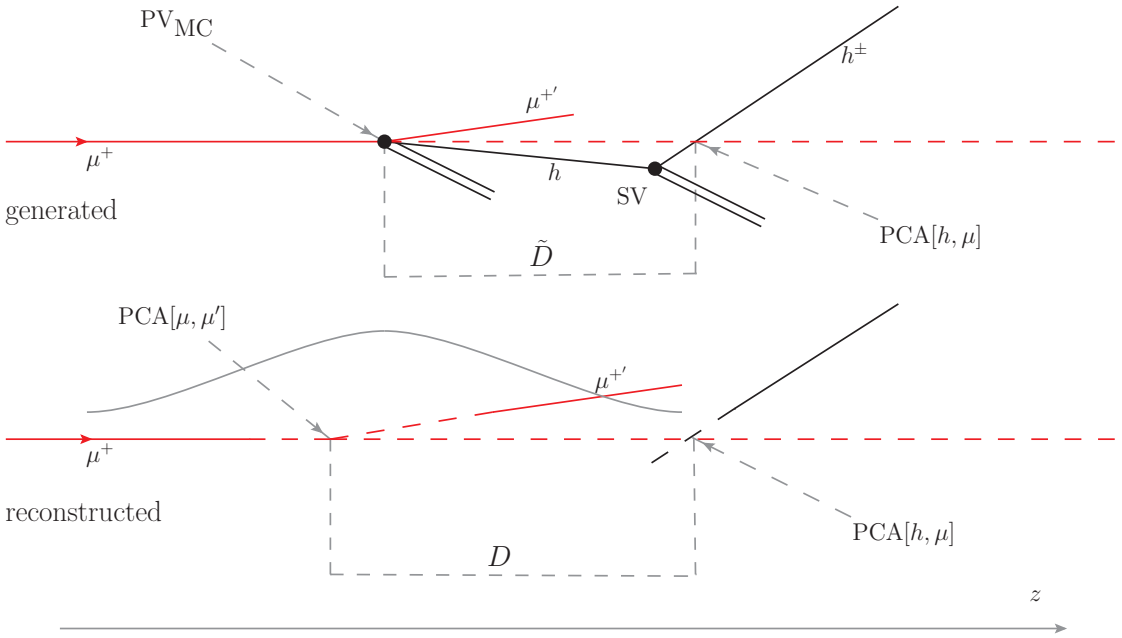


**Figure 6.7:** Definition the variables $\tilde{D}$ and $D$ for an event with a secondary interaction. The upper sketch shows the generated event topology, while the lower sketch illustrates the reconstructed event topology.

The $D$ distribution for signal hadrons in a $p_T$ bin from the GHEISHA simulation is shown in Fig. 6.8 (corresponding plot for FLUKA in Fig. B.3 (p. 152)). It is fitted with a double Gaussian function which is centered at zero,

$$f_{i,\mathrm{SIG}}(D) = A_{i,\mathrm{SIG}} \cdot (e^{-\frac{D^2}{2\sigma_1^2}} + a \cdot e^{-\frac{D^2}{2\sigma_2^2}}) \quad , \tag{6.4}$$

where the index $i$ denotes which of the $p_T$ bins is used. The fitted function describes the data sufficiently well.
In the case of background hadrons, there is a displacement between the true PV position, where the muon-scattering event was generated, and the PCA$[h, \mu]$. It is described by the distance variable

$$\tilde{D} = z_{\,\mathrm{PV\ of\ MC\ truth}} - z_{\,\mathrm{PCA}[h,\mu]} \quad . \tag{6.5}$$

The definition of $\tilde{D}$ is also illustrated in Fig. 6.7. The distribution of $\tilde{D}$ for the GHEISHA simulation is shown in Fig. 6.9 (corresponding plot for FLUKA in Fig. B.4 (p. 152)). The plot is integrated over all $p_T > 1\,\mathrm{GeV}/c$. It can be fitted with a double exponential function,

$$g(\tilde{D}) \propto e^{\alpha_1 \cdot \tilde{D}} + b \cdot e^{\alpha_2 \cdot \tilde{D}} \quad . \tag{6.6}$$

The fit results for the parameters $\alpha_1$, $\alpha_2$, and $b$ are listed directly in the plots of the $\tilde{D}$ distributions. The parameters are fixed by this fit and are not considered as free parameters in the subsequent fits which use the shape of $g(\tilde{D})$. The distribution of the variable $D$ for background events should be described by a convolution of the functions $f_{\mathrm{SIG}}$ and $g$, because the resolution of PCA$[\mu, \mu']$ remains just the same, whereas the actual position of PCA$[h, \mu]$ is displaced by $g$:

$$\begin{aligned} f_{i,\mathrm{BG}}(D) &= \bar{A}_{i,\mathrm{BG}} \cdot (f_{\mathrm{i,SIG}} \circ g) = \bar{A}_{i,\mathrm{BG}} \cdot \int f_{\mathrm{i,SIG}}(D - \tilde{D}) \cdot g(\tilde{D})\, \mathrm{d}\tilde{D} \\ &= A_{i,\mathrm{BG}} \cdot \int (e^{-\frac{(D-\tilde{D})^2}{2\sigma_1^2}} + a \cdot e^{-\frac{(D-\tilde{D})^2}{2\sigma_2^2}}) \cdot g(\tilde{D})\, \mathrm{d}\tilde{D} \quad . \end{aligned} \tag{6.7}$$

Figure 6.10 shows the distribution of the variable $D$ for the background hadrons in a $p_T$ bin of the GHEISHA simulation, which is fitted with the function $f_{i,\mathrm{BG}}$ (corresponding plot for FLUKA in Fig. B.5 (p. 152)). The parameters $\sigma_1$, $\sigma_2$, and $a$ have the same meaning as in Eq. (6.4). The asymmetric shape of the distribution of Fig. 6.10 is well described by the function $f_{\mathrm{BG}}$. A linear combination of the signal and background functions,

$$f_{i,\mathrm{ALL}}(D) = f_{i,\mathrm{SIG}}(D) + f_{i,\mathrm{BG}}(D) \quad , \tag{6.8}$$

can be fitted to the $D$ distribution of all hadrons, ignoring whether they are signal or background hadrons. The parameters $\sigma_1$, $\sigma_2$, and $a$ are common for the signal and the background functions in the combined fit. After the fit is completed, the background content in the bin can be calculated:

$$p_{i,\mathrm{BG}}^{\mathrm{fit}} = \frac{\int f_{i,\mathrm{BG}}(D)\, \mathrm{d}D}{\int f_{i,\mathrm{ALL}}(D)\, \mathrm{d}D} \quad . \tag{6.9}$$

Figure 6.11 shows the result of a simultaneous fit of ten functions $f_{i,\mathrm{ALL}}$ to the $D$ distributions of ten bins of $p_T$ for the GHEISHA simulation (corresponding plots for FLUKA in Fig. B.6 (p. 153)). The fit is a 23-parameters likelihood maximization with $10 \times 2$ normalization parameters $A_{i,\mathrm{SIG}}$

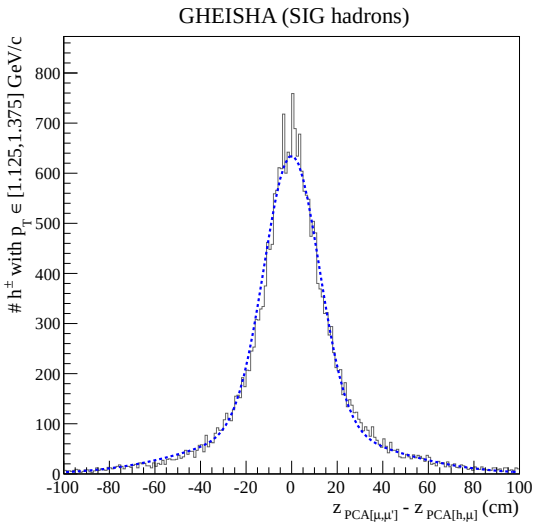


**Figure 6.8:** Distribution of $D$ (Eq. (6.3)) for signal hadrons from the simulation with GHEISHA. The distribution is fitted with the function $f_{\mathrm{SIG}}$ (Eq. (6.4)), which is centered at zero.

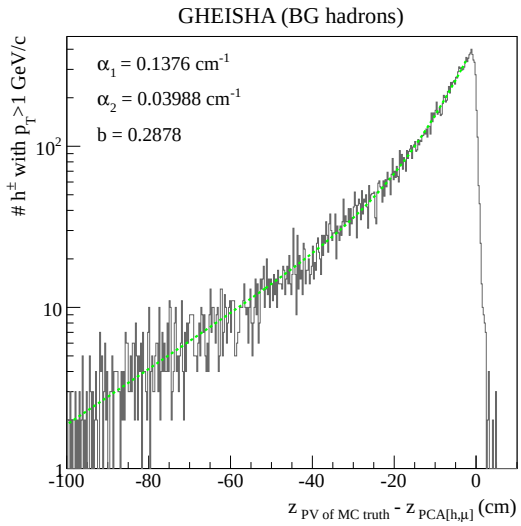


**Figure 6.9:** Distribution of $\tilde{D}$ (Eq. (6.5)) for background hadrons from the simulation with GHEISHA. The distribution is fitted with the function $g$ (Eq. (6.6)). The fitted parameters of the function $g$ are listed in the plot.

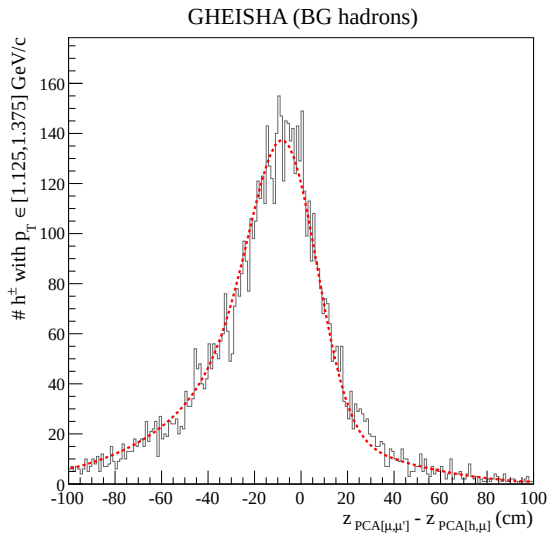


**Figure 6.10:** Distribution of $D$ (Eq. (6.3)) for background hadrons from the simulation with GHEISHA. The distribution is fitted with the function $f_{\mathrm{BG}}$ (Eq. (6.7)).

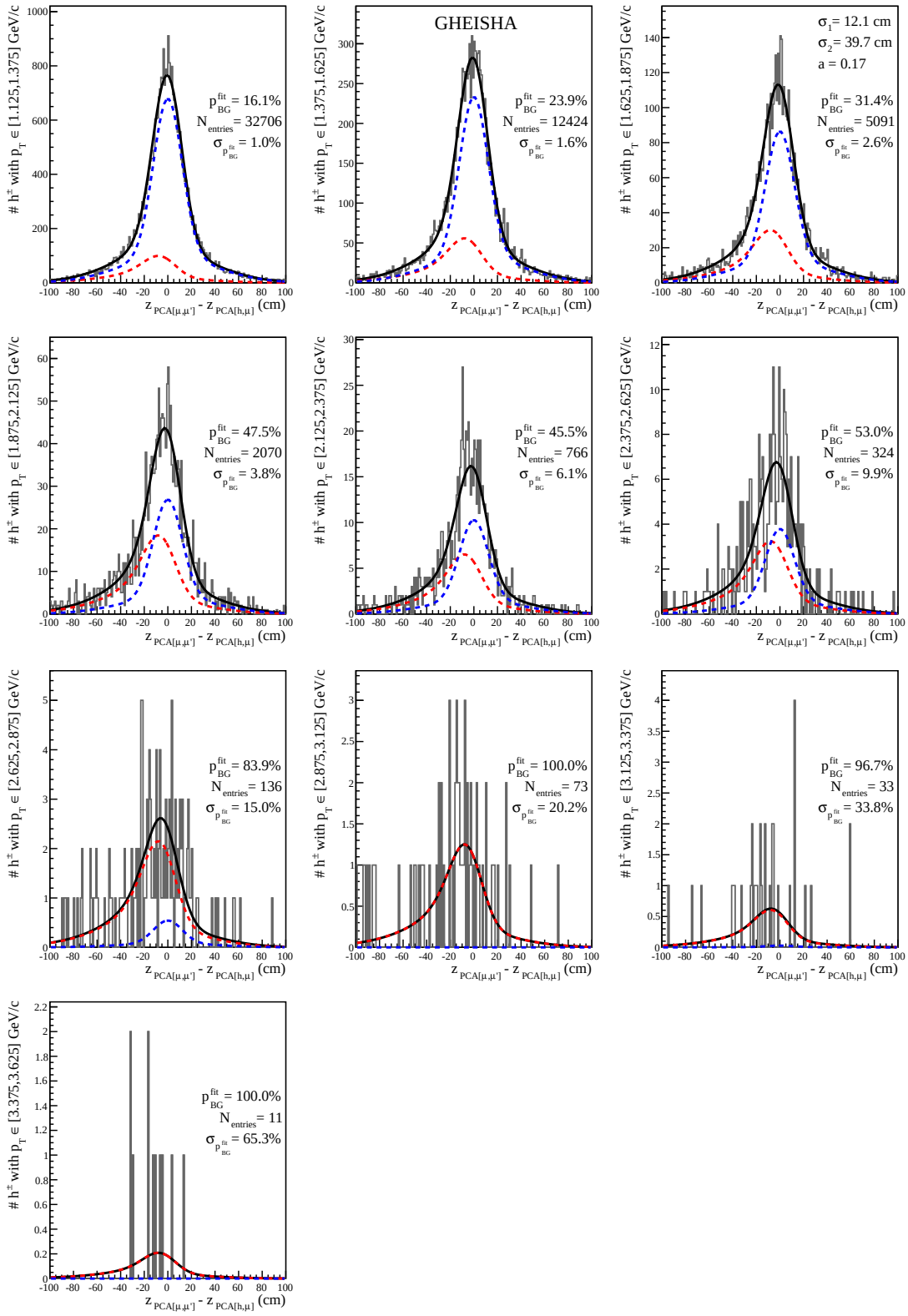


**Figure 6.11:** Distributions of $D$ for all hadrons from the simulation with GHEISHA in bins of $p_T$. The black lines show the fitted functions $f_{i,\mathrm{ALL}}$, which are the sums of the signal functions $f_{i,\mathrm{SIG}}$ (blue) and the background functions $f_{i,\mathrm{BG}}$ (red).

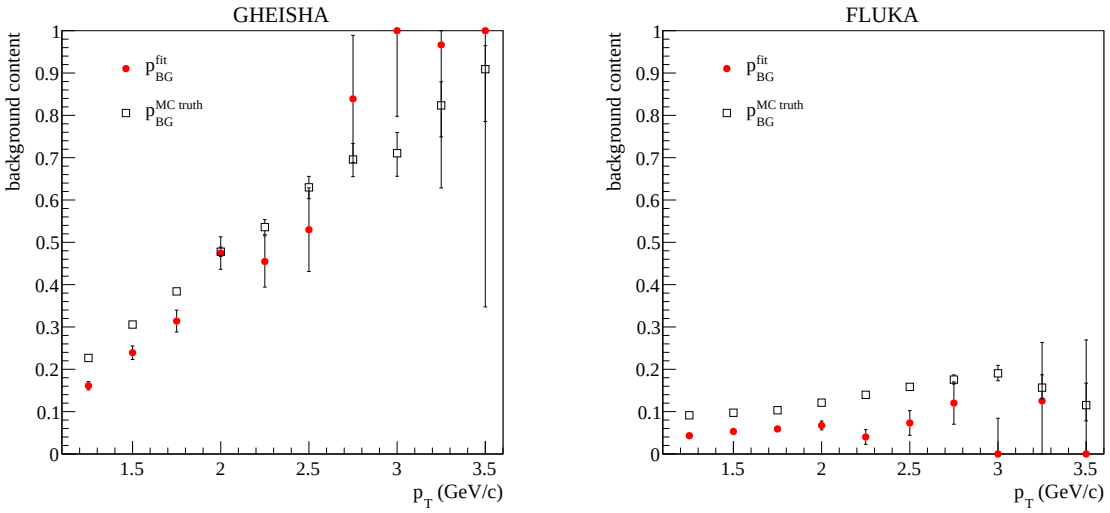


**Figure 6.12:** Comparison between the background content determined from the MC truth information (Eq. (6.10)) and from the fit of the functions $f_{i,\mathrm{ALL}}$ (Eq. (6.8)) for the GHEISHA and FLUKA simulations.

and $A_{i,\mathrm{BG}}$ and the 3 common parameters $\sigma_1$, $\sigma_2$, and $a$, whose fitted values are listed in the top right corner of the figure. The background content in each bin $p_{i,\mathrm{BG}}^{\mathrm{fit}}$ is calculated and quoted in the figure. The statistical error of the background content $\sigma_{p_{\mathrm{BG}}^{\mathrm{fit}}}$ is not taken directly from the fit. The numerical minimization program would only be able to correctly determine the statistical errors of the fit parameters if Gaussian statistics could be assumed throughout. This is not the case for the higher $p_T$ bins which have very few entries. $\sigma_{p_{\mathrm{BG}}^{\mathrm{fit}}}$ is instead determined with a simple, dedicated MC program, which is described in detail in appendix D.

The real background content in each bin is of course known from the MC truth information:

$$p_{i,\mathrm{BG}}^{\mathrm{MC\ truth}} = \frac{N_{i,\mathrm{MC}}^{\mathrm{rec,\ secondary}}}{N_{i,\mathrm{MC}}^{\mathrm{rec}}} = \frac{N_{i,\mathrm{MC}}^{\mathrm{rec,\ secondary}}}{N_{i,\mathrm{MC}}^{\mathrm{rec,\ primary}} + N_{i,\mathrm{MC}}^{\mathrm{rec,\ secondary}}} \quad , \tag{6.10}$$

where the association to the MC truth information is used to distinguish primary and secondary hadrons. Figure 6.12 shows the comparison between the background content from MC truth information and the background fraction which is determined by the fit procedure for the GHEISHA (left plot) and the FLUKA (right plot) simulations. There is a clear correlation between the two background contents in both plots; however, the background content determined by the fits is systematically too low. There seems to be a fraction of the background which is not described by the fit model $f_{\mathrm{ALL}}$. The missing fraction is rather constant even over bins with very different background contents. It is quantified from the results of the FLUKA simulation (using the GHEISHA results yields the same result) of Fig. 6.12:

$$\delta = \frac{\sum_i N_{i,\mathrm{MC}}^{\mathrm{rec}} \delta_i}{\sum_i N_{i,\mathrm{MC}}^{\mathrm{rec}}} = 0.06 \quad . \tag{6.11}$$

The sums run over the ten $p_T$ bins. $\delta_i$ is the difference between the real background content (black square in Fig. 6.12) and the value determined by the fit (red circle) in bin $i$.

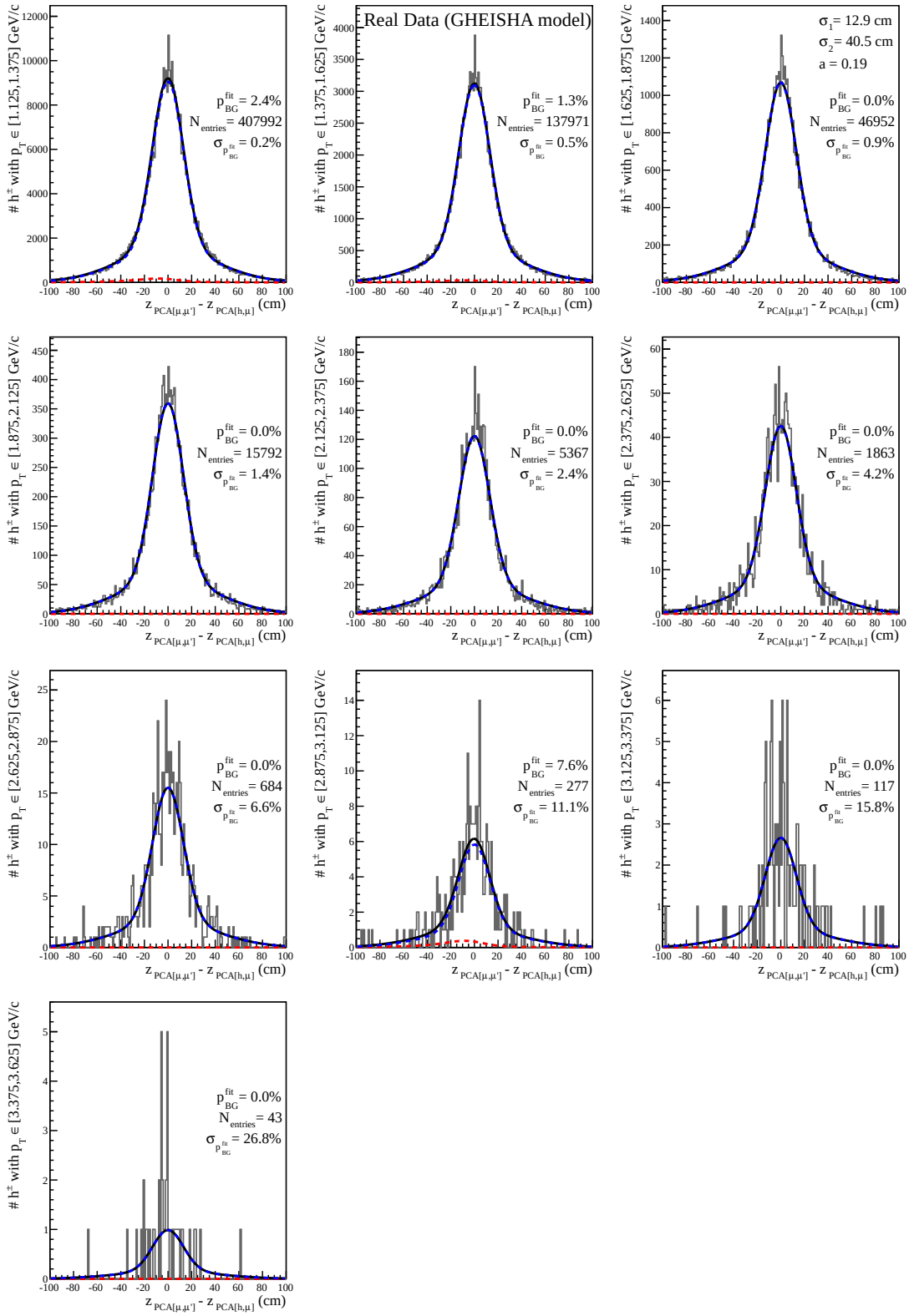


**Figure 6.13:** Distributions of $D$ for real data in $p_T$ bins. The fit is performed using the input function $g(\tilde{D})$ from the simulation with GHEISHA (Fig. 6.9). The black lines show the fitted functions $f_{i,\mathrm{ALL}}$, which are the sums of the signal functions $f_{i,\mathrm{SIG}}$ (blue) and the background functions $f_{i,\mathrm{BG}}$ (red).

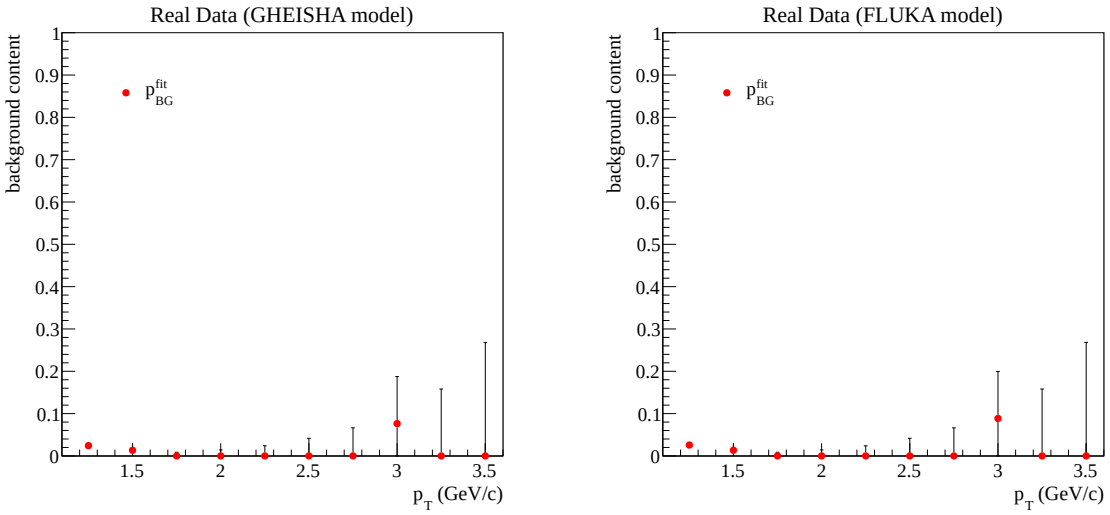


**Figure 6.14:** Summary of the background contents determined by the $f_{i,\mathrm{ALL}}$ fits to the real data with the GHEISHA model (Fig. 6.13) and the FLUKA model (Fig. B.7).

### 6.3.3 Application of the Background Quantification Method to the Real Data

The hadron shower models GHEISHA and FLUKA predict very different background contributions to the high-$p_T$ hadron yields from misreconstructed hadron-shower events. The background content can be deduced from fits of the functions $f_{\mathrm{ALL}}$ to the $D$ distributions, apart from a constant missing background fraction of $\delta = 0.06$. The model can now be applied to the real data to answer the question "how much background of the structure $g(\tilde{D})$ of the simulation does the real data contain?". The shape of the function $g(\tilde{D})$ (Eq. (6.6)) is used as an input to the fit procedure. The models GHEISHA and FLUKA result in similar, but still slightly different parameters for $g(\tilde{D})$. The real data is tested against both models.

The fit is once again a 23-parameters likelihood maximization with $10 \times 2$ normalization parameters $A_{i,\mathrm{SIG}}$ and $A_{i,\mathrm{BG}}$ and the 3 common parameters $\sigma_1$, $\sigma_2$, and $a$. The results of the fit to the $D$ distributions of real data in the ten $p_T$ bins with the GHEISHA model of $g(\tilde{D})$ are shown in Fig. 6.13 (corresponding plots for the FLUKA model in Fig. B.7 (p. 154)). The $D$ distributions look very symmetrical, and they are well centered around zero. The fitted values for $\sigma_1$ and $\sigma_2$ are slightly wider than for the fit to the MC data, but the double Gaussian shape is still a very good description. The background contents of all $p_T$ bins and their statistical uncertainties from the real-data fits with the GHEISHA and the FLUKA models are summarized in Fig. 6.14. The results are compatible with a very small background content or even a zero background content over the complete range of $p_T$. The few non-zero values are ignored, because they are statistically not very significant or are well within the systematic uncertainties which are described at the end of this section. The dramatic background of up to 90% which was suggested by the simulation with GHEISHA is certainly excluded. But even the moderate background level suggested by FLUKA seems to be too large. However, the statistical errors become quite large for the highest $p_T$ bins. The limited statistics in the $D$ distributions of Fig. 6.13 do not allow the complete exclusion of background due to hadron showers with the $f_{\mathrm{ALL}}$ fits.

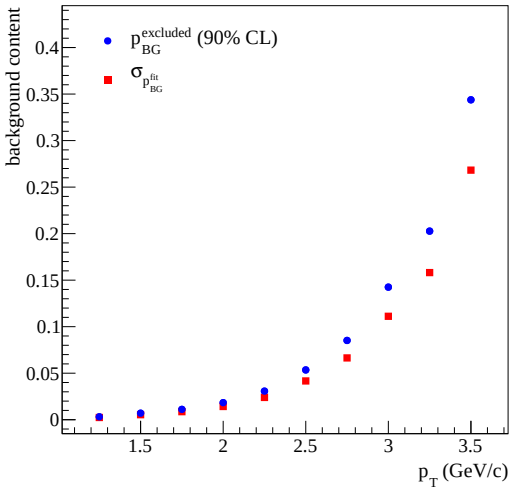


**Figure 6.15:** Statistical limitations of the background-fit model.

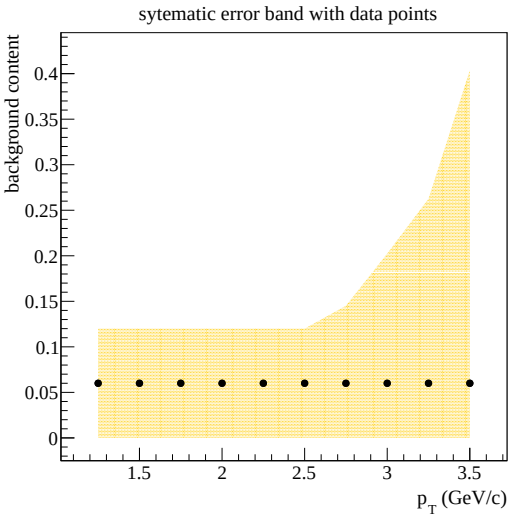


**Figure 6.16:** Systematic error band of the background fraction.

Under the assumption that $p_{\mathrm{BG}}^{\mathrm{fit}} = 0$, the background level which can be excluded with a 90% confidence level, $p_{\mathrm{BG}}^{\mathrm{excluded}}$, can be calculated from the statistical error $\sigma_{p_{\mathrm{BG}}^{\mathrm{fit}}}$ of the fit as follows:

$$\int_{-\infty}^{0} \frac{1}{\sqrt{2\pi}\sigma_{p_{\mathrm{BG}}^{\mathrm{fit}}}} \exp\left(-\frac{(x - p_{\mathrm{BG}}^{\mathrm{excluded}})^2}{2\sigma^2_{p_{\mathrm{BG}}^{\mathrm{fit}}}}\right) \mathrm{d}x \stackrel{!}{=} 0.1 \quad . \tag{6.12}$$

Figure 6.15 shows the values of $\sigma_{p_{\mathrm{BG}}^{\mathrm{fit}}}$ and $p_{\mathrm{BG}}^{\mathrm{excluded}}$ for all $p_T$ bins. The determination of the values of $\sigma_{p_{\mathrm{BG}}^{\mathrm{fit}}}$ is shown in Fig. D.2 (p. 165).
The number of reconstructed hadrons $N_{i,\mathrm{MC}}^{\mathrm{rec}}$ for the acceptance factor calculation of Eq. (6.2) is not taken directly from the simulation. Since the $f_{\mathrm{ALL}}$ fits suggest the absence of background from secondary hadrons, the number $N_{i,\mathrm{MC}}^{\mathrm{rec,\,primary}}$ is used instead, which only counts the hadrons which stem from the primary vertex. The test of the background fit on MC data has shown, however, that there is a margin of a background fraction of $\delta = 0.06$ which can not be identified with this method. A safety margin of $2\delta$ of background content is used to define the systematic error band due to the possibility of unidentified background. The central values which are used to draw the data points of the acceptance factors are placed in the center of the band. For the four highest $p_T$ bins, where a background beyond 0.06 can not be excluded with a 90% confidence level, this error band is insufficient. The upper limit of the systematic error band is changed to $p_{\mathrm{BG}}^{\mathrm{excluded}}$ for these bins. The number of reconstructed hadrons used for the acceptance calculation is

$$N_{i,\mathrm{MC}}^{\mathrm{rec}} = N_{i,\mathrm{MC}}^{\mathrm{rec,\,primary}} \cdot (1 + 0.06^{+\max(0.06, p_{i,\mathrm{BG}}^{\mathrm{excluded}})}_{-0.06}(\mathrm{syst.})) \quad . \tag{6.13}$$

This systematic error band of the background fraction which is added to $N_{i,\mathrm{MC}}^{\mathrm{rec,\,primary}}$ is shown in Fig. 6.16.

### 6.3.4 Comparison of Kinematical Distributions from Real Data and Monte Carlo Simulation

It is common practice to check the quality of the MC simulation used for the acceptance correction by comparing kinematical distributions from the simulation to the ones from the real data. This comparison is sensitive to the quality of the descriptions of the geometries, resolutions, and efficiencies of the detectors in the simulation, and also to the correctness of the hadronic shower model to simulate the secondary interactions in the target material. Another important issue which is tested with this comparison is the ability of the MC generator PYTHIA to populate the phase space for the quasi-real photoproduction of hadrons correctly. This phase space has at least four independent dimensions, two to describe the muon scattering ($Q^2$, $y$) and two more to describe the hadron, for instance ($z$, $p_T$). All variables except $p_T$ are, however, integrated over. If the phase space, which is integrated over, is wrongly populated, the acceptance correction will be systematically biased. Ideally, one would want to perform a four-dimensional acceptance correction to become insensitive to this issue. This is unfortunately not feasible because it would require an astronomical amount of computing time. For the one-dimensional acceptance correction, $2.3 \cdot 10^9$ events have been simulated which is just enough to reach twice the statistics of the real data. This simulation already used $\sim 4 \cdot 10^6$ HS06 hours [104] of computing time, which translates into about half a million CPU-core hours at the computing center at Lyon, where the simulation was performed. The systematic uncertainty due to the one-dimensional acceptance correction is studied by comparing the cross section which was corrected for acceptance with a binning in $(p_T, Q^2)$, $(p_T, y)$, $(p_T, x_{\mathrm{Bj}})$, $(p_T, W)$, $(p_T, z)$, and $(p_T, \theta)$ to the cross section which was corrected for acceptance with a binning only in $p_T$. This study is described in appendix E. The maximal observable difference is $\pm 3\%$ which is taken into account in the calculation of the systematic errors of the acceptance factors.

The acceptance correction is calculated from the simulation sample which uses the FLUKA model, but hadrons stemming from secondary interactions are rejected. This simulation sample is referred to as the "PRIMARY simulation" to distinguish it from the FLUKA and the GHEISHA simulations. The PRIMARY simulation is compared to the real data in Figs. 6.17 and 6.18. The overall agreement in the variables $Q^2$, $y$, $W$, $z$, and $\theta$ is quite good, especially in the region $p_T > 2\,\mathrm{GeV}/c$. In the range $p_T \in [1, 2]\,\mathrm{GeV}/c$ there are some disagreements up to the 20% level. The discussed comparison of the one-dimensional and the two-dimensional acceptance corrections ensures that this does not have a large effect on the final result. The disagreement between the $p_T$ spectra of real data and MC data is most likely a real physical effect. The hardening of the $p_T$ spectra in the real data above $2.5\,\mathrm{GeV}/c$ is not modelled in the PYTHIA generator. The influence of a different slope of the $p_T$ spectrum on the acceptance correction, especially the correction for bin migration, has not been studied in detail. The resolution for the measurement of $p_T$ depends on $p_T$ itself and ranges from $33\,\mathrm{MeV}/c$ at $p_T = 1.25\,\mathrm{GeV}/c$ to $94\,\mathrm{MeV}/c$ at $p_T = 3.5\,\mathrm{GeV}/c$ (see Fig. B.8 (p. 155)). The $p_T$ bin width of the presented analysis is $250\,\mathrm{MeV}/c$, which is much larger than the resolutions. This suggests that the effect of bin migration should be rather small.

The comparison of the real data to the FLUKA and GHEISHA simulations are shown in the appendix in Figs. B.9 (p. 156) to B.12 (p. 159). The dramatic disagreement between the MC simulation with the GHEISHA model and the real data is very apparent in these plots.

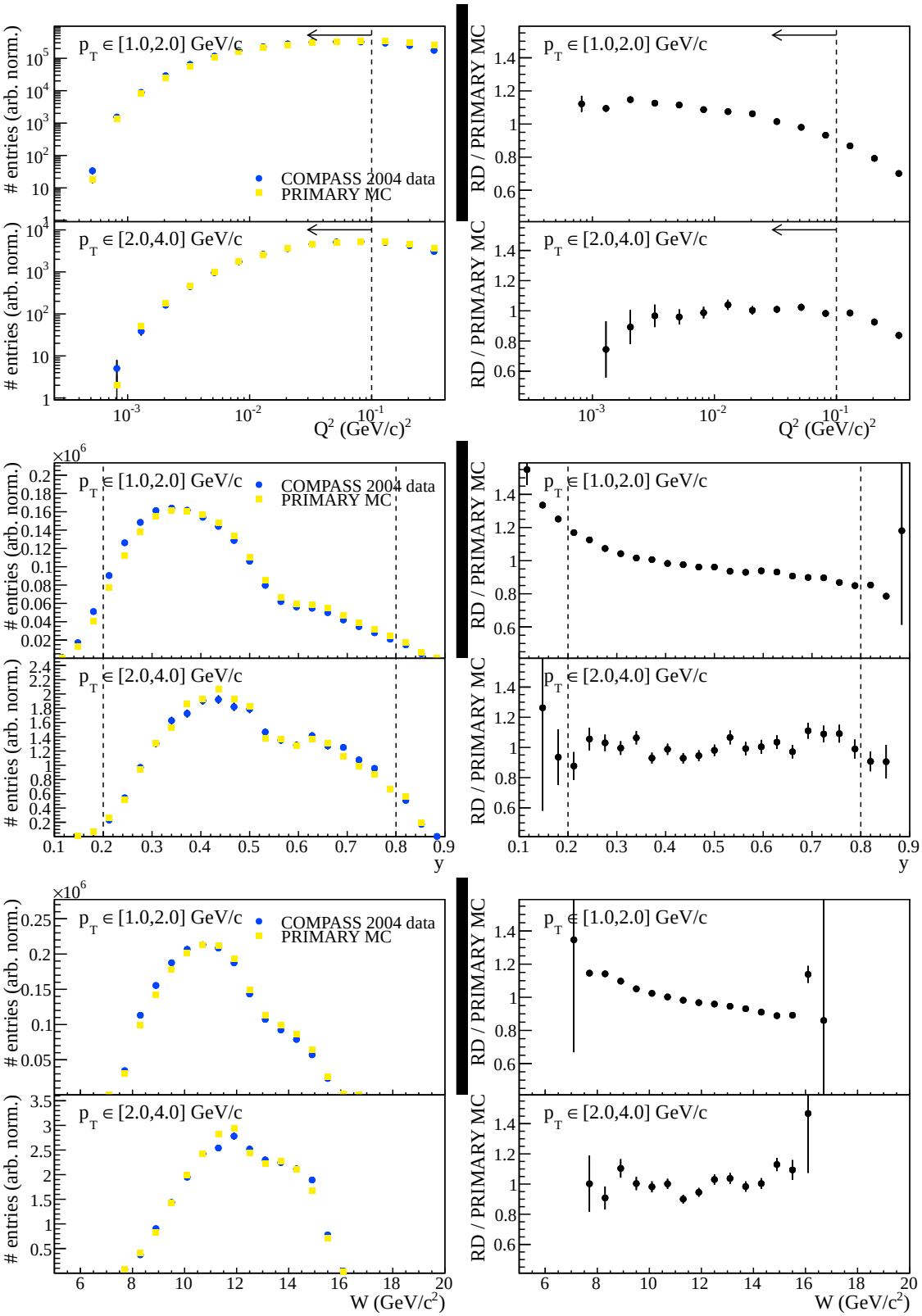


**Figure 6.17:** Comparison of kinematical distributions $Q^2$, $y$, and $W$ from real data and PRIMARY simulation. The distributions of each variable are independently normalized to have equal integrals inside the ranges defined by the cuts, which are indicated by the dashed lines.

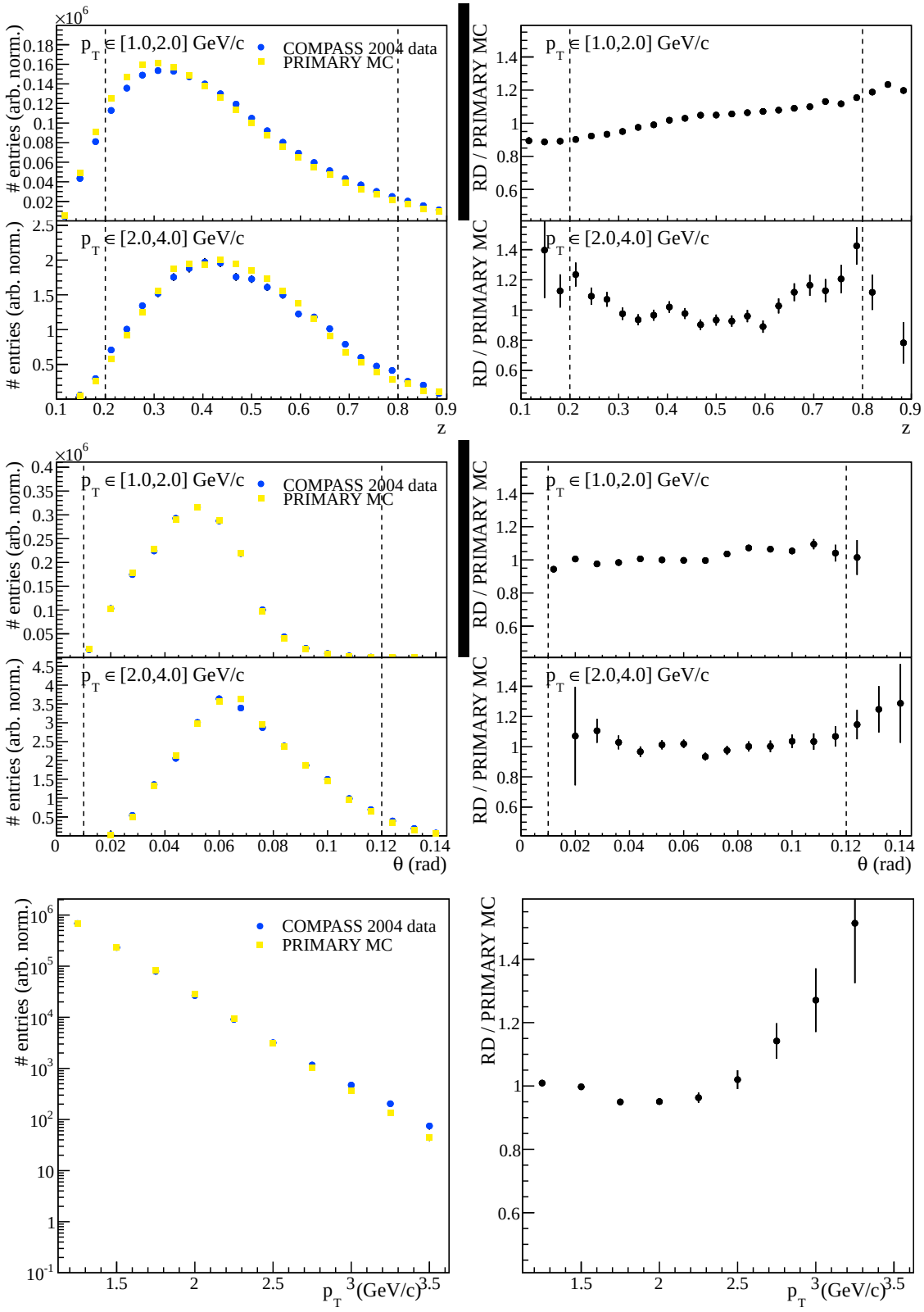


**Figure 6.18:** Comparison of kinematical distributions $z$, $\theta$, and $p_T$ from real data and PRIMARY simulation. The distributions of each variable are independently normalized to have equal integrals inside the ranges defined by the cuts, which are indicated by the dashed lines.

### 6.3.5 Event Scaling Factors for Dead Time Settings in COMGEANT

The dead time parameter for the veto signal $V'$ was set to 0.06 in the detector simulation COMGEANT. This means that 6 out of 100 LT triggers were ignored on average in the simulation. Since the $V'$ dead time is taken into account already in the weighting of real-data events that were triggered only in the LT (see Sec. 6.1), the additional MC correction has to be removed. The reconstructed MC events that were only triggered in the LT are thus weighted with 1/0.94.
There is an additional dead time parameter in COMGEANT which affects the IT and the LT, namely the dead time of the calorimetric component of the trigger, which was set to 0.05. The inefficiency of the calorimetric component of the IT and the LT was determined from real data to be 4% (see Sec. 6.2.2). The question whether this inefficiency is actually a dead time or not is not relevant in this context. Since the correction factors are not the same, all reconstructed MC events are weighted with the factor 0.96/0.95.

### 6.3.6 Acceptance Correction Factors with Statistical and Systematic Errors

The acceptance correction factor in bin $i$ which spans the range $p_T \in [p_{T,i,1}, p_{T,i,2}]$ is

$$\epsilon_i = \frac{N^{\text{rec}}_{i,\text{MC}}}{N^{\text{gen}}_{i,\text{MC}}} = 1.06 \cdot \frac{N^{\text{rec, primary}}_{i,\text{MC}}}{N^{\text{gen}}_{i,\text{MC}}} \quad , \tag{6.14}$$

where $N^{\text{rec}}_{i,\text{MC}}$ was taken from Eq. (6.13). The relative statistical error of this acceptance factor is

$$\frac{\sigma_{\epsilon_i}}{\epsilon_i} = \sqrt{\left(\frac{\sigma_{N^{\text{gen}}_{i,\text{MC}}}}{N^{\text{gen}}_{i,\text{MC}}}\right)^2 + \left(\frac{\sigma_{N^{\text{rec , primary}}_{i,\text{MC}}}}{N^{\text{rec, primary}}_{i,\text{MC}}}\right)^2} \quad . \tag{6.15}$$

This definition assumes that the numbers of generated and reconstructed hadrons are statistically independent, which is not quite correct. If the acceptance factor was a strict efficiency, which only counts whether a generated hadron could be reconstructed or not, the statistical error would be defined by binomial statistics. But the acceptance correction factor also contains the effect of bin migration, for which the definition of Eq. (6.15) is fine because the generated and reconstructed hadrons do not stem from the same sample of generated hadrons. The way it is defined, the acceptance factor is not even bound to values $\leq 1$. Equation (6.15) is used for the calculation of the statistical error of the acceptance factors, because the effects of efficiency and bin migration can not be completely disentangled. This is a conservative estimate, because the use of a possible knowledge of the degree of dependence of the number of generated hadrons and the number of reconstructed hadrons could only reduce the error.
The number of reconstructed hadrons is subject to weighting factors $w_j$ as described in the previous section. The calculation of statistical errors for weighted hadron samples is described in appendix F. The relative statistical error of the acceptance correction factor in bin $i$ is

$$\frac{\sigma_{\epsilon_i}}{\epsilon_i} = \sqrt{\frac{1}{N^{\text{gen}}_{i,\text{MC}}} + \frac{\sum_{j=1}^{n_i} w_j^2}{(\sum_{j=1}^{n_i} w_j)^2}} \quad , \tag{6.16}$$

where $n_i$ is the number of hadrons in bin $i$.
The systematic error of the acceptance correction is defined by the quadratic sum of the contributions of the multi-dimensional acceptance correction of 3% and the uncertainty due to hadron showers in the target material. The lower and upper limits of the systematic error band of the acceptance factors are

$$\epsilon_{i,\mathrm{l}} = \epsilon_i \cdot (1 - \sqrt{0.06^2 + 0.03^2}) \quad , \tag{6.17}$$

$$\epsilon_{i,\mathrm{u}} = \epsilon_i \cdot (1 + \sqrt{(\max(0.06, p_{i,\mathrm{BG}}^{\mathrm{excluded}}))^2 + 0.03^2}) \quad . \tag{6.18}$$

The acceptance correction factors are determined separately for positively and negatively charged hadrons. The $p_{i,\mathrm{BG}}^{\mathrm{excluded}}$ have been determined independently of the hadron charge, but the contribution of background due to hadron showers can be assumed to be charge independent.
The acceptance factors have not been calculated for bins with $N_{i,\mathrm{MC}}^{\mathrm{gen}} < 50$, because the statistical fluctuations of the acceptance correction would be unreasonably large. The acceptance correction factors for positively and negatively charged hadrons are shown in Fig. 6.19a. The cross section shall also be determined in bins of the angle $\theta$. The corresponding acceptance correction factors are presented in Fig. 6.19b.
The acceptance factors are much lower than 100%. The incomplete phase space coverage of the trigger hodoscopes and the track reconstruction efficiency in COMPASS of $\sim 90\%$ are partly responsible for this. Secondary reactions of hadrons in the target material are the most significant reason for the loss of hadrons.

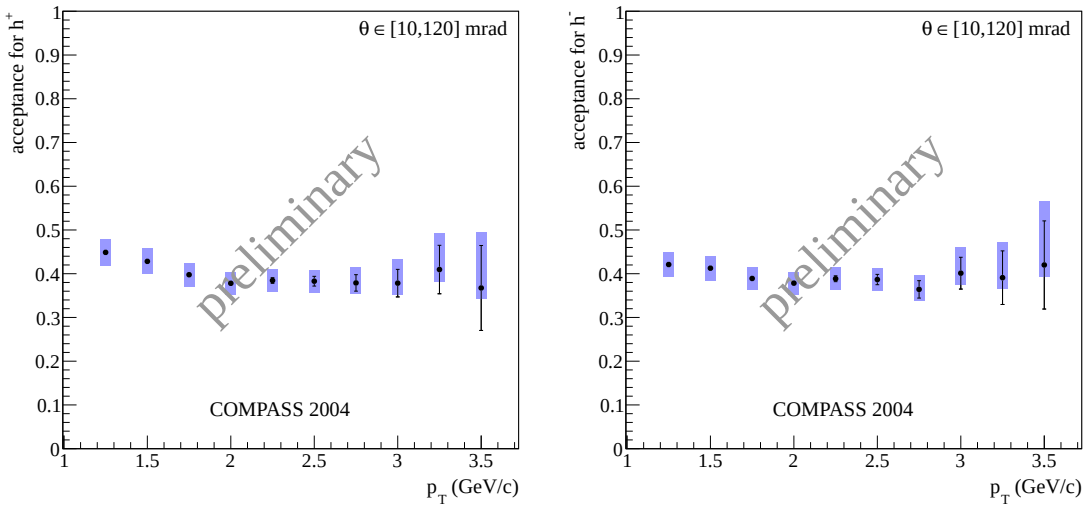


**(a)** Acceptance correction factors integrated over $\theta$.

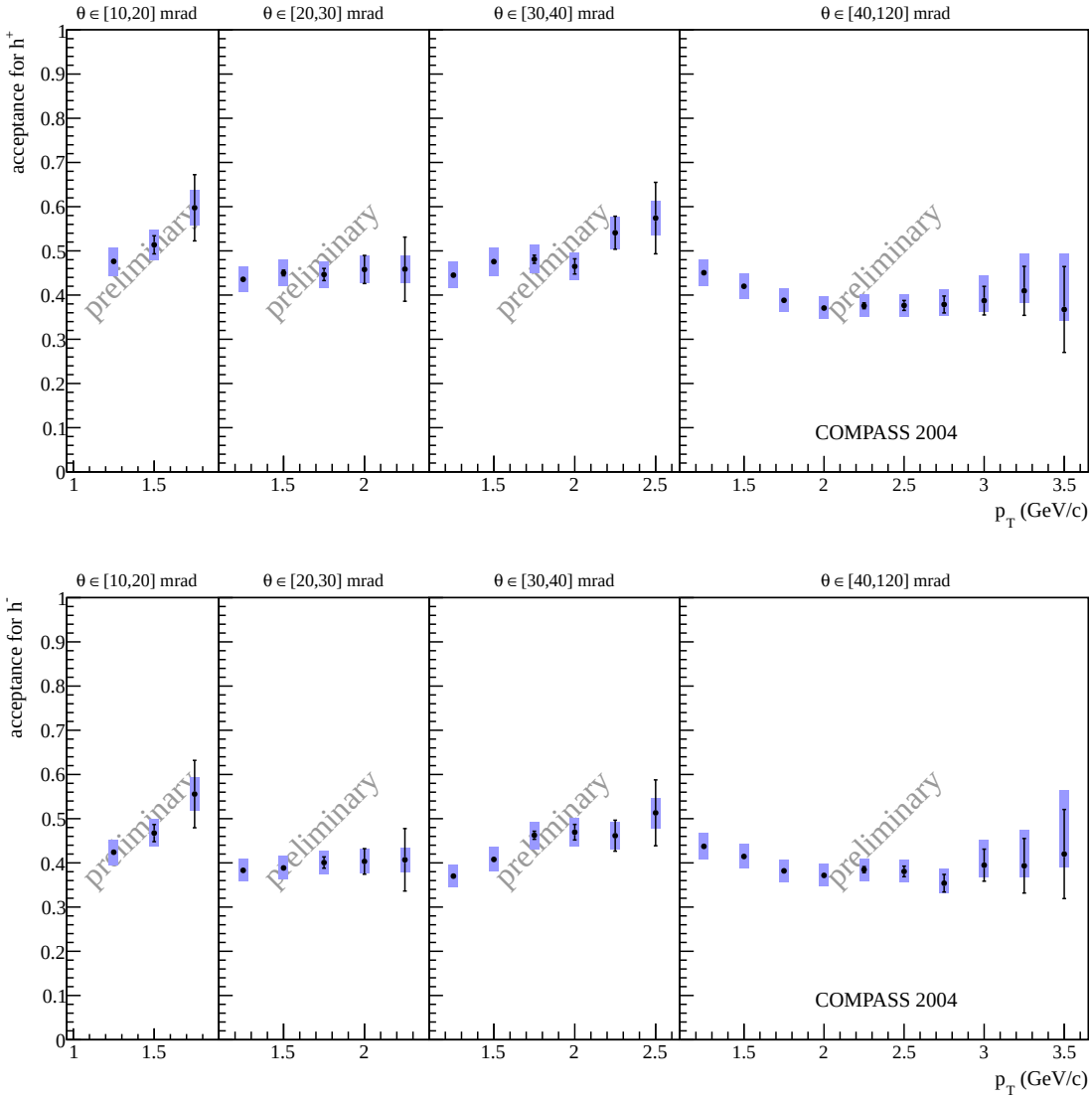


**(b)** Acceptance correction factors binned in $\theta$.

**Figure 6.19:** Acceptance correction factors for positively and negatively charged hadrons with statistical error bars and systematic errors (colored boxes).

## 6.4 Cross Section Results

### 6.4.1 Calculation of Data Points from Binned Cross Section

It is the goal of this analysis to determine values of the $p_T$-differential hadron production cross section at discrete values of $p_T$. However, such data points are not the direct outcome of the analysis, which is performed in bins of $p_T$. The value of the cross section in bin $i$, which spans the range $p_T \in [p_{T,i,1}, p_{T,i,2}]$, is

$$\left(\frac{\mathrm{d}\sigma}{\mathrm{d}p_T}\right)_i = \frac{\tilde{N}_i/\epsilon_i}{\tilde{L}} \frac{1}{p_{T,i,2} - p_{T,i,1}} \quad , \tag{6.19}$$

with the number of observed hadrons in the bin $\tilde{N}_i$, the acceptance $\epsilon_i$, and the effective integrated luminosity $\tilde{L}$. It is not unusual to plot the data point corresponding to this bin at a cross section value of $(\mathrm{d}\sigma/\mathrm{d}p_T)_i$ and the $p_T$ position of the bin center (BC) $(p_{T,i,1} + p_{T,i,2})/2$. Another approach, which is often used, is to plot $(\mathrm{d}\sigma/\mathrm{d}p_T)_i$ at the center of gravity (CG) of the bin

$$p_{T,i,\mathrm{CG}} = \frac{\sum_{j=1}^{n_i} p_{T,j}}{n_i} \quad , \tag{6.20}$$

where the sum runs over the $p_T$ values of all $n_i$ entries in the bin. Both procedures are incorrect, especially for steeply falling or rising distributions. This issue is discussed in detail by Lafferty & Wyatt (LW) [105]. A conversion of binned data into data points is not possible without assumptions on the parent distribution $g(p_T)$ the measured spectrum follows.

#### 6.4.1.1 The Lafferty & Wyatt Method to Calculate Data Points

According to Ref. [105], there are two possibilities for plotting the data point at the correct position:

1. Plot the data point at the ordinate $(\mathrm{d}\sigma/\mathrm{d}p_T)_i$ and the abscissa $p_{T,i,\mathrm{LW}}$ where the parent distribution would have a value of $g(p_{T,i,\mathrm{LW}}) = (\mathrm{d}\sigma/\mathrm{d}p_T)_i$.
2. Plot the data point at the abscissa of the BC $(p_{T,i,1} + p_{T,i,2})/2$ and the ordinate of the parent distribution at this value $g((p_{T,i,1} + p_{T,i,2})/2)$.

The second option is discarded because it seems tenuous to plot a data point which does not directly correspond to the measured cross section. Plotting the data point at a different abscissa is preferable. This abscissa $p_{T,i,\mathrm{LW}}$ is defined by:

$$g(p_{T,i,\mathrm{LW}}) = \frac{1}{p_{T,i,2} - p_{T,i,1}} \int_{p_{T,i,1}}^{p_{T,i,2}} g(p_T)\,\mathrm{d}p_T \quad . \tag{6.21}$$

It is easily visible that only the shape of the distribution $g$ over the bin width matters, while the normalization of $g$ cancels.

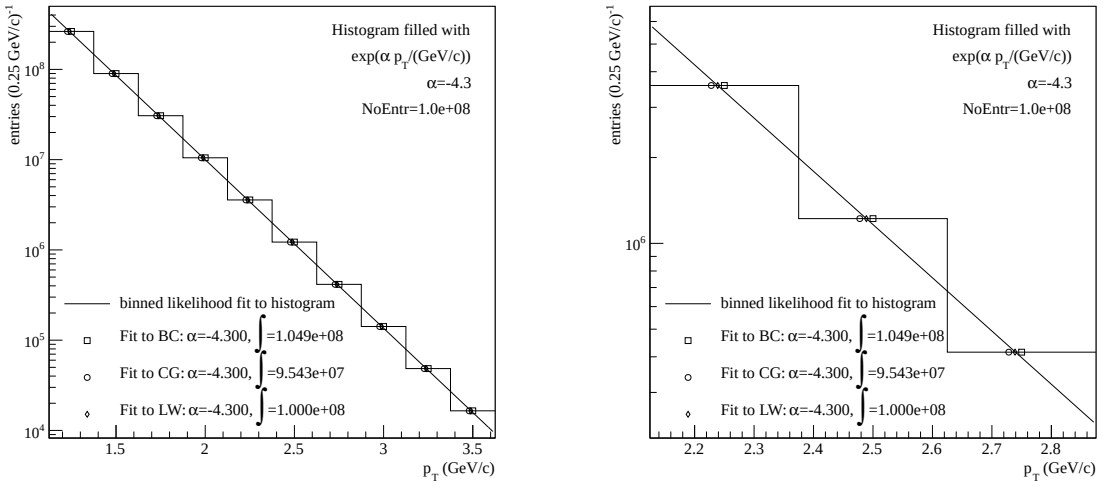


**Figure 6.20:** Output of a Toy Monte Carlo model to illustrate the effect of a wrong choice of $p_T$ values for plotting data points from a binned analysis. The compared methods are bin center (BC), center of gravity (CG), and Lafferty & Wyatt (LW). The right plot just shows a zoom into the left plot.

The procedure is tested with a small Toy-Monte-Carlo model, in which $10^8$ $p_T$ values are sampled from the parent distribution $g(p_T) \propto e^{-4.3(\,\mathrm{GeV}/c)^{-1} p_T}$ and filled into a histogram with the same binning which is used for the cross section results. The exponent of $-4.3$ is used in this example because it is close to the slope of the hadron yields. Data points are then calculated at the BC, at the CG, and with the LW method. The results are shown in Fig. 6.20. The data points from the LW method lie $\sim 11$ MeV/c below the bin center, and the CG data points lie another $\sim 11$ MeV/c below the LW points. Although this difference in the abscissa is small, it has a significant impact on the normalization of the steeply falling spectrum. The figure quotes the results of fits of exponential functions to the BC, CG, and LW data points. Only the LW points lead to a correct normalization of the spectrum, while the fit to the BC (CG) data points delivers a normalization of the spectrum which is 5% too high (too low). The fact that the BC and CG methods deliver the correct exponential shape is only due to the fact that the bins have equal widths. In the case of uneven bin widths, only the LW method would preserve the correct spectral shape.
The parent distribution of the measured cross section is of course not known. Different reasonable assumptions about the spectral shape are fitted to the binned cross sections with a binned likelihood fit. The difference between the data-point positions from the different fits serves as a measure for the systematic uncertainties of the $p_T$ values of the data points.

#### 6.4.1.2 Application of the Lafferty & Wyatt Method to the Measured Cross Sections

The five differential, binned cross sections for charged-hadron production in the $\theta$ bins $[10, 20]$ mrad, $[20, 30]$ mrad, $[30, 40]$ mrad, $[40, 120]$ mrad, and $[10, 120]$ mrad are fitted with two

alternative parent functions each:

$$g_A = P_1[e^{P_2 p_T} + P_3 e^{P_4 p_T}] \quad , \tag{6.22}$$

$$g_B = Q_1[e^{Q_2 p_T} + Q_3 p_T^{Q_4}] \quad . \tag{6.23}$$

The double exponential distribution is used because the shape of the cross sections suggests such a function. The alternative of an exponential plus a power law is motivated by the fact that pQCD calculations suggest power-law shapes in the high-$p_T$ region. The coefficients $P_3$ and $Q_3$ are quite small in all cases.
A binned likelihood fit is used. It minimizes the following figure of merit:

$$-\ln L = -\sum_i \left[ m_i^{\pm} \ln \mu_i^{\pm} - \mu_i^{\pm} - \ln \Gamma(m_i^{\pm} + 1) \right] \quad , \tag{6.24}$$

where the sum runs over all bins in the cross section. $m_i^{\pm}$ is the number of measured charged hadrons in bin $i$, including particle weighting, and $\mu_i^{\pm}$ is the expected number of charged hadrons from the parent distribution:

$$\mu_i^{\pm} = \tilde{L} \epsilon_i^{\pm} \int_{p_{T,i,1}}^{p_{T,i,2}} g(p_T) \mathrm{d}p_T \quad . \tag{6.25}$$

The $\Gamma$ function is used instead of the factorial in the Poisson probabilities because the $m_i$ are not integers due to the particle weights of the order 1.03 to 1.06 for hadrons from events which have only been triggered in the LT (see Sec. 6.1). Please note that the acceptance correction factors have been calculated for positively and negatively charged hadrons separately. For the calculation of the expected hadron yield of Eq. (6.25), the charge-averaged acceptance factors are needed:

$$\epsilon_i^{\pm} = \frac{\sigma_i^+ \cdot \epsilon_i^+ + \sigma_i^- \cdot \epsilon_i^-}{\sigma_i^+ + \sigma_i^-} \quad . \tag{6.26}$$

Please note that these charge-averaged acceptance factors are only used for the calculation of the positions of the data points which is described here. The results of the fits to the cross sections for the different $\theta$ ranges are shown in the appendix in Fig. B.13 (p. 160). The fitted functions are then used in Eq. (6.21) to numerically determine the values $p_{T,A,\mathrm{LW}}$ and $p_{T,B,\mathrm{LW}}$ corresponding to the functions $g_A$ and $g_B$ for each bin. The final $p_T$ value used to present the result is the mean value of $p_{T,A,\mathrm{LW}}$ and $p_{T,B,\mathrm{LW}}$. The systematic error of $p_T$ is given by the extrema $p_{T,A,\mathrm{LW}}$ and $p_{T,B,\mathrm{LW}}$. The results are listed in the appendix in Tab. B.1 (p. 160). The systematic errors are $< 0.5\,\mathrm{MeV/c}$ in almost all bins. They can safely be neglected.

### 6.4.2 Final Cross Section Results

The values of the cross section for all charged hadrons are determined by adding up the cross sections for positively and negatively charged hadrons:

$$\sigma_i = \frac{1}{\tilde{L}} \cdot \left( \frac{\tilde{N}_i^+}{\epsilon_i^+} + \frac{\tilde{N}_i^-}{\epsilon_i^-} \right) \quad . \tag{6.27}$$

The effective acceptance for the charge-summed case of Eq. (6.26) is not used. It was solely used for the calculation of the $p_T$ position of the data points in the previous section. The cross section results are subject to a 10% normalization uncertainty from the luminosity determination. The systematic point-to-point errors of the cross section stem from the systematic errors of the acceptance correction, which were detailed in Sec. 6.3.6. The upper limit of the systematical error band of the cross section is obtained by using the lower limit of the systematical error band of the acceptance correction and vice versa. The relative statistical errors of the cross sections for one particle charge are the quadratic sums of the relative statistical errors of the acceptance correction factors (as described in Sec. 6.3.6) and the relative statistical errors of the measured hadron yields. The absolute statistical errors of the charge-summed cross sections are the quadratic sums of the statistical errors of the cross sections for positively and negatively charged hadrons. Since the hadron yields involve particle weighting due to the $V'$ dead-time correction, their statistical errors are calculated with Eq. (F.5).

Figure 6.21a presents the final cross section result, integrated over the center-of-mass pseudo-rapidity, $\eta_{\text{c.m.s.}}$ (see Eq. (2.10)). The total errors are the quadratic sums of statistical and systematic errors; they are only visible for the two highest-$p_T$ data points. The relative statistical and systematic errors are shown in detail in the lower panel of the plot. The cross section spans over four orders of magnitude in intensity over the measured $p_T$ range. The only apparent feature of the cross section is a slight hardening of the spectrum around $p_T = 2.5\,\text{GeV}/c$. Please note that the presented cross section is not corrected for possible QED radiative effects.

The cross section binned in $\eta_{\text{c.m.s.}}$ is shown in Fig. 6.21b. The errors are displayed in the same way as for the rapidity-integrated plot. It is very apparent that the cross sections in the forward-rapidity bins, $\eta_{\text{c.m.s.}} > 1$, fall more steeply than the cross section at central rapidity, $\eta_{\text{c.m.s.}} < 1$. This is due to the fact that only the high-energy ends of the $y$ and $z$ spectra are available to produce high-$p_T$ particles at forward rapidities. The transverse momentum can be expressed as

$$p_T \approx \sin\theta \cdot E/c \cdot y \cdot z \quad , \tag{6.28}$$

where $E \approx c|\mathbf{k}|$ is the beam energy. Using the values $E = 160\,\text{GeV}$ and $\theta = 20\,\text{mrad}$ ($\eta_{\text{c.m.s.}} = 1.69$) for instance, the region $p_T > 2\,\text{GeV}/c$ can only be reached if $y \cdot z > 0.625$. Keeping in mind that $y < 0.8$ and $z < 0.8$ (i.e. $y \cdot z < 0.64$) are ensured in data selection, it becomes obvious why the high-$p_T$ region can not be reached at forward rapidities.

The ratio of the cross sections for the production of negatively over positively charged hadrons, integrated over all rapidities, is displayed in Fig. 6.21c. Within the statistical accuracy of the measurement, the charge ratio appears to be rather constant over $p_T$. The weighted mean of the charge ratios at the different $p_T$ values is $\mathrm{d}\sigma(h^-)/\mathrm{d}\sigma(h^+) = 0.87 \pm 0.01$. The fact that more positive than negative hadrons are produced can be due to the process of QCD Compton scattering (see Fig. 3.2b) in which the photon (from lepton scattering) couples to a quark from the nucleon. The electromagnetic coupling to $u$ quarks is four times larger than to $d$ quarks. The photon-gluon fusion process (see Fig. 3.2a) and all resolved-photon processes should not result in any charge asymmetry. The $p_T$ dependence of the charge ratio contains information about the mixing of the different processes that contribute to the overall cross section.

The charge ratios in the rapidity bins are shown in Fig. 6.21d. They are independent of $p_T$ as well and have very similar values as the rapidity-integrated charge ratio. All values of the cross sections and charge ratios in all rapidity ranges with their full errors are summarized in Tab. 6.2.

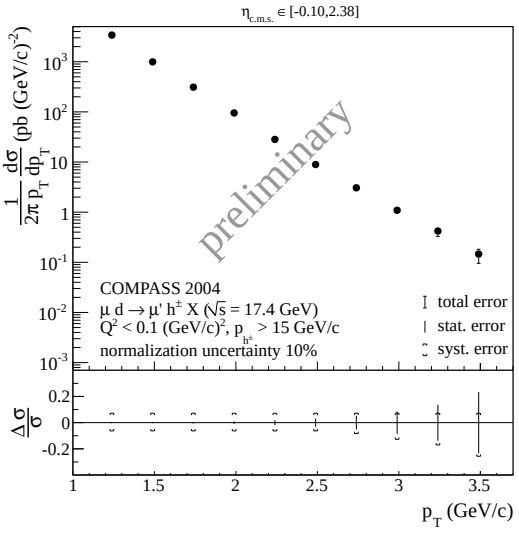


**(a)** Cross section integrated over $\eta_{\text{c.m.s.}}$.

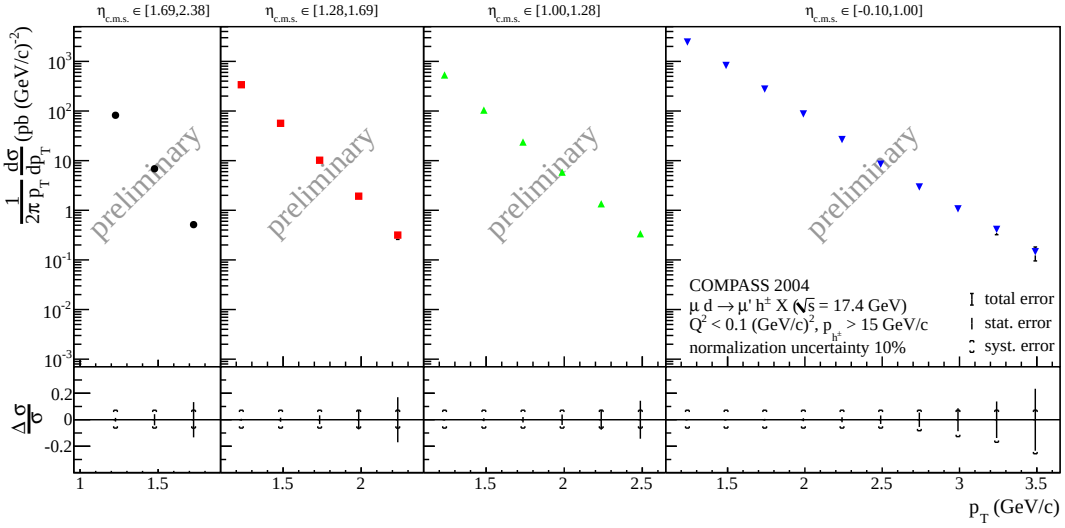


**(b)** Cross section binned in $\eta_{\text{c.m.s.}}$

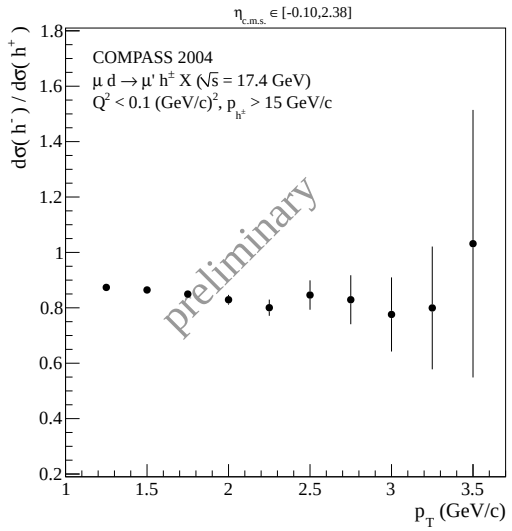


**(c)** Charge ratio of cross section integrated over $\eta_{\text{c.m.s.}}$.

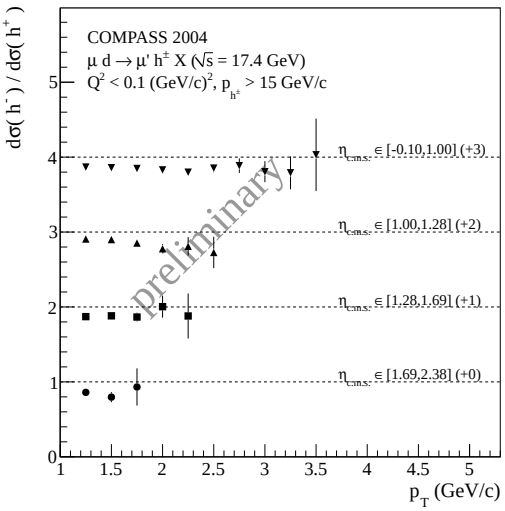


**(d)** Charge ratio of cross section binned in $\eta_{\text{c.m.s.}}$. Please note that the graphs are offset by constants, as indicated on the right (dashed lines indicate ratios of one).

**Figure 6.21:** Cross section for charged-hadron production at high $p_T$ in muon-deuteron scattering at low $Q^2$.

The cross section results have been released[8] for public presentation by the COMPASS collaboration in May 2011 [106] and have been shown on several conferences since then. These results represent the first absolutely normalized cross-section measurements that have been published from the muon-scattering program of COMPASS. A journal publication about the result will be submitted very soon.

[8] I am grateful to Y. Bedfer and A. Morreale for the COMPASS-internal cross checks, needed for the release process.

| $\eta_{\text{c.m.s.}} \in [-0.10, 2.38]$ | | | |
|---|---|---|---|
| $[p_{T,1}, p_{T,2}]$ (GeV/$c$) | $p_T$ (GeV/$c$) | $\frac{\mathrm{d}\sigma}{\mathrm{d}p_T} = \frac{1}{p_{T,2}-p_{T,1}} \int_{p_{T,1}}^{p_{T,2}} \frac{\mathrm{d}\sigma}{\mathrm{d}p_T} \mathrm{d}p_T$ (pb(GeV/$c$)$^{-1}$) | $\frac{\mathrm{d}\sigma}{\mathrm{d}p_T}(\mathrm{h}^-)/\frac{\mathrm{d}\sigma}{\mathrm{d}p_T}(\mathrm{h}^+)$ |
| [1.125, 1.375] | 1.239 | $[2.651 \pm 0.006\,(\text{stat.})\ ^{+0.191}_{-0.167}\,(\text{syst.})\ \pm 0.266\,(\text{lumi.})]\cdot 10^4$ | $0.874 \pm 0.004\,(\text{stat.})$ |
| [1.375, 1.625] | 1.489 | $[9.31 \pm 0.04\,(\text{stat.})\ ^{+0.67}_{-0.59}\,(\text{syst.})\ \pm 0.94\,(\text{lumi.})]\cdot 10^3$ | $0.864 \pm 0.007\,(\text{stat.})$ |
| [1.625, 1.875] | 1.739 | $3399 \pm 21\,(\text{stat.})\ ^{+245}_{-214}\,(\text{syst.})\ \pm 340\,(\text{lumi.})$ | $0.850 \pm 0.011\,(\text{stat.})$ |
| [1.875, 2.125] | 1.989 | $1190 \pm 13\,(\text{stat.})\ ^{+86}_{-75}\,(\text{syst.})\ \pm 120\,(\text{lumi.})$ | $0.829 \pm 0.018\,(\text{stat.})$ |
| [2.125, 2.375] | 2.239 | $398 \pm 8\,(\text{stat.})\ ^{+29}_{-25}\,(\text{syst.})\ \pm 40\,(\text{lumi.})$ | $0.800 \pm 0.030\,(\text{stat.})$ |
| [2.375, 2.625] | 2.489 | $139 \pm 5\,(\text{stat.})\ ^{+11}_{-9}\,(\text{syst.})\ \pm 14\,(\text{lumi.})$ | $0.85 \pm 0.06\,(\text{stat.})$ |
| [2.625, 2.875] | 2.739 | $52.7 \pm 2.8\,(\text{stat.})\ ^{+3.8}_{-4.4}\,(\text{syst.})\ \pm 5.3\,(\text{lumi.})$ | $0.83 \pm 0.09\,(\text{stat.})$ |
| [2.875, 3.125] | 2.989 | $20.5 \pm 1.8\,(\text{stat.})\ ^{+1.5}_{-2.7}\,(\text{syst.})\ \pm 2.1\,(\text{lumi.})$ | $0.78 \pm 0.14\,(\text{stat.})$ |
| [3.125, 3.375] | 3.239 | $8.6 \pm 1.2\,(\text{stat.})\ ^{+0.7}_{-1.5}\,(\text{syst.})\ \pm 0.9\,(\text{lumi.})$ | $0.80 \pm 0.23\,(\text{stat.})$ |
| [3.375, 3.625] | 3.490 | $3.21 \pm 0.75\,(\text{stat.})\ ^{+0.24}_{-0.83}\,(\text{syst.})\ \pm 0.33\,(\text{lumi.})$ | $1.0 \pm 0.5\,(\text{stat.})$ |

| $\eta_{\text{c.m.s.}} \in [1.69, 2.38]$ | | | |
|---|---|---|---|
| $[p_{T,1}, p_{T,2}]$ (GeV/$c$) | $p_T$ (GeV/$c$) | $\frac{\mathrm{d}\sigma}{\mathrm{d}p_T} = \frac{1}{p_{T,2}-p_{T,1}} \int_{p_{T,1}}^{p_{T,2}} \frac{\mathrm{d}\sigma}{\mathrm{d}p_T} \mathrm{d}p_T$ (pb(GeV/$c$)$^{-1}$) | $\frac{\mathrm{d}\sigma}{\mathrm{d}p_T}(\mathrm{h}^-)/\frac{\mathrm{d}\sigma}{\mathrm{d}p_T}(\mathrm{h}^+)$ |
| [1.125, 1.375] | 1.227 | $633 \pm 9\,(\text{stat.})\ ^{+46}_{-40}\,(\text{syst.})\ \pm 64\,(\text{lumi.})$ | $0.860 \pm 0.025\,(\text{stat.})$ |
| [1.375, 1.625] | 1.477 | $63.8 \pm 2.7\,(\text{stat.})\ ^{+4.6}_{-4.1}\,(\text{syst.})\ \pm 6.4\,(\text{lumi.})$ | $0.80 \pm 0.07\,(\text{stat.})$ |
| [1.625, 1.875] | 1.727 | $5.6 \pm 0.8\,(\text{stat.})\ ^{+0.5}_{-0.4}\,(\text{syst.})\ \pm 0.6\,(\text{lumi.})$ | $0.93 \pm 0.25\,(\text{stat.})$ |

| $\eta_{\text{c.m.s.}} \in [1.28, 1.69]$ | | | |
|---|---|---|---|
| $[p_{T,1}, p_{T,2}]$ (GeV/$c$) | $p_T$ (GeV/$c$) | $\frac{\mathrm{d}\sigma}{\mathrm{d}p_T} = \frac{1}{p_{T,2}-p_{T,1}} \int_{p_{T,1}}^{p_{T,2}} \frac{\mathrm{d}\sigma}{\mathrm{d}p_T} \mathrm{d}p_T$ (pb(GeV/$c$)$^{-1}$) | $\frac{\mathrm{d}\sigma}{\mathrm{d}p_T}(\mathrm{h}^-)/\frac{\mathrm{d}\sigma}{\mathrm{d}p_T}(\mathrm{h}^+)$ |
| [1.125, 1.375] | 1.233 | $2622 \pm 19\,(\text{stat.})\ ^{+189}_{-165}\,(\text{syst.})\ \pm 263\,(\text{lumi.})$ | $0.871 \pm 0.013\,(\text{stat.})$ |
| [1.375, 1.625] | 1.484 | $527 \pm 9\,(\text{stat.})\ ^{+38}_{-34}\,(\text{syst.})\ \pm 53\,(\text{lumi.})$ | $0.882 \pm 0.028\,(\text{stat.})$ |
| [1.625, 1.875] | 1.734 | $111 \pm 4\,(\text{stat.})\ ^{+8}_{-7}\,(\text{syst.})\ \pm 12\,(\text{lumi.})$ | $0.87 \pm 0.06\,(\text{stat.})$ |
| [1.875, 2.125] | 1.984 | $24.0 \pm 1.8\,(\text{stat.})\ ^{+1.8}_{-1.6}\,(\text{syst.})\ \pm 2.4\,(\text{lumi.})$ | $1.00 \pm 0.15\,(\text{stat.})$ |
| [2.125, 2.375] | 2.234 | $4.44 \pm 0.76\,(\text{stat.})\ ^{+0.32}_{-0.28}\,(\text{syst.})\ \pm 0.45\,(\text{lumi.})$ | $0.9 \pm 0.4\,(\text{stat.})$ |

| $\eta_{\text{c.m.s.}} \in [1.00, 1.28]$ | | | |
|---|---|---|---|
| $[p_{T,1}, p_{T,2}]$ (GeV/$c$) | $p_T$ (GeV/$c$) | $\frac{\mathrm{d}\sigma}{\mathrm{d}p_T} = \frac{1}{p_{T,2}-p_{T,1}} \int_{p_{T,1}}^{p_{T,2}} \frac{\mathrm{d}\sigma}{\mathrm{d}p_T} \mathrm{d}p_T$ (pb(GeV/$c$)$^{-1}$) | $\frac{\mathrm{d}\sigma}{\mathrm{d}p_T}(\mathrm{h}^-)/\frac{\mathrm{d}\sigma}{\mathrm{d}p_T}(\mathrm{h}^+)$ |
| [1.125, 1.375] | 1.234 | $4125 \pm 23\,(\text{stat.})\ ^{+297}_{-260}\,(\text{syst.})\ \pm 413\,(\text{lumi.})$ | $0.907 \pm 0.011\,(\text{stat.})$ |
| [1.375, 1.625] | 1.485 | $973 \pm 11\,(\text{stat.})\ ^{+70}_{-62}\,(\text{syst.})\ \pm 98\,(\text{lumi.})$ | $0.899 \pm 0.020\,(\text{stat.})$ |
| [1.625, 1.875] | 1.736 | $259 \pm 6\,(\text{stat.})\ ^{+19}_{-17}\,(\text{syst.})\ \pm 26\,(\text{lumi.})$ | $0.85 \pm 0.04\,(\text{stat.})$ |
| [1.875, 2.125] | 1.986 | $73.2 \pm 2.9\,(\text{stat.})\ ^{+5.3}_{-4.7}\,(\text{syst.})\ \pm 7.4\,(\text{lumi.})$ | $0.78 \pm 0.07\,(\text{stat.})$ |
| [2.125, 2.375] | 2.237 | $19.0 \pm 1.5\,(\text{stat.})\ ^{+1.4}_{-1.2}\,(\text{syst.})\ \pm 2.0\,(\text{lumi.})$ | $0.81 \pm 0.13\,(\text{stat.})$ |
| [2.375, 2.625] | 2.487 | $5.3 \pm 0.8\,(\text{stat.})\ ^{+0.4}_{-0.4}\,(\text{syst.})\ \pm 0.6\,(\text{lumi.})$ | $0.73 \pm 0.21\,(\text{stat.})$ |

| $\eta_{\text{c.m.s.}} \in [-0.10, 1.00]$ | | | |
|---|---|---|---|
| $[p_{T,1}, p_{T,2}]$ (GeV/$c$) | $p_T$ (GeV/$c$) | $\frac{\mathrm{d}\sigma}{\mathrm{d}p_T} = \frac{1}{p_{T,2}-p_{T,1}} \int_{p_{T,1}}^{p_{T,2}} \frac{\mathrm{d}\sigma}{\mathrm{d}p_T} \mathrm{d}p_T$ (pb(GeV/$c$)$^{-1}$) | $\frac{\mathrm{d}\sigma}{\mathrm{d}p_T}(\mathrm{h}^-)/\frac{\mathrm{d}\sigma}{\mathrm{d}p_T}(\mathrm{h}^+)$ |
| [1.125, 1.375] | 1.240 | $[1.912 \pm 0.005\,(\text{stat.})\ ^{+0.138}_{-0.121}\,(\text{syst.})\ \pm 0.192\,(\text{lumi.})]\cdot 10^4$ | $0.868 \pm 0.005\,(\text{stat.})$ |
| [1.375, 1.625] | 1.490 | $[7.75 \pm 0.04\,(\text{stat.})\ ^{+0.56}_{-0.49}\,(\text{syst.})\ \pm 0.78\,(\text{lumi.})]\cdot 10^3$ | $0.859 \pm 0.007\,(\text{stat.})$ |
| [1.625, 1.875] | 1.740 | $3026 \pm 20\,(\text{stat.})\ ^{+218}_{-191}\,(\text{syst.})\ \pm 303\,(\text{lumi.})$ | $0.848 \pm 0.012\,(\text{stat.})$ |
| [1.875, 2.125] | 1.990 | $1092 \pm 13\,(\text{stat.})\ ^{+79}_{-69}\,(\text{syst.})\ \pm 110\,(\text{lumi.})$ | $0.830 \pm 0.019\,(\text{stat.})$ |
| [2.125, 2.375] | 2.240 | $374 \pm 8\,(\text{stat.})\ ^{+27}_{-24}\,(\text{syst.})\ \pm 38\,(\text{lumi.})$ | $0.80 \pm 0.04\,(\text{stat.})$ |
| [2.375, 2.625] | 2.490 | $133 \pm 5\,(\text{stat.})\ ^{+10}_{-9}\,(\text{syst.})\ \pm 14\,(\text{lumi.})$ | $0.85 \pm 0.06\,(\text{stat.})$ |
| [2.625, 2.875] | 2.740 | $50.8 \pm 2.8\,(\text{stat.})\ ^{+3.7}_{-4.3}\,(\text{syst.})\ \pm 5.1\,(\text{lumi.})$ | $0.89 \pm 0.10\,(\text{stat.})$ |
| [2.875, 3.125] | 2.990 | $20.1 \pm 1.8\,(\text{stat.})\ ^{+1.5}_{-2.6}\,(\text{syst.})\ \pm 2.1\,(\text{lumi.})$ | $0.81 \pm 0.14\,(\text{stat.})$ |
| [3.125, 3.375] | 3.240 | $8.4 \pm 1.2\,(\text{stat.})\ ^{+0.7}_{-1.5}\,(\text{syst.})\ \pm 0.9\,(\text{lumi.})$ | $0.79 \pm 0.23\,(\text{stat.})$ |
| [3.375, 3.625] | 3.490 | $3.21 \pm 0.75\,(\text{stat.})\ ^{+0.24}_{-0.83}\,(\text{syst.})\ \pm 0.33\,(\text{lumi.})$ | $1.0 \pm 0.5\,(\text{stat.})$ |

**Table 6.2:** Cross section for charged-hadron production at high $p_T$ in muon-deuteron scattering at low $Q^2$ as shown in Fig. 6.21.

## 6.5 Comparison to NLO pQCD Calculations

The comparison of the measured cross section for high-$p_T$ hadron production with NLO pQCD calculations provides an important test for the applicability of pQCD methods to the process. The pQCD calculations have been introduced in detail in chapter 3 and the following discussion is based on the definitions made there. The pQCD curves presented in this chapter represent an update [37] of the calculations of Ref. [3]. They use the fragmentation functions for charged hadron production from the DSS set [107, 108], and implement the kinematical selection criteria $Q^2_{\text{max}} = 0.1\,(\text{GeV}/c)^2$, $y \in [0.2, 0.8]$, $z \in [0.2, 0.8]$, $p > 15\,\text{GeV}/c$, and $\theta \in [10, 120]\,\text{mrad}$ as used for the data analysis. Figure 6.22a shows the COMPASS measurement of the pseudo-rapidity-integrated cross section together with the updated NLO pQCD curves. The three curves correspond to different choices of the hard scales in the pQCD calculation. The scale uncertainty of the calculation is defined by varying the scale in the range $2p_T \geq \mu \geq p_T/2$ and the central value of the pQCD calculation is defined by the choice $\mu = p_T$. The scale uncertainty of the pQCD calculations at NLO is very large, spanning cross section values that are different by factors of five to six. In order to compare the results more quantitatively, the ratio of the experimental and pQCD cross sections shall be plotted. However, the theory curves are defined by discrete data points which are located at the bin centers, whereas the experimental data points are plotted at $p_T$ values slightly below the bin centers (see Sec. 6.4.1.2). Due to this difference, the cross-section ratio is best defined by the cross sections which are integrated over the $p_T$-bin widths. In the bin $p_T \in [p_{T,a}, p_{T,b}]$, the ratio of experimental cross section and the theory cross section at the scale $\mu = p_T$ is:

$$\frac{\mathrm{d}\sigma_{\text{COMPASS}}}{\mathrm{d}\sigma_{\text{NLO pQCD}}}\Big|_{\mu=p_T} = \frac{\int_{p_{T,a}}^{p_{T,b}} \frac{\mathrm{d}\sigma_{\text{COMPASS}}}{\mathrm{d}p_T}\mathrm{d}p_T}{\int_{p_{T,a}}^{p_{T,b}} \frac{\mathrm{d}\sigma_{\text{NLO pQCD}}}{\mathrm{d}p_T}\Big|_{\mu=p_T}\mathrm{d}p_T} \quad . \tag{6.29}$$

The integrated theory cross sections were computed for this work by W. Vogelsang [37]. Figure 6.22b shows the ratio of the measured cross sections and the pQCD results, including the scale uncertainty band. It is clearly visible that the central pQCD result ($\mu = p_T$) underpredicts the experimental cross section for $p_T \gtrsim 1.75\,\text{GeV}/c$ by a factor of three to four, but is following the spectral shape remarkably well. For $p_T \lesssim 1.75\,\text{GeV}/c$ the pQCD results should be discussed and interpreted very cautiously, because the factorization of the cross section is expected to break down eventually when going to small $p_T$ values. The pQCD calculation at NLO appears to be insufficient to accurately describe the quasi-real photoproduction of high-$p_T$ hadrons in muon-deuteron scattering at $\sqrt{s} = 17.4\,\text{GeV}$. Besides the difference in normalization, the very large scale uncertainty of the cross section shows that the application of fixed-order NLO pQCD to the high-$p_T$ hadron production at the COMPASS center-of-mass energy is a delicate matter.

It can be argued that the choice of the scale $\mu = p_T/2$ is really too low for the process under consideration [37]. The $p_T$ of the hadron is only a fraction $z_c$ of the transverse momentum of the fragmenting parton. Choosing $\langle z_c \rangle = 0.5$, the quoted scale uncertainty band $2p_T \geq \mu \geq p_T/2$ corresponds to $\hat{p}_{T,c} \geq \mu \geq \hat{p}_{T,c}/4$ on the parton level. It might be more appropriate to define the scale uncertainty band as $4p_T \geq \mu \geq p_T$ on the hadron level. This would reduce the scale uncertainty and accentuate the fact that the NLO pQCD calculations underpredict the experimental data.

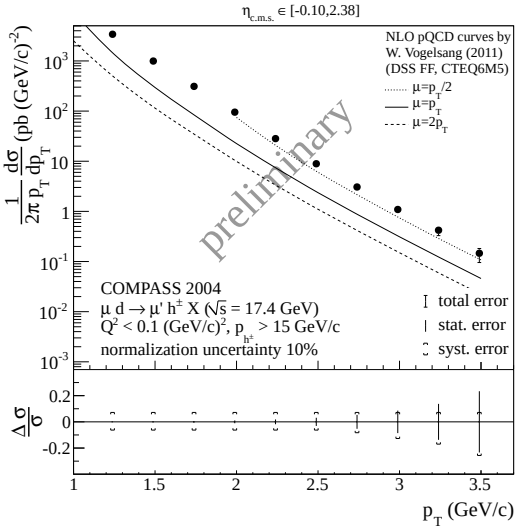


**(a)** Cross section integrated over $\eta_{\text{c.m.s.}}$.

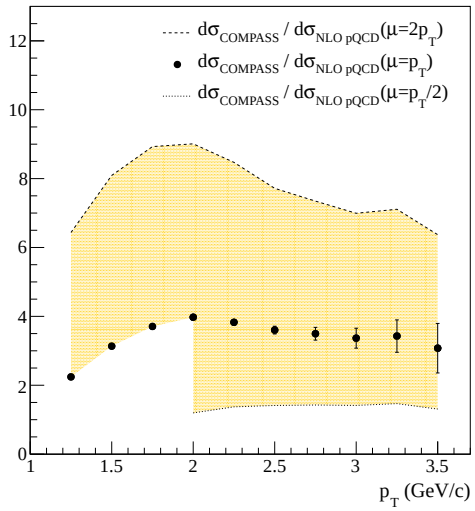


**(b)** Ratio of measured cross section (stat. errors only) and NLO pQCD cross section.

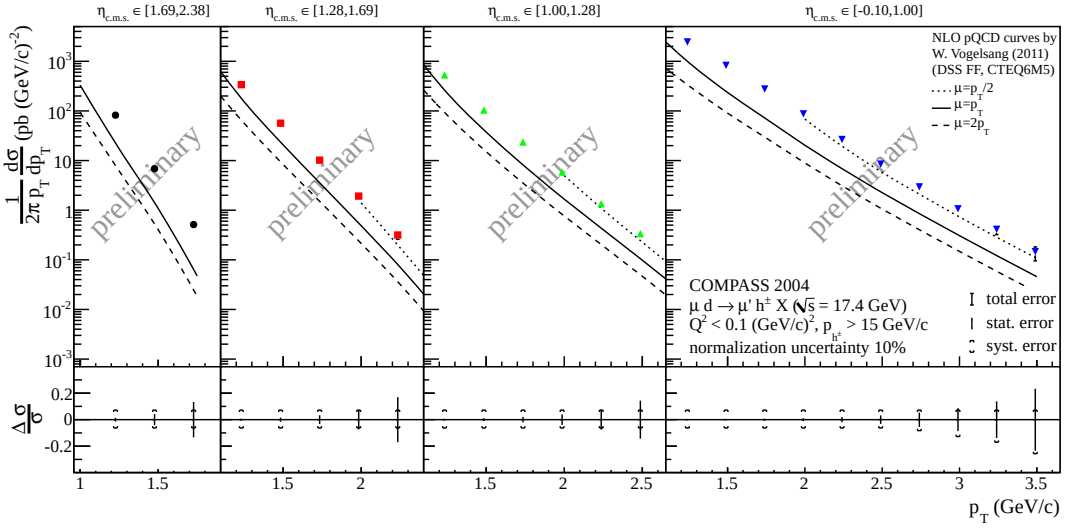


**(c)** Cross section binned in $\eta_{\text{c.m.s.}}$

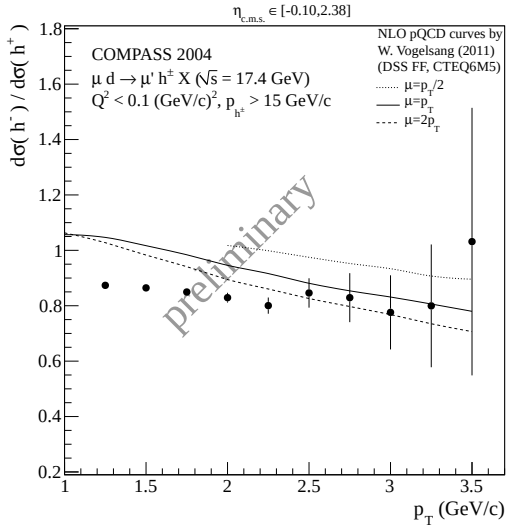


**(d)** Charge ratio of cross section integrated over $\eta_{\text{c.m.s.}}$.

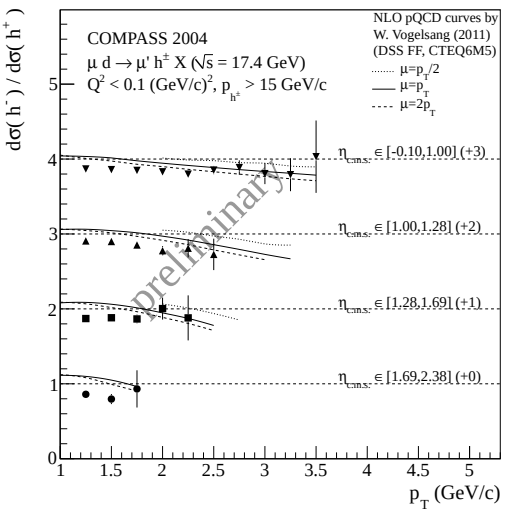


**(e)** Charge ratio of cross section binned in $\eta_{\text{c.m.s.}}$. Please note that the graphs are offset by constants, as indicated on the right (dashed lines indicate ratios of one).

**Figure 6.22:** Cross section for charged-hadron production at high $p_T$ in muon-deuteron scattering at low $Q^2$ in comparison to NLO pQCD calculations.

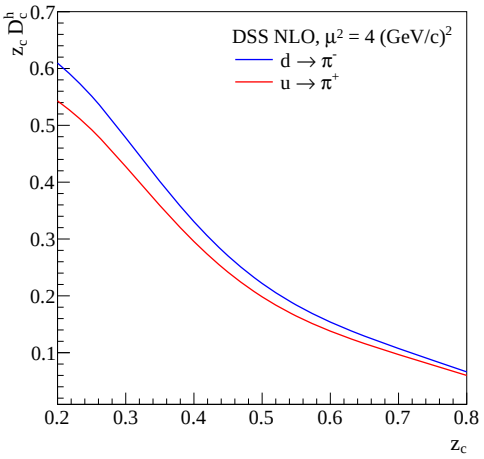


**Figure 6.23:** Comparison of fragmentation functions from the DSS [107, 108] set (data from Ref. [109]).

Figure 6.22c shows the comparison between the COMPASS measurement and the theory curves of the cross section in pseudo-rapidity bins. The different spectral slopes of the cross sections in the pseudo-rapidity bins are described well by the theory curves, and the normalization difference between the theory curves ($\mu = p_T$) and the experimental values is the same as in the rapidity-integrated case.
Figures 6.22d and 6.22e present the comparison of the pQCD predictions and the measured values of the ratio of the cross sections for the production of negatively charged hadrons over positively charged hadrons. The pQCD calculations predict that more negatively charged hadrons than positively charged hadrons should be produced at $p_T$ values below $\sim 1.5\,\mathrm{GeV}/c$ and that the charge ratio should decrease with increasing $p_T$. This is in clear disagreement to the experimental result that the charge ratio is less than one and constant over the probed $p_T$ range. It appears as if there could be some unphysical input to the pQCD calculations that causes this problem. The problem could be related to a surprising feature of the DSS fragmentation functions that would qualitatively explain an excess of negatively charged hadrons. Figure 6.23 shows the fragmentation functions for producing a $\pi^+$ meson in the fragmentation of a $u$ quark, and for producing a $\pi^-$ meson in the fragmentation of a $d$ quark (at the momentum scale $\mu = 2\,\mathrm{GeV}/c$). The plot shows that the probability for the fragmentation $d \to \pi^-$ is about $10 - 15\%$ higher than the probability for the fragmentation $u \to \pi^+$ (independent of $z_c$) in the DSS set, which constitutes a sizable violation of isospin symmetry. The presented measurement of the charge ratio for high-$p_T$ hadron production might be able to constrain such features of the fragmentation functions. The discussed feature of the DSS fragmentation functions does not, however, explain why the charge ratio should depend on $p_T$.

### Description of Quasi-Real Photoproduction - $Q^2_{\mathrm{max}}$ Dependence

The treatment of the quasi-real photoproduction of high-$p_T$ hadrons in pQCD was explained in detail in chapter 3. It is based on regarding the muon beam as a source of quasi-real photons whose

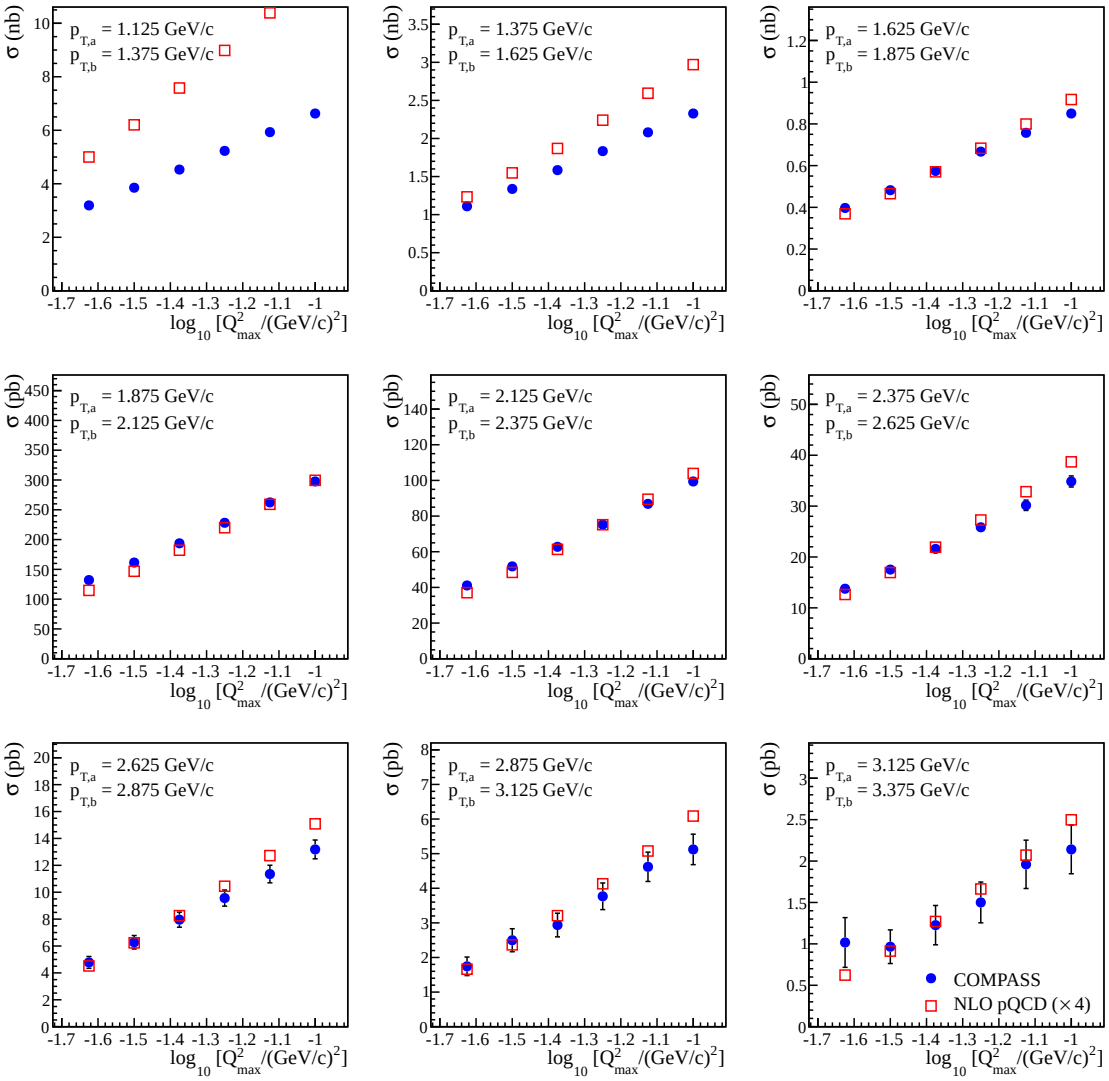


**Figure 6.24:** Comparison of the $Q^2_{\text{max}}$ dependence of the COMPASS and the NLO pQCD cross sections in $p_T$ bins. The theory cross sections have been computed for this work by W. Vogelsang [37] and are scaled up by an arbitrary factor of four to allow a better comparison of the $Q^2_{\text{max}}$ slopes. The error bars of the COMPASS data points are purely statistical.

energy spectrum is defined by the Weizsäcker-William formalism. The photons in this spectrum have a small, but non-zero virtuality which is completely neglected in the calculation. The realism of this procedure can be tested to some extent by comparing the dependence of the cross section on $Q^2_{\text{max}}$. For this purpose the NLO pQCD cross section ($\mu = p_T$) is scaled up by an arbitrary factor of four, which for $p_T \gtrsim 1.75\,\text{GeV}/c$ leads to a similar normalization of the cross sections and allows the simple comparison of the $Q^2_{\text{max}}$ dependence. This comparison is shown for nine $p_T$ bins in Fig. 6.24, where the two lowest bins with $p_T \leq 1.625\,\text{GeV}/c$ are ignored in the further discussion because the pQCD calculations might become problematic in this regime. Plotted are

the theoretical and experimental cross sections which are integrated over the bin widths:

$$\int_{p_{T,a}}^{p_{T,b}} \frac{\mathrm{d}\sigma}{\mathrm{d}p_T} \mathrm{d}p_T \quad .$$

Both cross sections depend on $Q^2_{\mathrm{max}}$ logarithmically, with very similar slopes, as expected from the unpolarized Weizsäcker-Williams equivalent photon spectrum of Eq. (3.13). This agreement provides some confidence in the correct treatment of the quasi-real photoproduction in the theory calculations.

**Dependence of the Underprediction by NLO pQCD on Photon Energy Fraction $y$**

The underprediction of the cross section by the NLO pQCD calculations by a factor of three to four is very similar to the case of the high-$p_T$ hadron production cross section in proton-proton collisions at fixed-target energies. As discussed in detail in Sec. 3.4, the all-order *resummation* of large logarithmic pQCD corrections, which are due to the emission of soft gluons, enhance the hadron production cross section in proton-proton scattering to a level of good agreement with the experimental data [42] and they also reduce the scale uncertainty. For the process of quasi-real photoproduction, such calculations are not yet available. The corrections should become largest when the center-of-mass energy of the partons $a$ and $b$, $\sqrt{\hat{s}} = \sqrt{(p_a + p_b)^2}$, participating in the hard scattering is close to the threshold for producing the parton $c$ with the transverse momentum $p_T/z_c$ at $\eta_{\mathrm{c.m.s.}}$. When observing hadrons at fixed $p_T$ and $\eta_{\mathrm{c.m.s.}}$, the size of the corrections increases with decreasing $\sqrt{\hat{s}}$. The partonic center-of-mass energy is related to the muon-deuteron center-of-mass energy as (see Eq. (3.17)):

$$\sqrt{\hat{s}} \approx \sqrt{y x_\gamma x_b}\, \sqrt{s_{lN}} \quad , \tag{6.30}$$

where $\sqrt{s_{lN}} = 17.4\,\mathrm{GeV}$. The corrections of the cross section due to the all-order resummation of large logarithms could hence be expected to increase with decreasing $y$.
Figure 6.25 presents the ratio of the COMPASS measurement and the *fixed-order* NLO pQCD calculation ($\mu = p_T$) of the double differential cross section $[\mathrm{d}^2\sigma/(\mathrm{d}p_T\mathrm{d}y)]$ in nine $p_T$ bins integrated over the $p_T$ bin widths:

$$\int_{p_{T,a}}^{p_{T,b}} \frac{\mathrm{d}^2\sigma}{\mathrm{d}p_T\mathrm{d}y} \mathrm{d}p_T \quad .$$

The cross-section ratio clearly increases with decreasing $y$, meaning that the underprediction of the cross section by NLO pQCD increases with decreasing $y$.
Once the resummed pQCD calculations for the quasi-real photoproduction process will be available, it will of course be checked whether they cure the underprediction of the $y$-integrated cross section, shown in Fig. 6.22b, just as in the case of proton-proton scattering. In addition, it will be very interesting to check whether the clear $y$-dependence in the comparison of the double-differential cross sections $[\mathrm{d}^2\sigma/(\mathrm{d}p_T\mathrm{d}y)]$ will be cured by the all-order resummations. Hopefully, all of this will make it possible to conclude whether the quasi-real photoproduction of high-$p_T$

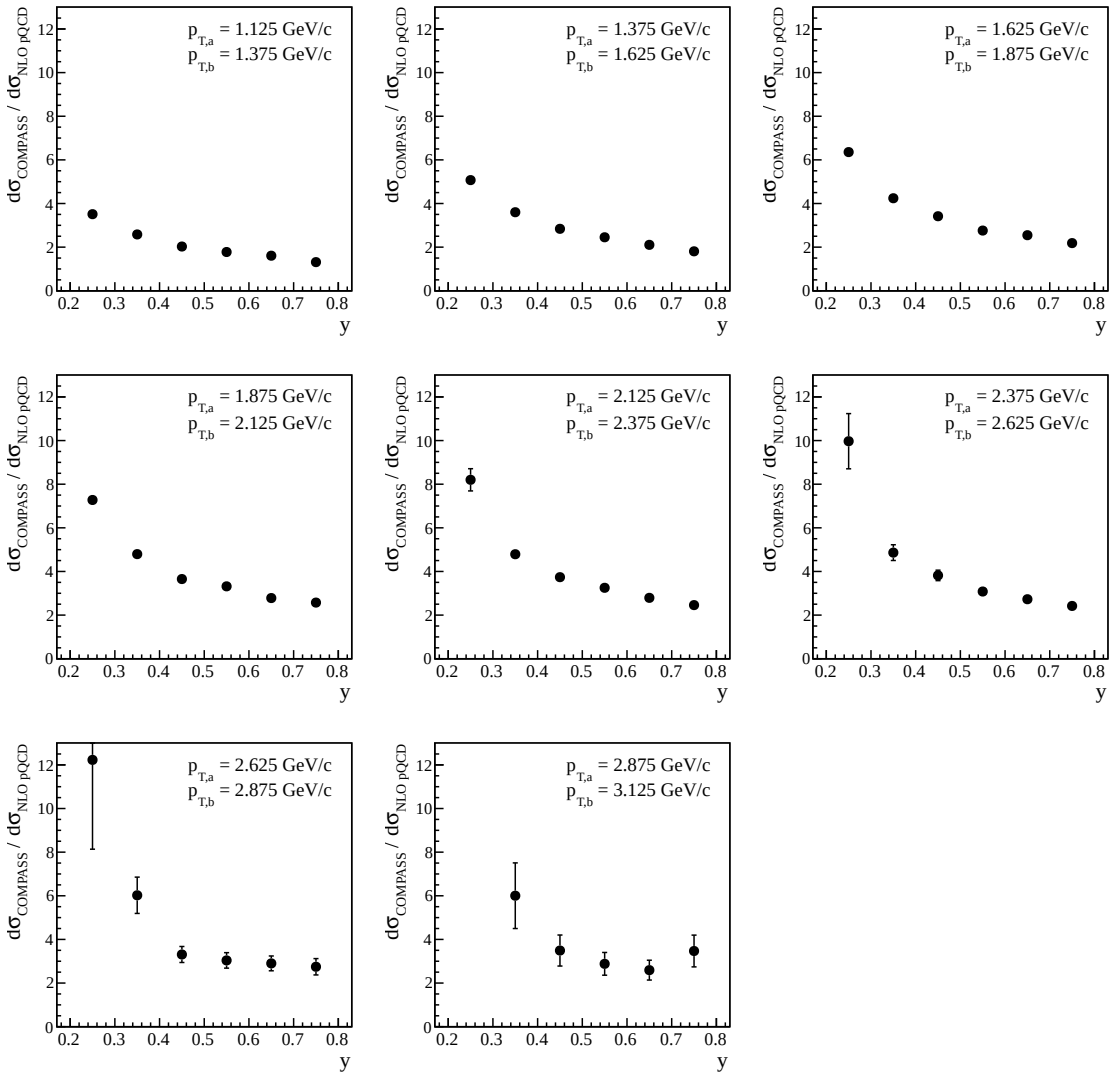


**Figure 6.25:** Ratio of the $y$-dependent cross section measured in COMPASS and calculated with NLO pQCD in $p_T$ bins. The theory cross sections have been computed for this work by W. Vogelsang [37]. The underprediction of the cross section by NLO pQCD is clearly $y$-dependent. The error bars of the COMPASS data points are purely statistical.

hadrons in muon-deuteron scattering is in the hard-scattering regime which can be described by pQCD, at least with the all-order resummation of threshold logarithms. The correct description of the spectral shape of the cross section by the NLO calculations is a very positive hint in this direction.

The first part of this dissertation (chapters 2 through 6) presented the measurement of the cross section for high-$p_T$ hadron production in COMPASS and its theoretical and experimental background. The second part, which begins with the next chapter, is devoted to the development of new technologies for charged-particle tracking in high-rate experiments. The developments were started in the framework of the future $\overline{\text{P}}$ANDA experiment, which is described in chapter 7. The development of a new type of TPC with GEM foils for gas amplification is presented in chapter 8. A novel, generic framework for track fitting in high energy physics experiments, called GENFIT, is introduced in chapter 9.

# Chapter 7

# The $\overline{\text{P}}$ANDA Experiment at FAIR

The Facility for Antiproton and Ion Research (FAIR) [110] will be an extension of the present site of the Gesellschaft für Schwerionenforschung (GSI) at Darmstadt, Germany. The recent signing of the international agreement on the joint construction of the facility by nine countries in October 2010 [111] has been a major milestone for the project. FAIR will host numerous experiments covering a wide field of topics in fundamental and applied research in hadronic physics, nuclear physics, plasma physics, and atomic physics, and is planned to go into operation in 2017.
A new proton and ion synchrotron (SIS100) will be the heart of the new facility. It will supply several production targets, separators, cooling rings, and storage rings to provide researchers with a large variety of antiproton and ion beams. A larger synchrotron (SIS300) is planned as a future extension of FAIR. The existing accelerator complex of GSI will be incorporated into the facility mostly for pre-acceleration.
$\overline{\text{P}}$ANDA (Anti-Proton ANnihilation at DArmstadt) [112] will be the main hadronic physics experiment at FAIR. It will investigate many aspects of the strong interaction in the non-perturbative regime, i.e. at large distances or low momentum transfers. The $\overline{\text{P}}$ANDA spectrometer shall provide near-$4\pi$ solid-angle coverage for charged-particle tracking with particle identification as well as for electromagnetic calorimetry. Together with a revolutionary data-acquisition concept, which is based on a trigger-less operation with continuous readout of all detectors and fully software-based event selection, it will allow exclusive measurements of a great variety of very rarely occurring final states on top of a very abundant QCD background. $\overline{\text{P}}$ANDA is an internal hydrogen-target experiment at the High Energy Storage Ring (HESR), which will provide continuous beams of antiprotons in the momentum range $1.5 - 15$ GeV/$c$ (center-of-mass energy $2.3 - 5.4$ GeV), cooled by stochastic as well as electron cooling.

## 7.1 Physics Program

This section briefly introduces selected topics of the $\overline{\text{P}}$ANDA physics program, which is described in detail in Ref. [113] including many detailed simulation studies.

**Precision Hadron Spectroscopy in the Charmonium Sector**

A meson which consists of a valence charm quark and a valence charm antiquark is called charmonium. Studying the mass spectrum of the charmonium states with different radial excitations, spin configurations, and orbital-angular-momentum excitations provides many insights into the intricate structure of the potential of the strong interaction at different distance scales. The spectroscopy of charmonia has major advantages over the spectroscopy in the light-meson sector: 1) The high mass of the charm quarks allow a non-relativistic treatment of QCD. 2) The spectrum in the charmonium mass range is much less populated because of the narrow widths of charmonium states, which leads to a much reduced mixing of states. There are eight charmonium states below the mass threshold for the decay into a pair of $D$ mesons and several states above the threshold, which are well established. Improved knowledge on the masses and widths of the known states as well as the measurement of yet unknown states in the charmonium spectrum will provide very valuable input for the further comprehension of the strong interaction in the non-perturbative regime.
The known charmonium states have mostly been studied in $e^+e^-$ collisions, in which only states with the spin-parity quantum numbers of the photon, $J^{PC} = 1^{--}$, can be formed directly. All other states need to be reached by particle decays. In this case, the resolution of the mass measurement of the states is limited by the detector resolution, which is often not sufficient for the very narrow widths of charmonium states. In $\bar{p}p$ (antiproton-proton) collisions on the other hand, all states in the charmonium spectrum can be formed directly when the center-of-mass energy of the beam-target system falls within the resonance of the state. The mass and width of a state can be measured by scanning the center-of-mass energy over the resonance region in small increments and by observing the cross section of a prominent decay channel. This way, the mass resolution is defined by the beam-momentum spread, which is very small, thanks to the techniques of stochastic and electron cooling employed in the HESR. This technique of center-of-mass energy scanning has been employed before by the $\bar{p}p$ experiment E835 at Fermilab which used a non-magnetic spectrometer (see e.g. [114]). The $\overline{\text{P}}$ANDA spectrometer is designed for the measurement of charged as well as neutral particles. The $\overline{\text{P}}$ANDA experiment should hence be able to measure the masses and widths of all states in the charmonium spectrum below and above the $D\bar{D}$ threshold with unprecedented accuracy.
As explained before in Sec. 4.1.2, QCD predicts the existence of color-neutral states other than ordinary mesons and baryons. Possible states include so-called *hybrid mesons*, which consist of a color-octet quark-antiquark pair that is color-neutralized by a valence gluon, and *glueballs*, which consist of just valence gluons in color-neutral configurations. The key to the detection of such states is that they can have *exotic* spin-parity quantum numbers, which are impossible to make up with a quark-antiquark pair (e.g. $0^{--}$, $0^{+-}$, $1^{-+}$, ...). In $\bar{p}p$ annihilation, exotic states can be produced in association with a recoiling meson. It is a simple signature for exotic quantum numbers if a state can be measured in associated production but does not appear in direct formation, when the center-of-mass energy is set to the resonance mass. With its uniform and large acceptance, the $\overline{\text{P}}$ANDA spectrometer should also be very adequate for the use of partial wave analyses (PWA, see Sec. 4.1.2) to determine the spin-parity quantum numbers of resonances. Lattice QCD calculations predict that there should be two glueball states with exotic quantum numbers in the mass range $4 - 5\,\text{GeV}/c^2$ with quantum numbers $J^{PC} = 0^{+-}$ and $J^{PC} = 2^{+-}$ [115]. There should also

be a number of charmed hybrids in the accessible mass range of $\overline{\text{P}}$ANDA.
The large number of so-called $XYZ$ states that has been detected over the past couple of years are of course also a prime application for $\overline{\text{P}}$ANDA. There are a lot of speculations as to the nature of these states. Some are believed to be $D\bar{D}$ molecules, others are interpreted as hadrocharmonium states which are intact charmonium states that are embedded in a shell of light-quark or gluonic matter, and yet others are believed to be charmed hybrids. For details on these highly interesting states please be referred to Ref. [116]. The $\overline{\text{P}}$ANDA experiment should be in a good position to shed light on many of these interesting speculations by acquiring high statistics samples of these states and by the determination of their quantum numbers.
For the complete spectroscopy program of $\overline{\text{P}}$ANDA it should, however, be clearly stated that it is not clear at this point how many of the discussed measurements will also be possible in other experiments before $\overline{\text{P}}$ANDA can begin to take data in 2017, such as the LHC experiments or the future BELLE-II facility, which will go into operation in 2015 and is designed to run at luminosities which are orders of magnitude higher than in BELLE.

### Nucleon Structure

Any process that can be measured in electron-proton or muon-proton scattering to investigate the structure of protons that leaves the protons intact can be measured in crossed kinematics in $\bar{p}p$ annihilations at $\overline{\text{P}}$ANDA. The space-like form factors of the proton are measured in elastic lepton-proton scattering, which is shown in Fig. 7.1. The squared 4-momentum transfer of the reaction is space-like $q^2 < 0$. The Sachs form factors $G_E$ and $G_M$ are real-valued functions that in the Breit frame[1] can be interpreted as the Fourier transforms of the charge and current distributions of the proton, respectively. The time-like form factors are complex valued functions whose moduli can be measured in the crossed channel $p\bar{p} \rightarrow l^+l^-$ ($l = e, \mu$) in $\overline{\text{P}}$ANDA, which is depicted in Fig. 7.2. The squared time-like 4-momentum transfer $q^2 > 0$ of the reaction is equal to the squared center-of-mass energy of the proton-antiproton system, $q^2 = s_{\bar{p}p}/c^2$. The cross section has the form [117]:

$$\frac{\mathrm{d}\sigma(p\bar{p} \rightarrow l^+l^-)}{\mathrm{d}\Omega} \propto |G_M|^2 \left(1 + \cos^2 \vartheta_{\text{c.m.s.}}\right) + \frac{4M^2c^2}{q^2}|G_E|^2 \sin^2 \vartheta_{\text{c.m.s.}} \quad , \tag{7.1}$$

where $\vartheta_{\text{c.m.s.}}$ is the production angle of the lepton pair in the center-of-mass system, and $M$ is the proton mass. Previous measurements in the proton-antiproton channel have been performed by the PS170 [117] and E835 [118] experiments. The time-like form factors can also be measured in the time-reversed reaction $e^+e^- \rightarrow p\bar{p}\gamma$, where a real photon, $\gamma$, is emitted as initial state radiation (ISR) before the annihilation. The energy of the ISR photon determines the center-of-mass energy of the annihilation of the $e^+e^-$ pair and hence the time-like $q^2$. This allows the measurement over a wide range of $q^2$ without actually changing the beam energies. This technique has been employed in the BABAR experiment for a measurement of $|G_M|$ over a large range of $q^2$ [119] from the threshold $4M^2c^2$ up to almost $20\,(\text{GeV}/c)^2$. The $\overline{\text{P}}$ANDA experiment will be able to measure the cross section (7.1) over an even larger range ($s_{\bar{p}p,\,\text{max}} = 29\,\text{GeV}^2$) with much higher statistics,

[1] the Breit frame is defined as the reference frame in which the exchange photon carries no energy. In the Breit frame the 4-momentum transfer and the 3-momentum transfer are identical.

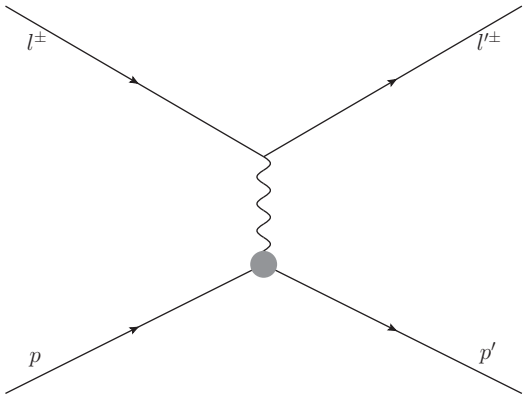


**Figure 7.1:** Elastic electron-proton scattering to investigate the space-like form factors of the proton.

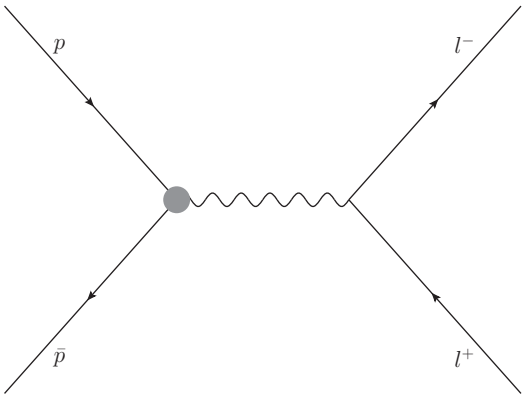


**Figure 7.2:** $\bar{p}p$ annihilation into $l^+l^-$ to investigate the time-like form factors of the proton.

because the requirement of ISR emission in $e^+e^- \rightarrow p\bar{p}\gamma$ reduces the available effective luminosity by a factor of $\mathcal{O}(\alpha_{\text{em}}^2)$. The $\overline{\text{P}}$ANDA measurement will allow the independent determination of $|G_M|$ and $|G_E|$ by analyzing the $\vartheta_{\text{c.m.s.}}$ distributions at each $q^2$ value (Rosenbluth-type separation). This separation has previously been attempted by PS170 and BABAR, but the limited statistics did not allow for an accuracy of the ratio $|G_E|/|G_M|$ better than $25-50\%$, whereas the planned $\overline{\text{P}}$ANDA measurement will yield an accuracy at the percent level [113].

Two other very important lepton-proton scattering processes which leave behind an intact final-state proton are Deeply Virtual Compton Scattering (DVCS, see Fig. 4.3) and Deeply Virtual Meson Production (DVMP), which have been described in Sec. 4.1.3 on the future physics program of COMPASS-II. These processes can be used to access the Generalized Parton Distributions (GPDs) of the proton. In the $\overline{\text{P}}$ANDA experiment, the crossed channels to DVCS, namely Wide Angle Compton Scattering (WACS) which is illustrated in Fig. 7.3, and the cross channel to DVMP can be measured. The GPDs are replaced by Generalized Distribution Amplitudes (GDAs) [120] in this process. It should however be mentioned that the factorization of the cross section of this process has yet to be proven theoretically.

Another very important process to access the proton structure in $\overline{\text{P}}$ANDA is the Drell-Yan process (see Fig. 4.4). It describes the annihilation of a quark and an antiquark into an $e^+e^-$ or $\mu^+\mu^-$ pair. The Drell-Yan process can be used to measure some of the Transverse Momentum Dependent parton distributions (TMDs) of the proton. This has been described in Sec. 4.1.3 on COMPASS-II as well. The main advantage of $\overline{\text{P}}$ANDA over COMPASS-II, which uses a pion beam instead of an antiproton beam, is that the TMDs of the valence antiquarks of the antiprotons are identical to the valance quark TMDs of the target protons. At first, $\overline{\text{P}}$ANDA will run without any polarizations of beam or target. In this configuration, only the Boer-Mulders function can be accessed, which describes the correlation of the intrinsic transverse momentum and the transverse spin of a quark in an unpolarized proton. At a later stage, $\overline{\text{P}}$ANDA might be equipped with transversely polarized targets. This would require a counter-solenoid surrounding the target region to neutralize the magnetic field of the target spectrometer, which would have to be as thin as possible to not spoil the momentum resolution of the measurement of the produced lepton pairs. With single polarization,

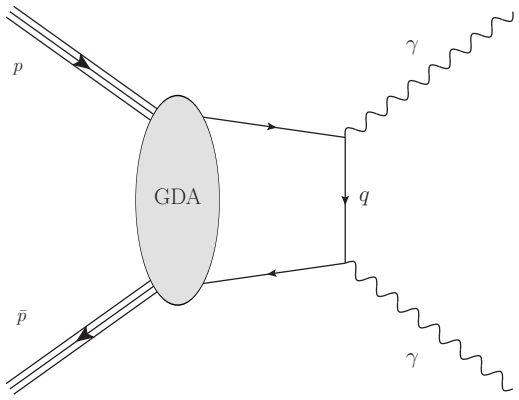


**Figure 7.3:** Wide Angle Compton Scattering (WACS), which is the crossed channel of DVCS.

the Sivers function, which describes the correlation between the transverse proton spin and the intrinsic transverse momentum of the quarks, and the transversity function, which describes the probability to find a transversely polarized quark in a transversely polarized nucleon where the intrinsic transverse momentum of the quarks is integrated over, could be accessed in addition to the Boer-Mulders function.

#### Other Topics

The physics program of $\overline{\text{P}}$ANDA covers more subjects which are not described in detail here, such as the investigation of $\Lambda\bar{\Lambda}$ production, in-medium modifications of the masses and widths of $D$ mesons, CP-violation in the $D$-meson sector, and the study of rare decays of $D$ mesons for the search of physics beyond the standard model. With a slightly modified setup, including an array of Germanium $\gamma$ detectors and an active nuclear target, $\overline{\text{P}}$ANDA will be able to carry out spectroscopy experiments of hypernuclei. For more details on these subjects, please be referred to Ref. [113].

## 7.2 The $\overline{\text{P}}$ANDA Spectrometer

The planned $\overline{\text{P}}$ANDA experiment consists of a 2 T solenoid spectrometer surrounding the interaction region and a 2 Tm dipole spectrometer in the forward region, together yielding a near-4$\pi$ solid-angle coverage for the measurement of the momenta of charged particles. The charged-particle tracking system is supplemented with particle identification measurements over a wide momentum range and electromagnetic calorimetry. A schematic view of the spectrometer is shown in Fig. 7.4.

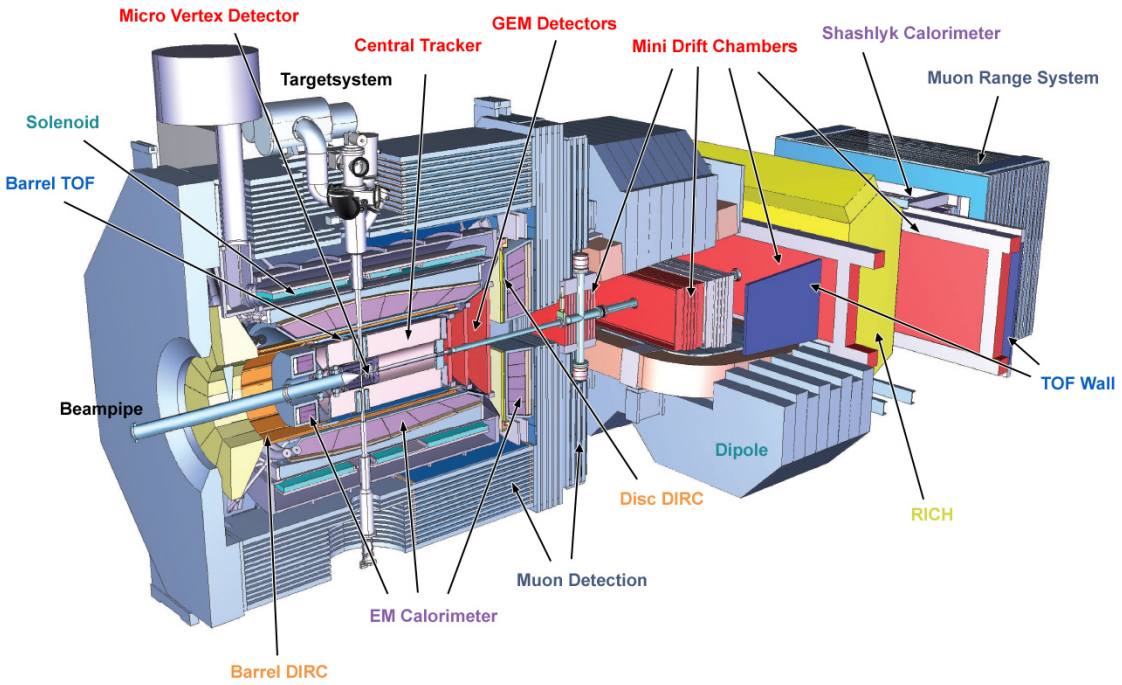


**Figure 7.4:** Schematic view of the $\overline{\text{P}}$ANDA spectrometer, which has an overall length of $\sim 12\,\text{m}$.

### Interaction Region

The HESR will deliver a continuous beam of antiprotons in the momentum range $1.5 - 15\,\text{GeV}/c$, which is cooled by stochastic and electron cooling. The beam has a time structure of active cycles of $2\,\mu\text{s}$ interrupted by 400 ns breaks. The design luminosity of $\overline{\text{P}}$ANDA is $2 \cdot 10^{32}\,\text{cm}^{-2}\text{s}^{-1}$ with a momentum spread $\sigma_p/p \approx 10^{-4}$ in a high-intensity mode, whereas a high-resolution mode shall yield a luminosity of $2 \cdot 10^{31}\,\text{cm}^{-2}\text{s}^{-1}$ with a reduced momentum spread of just $\sigma_p/p \approx 4 \cdot 10^{-5}$. The beam preparation times range from 120 s to 290 s [121] and are factored into the average luminosity considerations. The envisaged luminosity values are based on an assumed target density of $4 \cdot 10^{15}\,\text{atoms/cm}^2$, which is a very challenging goal.
Two different hydrogen-target systems are foreseen for $\overline{\text{P}}$ANDA. The first option is a cluster-jet target, in which hydrogen clusters are formed by a complex nozzle and collimator system and shot through the beam via a target pipe, which crosses the target spectrometer vertically. Compared to previous applications, e.g. at the ANKE experiment at the COSY storage ring at Forschungszentrum Jülich, the distance between the nozzle system and the interaction point $d$ is quite large at $\overline{\text{P}}$ANDA ($\sim 2\,\text{m}$), which makes the use of a cluster-jet target challenging as the density decreases like $d^{-2}$ [122]. Hard numbers on the achievable target densities are difficult to project but still seem to be about a factor of five lower than the envisaged $4 \cdot 10^{15}\,\text{atoms/cm}^2$. The adjustable target density that can counter-balance the beam intensity which decreases over time in a storage ring to achieve a constant luminosity is a virtue of this technology. The cluster-jet target could serve as a safe starting point for the operation of $\overline{\text{P}}$ANDA.
The second option is a hydrogen-pellet target, in which frozen pellets of hydrogen are shot through

the beam with velocities of $\sim 60\,\text{ms}^{-1}$. The pellet frequency is foreseen to be in the range 15-150 kHz and the pellet size shall be in the order of $20\,\mu$m. The density of hydrogen pellets is of course higher than those of the hydrogen cluster jet, but the average distance between clusters of a few millimeters leads to a reduced average density and additionally introduces a non-uniform time structure of the luminosity, which can be challenging for the detectors. The average density values which can currently be achieved seem to be of the same order as for the cluster-jet target. Significant improvements are still required from new research and development in order for $\overline{\text{P}}$ANDA to reach its design luminosity.
Heavier gases such as deuterium, nitrogen, or argon will also be available for experiments with nuclear targets. The use of metal-wire target is also under consideration in $\overline{\text{P}}$ANDA.

### Target Spectrometer

The magnet of the target spectrometer is a superconducting solenoid coil with an inner radius of 105 cm and a length of 2.8 m [123]. Such technologies have been successfully employed by many experiments, like ALEPH, BABAR, and many others. The magnet shall provide a highly uniform solenoid field of 2 T with deviations along the $z$-direction of $\lesssim 2\%$ and a normalized radial field integral $\int B_R/B_z\,\text{d}z < 2\,\text{mm}$.
The interaction region is directly surrounded by the Micro Vertex Detector (MVD) [124], which is a combined silicon-microstrip / silicon-pixel detector. The precise determination of the positions of the primary interaction vertices is very important for a good invariant-mass resolution. The second very important task of the MVD is the efficient reconstruction of displaced vertices of $D$-meson decays. The clear identification of $D$ mesons is of utmost importance for the complete spectroscopy program of $\overline{\text{P}}$ANDA as well as for the other physics topics involving $D$ mesons. The MVD consists of four cylindrical barrel layers, which are oriented parallel to the beam direction and reach from radii of 2.5 cm to 13 cm. The two innermost layers consist of silicon-pixel detectors, to cope with the highest hit rates, whereas the outer layers are double-sided silicon-microstrip detectors. Additionally, the MVD features six detector disks which are mounted perpendicular to the beam direction in the forward region. The four most upstream disks, which are closest to the interaction point, are equipped with pixel readout, followed by two disks with a mix of pixel readout at small distances to the beam axis and strip readout at larger distances. The pixel size is $100 \times 100\,\mu\text{m}^2$ and the strip pitch is $130\,\mu$m in the barrel layers and $67.5\,\mu$m in the forward disks. The wafer thicknesses is $100\,\mu$m for the pixel wafers and $200\,\mu$m for the strip wafers. The overall material budget of the MVD is in the order of 10% to 20% of a radiation length in most of the acceptance of $\overline{\text{P}}$ANDA (polar angle $< 140^\circ$) including cabling and supports. Overall, the MVD has $2 \cdot 10^5$ electronic channels for the readout of the strip detectors and $1.1 \cdot 10^7$ electronic channels for the readout of pixel detectors.
The MVD is surrounded by a cylindrical central tracking detector, for which two options are being considered: A novel, continuously-running Time Projection Chamber (TPC) with a Gas Electron Multiplier (GEM) readout or a more traditional Straw Tube Tracker that consists of $\sim 5000$ single-wire proportional tubes[2]. The development of the GEM-based TPC is discussed in detail in the

[2]The Straw Tube Tracker was chosen as the central tracking detector in September 2011 by the $\overline{\text{P}}$ANDA Collaboration Board.

next chapter. The dimensions of this detector are $r \in [15, 42]$ cm in the radial direction and $z \in [-40, 110]$ cm in the beam direction, where the interaction point is located at $z = 0$. The momentum resolution of this detector is very important for the resolution of invariant-mass measurements in $\overline{\text{P}}$ANDA. The mass resolution of all states with exotic quantum numbers, whose masses and widths can not be determined with resonance scans of the center-of-mass energy, is dominated by the momentum resolution of this device. With the TPC option, standalone momentum resolutions of $\sigma_p/p = 1.5\%$ at $p = 0.4\,\text{GeV}/c$ and $\sigma_p/p = 6.5\%$ at $p = 2\,\text{GeV}/c$ have been achieved in realistic simulation studies (muons at 90° polar angle) [125]. Besides the momentum measurement, the central tracker is also responsible for the reconstruction of secondary decay vertices of $\Lambda$ baryons and $K^0_S$ mesons, which decay to a large fraction outside of the MVD. The third very important task of the central tracker is the particle identification in the momentum range up to $\sim 1$ GeV/$c$ via the measurement of the specific ionization of charged particles. The separation of pions and kaons in this momentum range is of vital importance for all physics channels involving charged kaons. A good example is the identification of the decay $\eta_c \to \phi\phi \to K^+K^-K^+K^-$ on top the prominent background process $\bar{p}p \to \pi^+\pi^-\pi^+\pi^-$. The measurement of the specific ionization in TPCs is a well-proven concept, while such a measurement with an array of single-wire proportional tubes is unusual. Another important requirement to the central tracker is a minimal material budget of the order of $1 - 2\%$ of a radiation length in order to not disturb the surrounding electromagnetic calorimetry.

The central tracker is surrounded by a DIRC (Detection of Internally Reflected Cherenkov light [126]) detector made from 1.7 cm thick slabs of fused silica. The DIRC provides particle identification for $p > 700\,\text{MeV}/c$ via a measurement of the Cherenkov angle. The forward endcap of the target spectrometer is equipped with a disk-shaped DIRC detector (acceptance $\theta \in [5°, 22°]$). The DIRC detector is surrounded by a time-of-flight detector which consists of tiles of plastic scintillator (dimensions $28.5 \times 28.5\,\text{mm}^2$), which are read out with silicon photo multipliers.

The electromagnetic calorimeter (EMC) of $\overline{\text{P}}$ANDA [127] is located between the time-of-flight system and the iron yoke of the magnet. It consists of more than 15000 PWO-II (lead-tungstate) crystals, which are 20 cm (22 radiation lengths) long. The EMC covers the full barrel of the target spectrometer as well as the forward and backward endcaps. The dynamic range of the EMC reaches from $\sim 10 - 20\,\text{MeV}$ to several GeV with an energy resolution of $\sim 2\%$ at 1 GeV. The very low energy threshold is important for the suppression of background processes. The main background channels for the processes like $p\bar{p} \to \eta_c \to \gamma\gamma$ or $p\bar{p} \to h_c \to \eta_c\gamma \to \gamma\gamma\gamma$ are final states where one of the isolated photons is replaced by a $\pi^0$ meson. If one of the photons from the $\pi^0$ decay is lost, the background will be misinterpreted as a signal event, especially because the event will still fulfill the exclusivity selection due to the small amount of lost energy. The cross sections for these background processes are expected to be orders of magnitude higher [127]. An energy threshold of 10 MeV in the EMC leads to a misidentification of $\sim 1\%$ of the $\pi^0$ mesons, whereas a threshold of 30 MeV would already lead to a misidentification on the 10% level.

Finally, the iron yoke as well as the forward-endcap iron door of the solenoid magnet are interspersed with tracking detectors for the positive identification of muons. This is very important for the clean measurement of muon pairs from $J/\psi$ decays, from Drell-Yan reactions, for the measurement of the electromagnetic form factors, and other processes on top of a very abundant background of charged pions from $p\bar{p}$ reactions. Since the endcap door does not provide enough hadronic interaction lengths of material to fully shield pions in this region of the phase space, ad-

ditional detector layers, sandwiched with iron plates, are located between the forward yoke door and the dipole magnet.

### Forward Spectrometer

The dipole magnet of the forward spectrometer is made from normal-conducting copper coils [123]. It is situated 3.9 m downstream of the interaction point and has a vertical acceptance of $\pm 5^\circ$ and a horizontal acceptance of $\pm 10^\circ$. The magnet has a length of 2.5 m and a bending power of 2 Tm.
The disk layers of the MVD are the first detectors of the forward spectrometer. They are followed by three stations of GEM (Gas Electron Multiplier [128]) detectors, which are located just downstream of the central tracker, still inside the barrel of the target spectrometer. Each station is equipped with two detectors with a double-strip readout, with a resolution below 100 $\mu$m. The outer diameters increase with the distance from the interaction point, and range between 90 cm and 148 cm. GEM trackers of such large dimensions have never been built, mainly because GEM foils of these sizes can currently not be manufactured. Several GEM foils will probably have to be stitched together for the construction of this detector, which is mechanically and electrically challenging. The forward tracking system continues with stations of drift chambers each of which consist of eight layers of straw tubes in different orientations. The first station is located upstream of the dipole magnet, the second one is located in the gap of the dipole magnet, and the final station is located downstream of the dipole magnet. The forward spectrometer is completed by a time-of-flight system, a Ring Imaging Cherenkov (RICH) detector for particle identification, and a Shashlyk calorimeter, consisting of sandwiched layers of lead and scintillator material.

### Data Acquisition System and Trigger Concept

The data acquisition (DAQ) concept of many modern high-energy physics experiments is based on a multi-level approach. In such systems, only the lowest-level trigger decision is based on signals from fast particle detectors (mostly scintillators or resistive plate chambers) which preselect scattering events with certain crude signatures. This triggers the readout of the frontend electronics of the detectors, which is followed by event building, meaning that all detector data belonging to the same lowest-level trigger are formatted into one data object called an *event*. Higher-level triggers, which are purely software-based can then be used to increase the purity of the event sample, i.e. the fraction of interesting events that are written to permanent storage. Typical data rates which are usually written to tape over long periods of time are in the order of a few hundred Megabytes per second.
The $\overline{P}$ANDA experiment shall be the first high-energy physics experiment to run without any traditional hardware trigger for the readout of the frontend electronics of the detectors. Each detector is equipped with a data-driven readout system with time tagging and zero suppression. Event building is performed for *all* scattering events that occur in the spectrometer. The selection of events for permanent storage is *fully* software-based. This allows for the maximal flexibility which is called for in $\overline{P}$ANDA, because it is the goal of the experiment to efficiently detect a very large number of topologically different final states on top of a very abundant hadronic background. Please note that

the total $p\bar{p}$ cross section is as large as 100 mb (at an antiproton momentum of 1.5 GeV/$c$), while a lot of the signal cross sections are in the order of nanobarns. The data rate which is written to tape is of the same order as in other modern experiments. Crossing the frontier from a trigger-based to a triggerless operation can be regarded as the next logical step in the evolution of high-energy physics experiments. In this respect, $\overline{\text{P}}$ANDA is really a pioneering project.
The triggerless, continuous operation of $\overline{\text{P}}$ANDA inspired a novel design for a TPC which is operated without a traditional ion gate. This becomes possible by the use of GEM foils for gas amplification, in which the backflow of ions from the amplification to the drift volume is strongly suppressed. The design of a GEM-based TPC is presented in the next chapter.

# Chapter 8

# Development of a GEM-TPC

A Time Projection Chamber (TPC [131]) can be regarded as the ideal device for the measurement of the momenta of charged particles. When particles cross the gas volume of the detector they leave behind clusters of electron-ion pairs. In the classical setup, a TPC is aligned with a solenoidal magnetic field in which particles of different momenta describe helices with different radii. A highly uniform electrical field is applied across the gas volume of the TPC parallel to the magnetic field to make the electrons drift onto one of the end plates of the detector, where they are multiplied by a gas-amplification stage. The position and the arrival time of the cluster are electronically acquired with a highly segmented readout system. The three-dimensional positions of the ionization clusters are reconstructed by combining the two-dimensional positions of the clusters on the readout plane with the drift distance which is inferred from the drift time and the drift velocity. During the drift, the electrons diffuse in the transversal and longitudinal directions, where the transverse diffusion is strongly reduced by the magnetic field. Up to several space points per centimeter of track length can be reconstructed this way. Since the detector consists only of the active gas volume (besides the detector walls of course), the multiple scattering between the measured points is minimal and the momentum resolution is hence optimal. TPCs have been built with diameters and drift lengths up to a few meters. In addition to the momentum measurement, the specific ionization of particles, $\mathrm{d}E/\mathrm{d}x$, can be measured with an accuracy of a few percent (depending on the length of the tracks in the gas volume), which allows the measurement of the particle velocity $\beta = v/c$. Together with the momentum measurement this makes it possible to identify particles in the momentum range below $\sim 1\,\mathrm{GeV}/c$, most importantly to separate pions from kaons and kaons from protons.
A TPC has been considered as the central tracker of the $\overline{\mathrm{P}}$ANDA experiment. The requirements to the central tracker of $\overline{\mathrm{P}}$ANDA are:

- Length: 150 cm, inner diameter: 30 cm, and outer diameter 84 cm,
- overall material budget of $1 - 2\%$ of a radiation length,
- $\mathrm{d}E/\mathrm{d}x$ resolution in the range $5 - 10\%$, and
- a continuous, unpulsed operation.

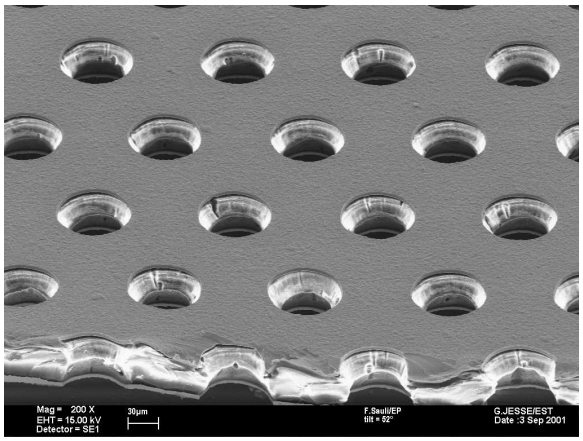


**Figure 8.1:** Electron-microscope picture of a GEM foil (taken from Ref. [129]).

The requirement of the continuous operation is out of the ordinary for TPC detectors. In the usual configuration with a plane of proportional wires for gas amplification, TPCs have to be operated with very large dead times in between event triggers. The proportional wires are usually operated at gains of several $10^4$, which means that for each incoming electron several $10^4$ ions are created. These ions need to be blocked from drifting back into the active gas volume of the detector by an *ion gate*. During one full electron drift time in the TPC of typically $50 - 100\,\mu$s, the ions travel distances of the order of a few millimeters. A grid of gating wires, which is located at this distance from the amplification wires, is used to evacuate the ions from the chamber by applying a certain voltage to the gating grid after all primary electrons have drifted to the amplification stage. The time needed to switch the potential of the gating grid and to evacuate the ions leads to the very large dead time. This disallows the use of TPCs in experiments with trigger rates beyond $\sim 1\,$kHz, which is a tremendous limitation for this otherwise very powerful particle detector. The suppression of the ion backflow from the amplification is the key to overcome this limitation, which is realized by replacing the proportional wires with GEM foils (Gas Electron Multiplier [128]).
A GEM is a typically $50\,\mu$m thin polyimide foil which is clad on both sides with $2 - 5\,\mu$m of copper. Holes with a diameter of $70\,\mu$m are etched into the foil in a hexagonal pattern in distances of $140\,\mu$m. An electron microscope picture of the surface of a GEM foil is shown in Fig. 8.1. When a voltage of $300 - 400\,$V is applied across the GEM foil, a very large field of the order of $50\,$kV/cm is created in the microscopic holes, which is high enough for avalanche amplification. Typically, three GEM foils are stacked which results in an effective gain of $\sim 10^4$ and allows a very stable operation of the detector. The COMPASS experiment has been the first large scale application of GEM detectors for particle tracking [78], which are nowadays used in many high-energy physics experiments, like LHCb [132], PHENIX [133], or TOTEM [134].
The backflow of ions from the avalanche amplification is strongly suppressed if the electric fields above and below the GEM are asymmetric, which is illustrated and explained in Fig. 8.2. A typical value for the drift field of a TPC (above the top-most GEM) is $400\,$V/cm, and typical transfer fields between GEMs (below the top-most GEM) are of the order of $\sim 4\,$kV/cm. The suppression of the ion backflow is, however, not perfect (as indicated in Fig. 8.2b – label "Backdrifting ion"). The magnitude of the remaining ion backflow depends on the exact high-voltage settings of the

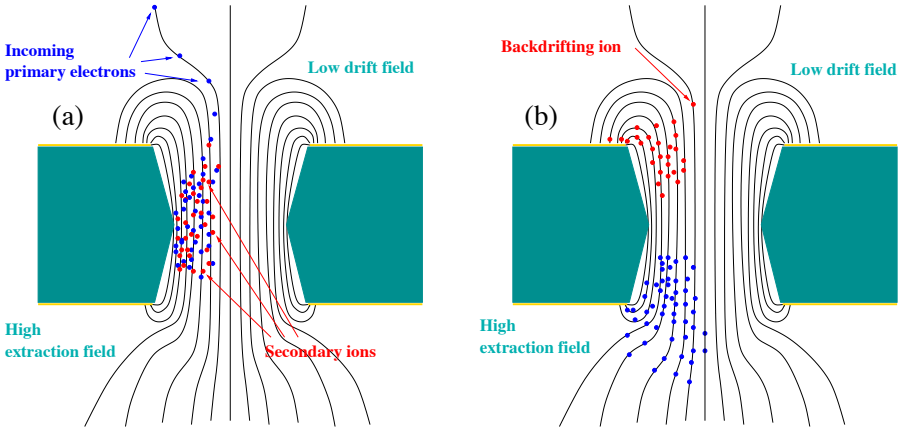


**Figure 8.2:** Suppression of the ion backflow from the avalanche amplification in a GEM with asymmetric electric fields above and below the GEM (taken from Ref. [130]). (a) shows the collection of the primary electrons and the creation of the charge avalanche in the region of the highest field, near the edges of the GEM holes, and (b) shows that while the electrons are rather efficiently extracted along the field lines at the bottom of the GEM, the ion drift lines mostly end on top of the GEM. The effect is further enhanced by the higher transverse diffusion of the electrons.

detector. Previous studies in the context of the development of a GEM-based TPC for the International Linear Collider project [135] have identified high-voltage settings which are optimized for a low ion backflow [136]. At a magnetic field of 2 T and a gain of 2000, which are the foreseen operational parameters for the $\overline{\text{P}}$ANDA experiment, they lead to a backflow of $4 - 6$ ions per incoming electron. At least without magnetic fields (which results in a higher ion backflow), these results have been reproduced in the framework of the $\overline{\text{P}}$ANDA GEM-TPC project [137]. The main finding of these studies is that a low transfer field $\mathcal{O}(100\,\text{V/cm})$ between the middle GEM and the bottom-most GEM and high fields between top-most GEM and middle GEM as well as between the bottom-most GEM and the readout plane $\mathcal{O}(5\,\text{kV/cm})$ significantly reduce the ion backflow.
In a triple-GEM based detector there are seven high-voltage potentials that have to be adjusted: The potential of the drift cathode and the two potentials on each GEM foil define the values of the drift field, the individual gains of the GEM foils, the transfer fields between the GEMs, and the induction field below the bottom-most GEM. An optimization of these high-voltage settings is one of the most important aspects of the development of a GEM-TPC for high-rate experiments. The ideal high-voltage settings for a GEM-TPC must be a compromise between several conflicting interests. While a very high gain in the top-most GEM is for instance optimal for the energy resolution of the detector, a lower gain in the top-most GEM is certainly desirable for the minimization of the ion backflow. While a very high gain in the bottom-most GEM is optimal for the ion backflow minimization, it might be problematic for the stability of the detector with respect to discharges.
The optimization of the high-voltage setting can be performed with experiments in which a triple-GEM detector is exposed to a high flux of radiation from a copper X-ray tube. The currents on all HV electrodes of the detector and on the readout plane are measured with current meters. The cur-

rent values are defined by the added rates of electrons and ions arriving at the several electrodes. The development of a new type of current meter with wireless readout for such experiments is presented in the next section.

## 8.1 High-Voltage Current Meters with Wireless Readout

The current meters that are required to optimize the HV settings of a triple-GEM detector need to be able to measure currents down to $\sim 0.1\,\text{nA}$ at HV potentials up to $\sim 5\,\text{kV}$. The circuit of such a device floats on the HV potential, which makes the design and construction challenging. The novel device presented here is based on a previous HV current meter which was designed and built[1] at Technische Universität München (TUM). The principle of the analog circuit of the new device is taken over from the previous design (see appendix G (p. 173) for the schematic of the new version). The current is measured by a voltage drop over a shunt resistor. Assuming a dynamic range for voltage measurements of $0.01 - 1\,\text{V}$, a shunt of $100\,\text{M}\Omega$ is needed to measure currents in the range $0.1 - 10\,\text{nA}$. Analog to digital converters (ADCs) which are needed to acquire the voltage drop over the shunt have input impedances of the order of $\sim 10\,\text{M}\Omega$, which is much too low for the measurement of a voltage drop over a $100\,\text{M}\Omega$ resistor. The measured voltage is decoupled from the ADC with a non-inverting operational amplifier, which buffers the voltage with an input impedance of $\sim 10\,\text{G}\Omega$. The amplifier AD549L is used for this purpose because it limits input currents to 60 fA and has a very good noise performance. The analog circuit includes a number of safety features to protect the amplifier in the case of HV discharges in the connected detector. It should, however, be mentioned that rare failures of the amplifiers still occur.
In the old design of the current meters, the output voltage of the amplifier is digitized with a digital voltmeter with a direct LCD display that can be read through a transparent window in the enclosure of the device. The current meter is equipped with four different shunt resistors[2] that can be switched via reed contacts. The circuit is powered by 9 V batteries which are also switched via reed contacts. The magnetic fields for closing of the individual reed contacts are generated by coils which are powered by a 12 V power supply at the laboratory potential and which are controlled by control knobs at the front panel of the device. The floating "ground potential" of the HV circuit which includes the current display and the 9 V batteries is galvanically isolated from the ground potential of the laboratory. The major shortfall of the old design is that it requires the user to manually take notes of the readings of the current displays. This is a very tedious task especially since a measurement with a triple-GEM detector involves eight current meters (seven HV electrodes and the current measurement at the readout plane which is at ground potential).
The ideal solution for the optimization of the HV settings would be an automated measurement, in which the parameter space of HV values is scanned by a computer that controls the HV power supply and electronically records the current values associated with each HV setting (provided that the X-ray source provides a stable flux). This requires a galvanically isolated data transmission from the current meters to the computer, which is realized in the new design of the current meters

[1] by I. Konorov (TUM) and the electronics workshop of the Physics Department of TUM.

[2] $100\,\text{M}\Omega$ for the range $0.1\,\text{nA} - 10\,\text{nA}$, $1\,\text{M}\Omega$ for the range $10\,\text{nA} - 1\,\mu\text{A}$, $10\,\text{k}\Omega$ for the range $1\,\mu\text{A} - 100\,\mu\text{A}$, and $100\,\Omega$ for the range $100\,\mu\text{A} - 10\,\text{mA}$.

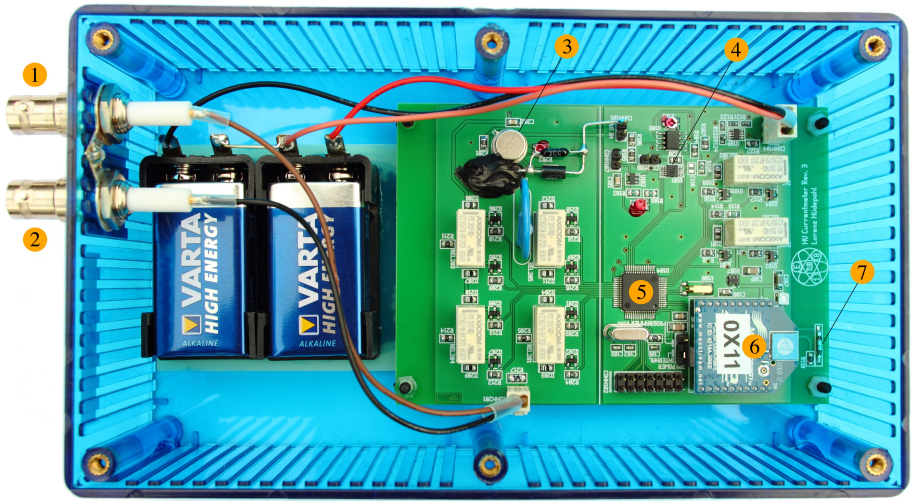


**Figure 8.3:** High-voltage (HV) current meter with wireless readout (open lid). (1) HV in; (2) HV out; (3) non-inverting operational amplifier (AD549L); (4) 16-bit ADC (AD7790); (5) microcontroller (MSP430); (6) XBee® wireless transceiver; (7) reed switch.

with the use of wireless XBee® transmitters[3].

A photograph of one of the newly designed[4] current meters is shown in Fig. 8.3. An MSP430 microcontroller (type MSP430f169) is at the heart of the new digital circuit of the current meters. The MSP430 has a very low power consumption and can be programmed in the C programming language. The output voltage of the operational amplifier is digitized with a 16-bit ADC (type AD7790, sampling rate of 16.6 Hz), which is controlled by the MSP430. While the ADC is taking a measurement, the microcontroller is in a sleep mode as are all other active components of the circuit in order not to disturb the measurement. Once the ADC has finished a digitization cycle, it activates the microcontroller via an interrupt. The microcontroller receives and saves the acquired voltage, initiates the next ADC measurement, and goes back into sleep mode. After 128 measurements have been acquired, which takes a little less than eight seconds, the microcontroller calculates the mean value and the standard deviation of the acquired voltage values. Then it activates the XBee® module and transmits the data. After the completion of the transmission is acknowledged by the XBee® transmitter, the microcontroller puts the XBee® module back into sleep mode, blinks an LED that indicates to the user that the device is switched on, and starts a new measurement cycle of 128 measurements.

The current meter needs a set of voltages: +9 V and −9 V are supplied directly by batteries, +3.3 V are derived from +9 V with a linear regulator (type MIC5205-3.3BM5), and the reference voltage for the ADC measurement is derived from the +3.3 V with a precision voltage-reference component (type ADR360). The new device is also equipped with four shunt resistors, which can be switched with bistable relays (type TYCO-3-1393788-3) that are controlled by the microcontroller. The use of bistable relays is very important for an extended battery life of the device,

[3] XBee® (produced by MaxStream) transmit at 2.4 GHz and use the IEEE 802.15.4 networking protocol.

[4] the layout of the printed circuit board and the C code development for the MSP430 were done by L. Hüdepohl, who worked as a "Werkstudent" under my supervision.

because they do not require a constant current to maintain an active state. There are currently two versions of the firmware: The first version features autoranging, i.e. the automated changing of the shunt resistors depending on whether the voltage drop over the current shunt is below or above the dynamic range of the measurement. The second firmware features a manual switching of the ranges. The firmwares can be loaded to the MSP430 via the JTAG interface.
As can be seen in Fig. 8.3, the device does not have any buttons or switches for power-on/power-off or for the range switching. The insulating polycarbonate enclosure of the device is only breached by the SHV connectors. A reed contact, which is placed near the enclosure (see label (7) in Fig. 8.3), can be switched with an ordinary refrigerator magnet from the outside of the enclosure. If the reed contact is closed while the device is powered off, the +9 V and +3.3 V voltages are switched via the reed contact, which powers the microcontroller. The firmware immediately connects the batteries for +9 V and −9 V to the circuit by switching two relays. This takes a few milliseconds after which the reed contact is no longer required to power the circuit. Once the device is running, the reed switch can be used to cycle through the different sensitivity ranges from the least sensitive (100 Ω shunt resistor) to the most sensitive (100 MΩ). If the reed contact is closed after the most sensitive range is reached, the device powers itself off. In case of the autoranging firmware, the reed switch is just used to power off the device. The firmware has built-in delays for the switching of the reed contact to avoid bouncing effects.
The XBee® module has a power consumption of $\sim$ 150 mW when it is in active mode. If the module was permanently active, it would empty the +9 V battery within about one day. The design of the firmware, which only activates the XBee® module to send data after 128 ADC measurements, extends the battery life by a large factor. All other components of the device have been chosen for their very low power consumption. The overall, mean power consumption of the device is $\sim$ 3 mA$\times$9 V, which allows a very long continuous operation (about one week with a 500 mAh battery). The current meters are equipped with a battery-monitoring component (type LTC 2909), which detects the depletion of the batteries before the microcontroller and the XBee® modules stop working (threshold is $\sim$ 7 V for both batteries).
The battery status, the ID of the active shunt resistor, and the mean value and standard deviation of the 128 measured voltage values are transmitted after the completion of each measurement cycle. The data from a large number of current meters (technically up 254 would be possible) are received by an XBee® module, which is connected to a computer via a USB interface board[5]. A program for the acquisition and display of the data has been written[6] in C++ based on the graphical-user-interface classes of the ROOT data-analysis framework [84]. Since the receiving XBee® module appears to the computer as a standard RS232 device, the inclusion into a LabView program for the combined HV control and current acquisition which is needed for the automated measurements for the optimization of the HV settings described above is very simple.
The calibration constants needed to translate the voltage values and shunt IDs into current values are applied in the acquisition software. The calibration of all measurement ranges of the current meters were performed manually with a precision current source (Keithley 6220DC). A possible future revision of the design might include a digital-to-analog converter that together with the precision voltage reference could be used for the implementation of an autocalibration procedure in

[5] the USB board is part of a MaxStream evaluation kit for the XBee® module.
[6] by M. Knötig, who worked as a "Werkstudent" under my supervision.

the firmware.
19 current meters of the described design were produced in the electronics workshop of the Physics Department of TUM. They have been calibrated and tested and are ready to be used for the optimization of the HV settings of a triple-GEM detector for a TPC application. Such measurements are planned for the near future.

## 8.2 GEM-TPC Family

The development of the GEM-TPC of $\overline{\text{P}}$ANDA proceeded in several steps of prototyping, which are summarized in the following table:

| **Detector** | **Readout Pads** | **Dimensions** | **Frontend Electronics** | **Constr. Date** | **Test Environment** | **Descr. in Sec.** |
|---|---|---|---|---|---|---|
| test chamber | 1536 rectangular | $\varnothing$ = 200 mm<br>$L$ = 77 mm | ALICE (ALTRO) 128 chan. | 2005 | Cosmic muon tracking at TUM | 8.3 |
| upgraded test chamber | 1500 hexagonal | $\varnothing$ = 200 mm<br>$L$ = 77 mm | T2K (AFTER) all chan. | 2008 | Test beams at ELSA and CERN | 8.4 |
| large prototype | 10254 hexagonal | $\varnothing_{\text{i.}}$ = 104 mm<br>$\varnothing_{\text{o.}}$ = 308 mm<br>$L$ = 728 mm | T2K (AFTER) all chan. | 2010 | Integrated into FOPI spectrometer | 8.6 |

**Table 8.1:** GEM-TPC family. $L$ denotes the drift length, and $\varnothing$ is the diameter of the chamber (the large prototype has a central hole, hence there are inner diameter $\varnothing_{\text{i.}}$ and outer diameter $\varnothing_{\text{o.}}$).

Since the $\overline{\text{P}}$ANDA Collaboration Board decided in September 2011 to not build a TPC as the central tracker of $\overline{\text{P}}$ANDA, the further development of the GEM-TPC project might move into different directions. The large prototype of the $\overline{\text{P}}$ANDA-TPC is already being used in the FOPI spectrometer for physics measurements, which is explained in Sec. 8.6.

## 8.3 GEM-TPC Test Chamber

A cylindrical GEM-TPC test chamber was designed and built in 2005 by Q. Weitzel [52] and S. Neubert [130] at TUM. The chamber has a diameter of 200 mm and a drift length of 77 mm. The drift endplate consists of a 0.3 mm thick copper plate which is glued on a 10 mm thick support plate made of fiber glass material. This electrode is kept at a negative HV potential of several thousand Volts and provides the drift field, $E_{\text{drift}}$, for the TPC. The barrel of the cylindrical chamber consists of the field-cage foil which is glued on the inside of a support of insulating polyimide foils, paper honeycomb, and a copper foil for electrical shielding. The field-cage foil is a polyimide foil with staggered copper strips on both sides (37 strips in total), which are interconnected with 10 M$\Omega$ resistors. The first strip of the field cage is at a potential close to the potential of the drift cathode

and the last strip is at a potential close to the potential of the GEM stack on the readout endplate (the exact potentials depend on the desired drift field and the distances to the drift endplate and the GEM stack). This configuration provides a highly uniform drift field. The TPC uses three squared GEM foils of size $100 \times 100\,\mathrm{mm}^2$, which are individually framed with glass fiber frames that are stacked at distances of 2 mm. The field lines outside of the active area of the GEMs are terminated with a copper electrode, which is mounted at a distance of 2 mm on top of the upper-most GEM foil and has a diameter matching the inner bore of the field cage and a central quadratic hole matching the GEM stack. The electrode is kept at a negative potential $E_{\mathrm{drift}} \cdot 2\,\mathrm{mm}$ above the potential of the top side of the upper-most GEM. The readout endplate on which the GEM stack is mounted is a 3 mm thick four-layer printed circuit board (PCB) with a $100 \times 100\,\mathrm{mm}^2$ pad plane below the GEM stack consisting of 1536 rectangular pads of size $6.2 \times 1\,\mathrm{mm}^2$. The readout pads are connected to high-density connectors on the other side of the readout PCB via displaced vias[7] to ensure the gas tightness of the readout endplate. The HV connections for the GEM stack are also routed via displaced vias from the SHV connectors on the outside of the chamber to soldering pads around the GEM stack. The HV connections inside the chamber are established via silver wires, which are soldered to the GEMs and the HV pads.
Up to the hardware upgrade of the chamber which is described in the next section, the charge signals from 128 of the readout pads were read out with the PASA/ALTRO frontend electronics (FEE) [138] developed for the ALICE TPC. Since this system was designed for the readout of positive-polarity signals from wire chambers, the negative signals from the GEM-TPC need to be inverted with a dedicated PCB, which lead to an increased nominal noise level of $\sim 2000\ e^-$. A very detailed description of the detector and the readout system can be found in Ref. [52].
The tracking performance of this detector was studied in measurements of cosmic-muon tracks for the duration of several months. The results from this campaign[8] have been published in Ref. [139] and are not repeated here. The pulse-shape-analysis and clustering algorithms that were used to obtain these results are described in detail in Sec. 8.6.

## 8.4 Upgrade of the GEM-TPC Test Chamber and Beam Tests

The most significant technological advances from the just described test chamber to the large GEM-TPC prototype are the use of a novel readout structure with hexagonal pads and of newly developed FEE based on the AFTER chip [140] developed for the T2K TPCs. These technologies are tested in an intermediate step of prototyping, by an upgrade of the pre-existing test chamber.
The charge from a point-like primary electron cluster in the TPC arrives at the readout pads as a distribution of charge with a width of the order of millimeters because of two effects:

- the transverse diffusion of the electrons in the drift, and
- the fact that the charge avalanche from a single electron in a triple-GEM detector has a width of the order $\sim 1$ mm.

[7] vias through adjacent layers of the PCB are not placed on top of each other.

[8] own contributions to the cosmics measurements and results: improvement of the grounding scheme of the detector to reach the nominal noise level, 50% of the conduction of the cosmics measurements, and development of the analysis software.

A hexagonal pad structure has the advantage over rectangular pads that the charge sharing between neighboring pads in two dimensions is more uniform, since the distances to all neighboring pads are equal. The resolution of the position reconstruction of the primary ionization clusters improves with decreasing pad size up to the point where the transverse diffusion starts to dominate. The pad radius $r$ for the hexagonal structure is defined as follows:

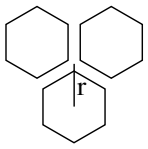


Monte Carlo simulations of the large prototype TPC[9] show that the spatial resolution does not improve anymore for pad sizes smaller than $r = 1.5\,\text{mm}$, which is hence chosen for the design of the pad plane of the large prototype. The new pad-plane PCB of the upgraded test chamber, which is shown in Fig. 8.4, features 1500 hexagonal readout pads. The PCB has a thickness of 2 mm and the hexagonal pads are made of $35\,\mu$m of copper, which is plated with $4\,\mu$m of nickel and $1\,\mu$m of gold (1.33% of a radiation length overall). In order to verify the mentioned simulation results to some extent, the PCB features pads of size $r = 1.5\,\text{mm}$ as well as pads of size $r = 1.25\,\text{mm}$. The distance between adjacent pads is 0.2 mm in both cases, which is, however, irrelevant for the track-imaging properties of the pad plane as all field lines end on the pads. The full layout[10] of the pad-plane PCB is shown in Fig. 8.5. The traces from the readout pads are routed through two intermediate layers (with displaced vias to ensure gas tightness) to six high-density connectors (type SAMTEC BTH-150 with 300 pins) on the outside of the detector.

The signals from the detector are read out with newly developed FEE cards[11] which plug directly into the pad plane (edge-mount connectors SAMTEC BSH-EM-150). Each card hosts four AFTER [140] chips for the readout of 256 detector channels and has a compact form factor of $103 \times 65 \times 4.8\,\text{mm}^3$. Each AFTER chip has 72 input channels of which 64 are connected to the detector. The feedback capacitor of the charge amplifier of each channel can be set in the range $200 - 1000\,\text{fF}$. The peaking time of the shaper can be selected in the range $116 - 1900\,\text{ns}$. The voltage outputs from the shapers of all channels are continuously sampled into switched capacitor arrays (SCA) with an adjustable frequency $f$ in the range $1 - 50\,\text{MHz}$. The SCAs have a depth of 511 samples and contain the charge signals of the past time interval $511 \times f^{-1}$ at any given time. The writing to the SCAs is stopped after a delay of one full electron drift time after the arrival of an event trigger. The digitization of the signals from the SCAs is done with ADC cards, which were developed[12] in the framework of the COMPASS experiment. Each ADC card can read out up to four FEE cards. The zero suppression of signals below threshold is performed directly on the ADC cards. The rest of the readout chain consists of the GeSiCA modules and spill buffer cards of the COMPASS experiment, which were described in Sec. 4.2.5. The FEE cards and their commissioning will be described in other dissertations [141, 142]. The achieved noise performance of

[9] the simulation uses the geometry of the $\overline{\text{P}}$ANDA central tracker, the gas mixture Ne/$CO_2$ (90/10), and a solenoid field of 2 T.

[10] the layout was done by L. Hüdepohl, who worked as a "Werkstudent" under my supervision, and M. Berger of the group of Prof. L. Fabbietti (TUM).

[11] developed by I. Konorov and H. Angerer (TUM).

[12] developed by I. Konorov (TUM).

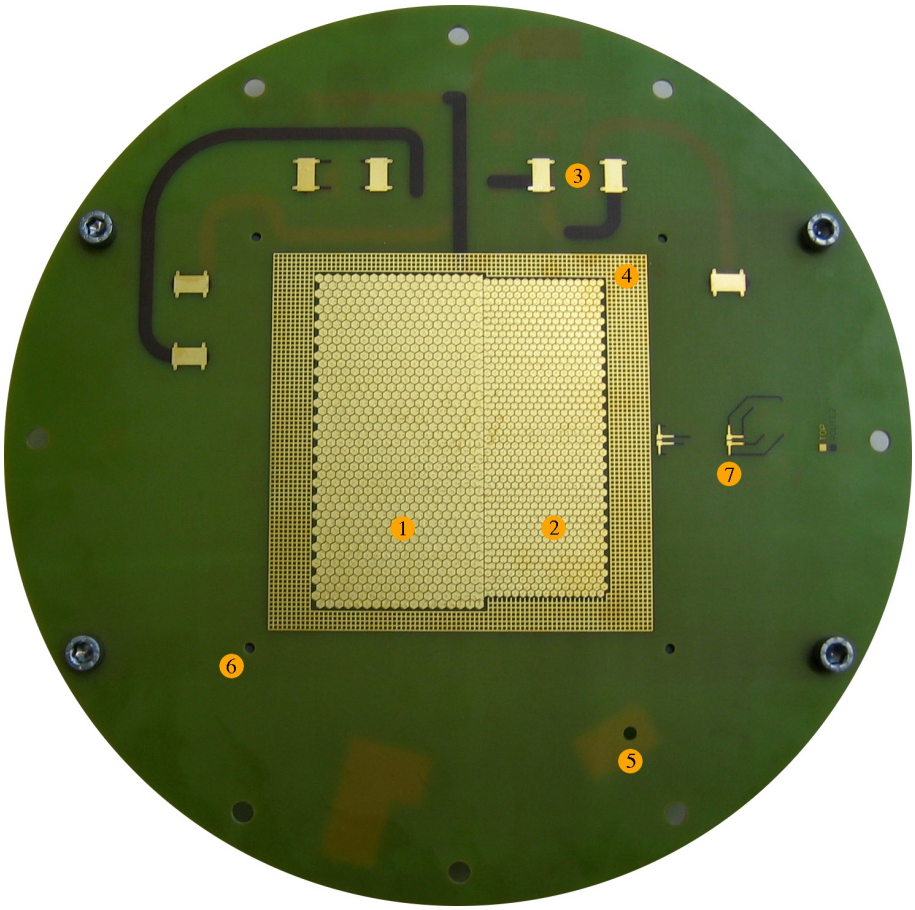


**Figure 8.4:** Photograph of the new pad-plane PCB of the GEM-TPC test chamber (diameter 260 mm). (1) Hexagonal pads $r = 1.5$ mm; (2) hexagonal pads $r = 1.25$ mm; (3) soldering pads for HV connections [×7]; (4) ground plane matching the size of active area of the GEMs; (5) gas inlet; (6) holes for mounting pillars of GEM stack [×4]; (7) soldering pads for temperature sensors [×2].

the FEE cards with the connected TPC is $\sim 625\,e^-$. This value is very close to the specifications of the chip, taking into account the rather large capacitance of the packaging of the AFTER of $\sim 10$ pF and the capacitance of the pads, connectors, and traces of $3 - 6$ pF.
The upgrade of the test chamber is completed by the construction of a thinner drift-cathode end-plate which is also a 2 mm thick PCB, which is fully covered with a 35 $\mu$m copper layer, that is plated with 4 $\mu$m of nickel and 1 $\mu$m of gold (1.33% of a radiation length overall). This reduces the multiple scattering of charged particles on their way into the TPC detector, which is important because the upgraded chamber is tested at particle beams with an external tracking telescope for the unbiased definition of the particle trajectories through the chamber.
A photograph of the test-beam setup is shown in Fig. 8.6. The beam telescope consists of a pair of scintillation detectors at the upstream and downstream ends of the setup for triggering, two sta-

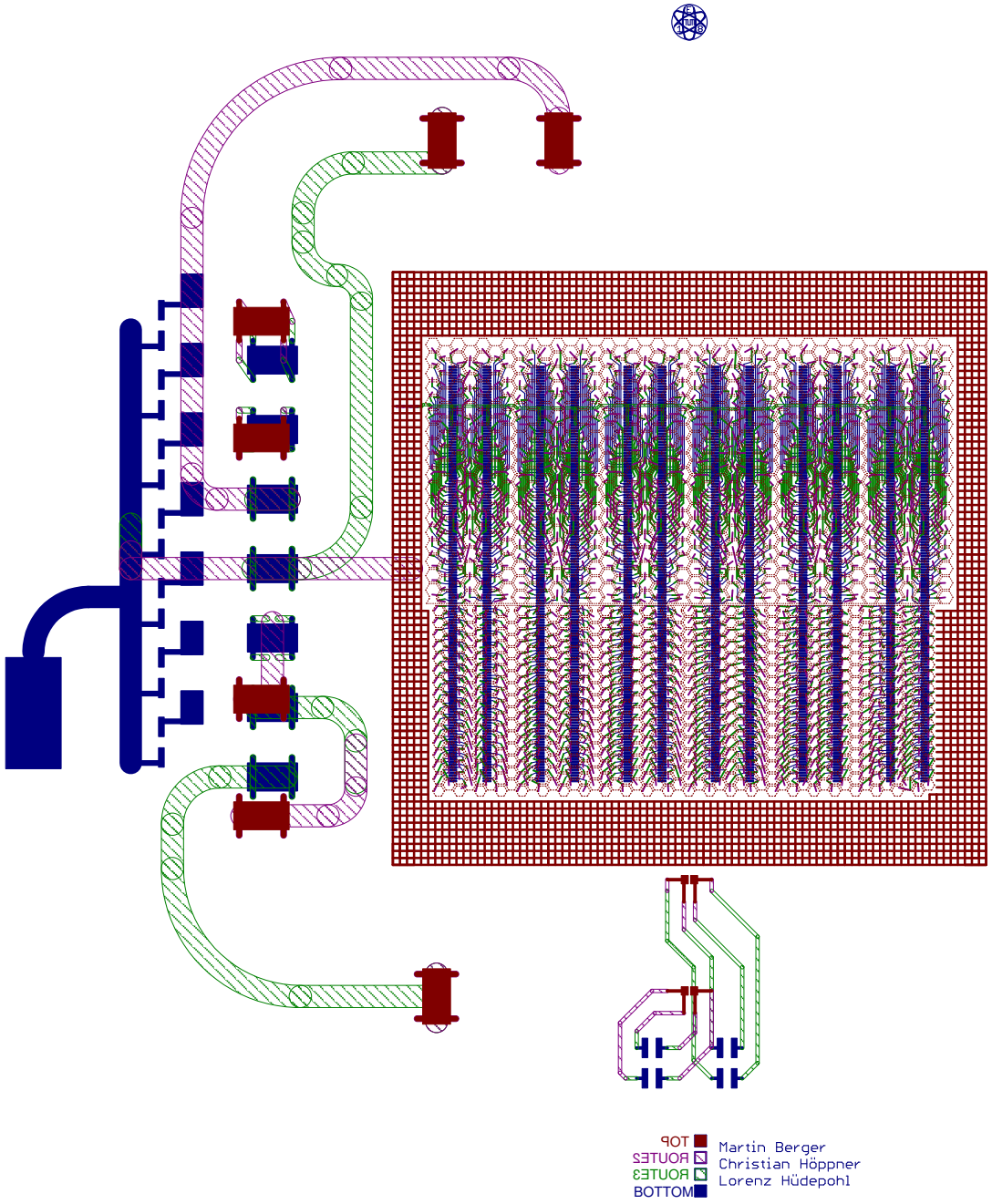


**Figure 8.5:** Layout of the pad-plane PCB (four layers). The routing of the 1500 readout pads (*TOP* layer) to the high density connectors (*BOTTOM* layer) via two routing layers (*ROUTE2* and *ROUTE3*) with displaced vias for gas tightness is visible in full detail by zooming into the PDF version of this document. The routing of the HV and ground connections can be seen on the left and the routing of the temperature sensors at the bottom.

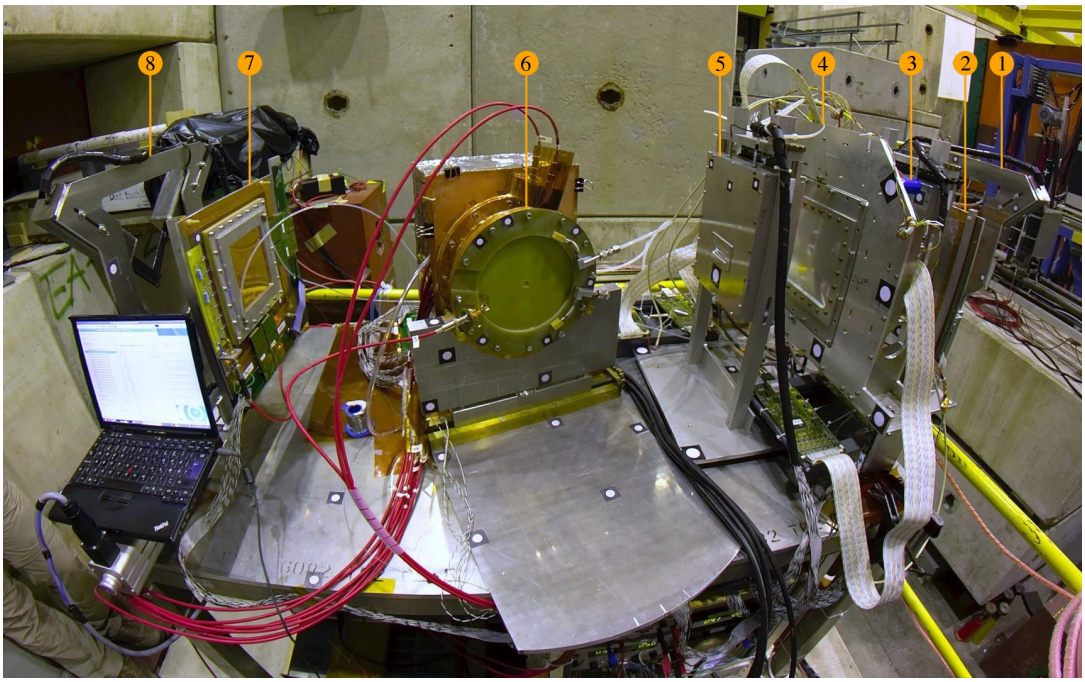


**Figure 8.6:** Photograph of the GEM-TPC test bench at the downstream end of the COMPASS experiment at CERN (beam comes from the right). (1) trigger scintillator #1; (2) GEM tracker #1; (3) HISKP Silicon tracker #1; (4) COMPASS silicon tracker; (5) HISKP Silicon tracker #2; (6) upgraded GEM-TPC test chamber; (7) GEM tracker #2; (8) trigger scintillator #2.

tions of silicon microstrip detectors[13], one spare silicon tracker of the COMPASS experiment[14], and two GEM trackers with double-strip readout[15]. The silicon and GEM detectors are read out with the standard silicon/GEM electronics of the COMPASS experiment described in Sec. 4.2.5. The detectors are mounted on an aluminum test bench [143].

After commissioning of the detector with a copper X-ray tube at TUM, the upgraded GEM-TPC test chamber was moved to the ELSA facility at Bonn where it was tested in combination with the tracking telescope with 500 MeV/$c$ electrons. The proper functioning of the setup was established by the observation of clear correlations between the coordinate measurements of all tracking detectors including the TPC. The effect of multiple Coulomb scattering leads to an uncertainty of the order of a few millimeters at 500 MeV/$c$, which disallowed the study of the intrinsic resolutions of the detectors. The most important outcomes of the measurements at ELSA were the experience gained on how to operate the new readout system of the GEM-TPC and the optimization of the electronics noise of the GEM-TPC as well as of the beam telescope. The setup and the performance of the detectors in the ELSA measurements is described in detail in Ref. [144].

The setup was then moved to CERN, where it was installed at the downstream end of the COM-

[13] developed at HISKP Bonn, each station consists of two silicon detectors with single-sided readout

[14] The COMPASS tracker consists of two silicon microstrip detectors with double-sided readout. It was installed only after the setup was moved to CERN.

[15] developed during the lab course of the lecture “Particle Detectors” at the Physics Department of TUM (2008) under my supervision.

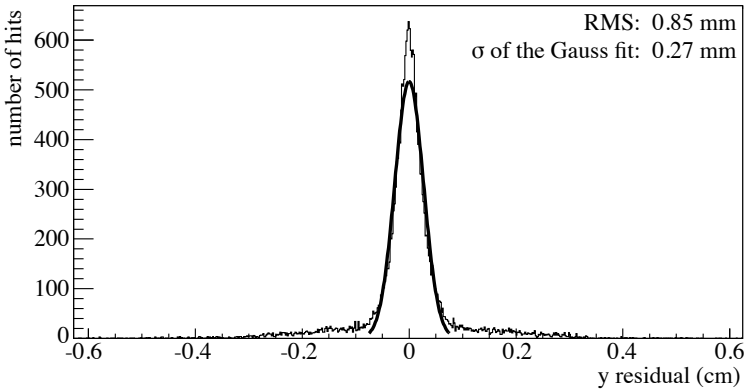


**Figure 8.7:** Biased residuals of the TPC clusters with respect to the fitted particle tracks from a very preliminary analysis of the CERN test-beam data of the upgraded test chamber. The background underneath the narrow peak is probably due to the imperfect tuning of the track-finding software.

PASS hall, where it was exposed to 160 GeV/$c$ muons from the halo of the COMPASS beam. Since the multiple scattering scales with the inverse particle momentum, the COMPASS beam is ideal for systematic studies of the resolution of the GEM-TPC with the beam telescope. The setup was operated successfully and data have been recorded in the summer of 2010 with Ar/$CO_2$ (70/30) and $E_{\text{drift}} = 250$ V/cm in the TPC. A preliminary analysis of the data indicates that the GEM-TPC works as expected. Figure 8.7 shows the distribution of the biased residuals of the reconstructed TPC clusters with respect to the tracks (the TPC clusters themselves have been used for the definition of the tracks). The narrow peak of the distribution proves that the detector works properly. The background underneath the narrow peak is most likely due to an imperfect tuning of the pattern recognition algorithm, which defines which clusters constitute the fitted particle tracks. The analysis of the test-beam data has not yet been finalized because all available manpower in the GEM-TPC project was required for measurements with the large GEM-TPC prototype, whose construction was completed in the forth quarter of 2010.
In conclusion it can be stated that although no quantitative results of the described measurements can be reported yet, the test-beam campaigns were essential for building the expertise required to construct and operate the large GEM-TPC prototype, which is described in Sec. 8.6.

## 8.5 Reconstruction Software

The raw event data from the GEM-TPC detector is a time-ordered list of zero-suppressed ADC samples over the complete drift frame of the chamber from all readout pads. The event-reconstruction scheme for a possible application of the TPC in $\overline{\text{P}}$ANDA would be different from the one presented here because some of the discussed tasks would have to be performed in real-time, during data taking in order to reduce the data-rate from the detector.

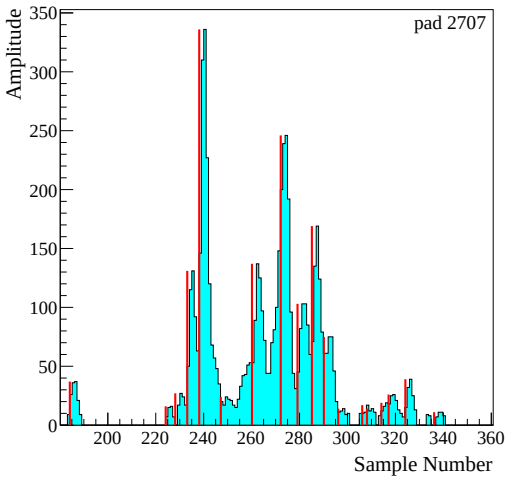


**Figure 8.8:** Pulse-shape-analysis algorithm at work on real data from one readout pad of the large prototype. The ADC samples are displayed in the cyan graph and the amplitudes and times of the resulting *digis* are indicated by the red lines. The sampling frequency of the signal is 16 MHz and the peaking time of the amplifier is 116 ns. The algorithm is described in the text.

### Pulse Shape Analysis

The first step in the event reconstruction is the pulse shape analysis (PSA), which is performed for each readout pad individually. The first task of the algorithm is the detection of discrete pulses in the continuous signal waveform. The algorithm starts a new pulse as soon as two consecutive samples above threshold are detected. The following samples are added to the pulse until a local minimum in the waveform is found or the signal falls below a configurable threshold. In the case of a local minimum, the next pulse is started immediately. Once the discrete pulses are defined, each pulse in converted into a so-called *digi*, which is a data object consisting of a pad ID, one charge amplitude value, and one time value for the pulse. The amplitude of the *digi* is defined by the maximum sample in the pulse and the time value is defined by the time of the maximum sample minus the peaking time of the shaper. The performance of the PSA algorithm is shown in Fig. 8.8, where the *digis* are indicated by the red lines. A valuable future improvement of the algorithm would be the implementation of a tail cancellation, which subtracts the tails of previously peaked charge pulses from the sample amplitudes. This should be possible because the signal shape for a single charge pulse is well known. Since it is quite usual that charge pulses can overlap in time in a TPC, the pile up of signals slightly distorts the time and amplitude calculations in the PSA without tail cancellation.

### Cluster Finding

The next step in the data processing is called cluster finding. This algorithm has the task to combine the *digis* from neighboring pads into *clusters* under certain conditions. As explained above, the charge from one primary ionization cluster can arrive at several readout pads because of the

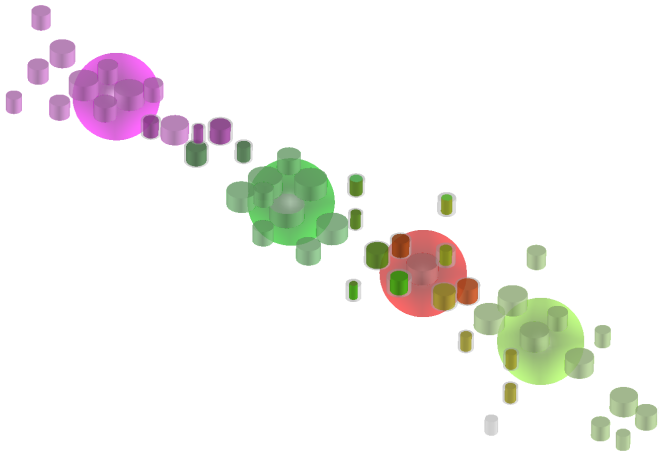

**Figure 8.9:** Illustration of the clustering algorithm performing on real data from the large prototype. The coin-shaped objects represent the *digis*, where the time axis is defined by the cylinder axis of the coins, and the spheres represent the *clusters*. The *digis* belonging to the same *cluster* are drawn in the same color as that *cluster*. The split *digis* in between the *clusters* have mixed colors.

transverse diffusion during the electron drift and the extended charge avalanche in the triple-GEM amplification. These effects lead to a mixing of the charge from the individual primary ionization clusters along the track on the readout plane. There are statistically distributed local maxima of the charge amplitude along the track, which either correspond to larger ionization clusters (consisting of many electrons) which occur every few millimeters or to short track pieces of the order of the pad size along which many small ionization clusters were created. Either way, the generation of a lot of primary charge along a short track length provides a good position measurement of the track path. There is no actual need to reconstruct the positions of the primary ionization clusters for the track reconstruction. The clustering algorithm has the task of contracting the *digis* around the local charge maxima, which define the positions of the *clusters*, and to use the amplitude information of the *digis* for an increased accuracy of the reconstruction of the *cluster* positions. When the tracks are not parallel to the readout plane, they travel a significant distance in the drift direction over the length scale of a primary-ionization maximum. The clustering algorithm hence needs to combine *digis* in two spatial dimensions as well as in the time dimension to calculate the optimal positions of the *clusters*.
The clustering algorithm begins by sorting the *digis* in the event by amplitude. The first *cluster* is initiated by the *digi* with the largest amplitude. The algorithm then loops over the *digis* with decreasing amplitudes. The current *digi* can be added to an already exiting *cluster*, if:

1. the pad of the *digi* is already part of the existing *cluster* or it is a direct neighbor of a pad which is part of the existing *cluster*, and

2. the time value of the *digi* is within a certain time interval of the time value of the existing *cluster*.

If no matching *cluster* is found, a new *cluster* is initiated. If $N \geq 2$ matching *clusters* are found, the *digi* is split and added to all clusters with the fraction $N^{-1}$ of its amplitude. The time values of the *clusters* which received additional *digis* are updated with the mean value of the time values of all *digis* in the *cluster* weighted by the *digi* amplitudes. Since each *digi* needs to be compared to each *cluster* in this algorithm, the computing time increases strongly with the number of *digis*. The algorithm is hence run independently in different geometrical sectors of the pad plane as well as in different slices of the drift time. Since the sectors have slight overlaps, this optimization only introduces minimal edge effects at the sector boundaries.
After all *digis* have been processed and distributed amongst the *clusters*, the position of each *cluster* is calculated as the center of gravity[16] in both spatial coordinates as well as in the time coordinate. The *cluster* time is then converted into a spatial coordinate by multiplying with the drift velocity. The three-dimensional error of the *cluster* position is currently defined by the propagation of the Gaussian errors of the *digis* in the center-of-gravity calculation. The definition of the *cluster* error is subject to further optimizations [145].
The performance of the cluster-finding algorithm is illustrated in Fig. 8.9. It nicely contracts around local maxima of the charge amplitude. The *digis* in between the maxima are mostly split between two *clusters*.

**Track Finding and Fitting**

The track-finding algorithm, also referred to as the pattern-recognition algorithm, has the task to determine which of the *clusters* constitute the individual particle *tracks* in an event. There are many possible approaches to this problem. Over the course of the past years a few solutions have been implemented for the GEM-TPC project, which are briefly explained in the following.

1) Straight-line Hough transformation [146] with histogram-based maximum search:
A straight-line track in the detector is described by the relation $y = a_y z + b_y$. Each *cluster* measured in the TPC $(y_i, z_i)$ corresponds to a straight line in the $a_y$-$b_y$ plane, $b_y = (z_i) \cdot a_y + y_i$. The lines corresponding to a set of collinear *clusters* intersect in one point in the $a_y$-$b_y$ plane. This intersection point is identified with a histogramming method.
This algorithm was implemented in the course of the presented PhD project and used for the analysis and publication of the cosmic-muon data recorded with the test chamber with the ALTRO readout [139].

2) Fast Hough transformation (FHT) in combination with a Riemann transformation for helical tracks implemented on a GPU:
The Riemann transformation is a conformal-mapping method that can be used in particle tracking [147] to transform the positions of the points on a circular track in the *x*-*y* plane (assuming a solenoid field in the *z* direction) onto a plane through the Riemann sphere. In this context the Riemann sphere is defined as the sphere of radius one, which is situated on top of the *x*-*y* plane. This way, the problem of finding a circular track is reduced to the fit of a plane, which is computationally much simpler. The Riemann transformation has the advantage over some other conformal mappings that it is not constrained to tracks which come from the primary interaction point (or

[16] mean value weighted by the charge amplitude.

from any one particular point) which is for instance very important for the detection of the decay particles of $\Lambda$ hyperons or for the clear identification of spiraling $\delta$-electrons. The plane through the Riemann sphere is defined by three parameters. There are two more parameters in the $r$-$z$ plane ($r$ denotes the distance of a point from the $z$ axis) which are needed to describe a helical track. Since a histogramming in five dimensions is computationally very expensive, the FHT [148] tree-search algorithm is used for the search of the intersection points of the hyperplanes in the Hough space which are associated to each hit. The described algorithm has been implemented in the C++ programming language on a standard CPU as well as on a graphics card (GPU) in the CUDA programming language, where it was shown to perform faster by a factor of $\sim 20$.
The algorithm has been developed and implemented by F. Böhmer [149, 150] and has been used for Monte Carlo simulation studies of the $\overline{\text{P}}$ANDA-TPC.

3) Straight-line FHT on a CPU:
A version of the described FHT algorithm, which was modified for straight line tracks, has been used for the pattern recognition of the tracks in the beam tests of the upgraded test chamber at CERN (author F. Böhmer).

4) Riemann track follower for straight lines and helical tracks:
This algorithm begins with a sorting of the *clusters* by one of the three numbers: a) $z$ position, b) distance from the beam axis $r$, and c) azimuthal angle $\phi$. The step of *tracklet* building which is described in the next paragraph is done for each of the three sortings and always works best for tracks oriented along the sorting direction. *Clusters* which are recognized as belonging to a *tracklet* of good quality in one sorting are not available for the *tracklet* building with the other sortings anymore. *Tracklets* which are built in one sorting can be further extended in the other sortings.
In the first sorting, the *tracklet* building starts with initialization of the first *tracklet* with the first *cluster*. The algorithm then iterates over all *clusters* to check whether the current *cluster* can be associated to an already existing *tracklet*. This check is performed by employing a set of *cluster-tracklet* correlator functions which evaluate the compatibility of a *cluster* with a *tracklet* in terms of different distance measures in the ordinary coordinate space as well as on the Riemann sphere. The correlators decide whether a *cluster* can be added to a *tracklet* or not. In case of a match they also define a number which measures the match quality. The *cluster* is added to the *tracklet* it matches best. If a *cluster* does not match any of the existing *tracklets*, a new *tracklet* is initialized. Just like in the case of the clustering algorithm, the computation time for the *tracklet* building increases very strongly with the number of tracks, which is why it also profits from an independent processing of several geometrical sectors on the pad plane.
Physical tracks are often split into several *tracklets* in the *tracklet* building, which is why the pattern recognition features the final step of *tracklet* merging. All *tracklets* are tested against each other by employing *tracklet-tracklet* correlators which operate in the ordinary coordinate space as well as on the Riemann sphere.
This algorithm is used for the reconstruction of the experimental data from the large prototype. It performs very well on cosmics data with and without magnetic field as well as on beam data (see example in Fig. 8.11). The algorithm has also been used for simulation studies of the $\overline{\text{P}}$ANDA-TPC. It has been developed and implemented by S. Neubert [57] and J. Rauch [145].

After the pattern recognition is completed, the tracks are fitted with the GENFIT toolkit, which is introduced in chapter 9.

## 8.6 Large GEM-TPC Prototype

The large GEM-TPC prototype has been designed to fit inside the central drift chamber (CDC) of the FOPI spectrometer [151] at GSI. The integration of the detector into the FOPI spectrometer provides the following opportunities:

- The FOPI solenoid magnet provides a uniform magnetic field of 0.6 T, which is very important for many systematic tests of the TPC,
- the other FOPI detectors can be used as external references for the definition of tracks through the TPC for the determination of the efficiency of the detector, and
- after the commissioning and calibration phase, the new spectrometer consisting of the GEM-TPC and the pre-existing FOPI spectrometer can be used for very interesting hadron-physics measurements.

The new GEM-TPC detector has a drift length of 728 mm, an inner radius of 104 mm, and an outer radius of 308 mm. A photograph of the chamber is shown in Fig. 8.10. The pad plane features 10254 hexagonal pads of size $r = 1.5$ mm, which are read out with 42 FEE cards based on the AFTER ASIC, as described in Sec. 8.4. The detector was built by the Detector Laboratory of GSI, Darmstadt. The inner and outer field-cage vessels as well as the drift cathode endplate consist of self-supporting structures which are made of sandwiched layers of Rohacell, polyimide foils, and skins of fiber-glass material (0.3% of a radiation length for each wall). The drift cathode is an aluminized polyimide foil, which is laminated on to the endplate. The field-cage foils at the inner and the outer radii are polyimide foils with staggered copper strips on both sides, which are interconnected with resistors outside of the gas volume. The outside of the field-cage vessel is coated with an aluminized polyimide foil for electrical shielding. The pad-plane PCB and the GEM stack are connected to the chamber via a "media flange", which features gas inlet and outlet, HV connections, and several sensors for temperature and gas-pressure measurements. The pad-plane PCB is basically a larger, more complex version of the pad-plane PCB of the test-chamber upgrade, described in Sec. 8.4. The routing of the connections from the 10254 readout pads to the 42 high-density connectors (type SAMTEC BTH-150) is done through two intermediate routing layers with displaced vias for gas tightness. The 42 FEE cards on the detector as well as the eleven ADC cards are cooled with a water-cooling system. The gas for the TPC is supplied by an open gas system, but an upgrade to a closed gas system with a purification unit is foreseen in the near future. The data acquisition (DAQ) of the GEM-TPC has been integrated into the FOPI DAQ to allow the combined analyses with the different detectors.
The chamber has been first operated in a commissioning run inside the FOPI spectrometer in November 2010[17]. Figure 8.11 shows a visualization of the TPC data of a typical event of a $^{22}$Ne

[17] the results presented in this section are the outcome of a joint effort by the GEM-TPC collaboration, which consists of $40 - 50$ scientists from the TUM, GSI Darmstadt, HISKP Bonn, SMI Vienna, and Heidelberg University.

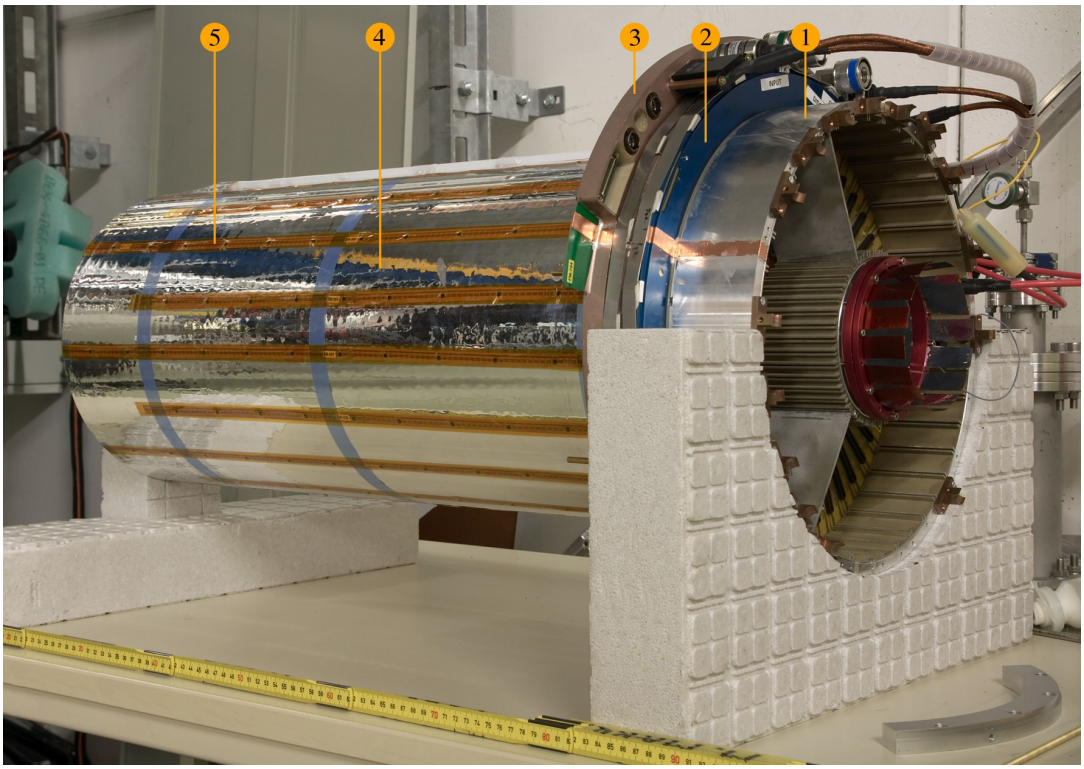


**Figure 8.10:** Photograph of the large GEM-TPC prototype. (1) cooling pot; (2) GEM-readout flange; (3) media flange; (4) outer field cage; (5) temperature sensors.

ion impinging on a 2%-interaction-length Al target at a momentum of 1.7 GeV/$c$ per nucleon. The TPC is able to reconstruct well separated tracks basically without any background. The picture also features the results of the Riemann pattern recognition algorithm described in the previous section. The efficiency of this algorithm has been studied with tracks defined by the CDC and is close to 100%.

The TPC has so far been operated with two different gas mixtures, namely Ar/$CO_2$ (90/10) and Ne/$CO_2$ (90/10). The gain of the GEM amplification stage of the chamber is calibrated and repeatedly checked by the injection of radioactive $^{83m}$Kr gas (activity in the chamber $\sim$ 1 MBq). Besides other decay modes, the $^{83m}$Kr atoms can emit 41.6 keV electrons that are detected as single clusters in the TPC when it is read out with random triggers. Figure 8.13 shows a map of the relative gains of all readout pads of the TPC resulting from such a calibration. The channel-by-channel gain calibration should slightly improve the spatial resolution of the chamber as the amplitudes of the charge pulses play a crucial role in the clustering algorithm. More importantly, the gain calibration will greatly improve the resolution for the measurement of the specific ionization $\mathrm{d}E/\mathrm{d}x$ in the TPC, which will play an important role in the identification of charged kaons in the chamber. Using particle tracks reconstructed in the CDC of FOPI, the TPC has been aligned very precisely with respect to the FOPI spectrometer, as shown in Fig. 8.12. This alignment is essential for the combined use of the GEM-TPC with the rest of the FOPI spectrometer.

Large data sets of cosmic-muon tracks have been recorded for the investigation of the spatial resolution of the detector, where coincidences between scintillation detectors of the FOPI time-

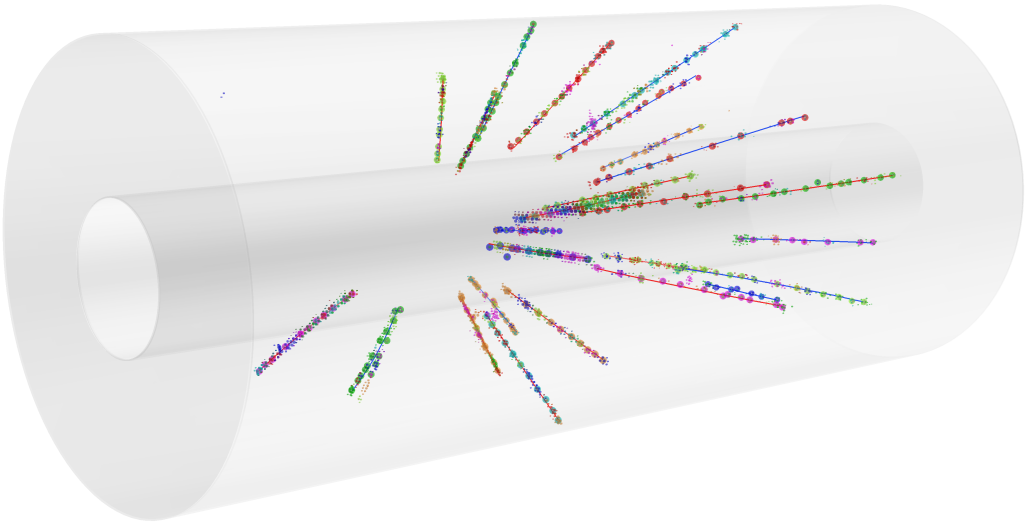

**Figure 8.11:** Visualization of a $^{22}$Ne-Al event in the TPC. The Riemann pattern recognition described in Sec. 8.6 has been used to identify the individual particle tracks, as indicated by the lines.

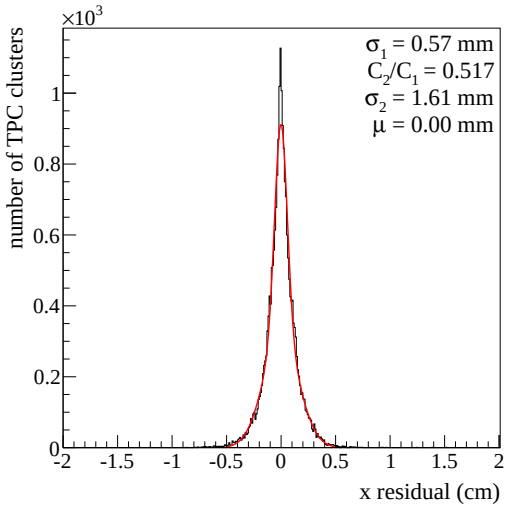


**Figure 8.12:** Residuals of the TPC clusters with respect to tracks defined by the CDC detector after the alignment of the TPC. The distribution has been fitted with the function $C_1 \cdot \exp[(x-\mu)^2/2\sigma_1^2] + C_2 \cdot \exp[(x-\mu)^2/2\sigma_2^2]$.

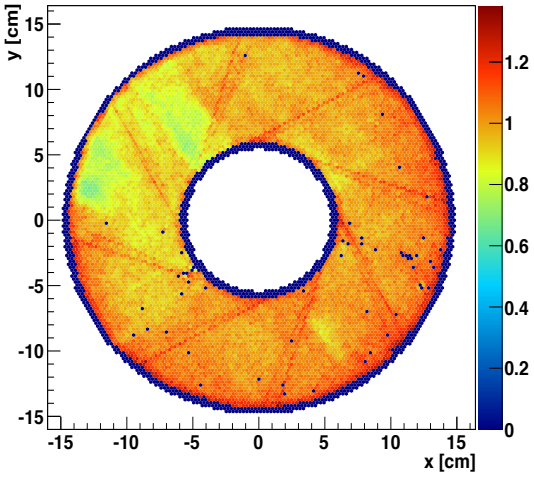


**Figure 8.13:** Relative gain of all readout channels of the detector obtained from a $^{83m}$Kr calibration. The iris-shaped pattern is due to the sector boundaries of the GEM foils.

of-flight detector have been used for triggering. Such measurements have been performed with both gas mixtures, with varying drift fields in the TPC, and with varying gains of the GEM-amplification stage. The $x$ coordinates of the residual vectors of TPC clusters with respect to cosmic-muon tracks, which traverse the detector in the $y$ direction, in several bins of the drift distance $z$ are shown in Fig. 8.14. The operational parameters for this particular data set are: gas $Ar/CO_2$ (90/10), drift field 310 V/cm (drift velocity 2.45 cm/$\mu$s), gain 1500, and solenoid field 0.6 T. The distributions are well described by the sums of two Gaussians. The mean spatial resolution is calculated as the mean value of the width parameters of the Gaussian functions, weighted by the integrals of the functions. The results of the fits and the mean values of the resolution are summarized in Fig. 8.15 as a function of the drift distance $z$. The transversal spatial resolution reaches from $\sim 300\,\mu$m for shortest drift distances to $\sim 750\,\mu$m for the longest drift distances, which is in agreement with the results of detailed Monte Carlo simulations of the detector within $10 - 20\,\mu$m [152]. The residual distributions of Fig. 8.14 have one entry per TPC cluster on a cosmic-muon track. The unbiased residual for each cluster is calculated with respect to the track which has been fitted using all clusters on the track but the one for which the residual is being calculated. This functionality is provided by the GENFIT framework [153]. Figure 8.16 shows cluster-size distributions for a sub-sample of the tracks of the residual distributions. The three-dimensional cluster size counts all *digis* (i.e. charge pulses, see Sec. 8.6) that constitute the cluster, allowing several *digis* on the same readout pad which are displaced in the time coordinate. The two-dimensional cluster size only counts the number of pads that are part of the cluster by counting just one *digi* per pad. The two distributions are very similar, which is expected because the tracks traverse the detector almost parallel to the readout plane. If there was a lot of clustering in the time coordinate of the *digis* for this track geometry, it would represent an oversampling of the signals. For inclined tracks, there is a greater difference between the two distributions. In its current state, the cluster-finding algorithm splits about $40 - 50\%$ of the *digis* in between the clusters, which leads to a significant double counting of *digis* in Fig. 8.16. Further optimizations of the algorithm to reduce this splitting are currently under investigation [145].

During a period of three weeks in June 2011, the large GEM-TPC chamber was operated very stably in the FOPI spectrometer recording events from a 1.7 GeV/$c$ $\pi^-$ beam impinging on different nuclear targets (C, Cu, Pb). This data set provides a great opportunity to evaluate the physics performance of this novel detector. The measurement of the momentum-dependent cross sections for the $\pi^-$-induced production of $K^+$, $K^-$, and $K^0_S$ mesons (and possibly for $\Lambda$ baryons) for different nuclear targets will allow very interesting insights into the propagation of strange hadrons in the nuclear medium. The FOPI experiment has previously published the cross sections for inclusive $K^0_S$ production in $\pi^-$-induced reactions with different nuclear targets [154], which allowed the extraction of a repulsive kaon-nucleon potential of $20 \pm 5$ MeV. The recently recorded data set with the TPC will significantly increase the acceptance at lower $K^0_S$ momenta where the sensitivity to the potential is strongest. In addition to the increased phase-space coverage for charged-particle tracking, the excellent vertex-reconstruction capabilities of the TPC will improve the identification of $K^0_S$ mesons and $\Lambda$ baryons. The identification of $K^+$ and $K^-$ mesons will be enhanced by the measurement of the specific ionization of charged particles in the TPC. With the excellent performance of the TPC and its successful integration into the FOPI spectrometer, very interesting results can be expected. The data analyses are currently ongoing.

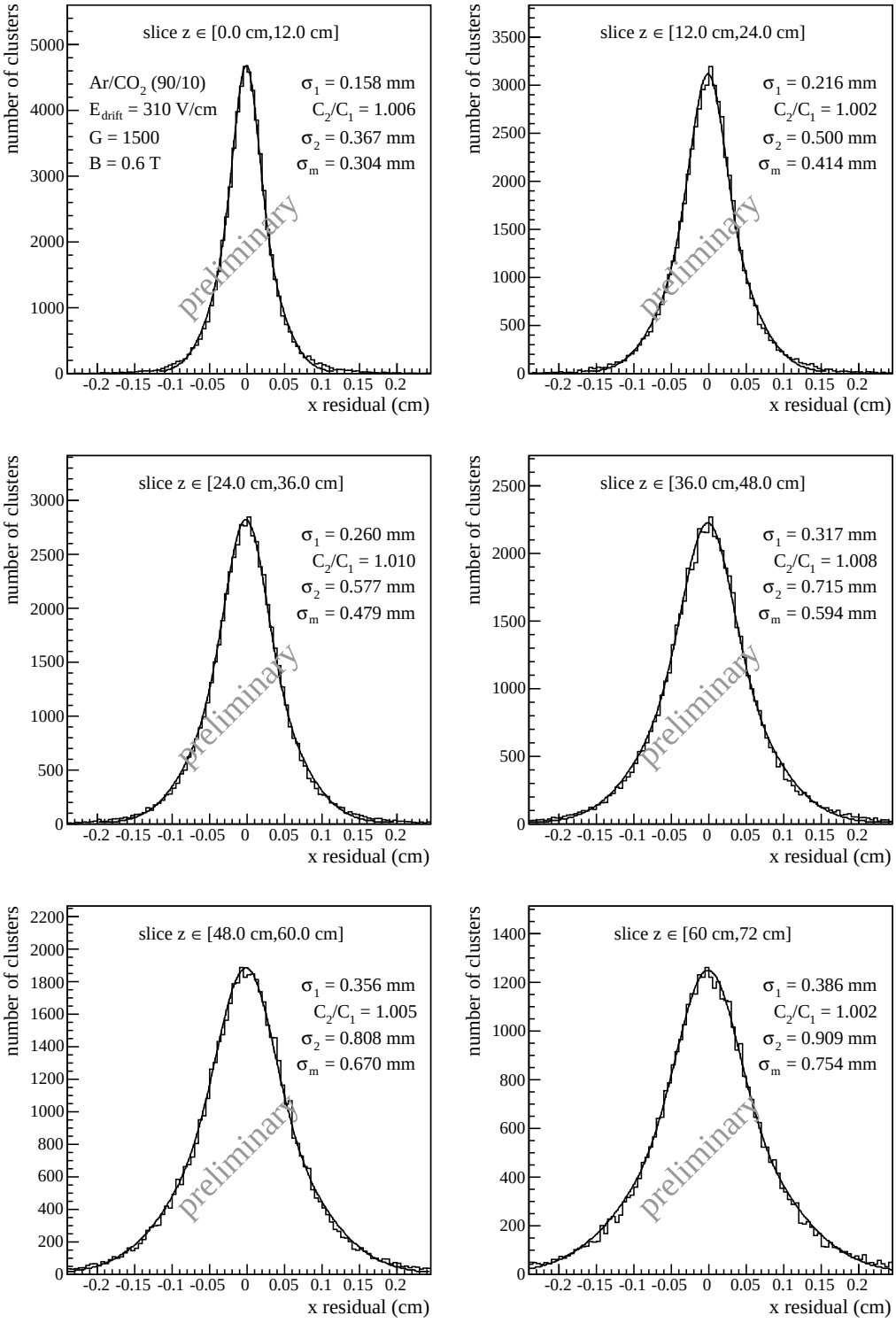


**Figure 8.14:** Unbiased residuals in the large GEM-TPC in the $x$ coordinate, which is parallel to the pad plane, in bins of the drift distance $z$. The distributions have been fitted with the functions $C_1 \cdot \exp[x^2/2\sigma_1^2] + C_2 \cdot \exp[x^2/2\sigma_2^2]$. The quoted spatial resolution $\sigma_\mathrm{m}$ is the mean value of $\sigma_1$ and $\sigma_2$, weighted by the Gaussian integrals. The resolution as a function of the drift distance is summarized in Fig. 8.15.

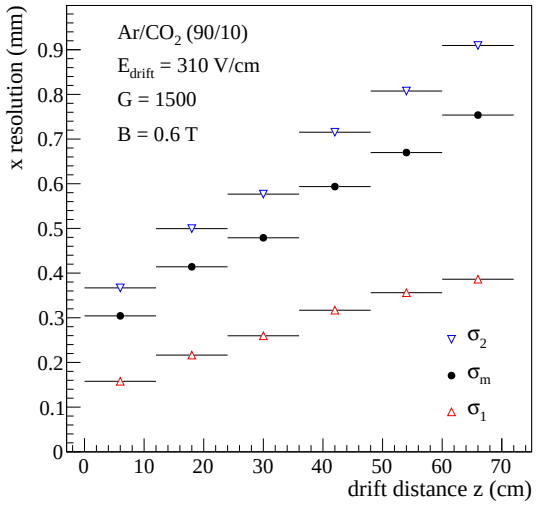


**Figure 8.15:** Summary of the resolution for the measurement of the $x$ coordinate in the large GEM-TPC as a function of the drift distance $z$. For the definitions of $\sigma_1$, $\sigma_2$, and $\sigma_\mathrm{m}$ see the caption of Fig. 8.14.

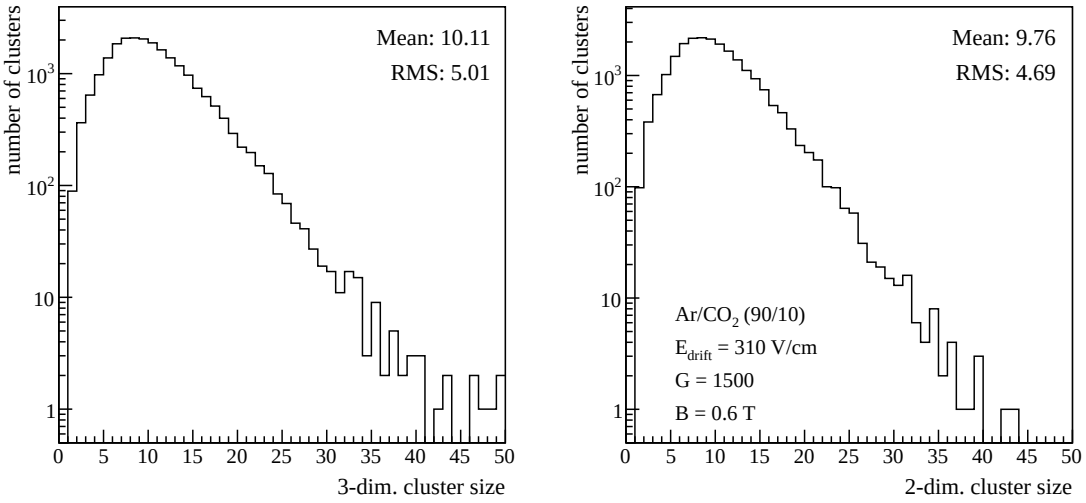


**Figure 8.16:** Cluster-size distributions for cosmic-muon tracks that are traversing the detector almost parallel to the pad plane. For the definitions of the 3-dim. (left) and 2-dim. (right) cluster sizes, see text.

# Chapter 9

# GENFIT - a Generic Toolkit for Track Fitting

The results of high-energy physics experiments are obtained from the analysis of the 4-momenta of particles at their scattering vertices. The 4-momenta of charged particles are obtained from the measurements of the particle trajectories in magnetic fields, which can be supplemented with calorimetric and particle-identification measurements. Position-sensitive detectors electronically record information on the passage of particles, which is then processed with signal-processing algorithms like pulse-shape analysis and hit clustering. Pattern recognition algorithms determine which detector hits constitute the individual particle tracks which are then passed on to the track fitting software.
The track-fitting software obtains the best estimates of the track parameters and their covariance matrix from the detector hits. To do so, the software requires track-extrapolation routines which take into account the magnetic field of the experiment as well as the materials, which are traversed in the extrapolations, because they increase the uncertainty (covariance matrix) of the track parameters. Even though every single high-energy physics experiment needs track-fitting software which essentially provides the same functionality, synergy effects between different experiments have been absolutely minimal up to now.
A novel, generic toolkit for track fitting, called GENFIT, has been designed in the course of the presented PhD project together with Sebastian Neubert at TUM [57]. It has at first been developed in the framework of the $\overline{\text{P}}$ANDA experiment, where it is well established as the standard tool for global track fitting. Moreover, it has been designed as an experiment-independent software for track fitting in high-energy physics. The amount of interface code that has to be developed to use GENFIT is minimal. This is possible due to a completely modular design, which is described in detail in a journal publication on GENFIT [4]. This paper is considered to be an important part of this dissertation and is included in appendix H. The GENFIT source code has been written in the C++ programming language and is available as free software [155]. The GENFIT package has by now become the global track fitter in the computing framework of the Belle-II experiment [156] and is also being used in the GEM-TPC, FOPI, and COMPASS projects.

# Chapter 10

# Conclusion and Outlook

The first determination of the luminosity for data from the muon-scattering program of the COMPASS experiment has been presented. Since the experiment does not feature a dedicated luminosity monitor, the luminosity was determined by the direct measurement of the beam flux on the target and the correction of all inefficiencies and dead times of the measurement. The normalized data set, which consists of about 30% of the muon-deuteron scattering data recorded in 2004, has an effective integrated luminosity of $142.4\,\mathrm{pb}^{-1}$ $\pm 10\%$ (syst.). This result has been successfully checked by the extraction of the structure function $F_2$ of the nucleon and its comparison to literature, and can now be used for the measurement of the cross sections of other processes in muon-deuteron scattering. In the future DVCS program of COMPASS-II, the presented technique for the determination of the luminosity will be the basis for the normalization of the event samples recorded with $\mu^+$ beam and $\mu^-$ beam, respectively.

Based on the luminosity result, the cross section for the quasi-real photoproduction of charged hadrons with high transverse momenta in muon-deuteron scattering at $\sqrt{s} = 17.4\,\mathrm{Gev}$ has been determined. Hadrons produced in secondary reactions in the thick target of COMPASS, i.e. not in the muon-nucleon scattering vertices, are a possible source of background for this measurement. The hadronic-shower models GHEISHA and FLUKA of GEANT3, which has been employed for the acceptance correction, have been demonstrated to be unrealistic in their description of this background. The upper limit of a possible contamination of the high-$p_T$ hadron yield by secondary hadrons has been quantified from the experimental data themselves and defines the main systematic error of the cross section result.

The presented cross section $[\mathrm{d}\sigma/\mathrm{d}p_T]$ reaches up to $p_T = 3.5\,\mathrm{GeV}/c$ and has been determined in bins of the pseudo-rapidity of the hadrons. Its comparison to NLO pQCD calculations serves as a test of the applicability of pQCD to the quasi-real photoproduction process at the COMPASS center-of-mass energy. The ratio of the experimental cross section over the NLO pQCD cross section has a value of three to four independently of $p_T$ beyond values of $p_T \sim 1.75\,\mathrm{GeV}/c$. The ratio of the experimental double-differential cross section $[\mathrm{d}^2\sigma/(\mathrm{d}p_T\mathrm{d}y)]$ over the NLO pQCD result increases monotonically with decreasing $y$ over the full $p_T$ range. It has been discussed that this behavior as well as the analogy to the high-$p_T$ hadron production in proton-proton scattering at fixed-target energies suggest that the all-order resummation of large threshold logarithms in the pQCD calculations might be able to reconcile the presented discrepancies. But since the thresh-

old resummations are not yet available for this process, it is not possible to conclude at this point on whether the quasi-real photoproduction of high-$p_T$ hadrons at COMPASS energies is in the hard-scattering regime, which can be described by pQCD, at least with resummations. The correct description of the spectral shape of the cross section by NLO pQCD is, however, a very positive hint in this direction. If the applicability of pQCD could be established, it would be possible to constrain the polarization of gluons in the nucleon in the range $x_g \in [0.1, 0.3]$ with a comparison of the calculated and experimentally measured double-spin asymmetries of the cross section for the quasi-real photoproduction of high-$p_T$ hadrons at COMPASS.
The discussed cross section is integrated over the values of the photon virtuality from a kinematically allowed minimum to an upper limit $Q^2_{\text{max}}$. It has been shown that the dependence of the cross section on $Q^2_{\text{max}}$ is very similar in the experiment and in NLO pQCD, which provides some confidence in the correct description of the photo-production process via the Weizsäcker-Williams formalism in the pQCD calculations. The comparison of the ratio of the cross sections for the production of negatively-charged hadrons over positively-charged hadrons as a function of $p_T$ between the COMPASS result and NLO pQCD shows a significant disagreement, which might provide interesting constraints to fragmentation functions.
The second part of this dissertation has been devoted to the development of new technologies for charged-particle tracking in high-rate experiments. The use of GEM foils for gas amplification instead of proportional wires in a TPC is a very promising solution for eliminating the need for an ion gate, which is the key for the usability of TPCs in experiments with trigger rates beyond about 1 kHz. Several important contributions to the development and prototyping of a GEM-TPC, including test-beam campaigns at the ELSA facility and at COMPASS, have been discussed. This development has recently culminated in the construction of a large GEM-TPC with $\sim 10,000$ electronic readout channels, 728 mm drift length, and 308 mm outer diameter by the GEM-TPC collaboration. This detector has been integrated in the FOPI spectrometer at GSI, where large data sets with cosmic muons, various heavy-ion beams, and a $\pi^-$ beam have been recorded. The detector performs very well up to high track densities from heavy-ion events. The measured spatial resolution of the TPC agrees well with the expectations from detailed Monte Carlo simulations of the detector. The next step in the development of a GEM-TPC for high-rate experiments will be the test of the detector in an environment of very high interaction rates. The existing GEM-TPC is planned to be operated inside the FOPI spectrometer until $\sim$ 2013 where it will be used for several more physics measurements with pion and proton beams. The construction of another, very similar chamber for an upgrade of the Crystal Barrel experiment at ELSA is foreseen for 2013. The ALICE collaboration has very recently stated its interest for an upgrade of the ALICE TPC with a GEM-amplification stage for the operation of the experiment at higher trigger rates based on the presented technology.
Lastly, the development of an experiment-independent framework for track fitting in high-energy physics, called GENFIT, has been presented. GENFIT has become the standard track-fitting software of the $\overline{\text{P}}$ANDA and Belle-II experiments and is also being used for the reconstruction of the data from the GEM-TPC in the FOPI spectrometer. The different experiments have already benefited greatly from each other through the use of GENFIT and there is much more potential for synergy if the software is employed in more experiments.

# Appendix A

# Statistics of Bad-Spill Removal

The removal of bad spills from the data sample was described in Sec. 5.3. This chapter lists the number of spills that were removed by the individual cuts. There are five bad-spill criteria:

- Spill is in COMPASS bad spill list (**BSL**).
- Spill is below event number ratio (**ENR**) cut (0.0125 below nominal value or below 0.34).
- Spill can not be used because it is not present with more than 1000 events in the **production** with the previous CORAL version, which is needed for the translation of the $t_1 - t_2$ cut into the $nev_1 - nev_2$ cut.
- No data is available in the previous production around the *time-in-spill* $\boldsymbol{t}_1$. In a few spills there are only reconstructed event with e.g. *time-in-spill* $> 3$ s.
- Not enough events are available in spill to extract **DAQ** dead time (*last event number*$<$ 7000 or *last event number - first event number*$<$ 5000) in the latest production.

Table A.1 summarizes the effect of the cuts on the data from the four data-taking periods used in the analysis.

| Period | # spills | BSL | ENR | Production | $t_1$ | DAQ |
|---|---|---|---|---|---|---|
| W28 | 23623 | 5757 (24.4%) | 287 (1.2%) | 439 (1.9%) | 5 | 0 |
| W29 | 20025 | 2201 (11.0%) | 367 (1.8%) | 239 (1.2%) | 0 | 3 |
| W30 | 15666 | 2764 (17.6%) | 2659 (17.0%) | 0 | 75 (0.5%) | 1 |
| W31 | 14277 | 1268 (8.9%) | 2454 (17.2%) | 198 (1.4%) | 249 (1.7%) | 1 |

**Table A.1:** Statistics of bad-spill removal. The cuts are applied from left to right. The quoted numbers indicate how many spills are additionally removed after the previous cut. The percentages refer to the total number of spills in the period.

# Appendix B

# Supplementary Figures and Tables for Chapter 6 on the High-$p_T$ Cross Section

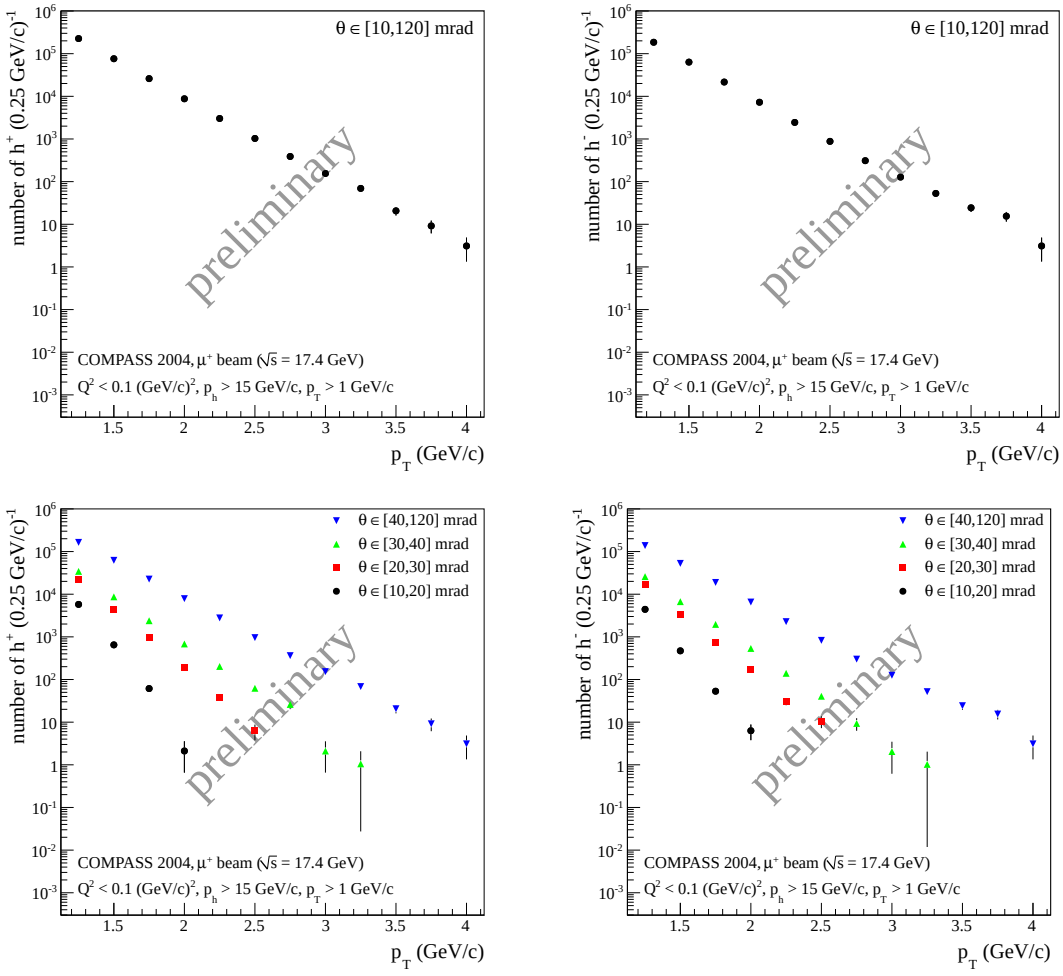


**Figure B.1:** High-$p_T$ particle yields separated by hadron charge. [*referenced from 6.1 (p. 68)*]

## B SUPPLEMENTARY FIGURES AND TABLES FOR CHAPTER 6 ON THE HIGH-$P_T$ CROSS SECTION

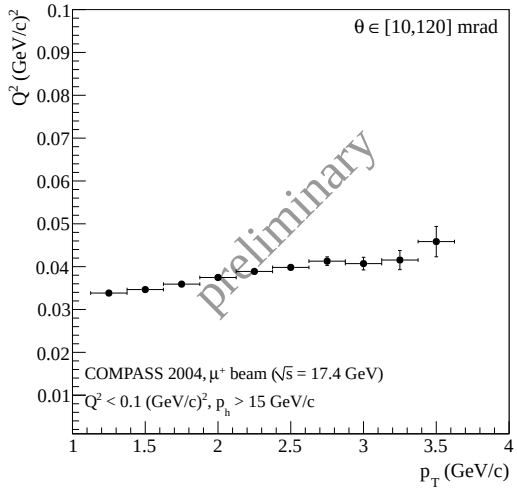


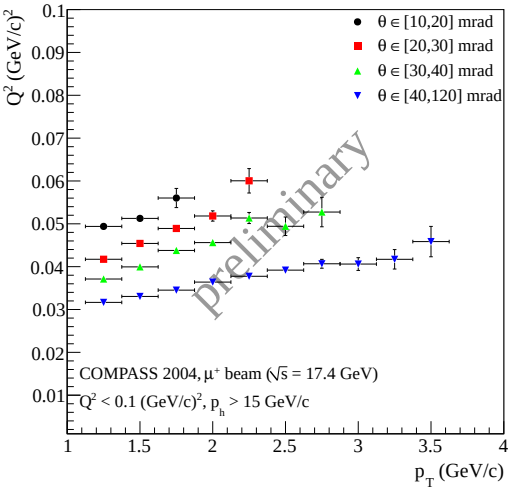


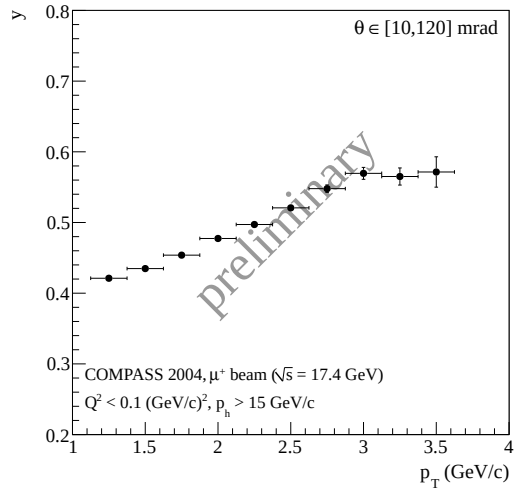


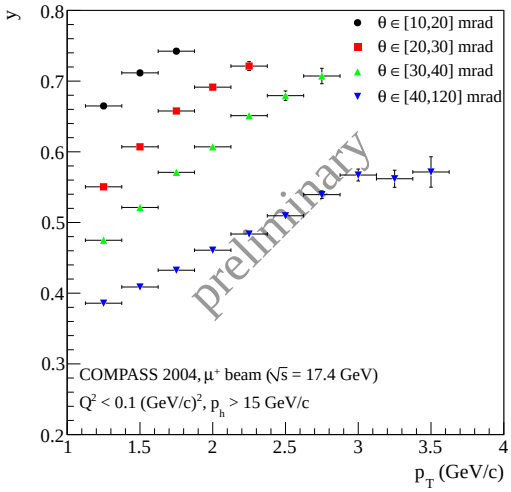


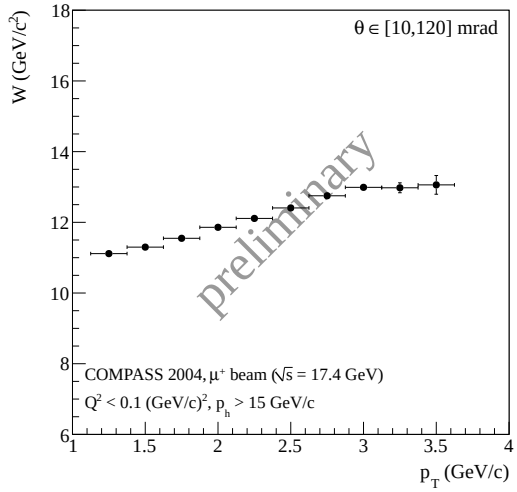


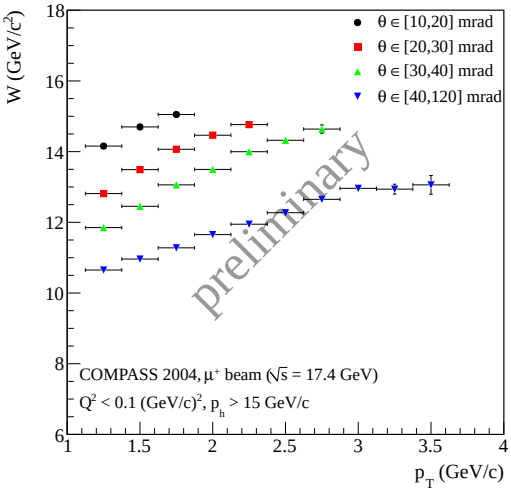

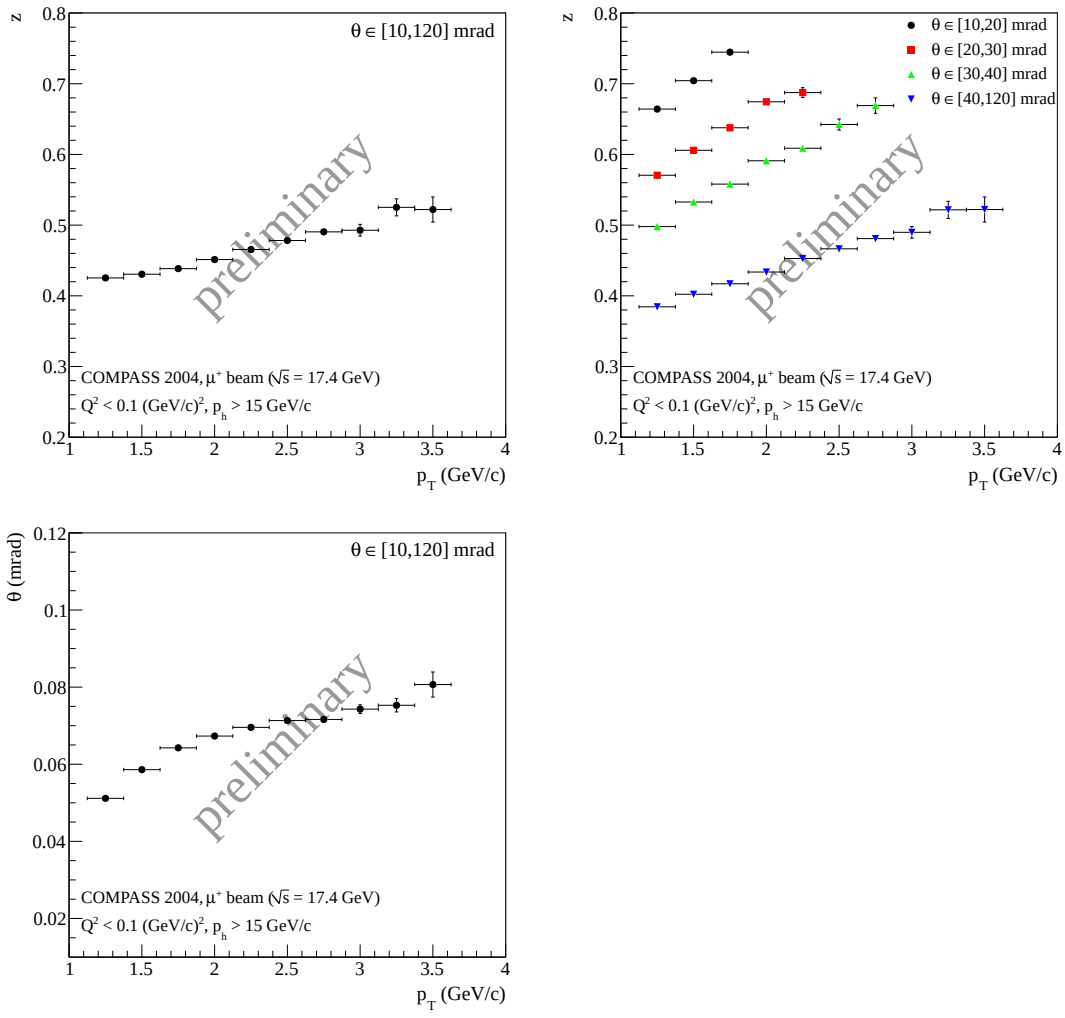


**Figure B.2:** Mean values of the kinematical variables $Q^2$, $y$, $W$, $z$, and $\theta$ as a function of $p_T$ of the final hadron sample. The plots in the left column are not binned in $\theta$, whereas the plots in the right column are binned in $\theta$. [*referenced from 6.1 (p. 68)*]

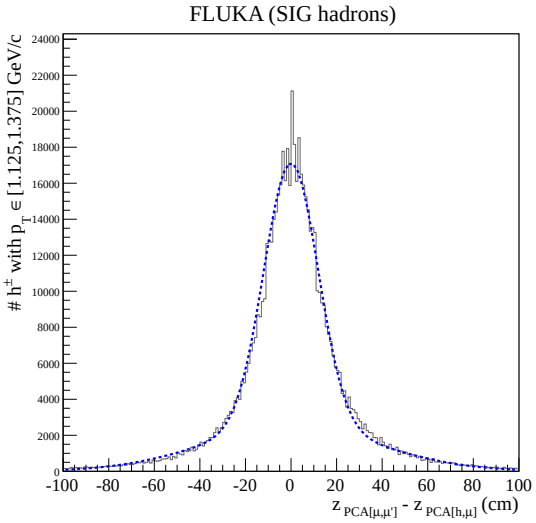


**Figure B.3:** Distribution of $D$ (Eq. (6.3)) for signal hadrons from the simulation with FLUKA. The distribution is fitted with the function $f_{\mathrm{SIG}}$ (Eq. (6.4)), which is centered at zero. [*referenced from 6.3.2 (p. 80)*]

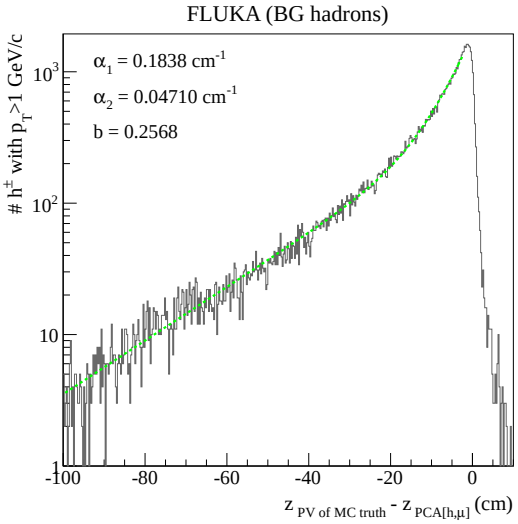


**Figure B.4:** Distribution of $\tilde{D}$ (Eq. (6.5)) for background hadrons from the simulation with FLUKA. The distribution is fitted with the function $g$ (Eq. (6.6)). The fitted parameters of the function $g$ are listed in the plot. [*referenced from 6.3.2 (p. 80)*]

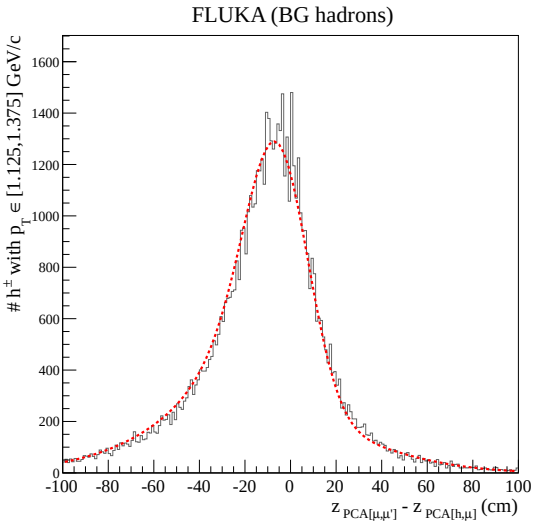


**Figure B.5:** Distribution of $D$ (Eq. (6.3)) for background hadrons from the simulation with FLUKA. The distribution is fitted with the function $f_{\mathrm{BG}}$ (Eq. (6.7)). [*referenced from 6.3.2 (p. 80)*]

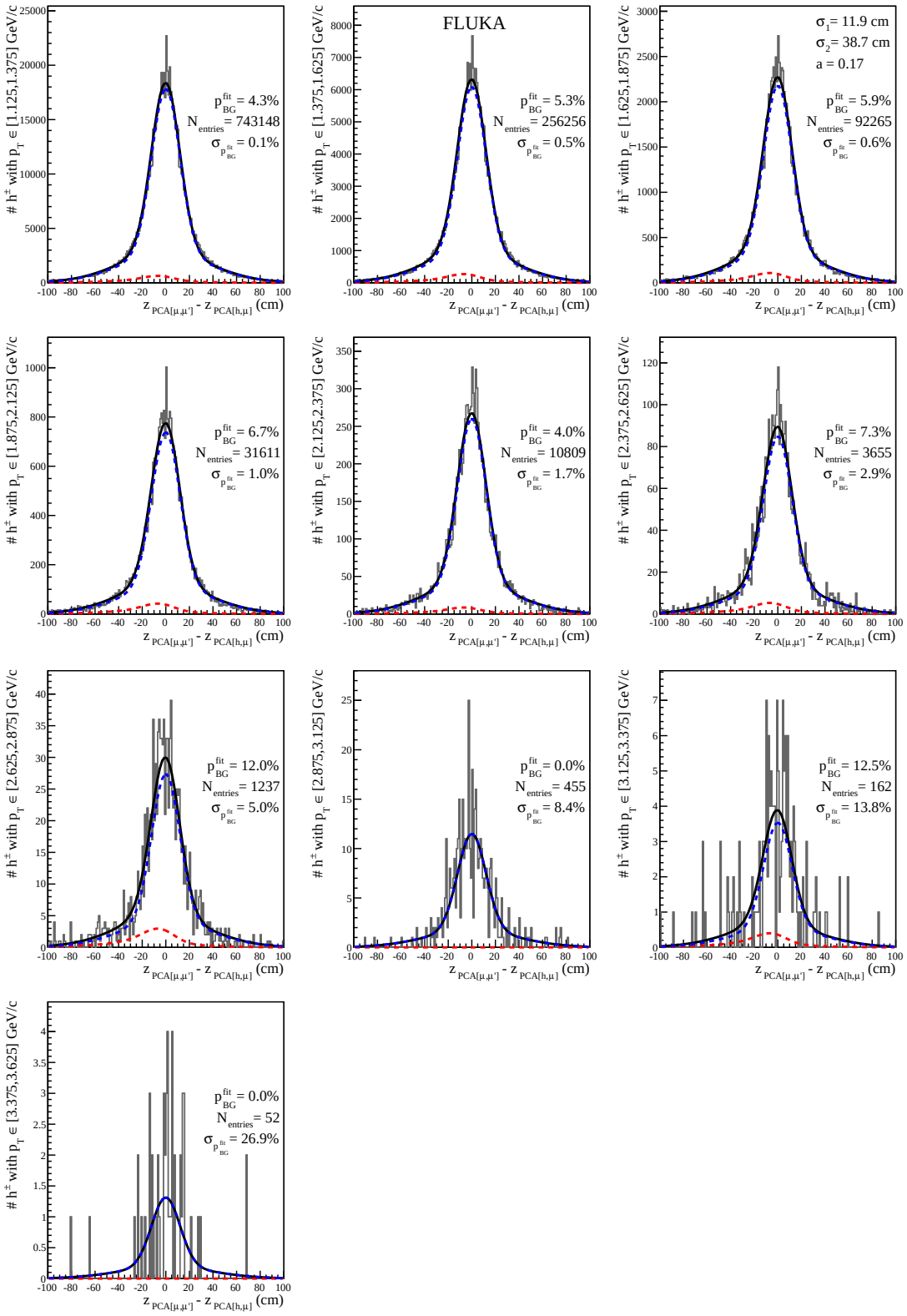


**Figure B.6:** Distributions of $D$ for all hadrons from the simulation with FLUKA in bins of $p_T$. The black lines show the fitted functions $f_{i,\mathrm{ALL}}$, which are the sums of the signal functions $f_{i,\mathrm{SIG}}$ (blue) and the background functions $f_{i,\mathrm{BG}}$ (red). [*referenced from 6.3.2 (p. 80)*]

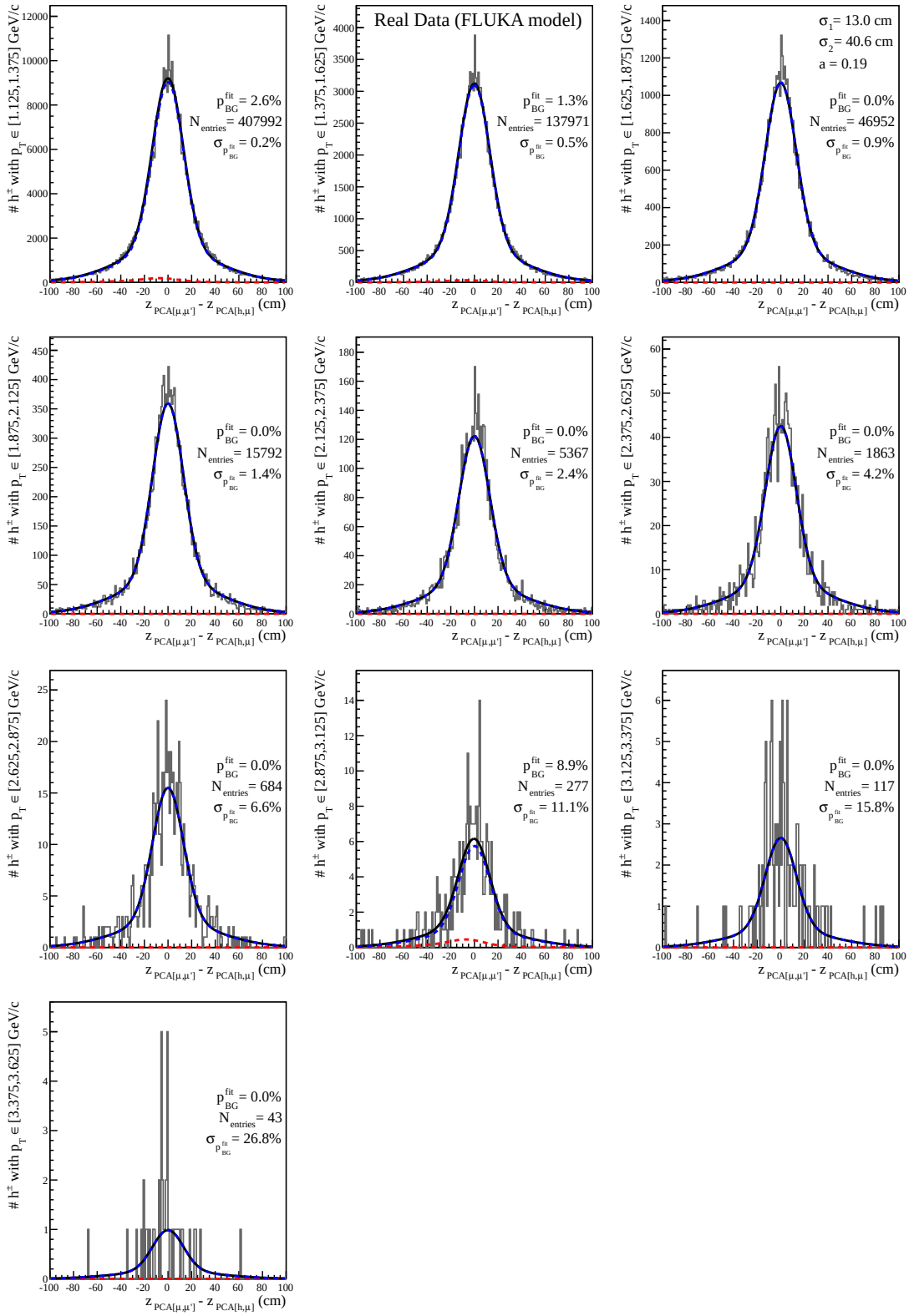


**Figure B.7:** Distributions of $D$ for real data in $p_T$ bins. The fit is performed using the input function $g(\tilde{D})$ from the simulation with FLUKA (Fig. B.4). The black lines show the fitted functions $f_{i,\mathrm{ALL}}$, which are the sums of the signal functions $f_{i,\mathrm{SIG}}$ (blue) and the background functions $f_{i,\mathrm{BG}}$ (red). [*referenced from 6.3.3 (p. 85)*]

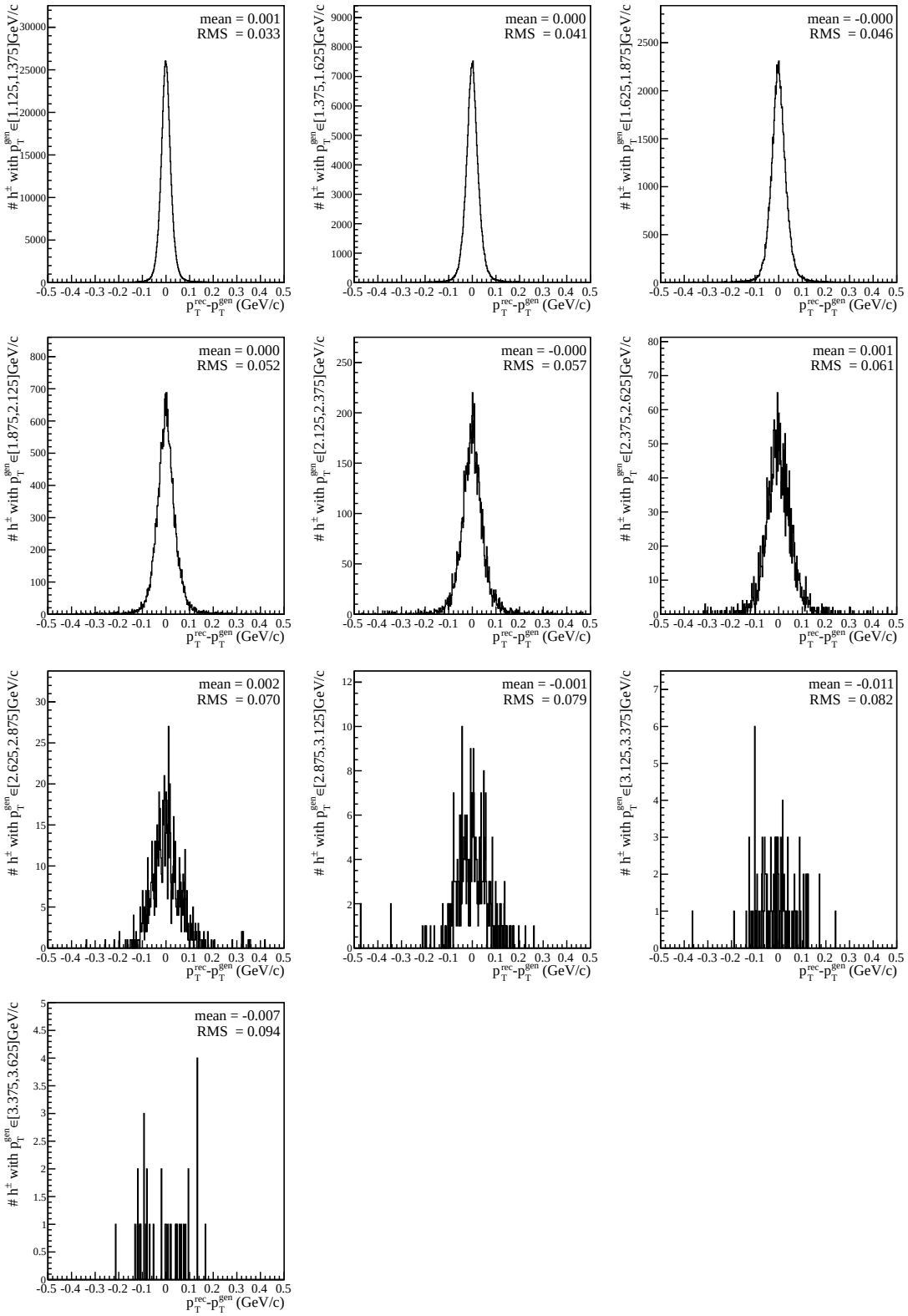


**Figure B.8:** Residuals between reconstructed $p_T$ and generated $p_T$ for tracks from the primary vertex in the MC simulation in different bins of generated $p_T$ (all cuts of Sec. 6.1 are applied). The resolution for the measurement of $p_T$ is characterized by the root mean square (RMS) of the distributions. [*referenced from 6.3.4 (p. 87)*]

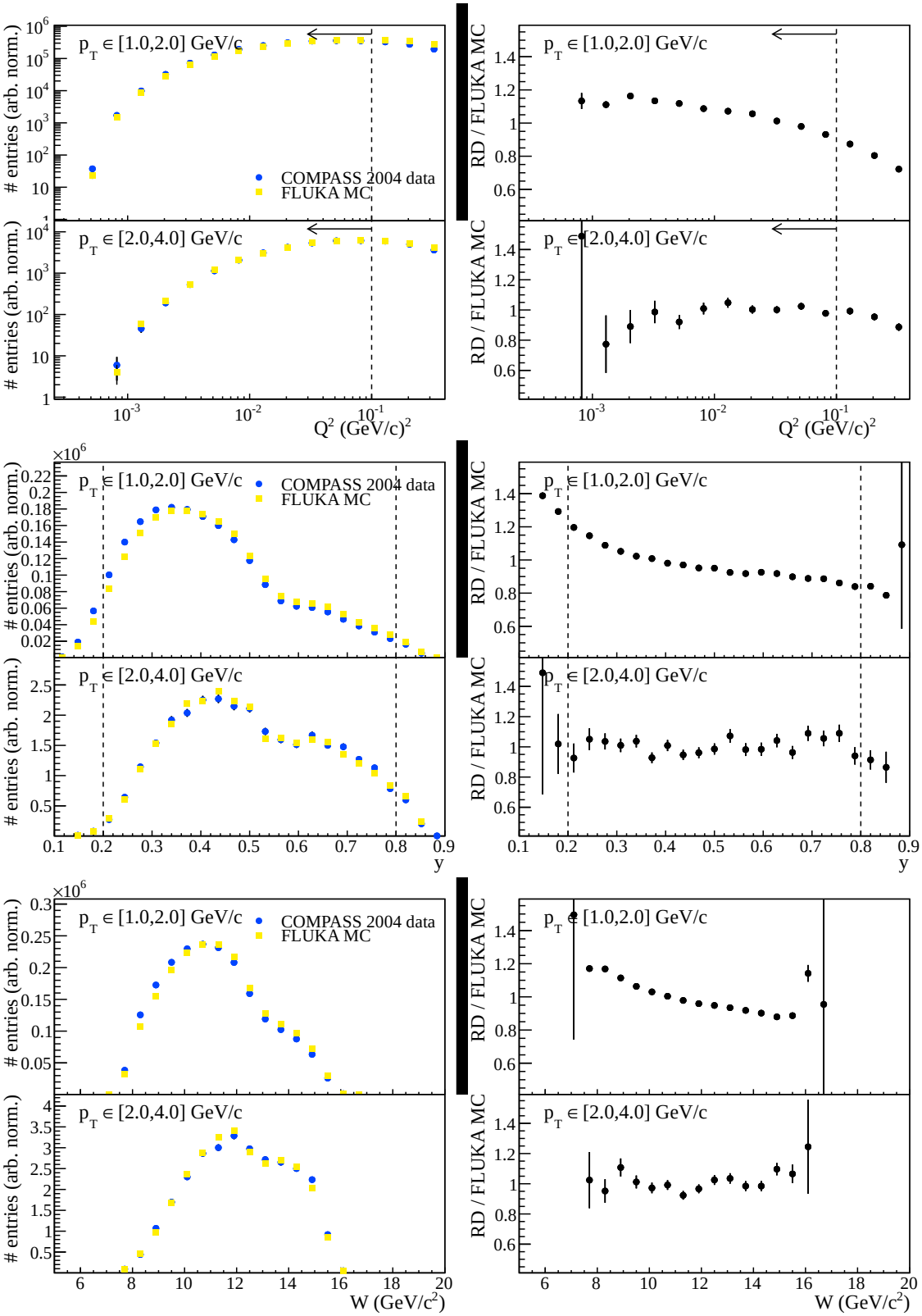


**Figure B.9:** Comparison of kinematical distributions $Q^2$, $y$, and $W$ from real data and FLUKA simulation. The distributions of each variable are independently normalized to have equal integrals inside the ranges defined by the cuts, which are indicated by the dashed lines. [*referenced from 6.3.4 (p. 87)*]

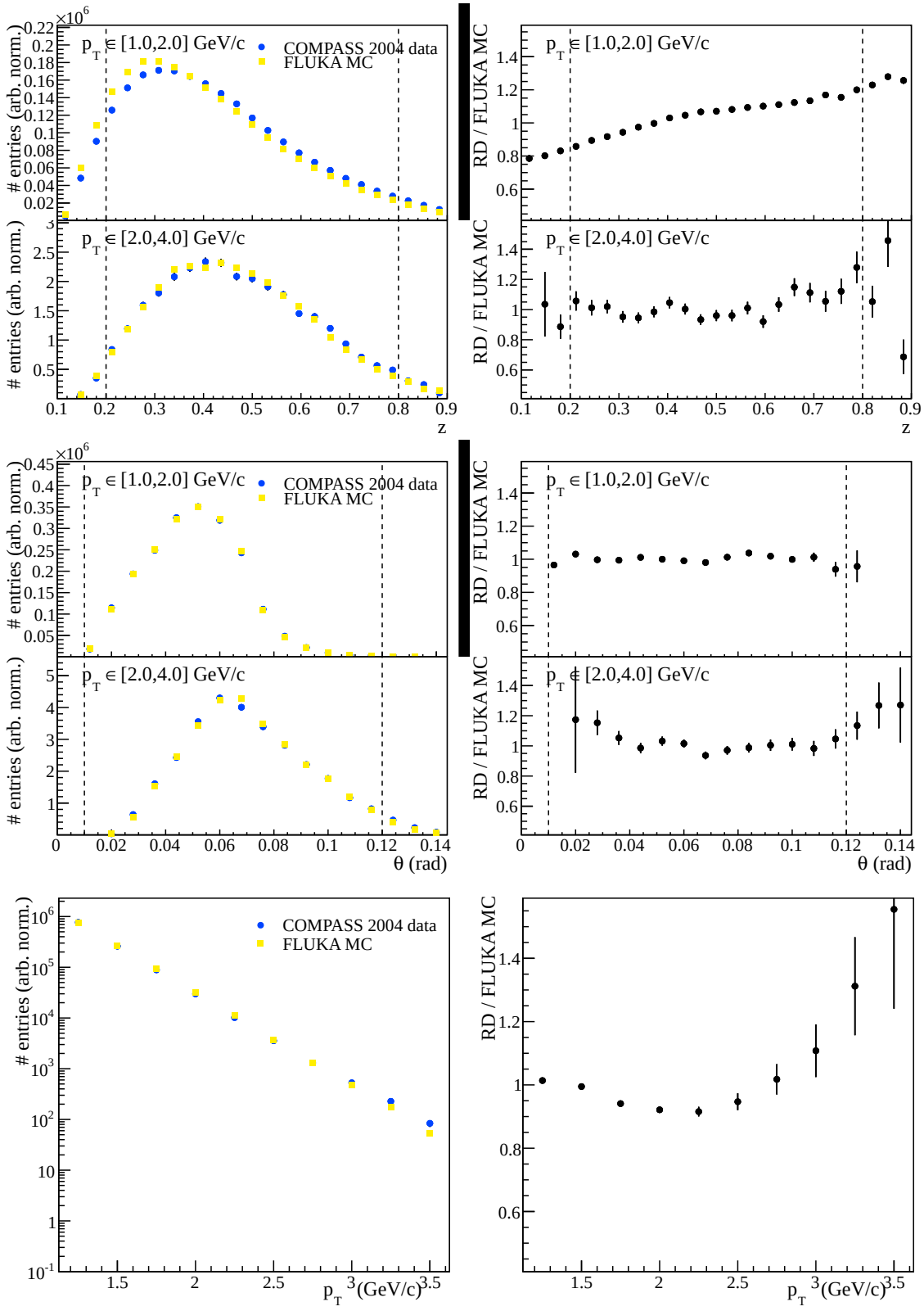


**Figure B.10:** Comparison of kinematical distributions $z$, $\theta$, and $p_T$ from real data and FLUKA simulation. The distributions of each variable are independently normalized to have equal integrals inside the ranges defined by the cuts, which are indicated by the dashed lines. [*referenced from 6.3.4 (p. 87)*]

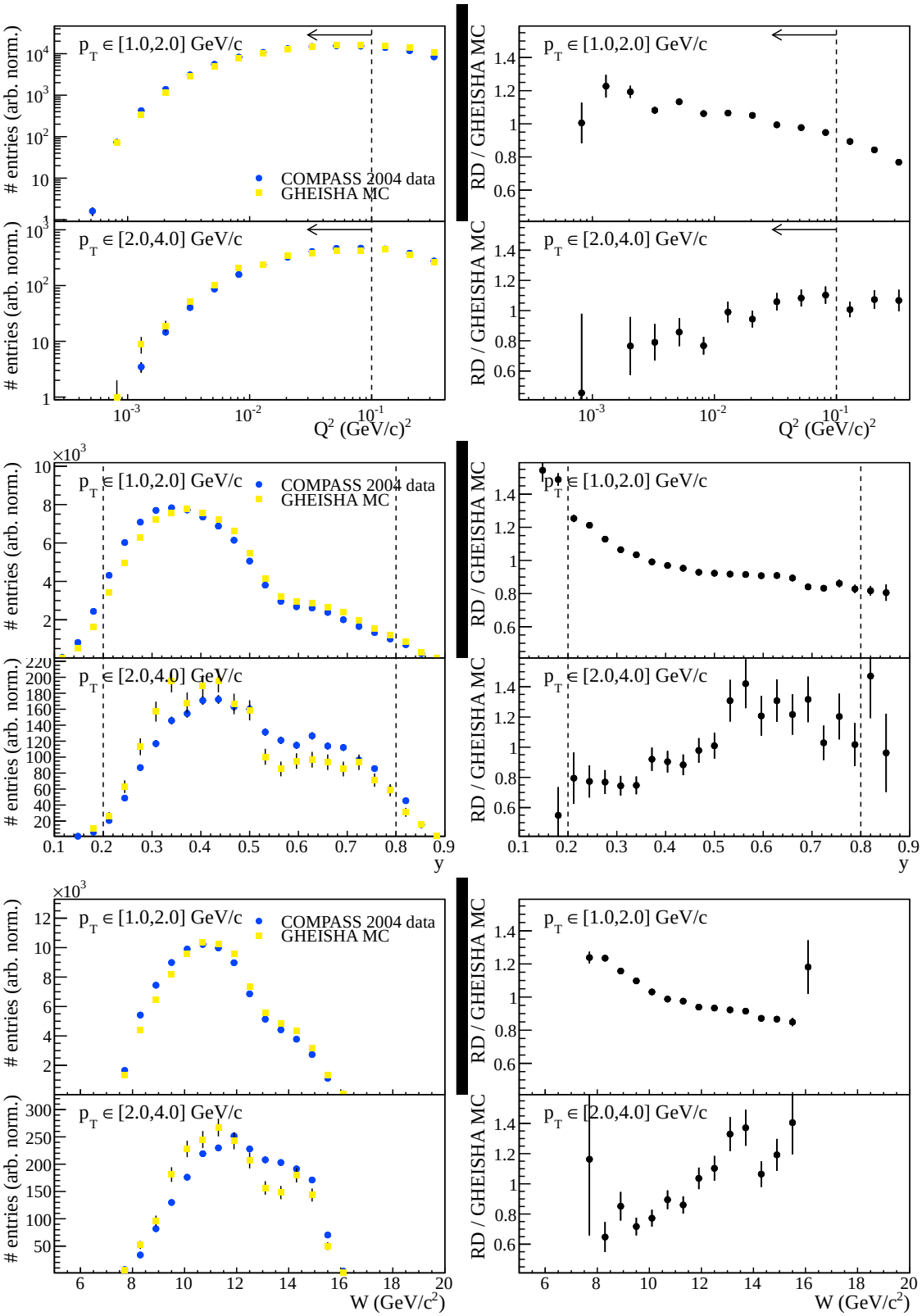


**Figure B.11:** Comparison of kinematical distributions $Q^2$, $y$, and $W$ from real data and GHEISHA simulation. The distributions of each variable are independently normalized to have equal integrals inside the ranges defined by the cuts, which are indicated by the dashed lines. [*referenced from 6.3.4 (p. 87)*]

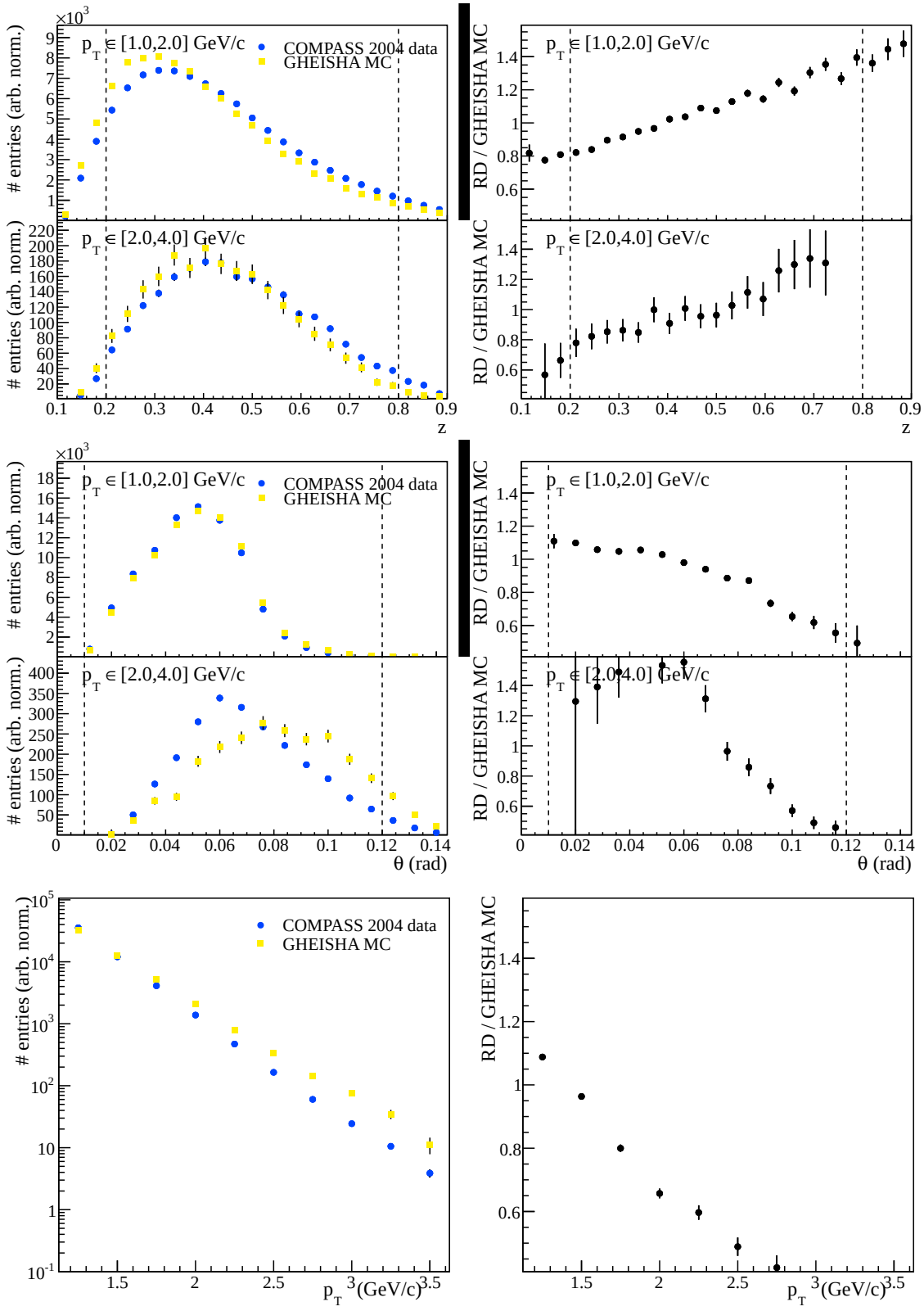


**Figure B.12:** Comparison of kinematical distributions $z$, $\theta$, and $p_T$ from real data and GHEISHA simulation. The distributions of each variable are independently normalized to have equal integrals inside the ranges defined by the cuts, which are indicated by the dashed lines. [*referenced from 6.3.4 (p. 87)*]

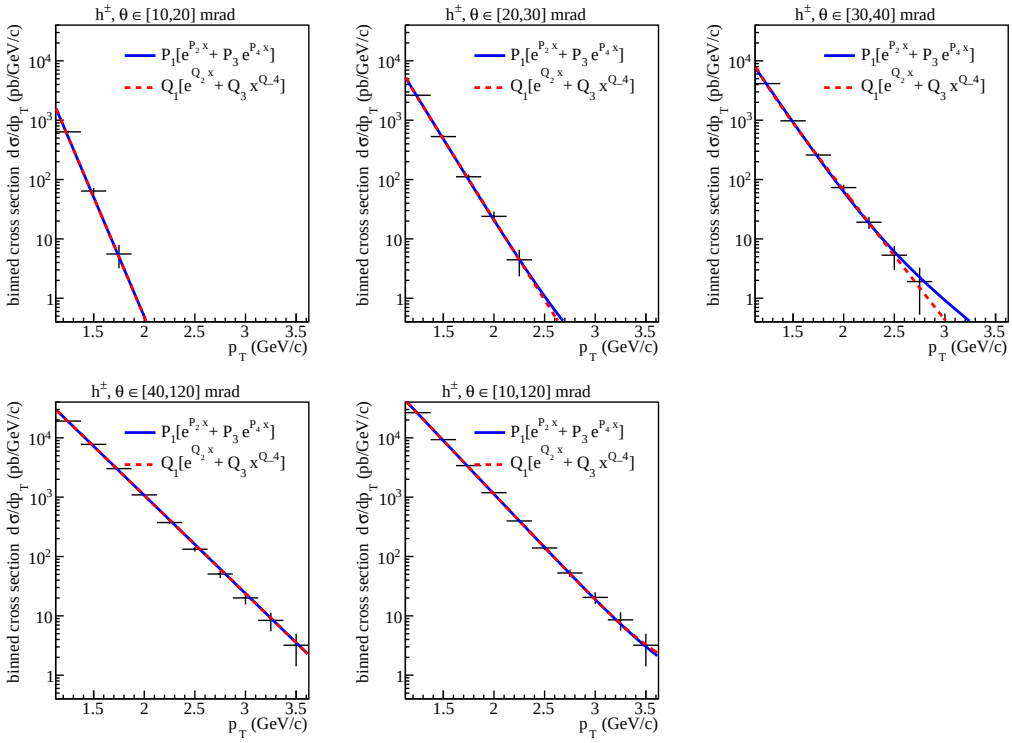


**Figure B.13:** Results of binned-likelihood fits of different parent functions to the binned cross sections for charged hadrons. [*referenced from 6.4.1.2 (p. 95)*]

| $\theta$ bin (mrad) | [1.125, 1.375] | [1.375, 1.625] | [1.625, 1.875] | [1.875, 2.125] | [2.125, 2.375] | [2.375, 2.625] | [2.625, 2.875] | [2.875, 3.125] | [3.125, 3.375] | [3.375, 3.625] |
|---|---|---|---|---|---|---|---|---|---|---|
| [10, 20] | 1.227± 0.000 | 1.477± 0.000 | 1.727± 0.000 | - | - | - | - | - | - | - |
| [20, 30] | 1.233± 0.001 | 1.484± 0.000 | 1.734± 0.000 | 1.984± 0.000 | 2.234± 0.000 | - | - | - | - | - |
| [30, 40] | 1.234± 0.002 | 1.485± 0.000 | 1.736± 0.000 | 1.986± 0.000 | 2.237± 0.000 | 2.487± 0.001 | - | - | - | - |
| [40, 120] | 1.240± 0.000 | 1.490± 0.000 | 1.740± 0.000 | 1.990± 0.000 | 2.240± 0.000 | 2.490± 0.000 | 2.740± 0.000 | 2.990± 0.000 | 3.240± 0.000 | 3.490± 0.000 |
| [10, 120] | 1.239± 0.000 | 1.489± 0.000 | 1.739± 0.000 | 1.989± 0.000 | 2.239± 0.000 | 2.489± 0.000 | 2.739± 0.000 | 2.989± 0.000 | 3.239± 0.000 | 3.490± 0.000 |

**Table B.1:** $p_T$ values of the data points of the cross sections as determined with the Lafferty & Wyatt method. The quoted errors are the systematic uncertainties due to the different choices of the parent distribution. All $p_T$ values are given in GeV/$c$. [*referenced from 6.4.1.2 (p. 95)*]

# Appendix C

# Additional Information on the MC Simulation for the High-$p_T$ Cross Section

| Parameter | Description |
|---|---|
| MSEL=2 | All processes are simulated, including low-$p_T$ scattering, single- and double-diffractive scattering, and elastic scattering. |
| CKIN(5)=0.9 (GeV/$c$) | Lower cut-off for $p_T$ values in processes which are singular in $p_T \to 0$ (default value is 1 GeV/$c$). |
| PARP(99)=0.5 (GeV/$c$) | Width parameter of primordial $k_\perp$-distribution inside photon (default value is 1 GeV/$c$). |
| CKIN(73)=0.05<br>CKIN(75)=0.05<br>CKIN(74)=0.95<br>CKIN(76)=0.95 | Photon energy fraction $y \in [0.05, 0.95]$. The event selection cut on this variable is $y \in [0.2, 0.8]$. |
| CKIN(65)=0<br>CKIN(67)=0<br>CKIN(66)=1.1 (GeV/$c$)<br>CKIN(67)=1.1 (GeV/$c$) | Photon virtuality $Q^2 < 1.1$ (GeV/$c$)$^2$. The event selection cut on this variable is $Q^2 < 0.1$ (GeV/$c$)$^2$. |

**Table C.1:** Tuning of the PYTHIA 6.028 program used for the acceptance correction of the high-$p_T$ cross section. [*referenced from 6.3 (p. 74)*]

| File path | Description |
|---|---|
| */hpss/in2p3.fr/group/compass/users/hoeppner/$PROD* | MC mDST files ($2.3 \cdot 10^9$ events), where *PROD* is one of *FL1, FL2, FL3, FL4, FL5, FL6, FL8, FL9, FLA, FLB, FLC,* and *FLD* |
| */hpss/in2p3.fr/group/compass/users/hoeppner/ config.prod.110407.tgz* | MC configuration files |
| */hpss/in2p3.fr/group/compass/users/hoeppner/ CSoft.prod.beamFix.110330.tgz* | CSoft MC generator package, including the PYTHIA generator |
| */hpss/in2p3.fr/group/compass/users/hoeppner/ Comgeant.prod.110318.tgz* | COMGEANT 7.02 |
| */hpss/in2p3.fr/group/compass/users/hoeppner/ coralNDEBUG.prod.110318.tgz* | CORAL 2007-10-5 libraries |
| */hpss/in2p3.fr/group/compass/users/hoeppner/ MCprodSoftware/phast.7.104NDEBUG.prod.110318.tgz* | PHAST for CORAL |

**Table C.2:** Paths to MC mDST files, as well as the used configuration files and programs on the tape system of CC.IN2P3 at Lyon. [*referenced from 6.3 (p. 74)*]

# Appendix D

# Statistical Errors of the Fits of the Background Content of the High-$p_T$ Yields due to Hadron Showers

The fits of the function $f_{\mathrm{ALL}}$ of Eq. (6.8) to the spectra of the variable $D$ have been shown to be capable of determining the background content of the high-$p_T$ yields due to hadrons picked up from secondary vertices. The variable $D$ denotes the displacement of the point of closest approach between the incoming muon track and the scattered muon track on one hand, and the point of closest approach of the hadron track and the incoming muon track on the other hand. There is a constant missing background fraction of $\delta = 0.06$ in the fit results, but besides that the method works reliably.

This chapter presents a dedicated MC program for the determination of the statistical errors of the background contents as determined with the $f_{\mathrm{ALL}}$ fits, which could depend on the number of entries $N_{\mathrm{entries}}$ in the $D$ distribution and the size of the background content itself. To determine the error for given values of $N_{\mathrm{entries}}$ and the background fraction $p_{\mathrm{BG}}^{\mathrm{input}}$, the program fills 1000 histograms with $N_{\mathrm{entries}}$ entries each from a parent distribution $f_{\mathrm{ALL}}(p_{\mathrm{BG}}^{\mathrm{input}})$ with different seed values. Each of the 1000 histograms is then fitted with the function $f_{\mathrm{ALL}}$ and the background content $p_{\mathrm{BG}}^{\mathrm{fit}}$ from each fit is filled into a histogram. The resulting histogram is of Gaussian shape, from which the sought-after $\sigma_{p_{\mathrm{BG}}^{\mathrm{fit}}}(N_{\mathrm{entries}})$ can be determined with a Gauss fit.

Figure D.1 shows the resulting histograms for a constant $N_{\mathrm{entries}} = 5367$ (corresponding to the number of $h^{\pm}$ in the bin $p_T \in [2.125, 2.375]\,\mathrm{GeV}/c$ of the real data) and varying values of $p_{\mathrm{BG}}^{\mathrm{input}}$. It is apparent that the statistical error of the background fit $\sigma_{p_{\mathrm{BG}}^{\mathrm{fit}}}$ does not depend on $p_{\mathrm{BG}}^{\mathrm{input}}$. The statistical errors for different values of $N_{\mathrm{entries}}$ can hence be determined with a constant $p_{\mathrm{BG}}^{\mathrm{input}}$.

Figure D.2 shows the determination of $\sigma_{p_{\mathrm{BG}}^{\mathrm{fit}}}$ for the $N_{\mathrm{entries}}$ values of the $p_T$ bins of the real data ($p_{\mathrm{BG}}^{\mathrm{input}} = 0.5$). Figure D.3 finally summarizes the $\sigma_{p_{\mathrm{BG}}^{\mathrm{fit}}}$ values for all $N_{\mathrm{entries}}$ values that occur in the real data, the GHEISHA simulation, and the FLUKA simulation. These are the values which are quoted in the plots which show the background fit results (Figs. 6.11 - 6.14, B.6, and B.7)

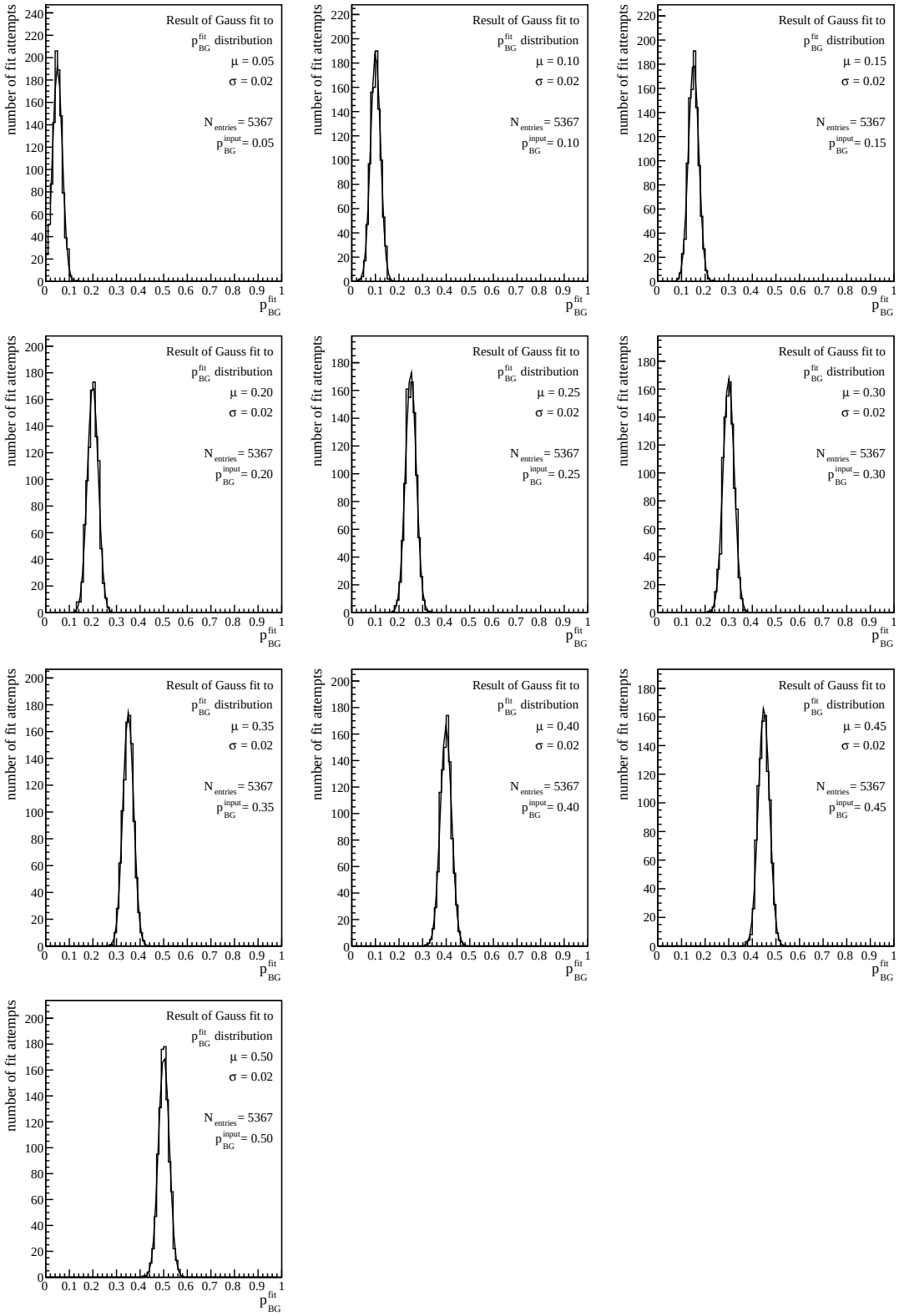


**Figure D.1:** Determination of the statistical errors of the background quantification. The statistical errors do not depend on the size of the background contents themselves.

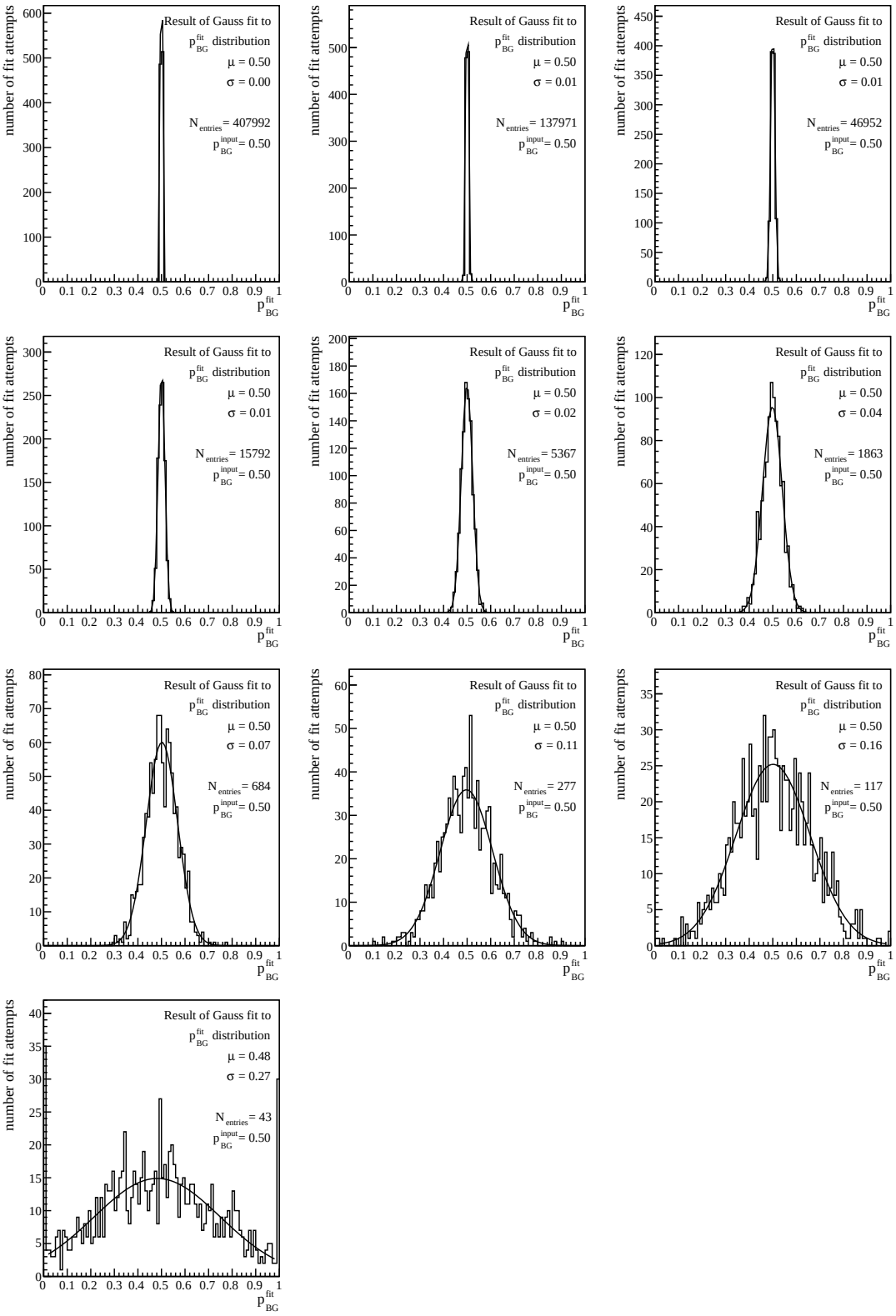


**Figure D.2:** Determination of the statistical errors of the background quantification for the values of $N_{\text{entries}}$ of the $p_T$ bins of the real data. The results for the lowest three $p_T$ bins are not very accurate, because the binning is insufficient. This problem can be ignored because only uncertainties beyond the few-percent level are of interest in this context. [*referenced from 6.3.3 (p. 86)*]

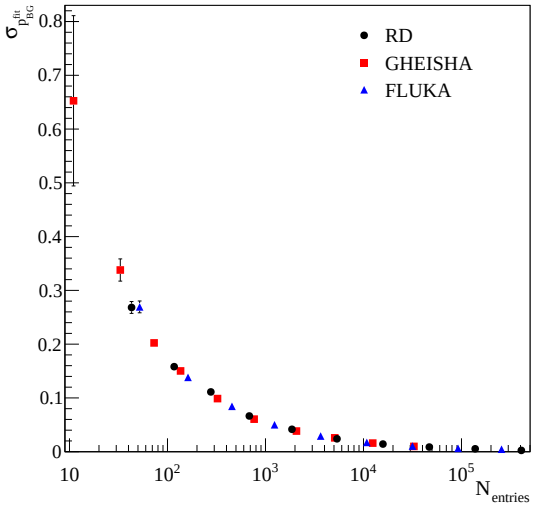


**Figure D.3:** Summary of the statistical errors of the background quantification for all values of $N_{\text{entries}}$ of the $p_T$ bins of the real data, the GHEISHA simulation, and the FLUKA simulation.

# Appendix E

# Systematic Uncertainty due to the One-Dimensional Acceptance Correction

This chapter describes a study that investigates the systematic uncertainty of the hadron production cross section due to the one-dimensional acceptance correction, which is described in Sec. 6.3. For this purpose, the hadron-production cross section, which is corrected for acceptance just in the $p_T$ bins, is compared with the cross section which is corrected for acceptance in two dimensions $(p_T, K)$, where $K$ is one of the kinematical variables $Q^2$, $y$, $x_{\mathrm{Bj}}$, $W$, $z$, or $\theta$. The ratio of the two cross sections in the $p_T$ bin number $i$ is:

$$R_{K,i} = \frac{\sum_j \left( \int_{K_{j,1}}^{K_{j,2}} \int_{p_{T,i,1}}^{p_{T,i,2}} \frac{\mathrm{d}^2\sigma^+}{\mathrm{d}p_T \mathrm{d}K} \mathrm{d}p_T \mathrm{d}K \right) + \sum_j \left( \int_{K_{j,1}}^{K_{j,2}} \int_{p_{T,i,1}}^{p_{T,i,2}} \frac{\mathrm{d}^2\sigma^-}{\mathrm{d}p_T \mathrm{d}K} \mathrm{d}p_T \mathrm{d}K \right)}{\int_{p_{T,i,1}}^{p_{T,i,2}} \frac{\mathrm{d}\sigma^+}{\mathrm{d}p_T} \mathrm{d}p_T + \int_{p_{T,i,1}}^{p_{T,i,2}} \frac{\mathrm{d}\sigma^-}{\mathrm{d}p_T} \mathrm{d}p_T} \quad . \tag{E.1}$$

The sum runs over all the bins in the variable $K$. As defined in Sec. 6.3, the acceptance for the detection of positively charged hadrons or negatively charged hadrons can only be calculated if $N^{\mathrm{gen}}_{i,j,\mathrm{MC}} > 50$ in each bin $i$, $j$. Consequently, the cross section

$$\int_{K_{j,1}}^{K_{j,2}} \int_{p_{T,i,1}}^{p_{T,i,2}} \frac{\mathrm{d}^2\sigma^{+/-}}{\mathrm{d}p_T \mathrm{d}K} \mathrm{d}p_T \mathrm{d}K = \frac{\tilde{N}^{+/-}_{i,j}}{\tilde{L} \cdot \frac{N^{\mathrm{rec},+/-}_{i,j,\mathrm{MC}}}{N^{\mathrm{gen},+/-}_{i,j,\mathrm{MC}}}} \tag{E.2}$$

can only be calculated if the condition $N^{\mathrm{gen},+/-}_{i,j,\mathrm{MC}} > 50$ is fulfilled for both particle charges. The ratio $R_{K,i}$ is only calculated if the cross section of Eq. (E.2) can be calculated for all bins $j$. This requirement leads to the loss of the highest $p_T$ bins in the comparison.

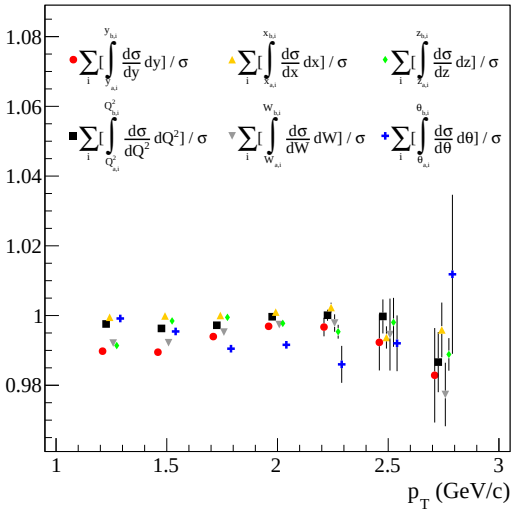


**Figure E.1:** Comparison of cross sections corrected for acceptance in bins of $p_T$ with the cross sections corrected for acceptance in bins of $(p_T, Q^2)$, $(p_T, y)$, $(p_T, x_{\mathrm{Bj}})$, $(p_T, W)$, $(p_T, z)$, and $(p_T, \theta)$ as described in the text.

The binning in the kinematical variables is chosen so that the ratio $R_{K,i}$ can be calculated up to the bin $p_T \in [2.625, 2.875]\,\mathrm{GeV}/c$. The variables $K$ are binned within their selected ranges as follows:

| | |
|---|---|
| $Q^2\,(\mathrm{GeV}/c)^2$ | $[0, 10^{-2.25}]; [10^{-2.25}, 10^{-2}]; [10^{-2}, 10^{-1.75}]; [10^{-1.75}, 10^{-1.5}]; [10^{-1.5}, 10^{-1.25}]; [10^{-1.25}, 0.1];$ |
| $y$ | $[0.2, 0.3]; [0.3, 0.4]; [0.4, 0.5]; [0.5, 0.6]; [0.6, 0.7]; [0.7, 0.8];$ |
| $x_{\mathrm{Bj}}$ | $[0, 10^{-4.25}]; [10^{-4.25}, 10^{-4}]; [10^{-4}, 10^{-3.75}]; [10^{-3.75}, 10^{-3.5}]; [10^{-3.5}, 10^{-3.25}]; [10^{-3.25}, 1];$ |
| $W\,(\mathrm{GeV}/c^2)$ | $[0, 10]; [10, 11]; [11, 12]; [12, 13]; [13, 14]; [14, 15]; [15, \infty];$ |
| $z$ | $[0.2, 0.3]; [0.3, 0.4]; [0.4, 0.5]; [0.5, 0.6]; [0.6, 0.7]; [0.7, 0.8];$ |
| $\theta\,(\mathrm{mrad})$ | $[10, 45]; [45, 65]; [65, 75]; [75, 80]; [80, 85]; [85, 90]; [90, 120].$ |

The ratios $R_{Q^2,i}$, $R_{y,i}$, $R_{x_{\mathrm{Bj}},i}$, $R_{W,i}$, $R_{z,i}$, and $R_{\theta,i}$ are shown in Fig. E.1. The deviations of the ratios from unity are well within 3%. The ratios of the highest $p_T$ bins exhibit statistical fluctuations. These might be due to the subdivision of the data sample into bins which can contain very few hadrons. In some cases there are $N^{\mathrm{rec},+/-}_{i,j,\mathrm{MC}} < 20$ or $\tilde{N}^{+/-}_{i,j} < 20$ hadrons in some bins. The fluctuations might be introduced by summing up cross section values which are subject to statistical fluctuations which do not follow Gaussian statistics.
The size of the fluctuations of the $R_{K,i}$ is quantified as follows: The hadron samples of the real data, reconstructed MC hadrons, and generated MC hadrons are split up into many disjoint subsamples. Each of the disjoint subsamples contains a fraction

$$\frac{\sigma_i}{\sigma_{i-4}} \equiv \frac{\int_{p_{T,i,1}}^{p_{T,i,2}} \frac{\mathrm{d}\sigma}{\mathrm{d}p_T}\mathrm{d}p_T}{\int_{p_{T,i-4,1}}^{p_{T,i-4,2}} \frac{\mathrm{d}\sigma}{\mathrm{d}p_T}\mathrm{d}p_T} \quad . \tag{E.3}$$

of the full statistics. The $p_T$ bin $i$ is compared to the $p_T$ bin $i-4$ so that at least 60 statistically independent subsamples can be created. This is only possible for the three highest $p_T$ bins. The concrete values are calculated from the cross sections of Tab. 6.2:

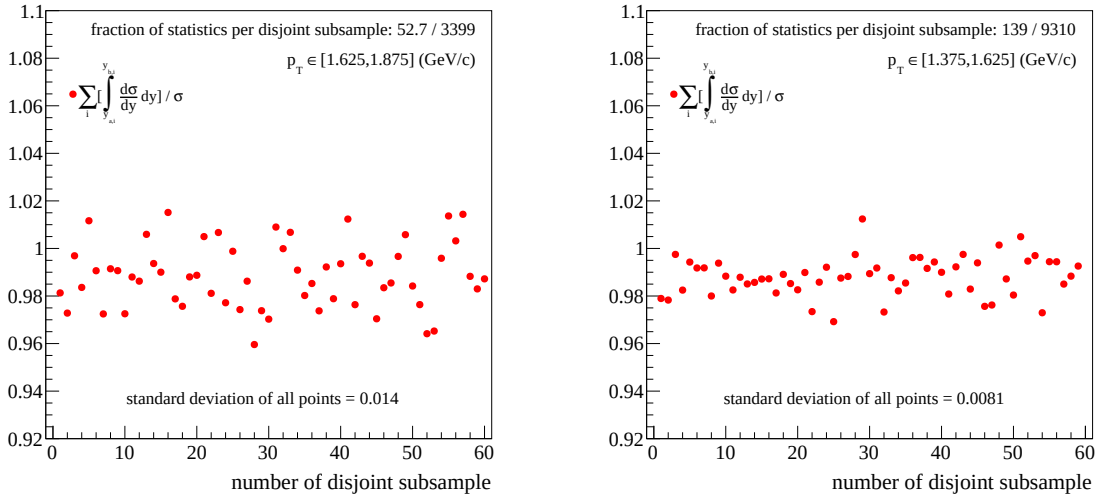


**Figure E.2:** Determination of error of $R_{y,7}$ (left) and $R_{y,6}$ (right) due to the splitting up of the hadron samples into small bins as described in the text.

- Fraction $\sigma_7/\sigma_3 = 52.7/3399$ to determine the fluctuations of $R_{K,7}$ from the standard deviation of 60 values of $R_{K,3}$.
- Fraction $\sigma_6/\sigma_2 = 139/9310$ to determine the fluctuation of $R_{K,6}$ from the standard deviation of 60 values of $R_{K,2}$.
- Fraction $\sigma_5/\sigma_1 = 398/26510$ to determine the fluctuation of $R_{K,5}$ from the standard deviation of 60 values of $R_{K,1}$.

This is shown as an example for the two highest $p_T$ bins and the variable $y$ in Fig. E.2.
The error bars which are shown in Fig. E.1 are determined with this method. It is clearly visible that the increased deviations from unity at the higher $p_T$ values are due to the fluctuation which were just described. Even if the highest $p_T$ values above 3 GeV/$c$ are not covered in this multi-dimensional acceptance study, there is no indication that an effect beyond the 3% level is to be expected.

# Appendix F

# Statistical Errors of Weighted Event Samples

The weighting of events has to be taken into account when the statistical error of the number of events is calculated. A typical situation where such a weighting can occur is the mix of different trigger systems which are subject to different dead times. If there are $m$ different event weighting factors $w_k$ with $N_k$ events each, the weighted number of events is:

$$N = \sum_{k=1}^{m} w_k \cdot N_k \quad . \tag{F.1}$$

If all of the $N_k$ are large enough for the application of Gaussian statistics, the absolute statistical error of $N$ is

$$\sigma_N^2 = \sum_{k=1}^{m} w_k^2 \cdot \sigma_{N_k}^2 = \sum_{k=1}^{m} w_k^2 \cdot N_k. \tag{F.2}$$

Equation (F.1) can be rewritten as

$$N = \sum_{j=1}^{n} w_j \quad , \tag{F.3}$$

where $n$ is the overall number of events, and $w_j$ is event weight of event $j$. There are only $m$ different values of the event weights. Equation (F.2) can be rewritten as

$$\sigma_N^2 = \sum_{j=1}^{n} w_j^2 \quad . \tag{F.4}$$

The weighting factors for the hadron yields that enter into the cross section result of Sec. 6.4 are not discretely distributed. They are due to the dead time of the veto system $V'$ which is used for the Ladder Trigger. This means that they are almost the same for spills with similar beam intensities. The weighting factors in the real data are either close to 1.03 for W28 and W29, or close to 1.06 for W30 and W31. As long as the weighting factors are distributed such that there are always

groups of hadrons with very similar event weights which are large enough for the use of Gaussian statistics, the use of Eq. (F.4) remains justified.
The final relative statistical error which is used for weighted hadron samples is

$$\frac{\sigma_N}{N} = \sqrt{\frac{\sum_{j=1}^{n} w_j^2}{\left(\sum_{j=1}^{n} w_j\right)^2}} \quad . \tag{F.5}$$

# Appendix G

# Schematic of the Analog Part of the High-Voltage Current Meters

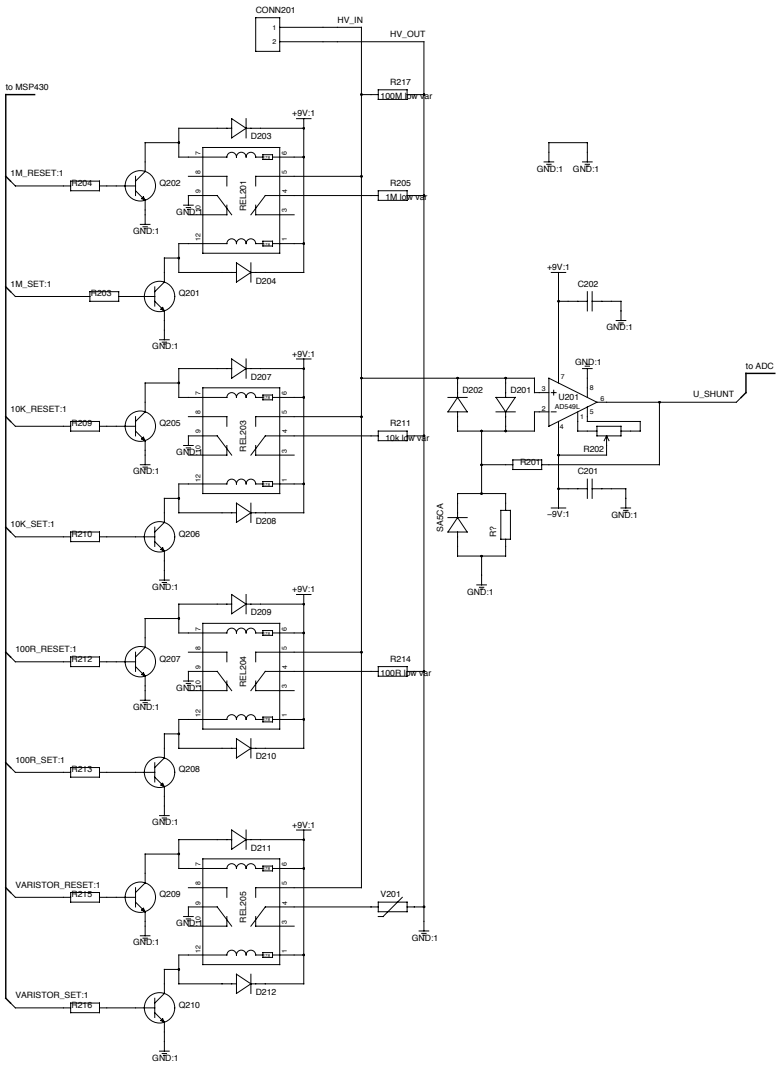

# Appendix H

# Journal Publication on GENFIT

The concepts and principles realized in the GENFIT track-fitting package are introduced and described in detail in the article “A novel generic framework for track fitting in complex detector systems” as published in Nuclear Instruments and Methods in Physics Research A 620 (2010) 518-525. This appendix includes a copy of the article.

Nuclear Instruments and Methods in Physics Research A 620 (2010) 518–525

Contents lists available at ScienceDirect

Nuclear Instruments and Methods in Physics Research A

journal homepage: www.elsevier.com/locate/nima

# A novel generic framework for track fitting in complex detector systems

C. Höppner *, S. Neubert, B. Ketzer, S. Paul

*Technische Universität München, Physik Department, 85748 Garching, Germany*

ARTICLE INFO

*Article history:*
Received 2 November 2009
Received in revised form
23 March 2010
Accepted 25 March 2010
Available online 1 April 2010

*Keywords:*
Track fitting
Track reconstruction
Kalman filter
Drift chamber
TPC

ABSTRACT

This paper presents a novel framework for track fitting which is usable in a wide range of experiments, independent of the specific event topology, detector setup, or magnetic field arrangement. This goal is achieved through a completely modular design. Fitting algorithms are implemented as interchangeable modules. At present, the framework contains a validated Kalman filter. Track parameterizations and the routines required to extrapolate the track parameters and their covariance matrices through the experiment are also implemented as interchangeable modules. Different track parameterizations and extrapolation routines can be used simultaneously for fitting of the same physical track. Representations of detector hits are the third modular ingredient to the framework. The hit dimensionality and orientation of planar tracking detectors are not restricted. Tracking information from detectors which do not measure the passage of particles in a fixed physical detector plane, e.g. drift chambers or TPCs, is used without any simplification. The concept is implemented in a light-weight C++ library called GENFIT, which is available as free software.



## 1. Introduction

Spectrometers in nuclear and particle physics have the purpose of identifying the 4-momenta and vertices of particles stemming from high-energy collisions and decays of particles or nuclei. In addition to calorimetric and other particle identification measurements, the 3-momenta and positions of charged particles are measured by tracking them in magnetic fields with the use of position sensitive detectors. Cluster finding procedures can be applied in some detectors to combine the responses of individual electronic channels in order to improve the accuracy of the position measurements. The position measurements will be referred to as *hits* throughout this paper, regardless of whether they stem from a single detector channel or from a combination of several of them. Pattern recognition algorithms determine which hits contribute to the individual particle tracks. The hits identified at this stage to belong to one track then serve as the input for a fitting procedure, which determines the best estimates for the position and momentum of a particle at any point along its trajectory. A novel framework for this task of track fitting in complex detector systems is presented in this paper. It organizes the task of track fitting, i.e. the interplay between fitting algorithms, detector hits, and particles trajectories, with a minimal amount of interfaces. It is a toolkit which is independent of specific detector setups and magnetic field geometries and hence can be used for many particle physics experiments.

Tracking of particles is usually performed with a combination of different species of detectors. They can be categorized according to the different geometrical information they deliver:

(1) detectors which measure the particle passage along one axis in a detector plane, e.g. silicon strip detectors or multiwire proportional chambers;
(2) detectors which measure the two-dimensional penetration point of a particle through a plane, e.g. silicon pixel detectors;
(3) detectors which measure a drift time relative to a wire position, i.e. a surface of constant drift time around the wire through which the particle passed tangentially, e.g. drift chambers or "straw tubes";
(4) detectors which measure three-dimensional space points on particle trajectories, like time projection chambers (TPC).
But also higher-dimensional hits can occur:
(5) detector systems which measure two-dimensional position information in combination with two-dimensional direction information, including correlations between these parameters. Examples could be stations of several planes of detectors of categories 1 and 2, or electromagnetic calorimeters.

For detectors which do not deliver tracking information in physical detector planes, e.g. those of categories 3 and 4, the track fitting software of many experiments resorts to simplifications, which may be justified for a particular application but prevent the usage of the same program for different experimental environments. Examples are the projection of TPC data onto planes defined by pad rows or the projection of the surfaces of constant

* Corresponding author.
*E-mail address:* christian.hoeppner@cern.ch (C. Höppner).

0168-9002/$ - see front matter © 2010 Elsevier B.V. All rights reserved.
doi:10.1016/j.nima.2010.03.136

drift time in drift chambers onto predefined planes, just leaving two lines with left-right ambiguities. This approach is problematic if the drift cells are not arranged in a planar configuration and if there is no preferred direction in which the detector is passed by the particles. Another common simplification is the treatment of two-dimensional hits (e.g. from silicon pixel detectors) as two independent one-dimensional measurements.

In the framework presented here these problems have been overcome to make optimal use of the information from combinations of all types of tracking detector systems. All detector hits are defined in detector planes. For hits in detectors which do not have physical detector planes, so-called *virtual detector planes* are calculated dynamically for every extrapolation of a track to a hit. The dimensionality of detector hits is not restricted. One-dimensional hits constrain the track only along the coordinate axis in the detector plane which they measure. Two-dimensional hits are used in one fitting step to constrain the track in two dimensions in their detector planes. For hits in non-planar detectors (categories 3 and 4), the hit information (e.g. a surface of constant drift time) is converted into a position measurement in a plane perpendicular to the track, so that a fit is able to minimize the perpendicular distances between the track and the position measurements. The information from hits with higher dimensionality, like those of category 5, is used in four-dimensional hits, which contain all correlations between the parameters.

Tracks of charged particles in magnetic fields are (usually) described by five parameters and a corresponding covariance matrix. The ability to extrapolate a track described by these parameters and their covariances, taking into account the effects of materials and magnetic fields, to different positions in the spectrometer is mandatory for track fitting. The concept presented here provides a well defined interface for the invocation of external programs or libraries to perform these track extrapolations. It thus allows the straightforward use of established track following codes with their native geometry and magnetic field interfaces, such as GEANE [1], which is nowadays distributed as part of CERN's Virtual Monte Carlo (VMC) package [2]. This is the most significant difference to other projects (e.g. RecPack [3]), which offer more monolithic approaches to track fitting (e.g. defining their own geometry classes). The concept allows the simultaneous fitting of several representations of tracks to the same set of hits, i.e. to the same physical track. This flexibility is especially useful in the early phase of an experiment when different track parameterizations and extrapolation approaches can be compared with each other, in order to identify the ones with optimal performance. But also the flexible coverage of different phase space regions with different track models, or the fitting of different mass hypotheses with the same track model can be desirable. The implementation of the concept has been realized in a software toolkit called GENFIT. It is written in C++ and is designed in a fully object oriented way. It has been developed in the framework of the PANDA experiment [4], as part of the computing framework PANDAroot [5], but is now distributed as a stand-alone package [6].

GENFIT contains a validated Kalman filter. This algorithm is commonly used for track fitting in particle spectrometers [7], since it performs much better than global minimization approaches in the presence of materials and inhomogeneous magnetic fields. The concept is, however, not limited to the use of the Kalman filter. Other fitting algorithms, like Gaussian sum filters [8] or deterministic annealing filters [9], can be implemented easily.

Section 2 describes the concept of this new approach to track fitting in detail. Section 3 points out the key features of the implementation of GENFIT. Some examples of concrete track representations, on the dimensionalities of reconstruction hits and track representations, and the interplay between them follow in Section 4. Simulation studies which validate the Kalman filter implemented in GENFIT are presented in Section 5.

## 2. Concept

The basic functionalities which are required for any procedure of track fitting are the extrapolation of tracks to the positions of the hits in the detectors, and the calculation of the distances between hits and tracks, i.e. the residuals. The concept discussed here divides the problem of track fitting into three main entities which are separated from each other as much as possible and interact through well defined interfaces: (1) track fitting algorithms, (2) track representations, and (3) reconstruction hits. Fig. 1 presents this structure. The following sections explain these objects in detail.

### 2.1. Track fitting algorithms

"Progressive" fitting algorithms like the extended Kalman filter [7,10] are widely used for track fitting in high energy physics experiments. Although the track fitting concept discussed in this paper is not limited to the use of the Kalman filter, this algorithm shall serve as an example to illustrate which functionalities are generally required.

The extended Kalman filter is an efficient recursive algorithm that finds the optimum estimate $\vec{x}_k$ for the unknown true state vector $\hat{\vec{x}}_k$ of a system from a series of noisy measurements, together with the corresponding covariance matrix $C_k$ of $\vec{x}_k$. The state vector contains the track parameters and the index $k$ indicates that the state vector, and its covariance matrix are given at the detector plane of hit $k$.

Before a recursion step, the state vector $\vec{x}_{k-1}$ and covariance matrix $C_{k-1}$ contain the information of all hits up to index $k-1$. In the *prediction* step the state vector and covariance matrix are extrapolated to the detector plane of hit $k$ by the track following code. The predicted state vector is denoted by $\tilde{\vec{x}}_k$ and the predicted covariance matrix by $\tilde{C}_k$. This covariance matrix is the sum of the propagated track covariance matrix $C_{k-1}$ (Gaussian error propagation by transformation with the Jacobian matrix of the propagation operation $\tilde{\vec{x}}_k = f(\vec{x}_{k-1})$), and a noise matrix which takes into account effects like multiple scattering and energy loss straggling. Then, the algorithm calculates the *update* for the state vector and the covariance matrix by taking into account the measurement $\vec{m}_k$:

$$\vec{x}_k = \tilde{\vec{x}}_k + K_k \tilde{\vec{r}}_k \tag{1}$$

$$C_k = (I - K_k H_k)\tilde{C}_k \tag{2}$$

with the residual

$$\tilde{\vec{r}}_k = \vec{m}_k - H_k \tilde{\vec{x}}_k \tag{3}$$

the weight of the residual (or Kalman gain)

$$K_k = \tilde{C}_k H_k^T (H_k \tilde{C}_k H_k^T + V_k)^{-1} \tag{4}$$

and the covariance matrix $V_k$ of the measurement $\vec{m}_k$. $I$ is the unit matrix of corresponding dimensionality. The projection matrix $H_k$ is a linear transformation from the coordinate system of the state vector $\vec{x}_k$, to the coordinate system of the position measurement $\vec{m}_k$ of hit $k$, i.e. the detector plane of the hit. A discussion about dimensions of the vectors and matrices in the above equations can be found in Section 4.2 together with concrete examples for the matrix $H_k$. The elements of the covariance matrix $C_k$ shrink with the inclusion of more hits, thus reducing the impact of a

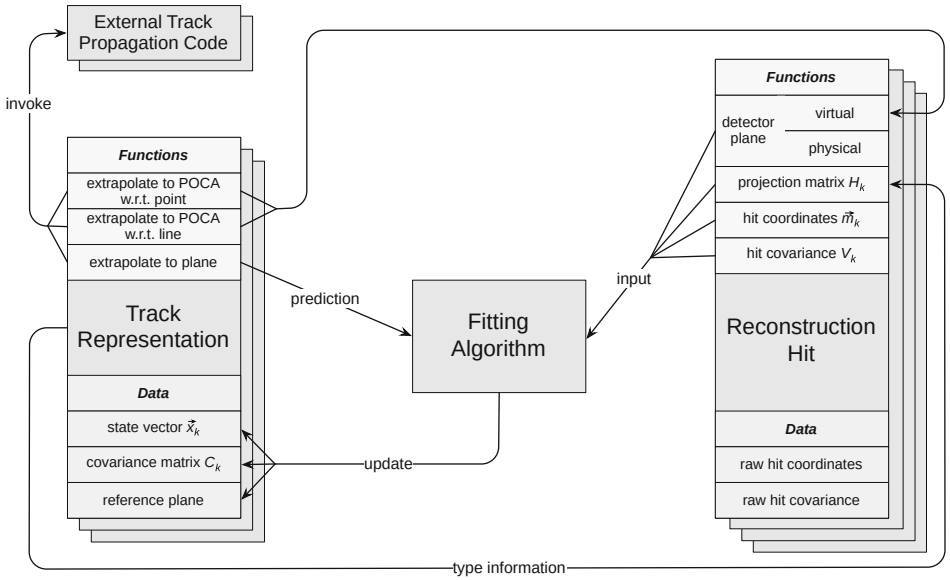


**Fig. 1.** General structure of objects for track fitting: fitting algorithm, track representation, and reconstruction hit. The arrows indicate the interactions between the objects, which are described in this chapter. POCA stands for point of closest approach.

single hit on the value of the state vector. The $\chi^2$- contribution of hit $k$ is $\chi^2_k = \vec{r}_k^T(V_k - H_k C_k H_k^T)^{-1}\vec{r}_k$ with the filtered residual $\vec{r}_k = \vec{m}_k - H_k\vec{x}_k$. It adds $\dim(\vec{m}_k)$ degrees of freedom to the total $\chi^2$.

After the Kalman steps have been performed on all hits of the track, the track can still be biased due to wrong starting values $\vec{x}_0$. This bias can be reduced by the repeated application of the procedure in the opposite order of hits, using the previous fit result as starting values for the track parameters. Before the fit is repeated, the elements of the covariance matrix have to be multiplied with a large factor ($\mathcal{O}(1000)$) in order not to include the same information in the track several times.

As can be seen in Fig. 1 the fitting algorithm operates on entities called reconstruction hits and track representations, which are detailed in the following.

### 2.2. Track representations

A particle track is described by a set of track parameters and a corresponding covariance matrix, which are defined at a given position along the track. Often, the track parameters are e.g. given at a particular $z$-position. In the concept presented here, track parameters are always defined in reference planes.

In order to use a track model in a track fitter, one needs to be able to extrapolate the track parameters to different places in the spectrometer. The combination of the track parameterization and the track extrapolation functionality will be called a *track representation*. A track representation holds the data of the state vector $\vec{x}_k$, and the covariance matrix $C_k$ of a track, as well as the reference plane at which these are defined. Also it provides a well defined interface for the invocation of the external routines needed to extrapolate the parameters to different positions. As can be seen in Fig. 1, there are three track extrapolation functions which are needed for each track representation: Extrapolation to a plane, extrapolation to the point of closest approach (POCA) to a point, and extrapolation to the point of closest approach to a line. Fitting algorithms access the track parameters and extrapolation functions in a common way via the track representation interface without knowledge of the specific form of the track parameterization or the way the extrapolations are carried out.

Different track representations can be used in parallel. It is possible to fit the same track, i.e. the same set of hits, with different track representations simultaneously. There are several reasons why this is desirable: For low momentum particles the fitting of different mass hypotheses with the same track representation can give a clue to the particle identity via the $\chi^2$ of the fits, because the different energy loss for different particle masses at a given momentum leads to different extrapolations. Fitting of the same track with different parameterizations and extrapolation tools can be advantageous as well. In the early phase of an experiment one can compare different track representations to identify the ones which perform best, or there could be regions in phase space in experiments where it might not be clear beforehand which track representation will give the best results. Then one can just fit several of them simultaneously and retain the best result.

### 2.3. Reconstruction hits

The object which represents a position measurement from a detector used in a track fit is called a *reconstruction hit*. It contains the vector of the raw measurement coordinates and its corresponding covariance matrix. As discussed in the introduction, the nature of this raw hit information can be quite diverse. It can e.g. be a direct position measurement or a drift time. As can be seen in Fig. 1, a reconstruction hit provides its detector plane, the measurement coordinates $\vec{m}_k$ in the detector plane coordinate system, the covariance matrix $V_k$ in the detector plane coordinate system, and the projection matrix $H_k$ to the fitting algorithm. For detectors, which measure positions in a physical detector plane (categories 1 and 2 of Section 1), the detector plane is identical with the physical plane.

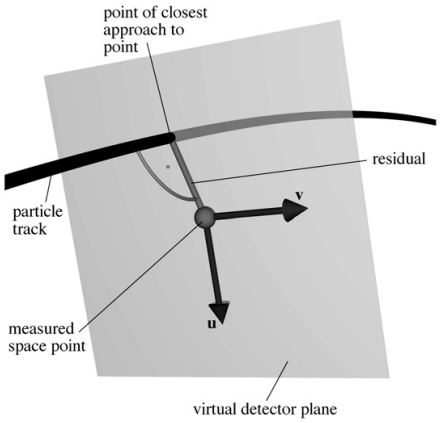


**Fig. 2.** Virtual detector plane (spanning vectors $\vec{u}$ and $\vec{v}$) for a space-point hit.

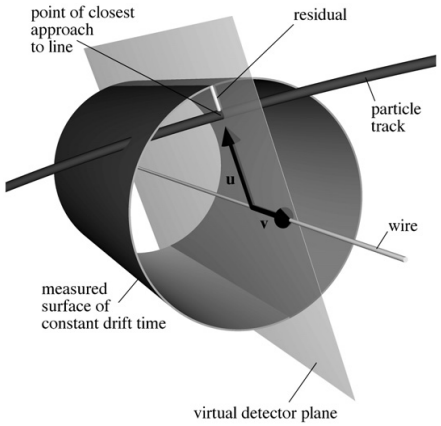


**Fig. 3.** Virtual detector plane (spanning vectors $\vec{u}$ and $\vec{v}$) for a wire-based drift detector.

For non-planar detectors like wire-based drift chambers or TPCs (categories 3 and 4 of Section 1), no such physical detector planes are defined. Instead, the concept of virtual detector planes is introduced. For space-point detectors, the track fit has to minimize the perpendicular distances of the track to the hits. Therefore, the virtual detector plane for each hit must contain the hit position and the point of closest approach of the track to the hit point. Then the residual vector which points from the hit point to the point of closest approach will be perpendicular to the track. This geometry is illustrated in Fig. 2. The orientation of the spanning vectors $\vec{u}$ and $\vec{v}$ is chosen arbitrarily in the plane. For wire-based drift detectors the virtual detector plane contains the point of closest approach of the track to the wire, and is oriented to contain the whole wire. The spanning vectors are chosen to lie perpendicular ($\vec{u}$) and along ($\vec{v}$) the wire. This geometry is presented in Fig. 3. The wire position and drift time are then measurements of $u$ (the $v$ coordinate could be measured via double-sided readout with charge sharing or time of propagation). In both cases, the orientation of the plane will directly depend on the track parameters. The consequence is that virtual detector planes have to be calculated each time a hit is to be used in a fitting step. The reconstruction hit uses the corresponding extrapolation function of the given track representation to find the point of closest approach as indicated in Fig. 1.

Different kinds of reconstruction hits are accessed via a common interface. When the fitting algorithm obtains the detector plane from a reconstruction hit, it does not know whether it will receive a physical or a virtual detector plane. This distinction is fully handled inside the reconstruction hit.

After the detector plane is defined, the reconstruction hit can provide the measurement coordinate vector $\vec{m}_k$, and the hit covariance matrix $V_k$. For non-planar detectors, these quantities are results of coordinate transformations into the virtual detector plane (hence the difference between the raw hit coordinates/covariance and the vector $\vec{m}_k$ and matrix $V_k$ in Fig. 1). The three-dimensional hit vector and the $3\times3$ covariance matrix of a space-point hit are transformed into a two-dimensional vector in the detector plane and a $2\times2$ covariance matrix. Even if the errors of the space point were uncorrelated, the matrix $V_k$ will in general contain a correlation, which is taken into account in the fit. For wire-based drift chambers, the drift time information is converted to a position information in the calculation of $\vec{m}_k$ and $V_k$.

The projection matrix $H_k$ transforms the state vector from the given track parameterization into the coordinate system of the hit. In order to determine this matrix, the concrete coordinate systems of the track representation and the reconstruction hit must be known. Since there will be typically more different types of reconstruction hits than track representations, the projection matrix is determined in the reconstruction hit object. The matrix $H_k$ provides the only link between a given track parameterization and the different hit coordinate systems. If a fit is performed with several track representations, the same reconstruction hit will provide a different matrix $H_k$ for each track representation.

## 3. Implementation—GENFIT

The software package which implements the concept presented in this paper is called GENFIT [6]. It is completely written in C++ and makes extensive use of object oriented design. It uses the C++ standard template library [11] and the ROOT data analysis framework [12].

Fig. 4 presents the general class structure of GENFIT. The classes representing the fitting algorithms operate on instances of the class `GFTrack`[1]. A `GFTrack` object contains a `std::vector<GFAbsRecoHit*>` and a `std::vector<GFAbsTrackRep*>`. The reconstruction hits and track representations of Sections 2.2 and 2.3 are realized as polymorphic classes. The class `GFAbsRecoHit` is the interface class to the reconstruction hits, and `GFAbsTrackRep` is the interface class to the track representations.

The reconstruction hit objects are created from the position information acquired in the detectors. The pattern recognition algorithms, which precede the use of GENFIT, determine which of these detector hits belong to a certain track. They deliver an instance of the class `GFTrackCand`, which holds a list of indices which identify the hits belonging to the track. A mechanism called `GFRecoHitFactory` has been implemented to load the reconstruction hits into the `GFTrack` object.

### 3.1. Track representations

In order to use a particular track parameterization for track fitting in GENFIT, one needs code which can extrapolate such track parameters, taking into account material effects on the track parameters and their covariance matrix. In order to interface the

[1] class names or other code fragments are set in `typewriter font`.

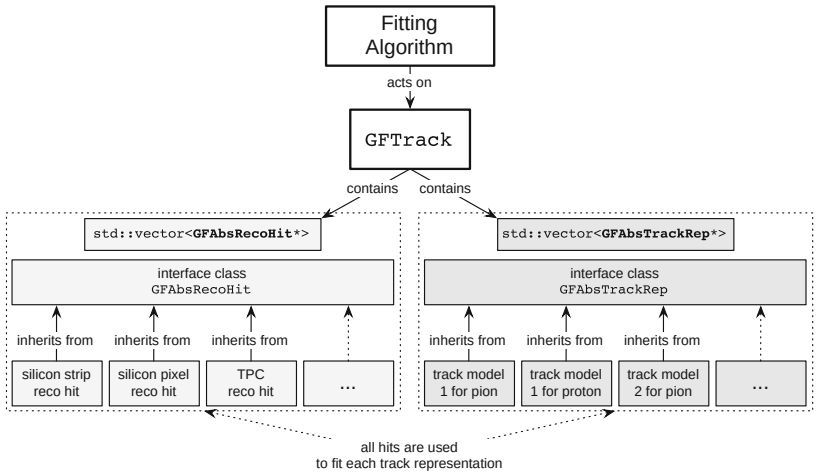


**Fig. 4.** Class structure of GENFIT. The detailed inheritance structure of reconstruction hits is shown in Fig. 5.

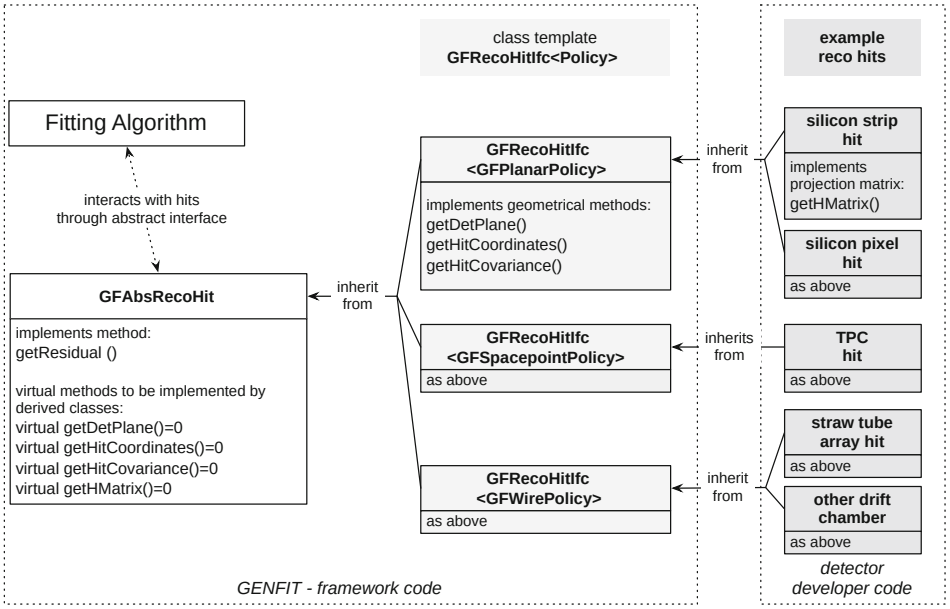


**Fig. 5.** Inheritance structure of reconstruction hits in GENFIT.

track model to GENFIT, one implements a C++ class which inherits from the abstract base class `GFAbsTrackRep` and provides an implementation for the virtual methods `extrapolate(...)`, `extrapolateToPoint(...)`, and `extrapolateToLine(...)`. Section 4.1 presents examples of concrete track representations.

### 3.2. Reconstruction hits

The fitting algorithms interact with the reconstruction hits via the abstract base class `GFAbsRecoHit`. The reconstruction hits do, however, not inherit directly from this class, but from the intermediate interface class

`GFRecoHitIfc<Policy>`. This is illustrated in Fig. 5. For more information about the policy design pattern, please see [13]. There are (currently) three geometrical categories of reconstruction hits: Hits in planar detectors, space-point hits, and hits in wire-based drift chambers, which deliver their wire position and a drift time. This categorization is expressed in the code by the three different policy classes `GFPlanarPolicy`, `GFSpacepointPolicy`, and `GFWirePolicy`. These policy classes all implement functions for calculating or delivering the detector plane, the hit coordinates in the detector plane, and the hit covariance matrix in the detector plane. They are used to unify the geometrical properties of reconstruction hits to avoid any code duplication in the implementation of similar reconstruction hits.

The latter two policies use the corresponding track representations to calculate the virtual detector planes, as detailed in Section 2.3.

As described in Section 2.1, the fitting algorithm needs a matrix $H_k$ which is a linear transformation from the vector space of track parameters to the coordinate system defined by the detector plane. The virtual method

`GFAbsRecoHit::getHMatrix(...)` is overridden in the implementations of the concrete reconstruction hits. In order to provide the correct matrix, the reconstruction hit determines the concrete type[2] of the track representation it is asked to interact with in this particular fitting step. This type checking is represented by the lower arrow in Fig. 1. It is the only place in GENFIT where a direct type compatibility of tracks and hits is checked. A maximal modularity of the system is achieved through this mechanism. If one adds an additional track representation, it is quite obvious that one has to provide new coordinate transformations from this new parameter space into the coordinate systems in which the hits are defined.

## 4. Examples

### 4.1. Concrete track representations

A concrete interface to an external track propagation package which has been realized with GENFIT is the track representation called `GeaneTrackRep2`. It is based on the FORTRAN code GEANE. The detector geometry is included via the `TGeo` classes of ROOT [12] and the magnetic field maps are accessed via a simple interface class called `GFAbsBField`. State vectors for this track representation are defined as $\vec{x}_k=(q/|\vec{p}|,du/dw,dv/dw,u,v)^T$, where the detector plane is spanned by the vectors $\vec{u}$ and $\vec{v}$ (normal vector $\vec{w}=\vec{u}\times\vec{v}$). $q$ denotes the particle charge and $\vec{p}$ is the particle momentum. The quantitative tests of GENFIT in Section 5 are carried out with this track representation.

Another track representation included in the GENFIT distribution is called `RKTrackRep`. It was adopted from the COMPASS experiment [14] and uses a Runge–Kutta solver to follow particles through magnetic fields. It has the same state vector definition as `GeaneTrackRep2`. It also uses the `TGeo` classes for the geometry interface.

### 4.2. Interplay between track representations and reconstruction hits

The classes which represent the fitting algorithms just carry out their linear algebra without knowing about the dimensions of the state vectors $\vec{x}_k$ and the measurement vectors $\vec{m}_k$. The matrix $H_k$ is provided by the reconstruction hit class to transform state vectors and covariance matrices of a specific parameterization into the measurement vector coordinate system. This projection matrix ensures that the dimensionalities of the vectors and matrices in the fitting algorithm are compatible with each other. The following examples shall illustrate this:

1. A four-dimensional track model can be used for tracking without magnetic fields. The state vector is defined as $\vec{x}_k=(u,v,du/dw,dv/dw)^T$ for a straight line where $\vec{u}$ and $\vec{v}$ span the detector plane, and $\vec{w}=\vec{u}\times\vec{v}$ is the normal vector. A strip detector shall measure the $u$ coordinate. Then the measurement vector of Eq. (3), $\vec{m}_k$, is a scalar. The projection matrix is defined as $H_k=(1,0,0,0)$, so that $H_k\cdot\vec{x}_k$ is one-dimensional, just as the residual $\vec{r}_k$. The Kalman gain is a $4\times1$ matrix, and the $\chi^2-$increment is correctly calculated for one degree of freedom, in the sense that $\vec{r}_k$ and $(V_k-H_k\,C_k\,H_k^T)$ are scalars.
2. A pixel detector is used in combination with a five-dimensional trajectory model for charged particle tracking in magnetic fields. The detector measures the coordinates $u$ and $v$ in the detector plane, and the state vector is $\vec{x}_k=(q/|\vec{p}|,du/dw,dv/dw,u,v)^T$. The $2\times5$ projection matrix is then:

$$H_k=\begin{pmatrix}0&0&0&1&0\\0&0&0&0&1\end{pmatrix}$$

   All matrices and vectors automatically appear with correct dimensions: $\vec{m}_k$ and $\vec{r}_k$ are 2-vectors, $V_k$ is a $2\times2$ matrix, the Kalman gain is a $5\times2$ matrix, and $\chi^2$ is a scalar which is calculated from two degrees of freedom ($\vec{r}_k$ is a 2-vector, and $(V_k-H_k\,C_k\,H_k^T)$ is a $2\times2$ matrix).
   If the next hit in the same track only measures one coordinate (e.g. $u$ in the detector plane coordinate system of the next hit), $\vec{m}_k$ will be scalar, $H_k$ will be of dimension $1\times5$, and there will be only one degree of freedom added to the overall $\chi^2$.
3. A TPC delivers space-point hits. The track model is the same as in example 2. The TPC measures three spatial coordinates but this information is transformed into a two-dimensional hit in the virtual detector plane, which is perpendicular to the track. This two-dimensional hit is treated identically to example 2. This is the desired behaviour, since measurements or errors along the flight direction do not contribute to the track fit.

## 5. Simulation studies

The statistical and numerical correctness of a Kalman filter fit depends on the following items: (1) The mathematics of the Kalman filter have to be implemented correctly. (2) The projections of the covariance matrices of the hits onto the (virtual) detector planes have to be correct. (3) The propagation of the track parameters and the covariance matrix are done correctly. For the covariance matrix this means the correct estimation of the Jacobian matrices needed for the Gaussian error propagation. (4) The effects of traversed materials must be taken into account correctly: the state vector has to be modified (momentum loss) and the entries of the covariance matrix need to be increased by the addition of noise matrices (e.g. due to multiple scattering) [7]. Since the track representations are external modules, the Kalman filter and the reconstruction hit implementation in GENFIT are tested with a simplified setup, where the particles traverse a vacuum. This way, the effects number 1–3 are tested, while the effect number 4 is decoupled and not tested here. The setup contains a homogeneous magnetic field, since possible problems arising from field inhomogeneities would only point to problems in the external track representation module and not in the GENFIT core classes. Instead of detector responses with full digitization simulations, which result in unknown detector resolutions, known measurement errors are used.

The track representation `GeaneTrackRep2` is used for these tests. The program samples 30 space points on the trajectory at distances of 1 cm, which are smeared with Gaussian distributions of known widths. Like in a TPC, the $x$- and $y$-measurements are assumed to have equal and better resolutions than the $z$-coordinate measurements ($\sigma_x=\sigma_y=1/2\cdot\sigma_z$). These smeared points are used in the fit as reconstruction hits based on `GFSpacepointPolicy` similar to TPC measurements (see Fig. 5). In front of the first hit, a reference plane is defined in which the fitted track parameters are compared to their true

[2] by performing a C++ `dynamic_cast` on the base class pointer `GFAbsTrackRep*`.

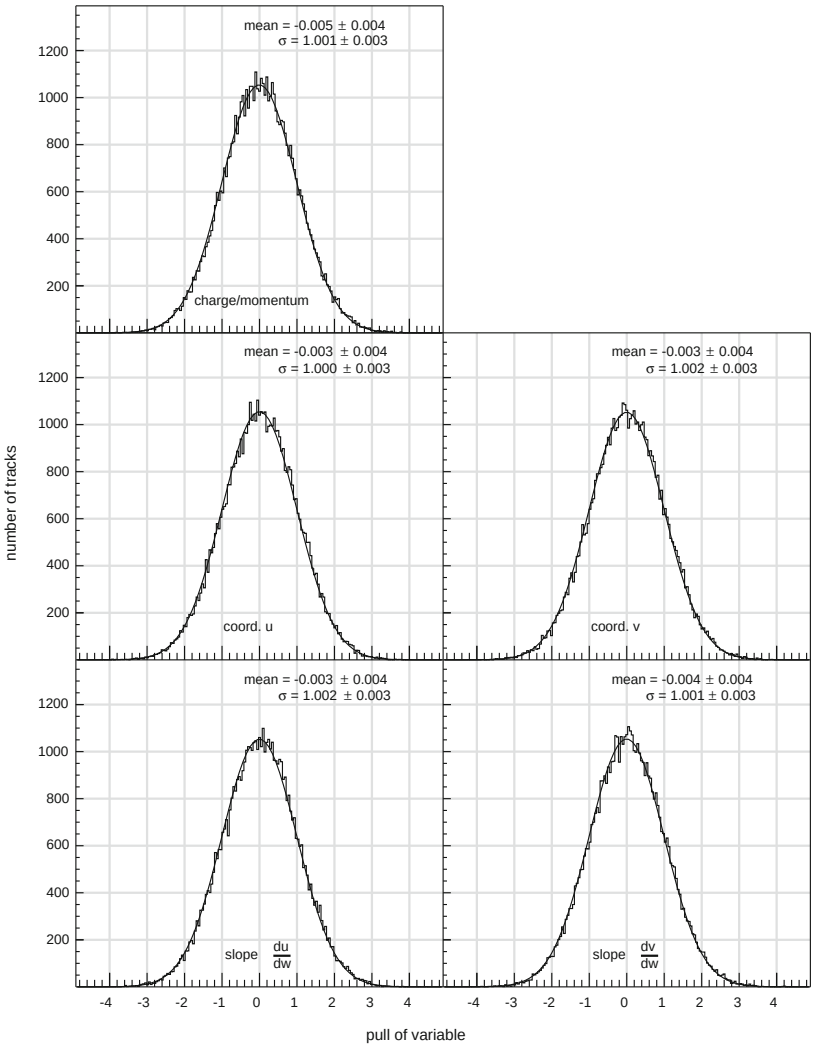


**Fig. 6.** Pull distributions for the five track parameters of `GeaneTrackRep2`. The pull of a variable $x$ is defined as $(x_{\text{fit}}-x_{\text{true}})/\sigma_x$.

values to obtain residual and pull distributions[3]. If the fit is able to correctly determine the track parameters and their errors, the pull distributions will be Gaussians of width $\sigma=1$ and of mean value 0. Fig. 6 presents the five pull distributions for the track parameters, which fulfill these criteria within the corresponding errors, proving that the non-uniform errors of the hits are taken into account correctly.

Another test is carried out with a slightly different detector geometry. Hits from 15 crossed planes of strip detectors are fitted together with 15 space-point hits. The strip hits each contribute one degree of freedom, the space-point hits each contribute two degrees of freedom (they only constrain the track in a plane perpendicular to the track), and the track parameters subtract five degrees of freedom ($15+2\cdot 15-5=40$). The $\chi^2-$probabilities for these fits are presented in Fig. 7. If the number of degrees of freedom is taken into account correctly, this distribution is expected to be flat. A $\chi^2-$test against a uniform distribution results in a $\chi^2/\text{n.d.f.}=87.1/99$, close to unity, as expected.

The execution time per track is 14 ms on one core of an AMD Phenom™ II X4 940 CPU for 30 space-point hits with one forward and one backward fitting pass of all hits. Of this time, a fraction of 91% is spent in the external extrapolation routines of `GeaneTrackRep2`, as determined with Valgrind [15]. The GENFIT core classes have not yet been optimized for execution time, but the above result shows that optimizations would be most rewarding in the track extrapolation routines.

## 6. Conclusions and outlook

A novel framework for track fitting in particle physics experiments has been presented in this paper. Its implementation is a C++ library called GENFIT, which is available freely. Its modular

[3] the pull of a variable $x$ is defined as $(x_{\text{fit}}-x_{\text{true}})/\sigma_x$.

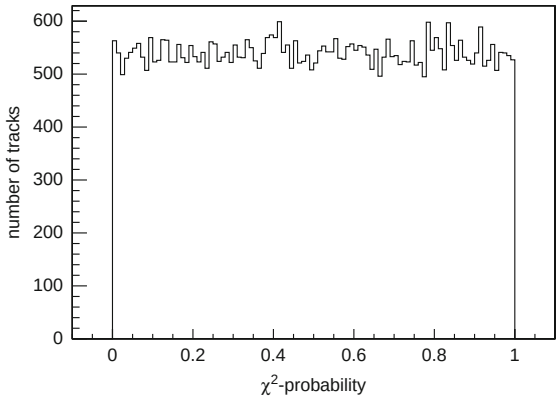


**Fig. 7.** $\chi^2$−probability distribution for a series of track fits through 15 planes of strip detectors and 15 space points.

design consists of three major building blocks: Fitting algorithms, track representations, and reconstruction hits. GENFIT contains a validated Kalman filter. A standard Kalman smoother is planned to be implemented in the future, as well as other fitting algorithms. The possibility of the application of GENFIT to pattern recognition tasks seems promising and will be investigated.

The generic design of the track representation interface enables the user to use any external track following code with GENFIT. The framework allows simultaneous fits of the same particle track with different track representations. Possible applications of this feature are the fitting of different mass hypotheses with the same track model, or the test and validation of different track parameterizations and track following codes. Also the coverage of different regions of phase space with specialized track representations is an important feature in many experiments. At present, GENFIT contains two track representations which provide interfaces to the track following code GEANE and a Runge–Kutta based track extrapolation code adopted from the COMPASS experiment. New track representations which allow the use of other track following codes can be implemented in a straightforward way. The interfaces to the detector geometry and the magnetic field maps can be chosen freely and are all encapsulated in the track representation class.

The geometrical properties of reconstruction hits are not restricted in this framework. The dimensionality of hits is not fixed to particular values, and the orientation of detector planes can be chosen freely. Hits from detectors which do not measure the passage of particles in predefined planes, such as drift chambers or TPCs, are handled in the concept of virtual detector planes. This leads to a direct minimization of the perpendicular distances between the particle tracks and the position measurements from the detectors, i.e. the surfaces of constant drift time or the space points measured in a TPC.

GENFIT provides an easy-to-use toolkit for track fitting to the community of nuclear and particle physics. It is used in the PANDA computing framework. Applications in other experiments are being considered (e.g. Belle II).

## Acknowledgements

This project has been supported by the Sixth Framework Program of the EU (Contract no. RII3-CT-2004-506078, I3 Hadron Physics) and the German Bundesministerium für Bildung und Forschung.

## References

[1] M. Innocente, V. Mairie, E. Nagy, GEANE: average tracking and error propagation package, CERN Program Library, W5013-E, 1991.
[2] I. Hrivnacova, D. Adamova, V. Berejnoi, R. Brun, F. Carminati, A. Fasso, E. Futo, A. Gheata, I. Gonzalez Caballero, A. Morsch, for the ALICE Collaboration, The virtual Monte Carlo, ArXiv Computer Science e-prints, cs/0306005.
[3] A. Cervera-Villanueva, J.J. Gomez-Cadenas, J.A. Hernando, Nuclear Instruments and Methods in Physics Research A 534 (2004) 180.
[4] The PANDA Collaboration, Physics performance report for PANDA: strong interaction studies with antiprotons, ArXiv e-prints 0903.3905.
[5] S. Spataro, Journal of Physics: Conference Series 119 (3) (2008) 032035 (10pp).
[6] 〈http://sourceforge.net/projects/genfit〉.
[7] R. Frühwirth, Nuclear Instruments and Methods in Physics Research A 262 (1987) 444.
[8] G. Kitagawa, Annals of the Institute of Statistical Mathematics 46 (4) (1994) 605.
[9] R. Frühwirth, A. Strandlie, Computer Physics Communications 120 (1999) 197.
[10] R.E. Kalman, Transactions of the ASME—Journal of Basic Engineering Series D 82 (1960) 35.
[11] B. Stroustrup, The C++ Programming Language, Special ed., Addison-Wesley Longman, Amsterdam, 2000.
[12] R. Brun, F. Rademakers, Root—an object oriented data analysis framework, in: AIHENP'96 Workshop, Lausane, vol. 389, 1996, pp. 81–86.
[13] A. Alexandrescu, Modern C++ Design: Generic Programming and Design Patterns Applied, Addison-Wesley Longman, Amsterdam, 2001.
[14] P. Abbon et al. (The COMPASS collaboration), Nuclear Instruments and Methods in Physics Research A 577 (2007) 455.
[15] 〈http://valgrind.org〉.

# List of Figures

**The $\overline{\text{P}}$ANDA Experiment at FAIR**



**Development of a GEM-TPC**



**Supplementary Figures and Tables for Chapter 6 on the High-$p_T$ Cross Section**

# List of Tables

# Bibliography


[1] E. Rutherford. *The Scattering of α and β Particles by Matter and the Structure of the Atom*. Philosophical Magazine **6 21** (1911) 669 - 688. *cited in 1 (p. 1)*

[2] G. Baum et al. (COMPASS Collaboration), *COMPASS: A proposal for a COmmon Muon and Proton Apparatus for Structure and Spectroscopy*. CERN/SPSLC 96-14, SPSC/P 297, 1996. *cited in 1 (p. 2), 4.1 (p. 29)*

[3] B. Jäger, M. Stratmann, and W. Vogelsang. *Longitudinally polarized photoproduction of inclusive hadrons at fixed-target experiments*. European Physical Journal C **44** (2005) 533-543. arXiv:hep-ph/0505157. *cited in 1 (p. 2), 2.4 (p. 16), 3 (p. 20), 3.2 (p. 23), 3.3 (p. 24), 2 (p. 24), 3.3 (p. 25), 3.4 (p. 25), 6.5 (p. 100)*

[4] C. Höppner, S. Neubert, B. Ketzer, and S. Paul. *A novel generic framework for track fitting in complex detector systems*. Nuclear Instruments and Methods in Physics Research A **620** (2010) 518-525. arXiv:0911.1008. *cited in 1 (p. 4), 9 (p. 141)*

[5] F. Halzen and A.D. Martin. *Quarks and leptons: an introductory course in modern particle physics*. Wiley, 1984. *cited in 2 (p. 7), 3 (p. 10)*

[6] A.W. Thomas and W. Weise. *The structure of the nucleon*. Wiley-VCH, 2001. *cited in 2 (p. 7)*

[7] S.E. Kuhn, J.-P. Chen, and E. Leader. *Spin structure of the nucleon – status and recent results*. Progress in Particle and Nuclear Physics **63 1** (2009) 1 - 50. arXiv:0812.3535. *cited in 2 (p. 7), 2.3 (p. 12), 2.3 (p. 14)*

[8] E. D. Bloom et al. *High-Energy Inelastic $e-p$ Scattering at* $6^\circ$ *and* $10^\circ$. Physical Review Letters **23** (1969) 930-934. *cited in 2.2 (p. 8)*

[9] M. Breidenbach et al. *Observed Behavior of Highly Inelastic Electron-Proton Scattering*. Physical Review Letters **23** (1969) 935-939. *cited in 2.2 (p. 8)*

[10] M. Gell-Mann. *The Symmetry group of vector and axial vector currents*. Physics **1** (1964) 63-75. *cited in 2.2 (p. 8)*

[11] F. Myhrer and A. W. Thomas. *A possible resolution of the proton spin problem*. Physics Letters B **663** (2008) 302-305. arXiv:0709.4067. *cited in 2.3 (p. 11)*

[12] V. Y. Alexakhin et al. (COMPASS Collaboration). *The deuteron spin-dependent structure function $g_1^d$ and its first moment*. Physics Letters B **647** (2007) 8-17. arXiv:hep-ex/0609038. *cited in 2.3 (p. 12), 2.3 (p. 13)*

[13] V. Y. Alexakhin et al. (COMPASS Collaboration). *Spin asymmetry $A_1^d$ and the spin-dependent structure function $g_1^d$ of the deuteron at low values of x and $Q^2$*. Physics Letters B **647** (2007) 330-340. arXiv:hep-ex/0701014. *cited in 2.3 (p. 12), 4.1.1 (p. 30)*

[14] D. de Florian, R. Sassot, M. Stratmann, and W. Vogelsang. *Extraction of spin-dependent parton densities and their uncertainties*. Physical Review D **80 3** (2009) 034030. arXiv:0904.3821. *cited in 2.3 (p. 14), 2.4 (p. 15)*

[15] W. Vogelsang. *Rederivation of the spin-dependent next-to-leading order splitting functions*. Physical Review D **54** (1996) 2023-2029. arXiv:hep-ph/9512218. *cited in 2.3 (p. 14)*

[16] R. Mertig and W. L. van Neerven. *The Calculation of the Two-Loop Spin Splitting Functions $P_{ij}^{(1)}(x)$*. Zeitschrift für Physik C **70** (1996) 637. arXiv:hep-ph/9506451. *cited in 2.3 (p. 14)*

[17] R. D. Ball, S. Forte, and G. Ridolfi. *Next-to-leading order determination of the singlet axial charge and the polarized gluon content of the nucleon*. Physics Letters B **378** (1996) 255-266. arXiv:hep-ph/9510449. *cited in 2.3 (p. 14)*

[18] R. D. Carlitz, J. C. Collins, and A. H. Mueller. *The role of the axial anomaly in measuring spin-dependent parton distributions*. Physics Letters B **214** (1988) 229-236. *cited in 2.3 (p. 14)*

[19] E. Leader, A. V. Sidorov, and D. B. Stamenov. *Determination of polarized parton densities from a QCD analysis of inclusive and semi-inclusive deep inelastic scattering data*. Physical Review D **82 11** (2010) 114018. arXiv:1010.0574. *cited in 2.4 (p. 15)*

[20] K. Kurek on behalf of the COMPASS Collaboration, *$\Delta G$ from Open Charm (LO and NLO) including $D^*$ production cross sections*. XIX International Workshop on Deep-Inelastic Scattering and Related Subjects, 2011. *cited in 2.4 (p. 15)*

[21] COMPASS Collaboration, *Determination of $\Delta G/G$ from DIS events with high-$p_T$ hadron pairs*. To be submitted to Physics Letters B, 2011. *cited in 2.5 (p. 16)*

[22] T. Sjöstrand et al., *PYTHIA 6 Physics and Manual*. http://home.thep.lu.se/∼torbjorn, 2006. *cited in 2.4 (p. 16), 6.3 (p. 74)*

[23] G. Ingelman, A. Edin, and J. Rathsman. *LEPTO 6.5 - A Monte Carlo generator for deep inelastic lepton-nucleon scattering*. Computer Physics Communications **101** (1997) 108-134. arXiv:hep-ph/9605286. *cited in 2.4 (p. 16), 5.7 (p. 59)*

[24] A. Adare et al. (PHENIX Collaboration). *Inclusive cross section and double helicity asymmetry for $\pi^0$ production in $p+p$ collisions at $\sqrt{s} = 200$ GeV: Implications for the polarized gluon distribution in the proton*. Physical Review D **76 5** (2007) 051106. arXiv:0704.3599. *cited in 2.4 (p. 16), 3.4 (p. 26)*

[25] B. I. Abelev et al. (STAR Collaboration). *Longitudinal Double-Spin Asymmetry for Inclusive Jet Production in $p^{\rightarrow} + p^{\rightarrow}$ Collisions at $\sqrt{s} = 200\,GeV$*. Physical Review Letters **100 23** (2008) 232003. arXiv:0710.2048. *cited in 2.4 (p. 16), 3.4 (p. 26)*

[26] B. I. Abelev et al. (STAR Collaboration). *Longitudinal double-spin asymmetry and cross section for inclusive neutral pion production at midrapidity in polarized proton collisions at $\sqrt{s} = 200\,GeV$*. Physical Review D **80 11** (2009) 111108. arXiv:0911.2773. *cited in 2.4 (p. 16), 3.4 (p. 26)*

[27] T. H. Bauer, R. D. Spital, D. R. Yennie, and F. M. Pipkin. *The hadronic properties of the photon in high-energy interactions*. Reviews of Modern Physics **50** (1978) 261-436. *cited in 3.1 (p. 20)*

[28] T. H. Bauer, R. D. Spital, D. R. Yennie, and F. M. Pipkin. *Erratum: The hadronic properties of the photon in highenergy interactions*. Reviews of Modern Physics **51** (1979) 407-410. *cited in 3.1 (p. 20)*

[29] K. Ackerstaff et al. (Opal Collaboration). *Measurement of the $Q^2$ evolution of the photon structure function $F_2^{\gamma}$*. Physics Letters B **411** (1997) 387-401. arXiv:hep-ex/9708019. *cited in 3.1 (p. 21)*

[30] M. Glück, E. Reya, and A. Vogt. *Photonic parton distributions*. Physical Review D **46** (1992) 1973-1979. *cited in 3.1 (p. 21)*

[31] M. Stratmann and W. Vogelsang. *Spin-dependent parton distributions of the longitudinally polarized photon beyond the leading order*. Physics Letters B **386** (1996) 370-378. arXiv:hep-ph/9606346. *cited in 3.1 (p. 21)*

[32] D. de Florian and S. Frixione. *Jet cross sections in polarized photon-hadron collisions*. Physics Letters B **457** (1999) 236-244. arXiv:hep-ph/9904320. *cited in 3.2 (p. 23), 3.4 (p. 26)*

[33] S. Frixione, M. L. Mangano, P. Nason, and G. Ridolfi. *Improving the Weizsäcker-Williams approximation in electron-proton collisions*. Physics Letters B **319** (1993) 339-345. arXiv:hep-ph/9310350. *cited in 3.2 (p. 23), 3.4 (p. 26)*

[34] J. Pumplin, D. R. Stump, J. Huston, H.-L. Lai, P. Nadolsky, and W.-K. Tung. *New Generation of Parton Distributions with Uncertainties from Global QCD Analysis*. Journal of High Energy Physics **7** (2002) 12. arXiv:hep-ph/0201195. *cited in 3.2 (p. 23)*

[35] M. Glück, E. Reya, M. Stratmann, and W. Vogelsang. *Models for the polarized parton distributions of the nucleon*. Physical Review D **63 9** (2001) 094005. arXiv:hep-ph/0011215. *cited in 3.2 (p. 23)*

[36] B. A. Kniehl, G. Kramer, and B. Pötter. *Fragmentation functions for pions, kaons, and protons at next-to-leading order*. Nuclear Physics B **582** (2000) 514-536. arXiv:hep-ph/0010289. *cited in 3.3 (p. 25), 3.4 (p. 25)*

[37] W. Vogelsang, *E-mail exchange about the pQCD calculations of quasi-real photoproduction of high-$p_T$ hadrons at COMPASS*. Private communication, 2011. *cited in 3.4 (p. 26), 3.4 (p. 28), 6.5 (p. 100), 6.5 (p. 100), 6.24 (p. 103), 6.25 (p. 105)*

[38] S. Adler et al. *Midrapidity Neutral-Pion Production in Proton-Proton Collisions at $\sqrt{s}$=200 GeV*. Physical Review Letters **91 24** (2003) 241803. arXiv:hep-ex/0304038. *cited in 3.4 (p. 26)*

[39] J. Adams et al. *Cross Sections and Transverse Single-Spin Asymmetries in Forward Neutral-Pion Production from Proton Collisions at $\sqrt{s}$=200 GeV*. Physical Review Letters **92 17** (2004) 171801. arXiv:hep-ex/0310058. *cited in 3.4 (p. 26)*

[40] J. Adams et al. *Forward Neutral Pion Production in p+p and d+Au Collisions at $\sqrt{s_{NN}}$=200GeV*. Physical Review Letters **97 15** (2006) 152302. arXiv:nucl-ex/0602011. *cited in 3.4 (p. 26)*

[41] C. Bourrely and J. Soffer. *Do we understand the single-spin asymmetry for $\pi^0$ inclusive production in pp collisions?* European Physical Journal C **36** (2004) 371-374. arXiv:hep-ph/0311110. *cited in 3.4 (p. 26)*

[42] D. de Florian and W. Vogelsang. *Threshold resummation for the inclusive-hadron cross section in pp collisions*. Physical Review D **71 11** (2005) 114004. arXiv:hep-ph/0501258. *cited in 3.4 (p. 26), 6.5 (p. 104)*

[43] E. Nappi et al., *Letter of Intent: Semi-inclusive Muon Scattering from a Polarized Target*. CERN/SPSLC 95-27, 1995. *cited in 4.1 (p. 29)*

[44] Yu. Alexandrov et al., *Letter of Intent: Charm Experiment with Omni-Purpose Setup*. CERN/SPSLC 95-22, 1995. *cited in 4.1 (p. 29)*

[45] COMPASS Collaboration, *COMPASS-II Proposal*. CERN-SPSC-2010-014, 2010. *cited in 4.1 (p. 29), 4.1.3 (p. 32), 4.1.3 (p. 34)*

[46] M. G. Alekseev et al. (COMPASS Collaboration). *The spin-dependent structure function of the proton $g_1^p$ and a test of the Bjorken sum rule*. Physics Letters B **690** (2010) 466-472. arXiv:1001.4654. *cited in 4.1.1 (p. 30)*

[47] M. G. Alekseev et al. (COMPASS Collaboration). *Quark helicity distributions from longitudinal spin asymmetries in muon-proton and muon-deuteron scattering*. Physics Letters B **693 3** (2010) 227-235. arXiv:1007.4061. *cited in 4.1.1 (p. 30), 6.1 (p. 67)*

[48] E. S. Ageev et al. (Compass Collaboration). *A new measurement of the Collins and Sivers asymmetries on a transversely polarised deuteron target*. Nuclear Physics B **765** (2007) 31-70. arXiv:hep-ex/0610068. *cited in 4.1.1 (p. 30)*

[49] M. G. Alekseev et al. (COMPASS Collaboration). *Collins and Sivers asymmetries for pions and kaons in muon-deuteron DIS*. Physics Letters B **673** (2009) 127-135. arXiv:0802.2160. *cited in 4.1.1 (p. 30)*

[50] M. G. Alekseev et al. (COMPASS Collaboration). *Measurement of the Collins and Sivers asymmetries on transversely polarised protons*. Physics Letters B **692** (2010) 240-246. arXiv:1005.5609. *cited in 4.1.1 (p. 30)*

[51] U. Amaldi, M. Jacob, and G. Matthiae. *Diffraction of Hadronic Waves*. Annual Review of Nuclear and Particle Science **26** (1976) 385-456. *cited in 4.1.2 (p. 31)*

[52] Q. Weitzel. *Precision Meson Spectroscopy: Diffractive Production at COMPASS and Development of a GEM-based TPC for PANDA*. PhD thesis, Technische Universität München, Physik Department, 2008. *cited in 4.1.2 (p. 32), 8.3 (p. 123), 8.3 (p. 124)*

[53] M. G. Alekseev et al. (COMPASS Collaboration). *Observation of a $J^{PC} = 1^{-+}$ Exotic Resonance in Diffractive Dissociation of 190 GeV/c $\pi^-$ into $\pi^-\pi^-\pi^+$*. Physical Review Letters **104 24** (2010) 241803. arXiv:0910.5842. *cited in 4.1.2 (p. 32)*

[54] G. S. Adams et al. (E852 Collaboration). *Observation of a New $J^{PC} = 1^{-+}$ Exotic State in the Reaction $\pi^- p \to \pi^+\pi^-\pi^- p$ at 18 GeV/c*. Physical Review Letters **81** (1998) 5760-5763. *cited in 4.1.2 (p. 32)*

[55] S. U. Chung et al. *Exotic and $q\bar{q}$ resonances in the $\pi^+\pi^-\pi^-$ system produced in $\pi^- p$ collisions at 18 GeV/c*. Physical Review D **65 7** (2002) 072001. *cited in 4.1.2 (p. 32)*

[56] Y. Khokhlov. *Study of X(1600) $1^{-+}$ hybrid*. Nuclear Physics A **663-664 0** (2000) 596c - 599c. *cited in 4.1.2 (p. 32)*

[57] S. Neubert, *PhD thesis in preparation*. Technische Universiät München, Physik Department. *cited in 4.1.2 (p. 32), 8.5 (p. 133), 9 (p. 141)*

[58] F. Haas, *PhD thesis in preparation*. Technische Universiät München, Physik Department. *cited in 4.1.2 (p. 32)*

[59] A. Austregesilo, *PhD thesis in preparation*. CERN and Technische Universiät München, Physik Department. *cited in 4.1.2 (p. 32)*

[60] H. Primakoff. *Photo-Production of Neutral Mesons in Nuclear Electric Fields and the Mean Life of the Neutral Meson*. Phys. Rev. **81** (1951) 899. *cited in 4.1.2 (p. 32)*

[61] J. Gasser, M. A. Ivanov, and M. E. Sainio. *Revisiting $\gamma\gamma \to \pi\pi$ at low energies*. Nuclear Physics B **745** (2006) 84-108. arXiv:hep-ph/0602234. *cited in 4.1.2 (p. 32)*

[62] T. Nagel, *PhD thesis in preparation*. Technische Universiät München, Physik Department. *cited in 4.1.2 (p. 32)*

[63] M. G. Alekseev et al. (COMPASS Collaboration), *First Measurement of Chiral Dynamics in $\pi^-\gamma \to \pi^-\pi^-\pi^+$*. Submitted to Physical Review Letters. arXiv:1111.5954, 2011. *cited in 4.1.2 (p. 32)*

[64] M. Burkardt. *Impact Parameter Space Interpretation for Generalized Parton Distributions*. International Journal of Modern Physics A **18** (2003) 173-207. arXiv:hep-ph/0207047. *cited in 4.1.3 (p. 34)*

[65] X. Ji. *Gauge-Invariant Decomposition of Nucleon Spin*. Physical Review Letters **78** (1997) 610-613. arXiv:hep-ph/9603249. *cited in 4.1.3 (p. 34)*

[66] V. Barone, A. Drago, and P. G. Ratcliffe. *Transverse polarisation of quarks in hadrons*. Physics Reports **359** (2002) 1-168. arXiv:hep-ph/0104283. *cited in 4.1.3 (p. 35)*

[67] J. C. Collins. *Leading-twist single-transverse-spin asymmetries: Drell-Yan and deep-inelastic scattering*. Physics Letters B **536** (2002) 43-48. arXiv:hep-ph/0204004. *cited in 4.1.3 (p. 35)*

[68] P. Abbon et al. (COMPASS Collaboration). *The COMPASS experiment at CERN*. Nuclear Instruments and Methods in Physics Research A **577** (2007) 455-518. arXiv:hep-ex/0703049. *cited in 4.2 (p. 36), 4.2.3 (p. 38)*

[69] A. Abragam and M. Goldman. *REVIEW: Principles of dynamic nuclear polarisation*. Reports on Progress in Physics **41** (1978) 395-467. *cited in 4.2.2 (p. 37)*

[70] D. Adams et al. (SMC Collaboration). *The polarized double cell target of the SMC*. Nuclear Instruments and Methods in Physics Research A **437** (1999) 23-67. *cited in 4.2.2 (p. 38)*

[71] B. Grube. *A Trigger Control System for COMPASS and a Measurement of the Transverse Polarization of $\Lambda$ and $\Xi$ Hyperons from Quasi-Real Photo-Production*. PhD thesis, Technische Universität München, Physik Department, 2006. *cited in 4.5 (p. 39), 4.2.5 (p. 44)*

[72] H. Angerer et al. *Present status of silicon detectors in Compass*. Nuclear Instruments and Methods in Physics Research A **512** (2003) 229-238. *cited in 4.2.3 (p. 38)*

[73] J. Bisplinghoff et al. *A scintillating fibre hodoscope for high rate applications*. Nuclear Instruments and Methods in Physics Research A **490** (2002) 101-111. *cited in 4.2.3 (p. 38)*

[74] S. Horikawa et al. *Development of a scintillating-fibre detector with position-sensitive photomultipliers for high-rate experiments*. Nuclear Instruments and Methods in Physics Research A **516** (2004) 34-49. *cited in 4.2.3 (p. 38)*

[75] O. Allkofer et al. (EMC Collaboration). *A large magnetic spectrometer system for high-energy muon physics*. Nuclear Instruments and Methods **179** (1981) 445-466. *cited in 4.2.3 (p. 38)*

[76] C. Bernet et al. *The 40x40cm$^2$ gaseous microstrip detector Micromegas for the high-luminosity COMPASS experiment at CERN*. Nuclear Instruments and Methods in Physics Research A **536** (2005) 61-69. *cited in 4.2.3 (p. 38)*

[77] V. N. Bychkov et al. *The large size straw drift chambers of the COMPASS experiment*. Nuclear Instruments and Methods in Physics Research A **556** (2006) 66-79. *cited in 4.2.3 (p. 40)*

[78] B. Ketzer, Q. Weitzel, S. Paul, F. Sauli, and L. Ropelewski. *Performance of triple GEM tracking detectors in the COMPASS experiment*. Nuclear Instruments and Methods in Physics Research A **535** (2004) 314-318. *cited in 4.2.3 (p. 40), 8 (p. 118)*

[79] E. Albrecht et al. *Status and characterisation of COMPASS RICH-1*. Nuclear Instruments and Methods in Physics Research A **553** (2005) 215-219. *cited in 4.2.3 (p. 40)*

[80] C. Bernet et al. *The COMPASS trigger system for muon scattering*. Nuclear Instruments and Methods in Physics Research A **550** (2005) 217-240. *cited in 4.2.4 (p. 41), 5.1 (p. 50), 5.5 (p. 57), 6.1 (p. 67)*

[81] M.J. French et al. *Design and results from the APV25, a deep sub-micron CMOS front-end chip for the CMS tracker*. Nuclear Instruments and Methods in Physics Research A **466 2** (2001) 359 - 365. *4th Int. Symp. on Development and Application of Semiconductor Tracking Detectors*. *cited in 4.2.5 (p. 45)*

[82] J.C. Santiard et al. *GASSIPLEX: a low noise analog signal processor for read-out of gaseous detectors*. 6th Pisa Meeting on Advanced Detectors (2004) . *cited in 4.2.5 (p. 45)*

[83] H. Fischer et al. *Implementation of the dead-time free F1 TDC in the COMPASS detector readout*. Nuclear Instruments and Methods in Physics Research Section A: Accelerators, Spectrometers, Detectors and Associated Equipment **461 1-3** (2001) 507 - 510. *8th Pisa Meeting on Advanced Detectors*. *cited in 4.2.5 (p. 45)*

[84] R. Brun and F. Rademakers. *ROOT - An object oriented data analysis framework*. Nuclear Instruments and Methods in Physics Research A **389** (1997) 81-86. *cited in 4.2.6 (p. 46), 8.1 (p. 122)*

[85] R. E. Kalman. *A New Approach to Linear Filtering and Prediction Problems*. Transactions of the ASME–Journal of Basic Engineering, Series D **82** (1960) 35-45. *cited in 4.2.6 (p. 47)*

[86] R. Frühwirth. *Application of Kalman filtering to track and vertex fitting*. Nuclear Instruments and Methods in Physics Research A **262** (1987) 444-450. *cited in 4.2.6 (p. 47)*

[87] S. Gerassimov, *PHysics Analysis Software Tools for the COMPASS experiment*. http://ges.web.cern.ch/ges/phast. *cited in 4.2.6 (p. 48)*

[88] M. Arneodo et al. (NMC Collaboration). *Measurement of the proton and the deuteron structure functions, Fp2 and Fd2*. Physics Letters B **364** (1995) 107-115. arXiv:hep-ph/9509406. *cited in 5 (p. 49), 5.7 (p. 62), 5.16 (p. 63)*

[89] F.-H. Heinsius and S. Koblitz, *COMPASS Luminosity for 2002-2004*. COMPASS note 2006-5, 2006. *cited in 5 (p. 50)*

[90] S. Koblitz, *COMPASS bad spill lists*. COMPASS data-stability website. *cited in 5.3 (p. 53)*

[91] S. Koblitz. *Determination of the Gluon Polarisation from Open Charm Production at COMPASS*. PhD thesis, University of Mainz, 2008. *cited in 5.3 (p. 53)*

[92] S. Koblitz, *"Bad spill lists for 2004W30 and W31."*. private communications, June 2010. *cited in 5.3 (p. 54)*

[93] C. Höppner, *"Luminosity (2004W28-W31) and $F_2^d$ Comparison with Literature"*. COMPASS Release - 2010 - august_lumi_and_f2. *cited in 5.3 (p. 54), 5.5 (p. 57), 5.7 (p. 62)*

[94] J. Pretz, *Measurements of the veto dead times during the 2004 COMPASS run*. Private communication (COMPASS run logbook), 2004. *cited in 5.5 (p. 58)*

[95] J. Koivuniemi, *Target material data of run 2004*. Private Communication (Polarized target ELOG-entry 78), 2009. *cited in 5.6 (p. 58)*

[96] A. D. Martin, W. J. Stirling, R. S. Thorne, and G. Watt. *Parton distributions for the LHC*. European Physical Journal C **63** (2009) 189-285. arXiv:0901.0002. *cited in 5.7 (p. 59)*

[97] B. Badelek, *Ratio of the longitudinal and transverse virtual photon absorption cross sections and radiative corrections for inclusive muon scattering at NMC*. Private communication, 2010. *cited in 5.7 (p. 61), 5.7 (p. 62)*

[98] B. Badelek, D. Bardin, K. Kurek, and C. Scholz. *Radiative correction schemes in deep inelastic muon scattering*. Zeitschrift für Physik C Particles and Fields **66** (1995) 591-599. arXiv:hep-ph/9403238. *cited in 5.7 (p. 62)*

[99] B. Adeva et al. (SMC Collaboration). *Polarised quark distributions in the nucleon from semi- inclusive spin asymmetries*. Physics Letters B **420** (1998) 180-190. hep-ex/9711008. *cited in 6.1 (p. 67)*

[100] E. S. Ageev et al. (Compass Collaboration). *Gluon polarization in the nucleon from quasi-real photoproduction of high-$p_T$ hadron pairs*. Physics Letters B **633** (2006) 25-32. arXiv:hep-ex/0511028. *cited in 6 (p. 74)*

[101] A. Ferrari and P.R. Sala, *"GEANT Hadronic Event Generators: a comparison at the single interaction level"*. ATLAS Internal Note PHYS-No-086, 1996. *cited in 6.3 (p. 75)*

[102] D. Heck. *Low-energy hadronic interaction models*. Nuclear Physics B Proceedings Supplements **151** (2006) 127-134. arXiv:astro-ph/0410735. *cited in 6.3 (p. 75)*

[103] A. Bhadra, S. K. Ghosh, P. S. Joarder, A. Mukherjee, and S. Raha. *Study of low energy hadronic interaction models based on BESS observed cosmic ray proton and antiproton spectra at medium high altitude*. Physical Review D **79 11** (2009) 114027. arXiv:0901.0905. *cited in 6.3 (p. 75)*

[104] Standard Performance Evaluation Corporation, *SPEC CPU2006 benchmark suite*. http://www.spec.org/cpu2006. *cited in 6.3.4 (p. 87)*

[105] G. D. Lafferty and T. R. Wyatt. *Where to stick your data points: The treatment of measurements within wide bins*. Nuclear Instruments and Methods in Physics Research A **355** (1995) 541-547. *cited in 6.4.1 (p. 93), 6.4.1.1 (p. 93)*

[106] C. Höppner et al., *"Cross Section of Quasi-Real Photoproduction of Charged Hadrons with High Transverse Momenta"*. COMPASS Release - 2011 - may_highpt_lowq2. *cited in 6.4.2 (p. 98)*

[107] D. de Florian, R. Sassot, and M. Stratmann. *Global analysis of fragmentation functions for pions and kaons and their uncertainties*. Physical Review D **75 11** (2007) 114010. arXiv:hep-ph/0703242. *cited in 6.5 (p. 100), 6.23 (p. 102)*

[108] D. de Florian, R. Sassot, and M. Stratmann. *Global analysis of fragmentation functions for protons and charged hadrons*. Physical Review D **76 7** (2007) 074033. arXiv:0707.1506. *cited in 6.5 (p. 100), 6.23 (p. 102)*

[109] F. Arleo and J.-P. Guillet, *Fragmentation Function Generator*. http://lapth.in2p3.fr/ffgenerator, 2011. *cited in 6.23 (p. 102)*

[110] W.F. Henning et al., *An International Accelerator Facility for Beams of Ions and Antiprotons; Conceptual Design Report*. GSI, Nov 2001. *cited in 7 (p. 107)*

[111] *Startschuss für Forschungszentrum FAIR in Darmstadt*. Press Release 174/2010 of the German Bundesministerium für Bildung und Forschung, Oct 2010. *cited in 7 (p. 107)*

[112] PANDA Collaboration, *Technical Progress Report*. http://www-panda.gsi.de/archive/public/panda_tpr.pdf, 2005. *cited in 7 (p. 107)*

[113] PANDA Collaboration. *Physics Performance Report for PANDA: Strong Interaction Studies with Antiprotons*. arXiv:0903.3905 (2009). *cited in 7.1 (p. 107), 7.1 (p. 110), 7.1 (p. 111)*

[114] M. Andreotti et al. (E835 Collaboration). *Measurement of the resonance parameters of the $\chi_1(1^3P_1)$ and $\chi_2(1^3P_2)$ states of charmonium formed in antiproton proton annihilations*. Nuclear Physics B **717** (2005) 34-47. arXiv:hep-ex/0503022. *cited in 7.1 (p. 108)*

[115] Y. Chen et al. *Glueball spectrum and matrix elements on anisotropic lattices*. Physical Review D **73 1** (2006) 014516. arXiv:hep-lat/0510074. *cited in 7.1 (p. 108)*

[116] N. Brambilla et al. *Heavy quarkonium: progress, puzzles, and opportunities*. European Physical Journal C **71** (2011) 1534. arXiv:1010.5827. *cited in 7.1 (p. 109)*

[117] G. Bardin et al. (PS170 Collaboration). *Determination of the electric and magnetic form factors of the proton in the time-like region*. Nuclear Physics B **411** (1994) 3-32. *cited in 7.1 (p. 109), 7.1 (p. 109)*

[118] M. Ambrogiani et al. (E835 Collaboration). *Measurements of the magnetic form factor of the proton in the timelike region at large momentum transfer*. Physical Review D **60 3** (1999) 032002. *cited in 7.1 (p. 109)*

[119] B. Aubert et al. (BABAR Collaboration). *Study of $e^+e^- \to p\bar{p}$ using initial state radiation with BABAR*. Physical Review D **73 1** (2006) 012005. arXiv:hep-ex/0512023. *cited in 7.1 (p. 109)*

[120] P. Kroll and A. Schäfer. *The process $p\bar{p} \to \gamma\pi^0$ within the handbag approach*. European Physical Journal A **26** (2005) 89-98. arXiv:hep-ph/0505258. *cited in 7.1 (p. 110)*

[121] PANDA Collaboration, *Technical Design Report for the Central Tracking System of the $\overline{P}$ANDA Experiment*. to be published, 2011. *cited in 7.2 (p. 112)*

[122] E. Köhler, *The cluster-jet target for the $\overline{P}$ANDA experiment*. Talk at the DPG Frühjahrstagung, Hadronen und Kerne, 2010, Bonn (HK 7.3). *cited in 7.2 (p. 112)*

[123] PANDA Collaboration. *Technical Design Report for the PANDA Solenoid and Dipole Spectrometer Magnets*. arXiv:0907.0169 (2009). *cited in 7.2 (p. 113), 7.2 (p. 115)*

[124] PANDA Collaboration, *Technical Design Report for the Micro Vertex Detector of the $\overline{P}$ANDA Experiment*. In preparation, preliminary presentation at the $\overline{P}$ANDA Collaboration meeting at Protvino (T. Stockmanns), June 2011. *cited in 7.2 (p. 113)*

[125] F. Böhmer, *PhD thesis in preparation*. Technische Universiät München, Physik Department. *cited in 7.2 (p. 114)*

[126] I. Adam et al. *The DIRC particle identification system for the BaBar experiment*. Nuclear Instruments and Methods in Physics Research A **538** (2005) 281-357. *cited in 7.2 (p. 114)*

[127] PANDA Collaboration. *Technical Design Report for PANDA Electromagnetic Calorimeter (EMC)*. arXiv:0810.1216 (2008). *cited in 7.2 (p. 114)*

[128] F. Sauli. *GEM: A new concept for electron amplification in gas detectors*. Nuclear Instruments and Methods in Physics Research A **386** (1997) 531-534. *cited in 7.2 (p. 115), 8 (p. 118)*

[129] F. Sauli. *Development and applications of gas electron multiplier detectors*. Nuclear Instruments and Methods in Physics Research A **505 1-2** (2003) 195 - 198. *Proceedings of the tenth Symposium on Radiation Measurements and Applications*. *cited in 8.1 (p. 118)*

[130] S. Neubert. *A GEM based TPC for PANDA - Simulations and Prototype Design*. Diploma thesis, Technische Universität München, Physik Department, 2005. *cited in 8.2 (p. 119), 8.3 (p. 123)*

[131] J. N. Marx and D. R. Nygren. *The time projection chamber*. Physics Today **31** (1978) 46-53. *cited in 8 (p. 117)*

[132] G Bencivenni et al. *A triple GEM detector with pad readout for high rate charged particle triggering*. Nuclear Instruments and Methods in Physics Research A **488** (2002) 493 - 502. *cited in 8 (p. 118)*

[133] Z. Fraenkel et al. *A hadron blind detector for the PHENIX experiment at RHIC*. Nuclear Instruments and Methods in Physics Research A **546** (2005) 466 - 480. *cited in 8 (p. 118)*

[134] M.G. Bagliesi et al. *The TOTEM T2 telescope based on triple-GEM chambers*. Nuclear Instruments and Methods in Physics Research A **617** (2010) 134 - 137. *11th Pisa Meeting on Advanced Detectors*. *cited in 8 (p. 118)*

[135] P. Schade, J. Kaminski et al. (LCTPC Collaboration). *A large TPC prototype for a linear collider detector*. Nuclear Instruments and Methods in Physics Research Section A **628 1** (2011) 128 - 132. *VCI 2010 - Proceedings of the 12th International Vienna Conference on Instrumentation*. *cited in 8 (p. 119)*

[136] M. Killenberg et al. *Charge transfer and charge broadening of GEM structures in high magnetic fields*. Nuclear Instruments and Methods in Physics Research A **530** (2004) 251-257. arXiv:physics/0402121. *cited in 8 (p. 119)*

[137] T. Huber. *Ion Backflow Studies with a Triple GEM Detector*. Master's thesis, Technische Universität München, Physik Department, 2007. *cited in 8 (p. 119)*

[138] L. Musa et al. *The ALICE TPC front end electronics*. IEEE Nuclear Science Symposium Conference Record (2003) 3647-3651. *cited in 8.3 (p. 124)*

[139] Q. Weitzel, F. Böhmer, C. Höppner, T. Huber, B. Ketzer, I. Konorov, A. Mann, S. Neubert, S. Paul, and C. Simonetto. *Development of a high-rate GEM-based TPC for PANDA*. IEEE Nuclear Science Symposium Conference Record (2007) 227-233. *cited in 8.3 (p. 124), 8.5 (p. 132)*

[140] P. Baron et al. *AFTER, an ASIC for the Readout of the Large T2K Time Projection Chambers*. IEEE Transactions on Nuclear Science **55** (2008) 1744-1752. *cited in 8.4 (p. 124), 8.4 (p. 125)*

[141] M. Vandenbroucke, *PhD thesis in preparation*. University Pierre et Marie Curie and Technische Universiät München, Physik Department. *cited in 8.4 (p. 125)*

[142] S. Dørheim, *PhD thesis in preparation*. Technische Universiät München, Physik Department. *cited in 8.4 (p. 125)*

[143] A. Winnebeck. *Design Studies for a Tracking Upgrade of the Crystal Barrel Experiment at ELSA and Installation of a Tracking Test Bench*. PhD thesis, Rheinische Friedrich-Wilhelms-Universität Bonn, 2009. *cited in 8.4 (p. 128)*

[144] S. Dørheim. *Track Reconstruction in a Setup for the Characterization of a GEM-TPC at ELSA*. Master's thesis, Technische Universität München, Physik Department, 2009. *cited in 8.4 (p. 128)*

[145] J. Rauch, *Diploma thesis in preparation*. Technische Universiät München, Physik Department. *cited in 8.5 (p. 132), 8.5 (p. 133), 8.6 (p. 137)*

[146] R. O. Duda and P. E. Hart. *Use of the Hough transformation to detect lines and curves in pictures*. Communications of the ACM **15** (1972) 11-15. *cited in 8.5 (p. 132)*

[147] A. Strandlie, J. Wroldsen, R. Frühwirth, and B. Lillekjendlie. *Particle tracks fitted on the Riemann sphere*. Computer Physics Communications **131** (2000) 95-108. *cited in 8.5 (p. 132)*

[148] H. Li, M. A. Lavin, and R. J. Le Master. *Fast Hough Transform: A hierarchical approach*. Computer Vision, Graphics and Image Processing **36** (1986) 139161. *cited in 8.5 (p. 133)*

[149] F. V. Böhmer et al. *Simulations of a High-Rate TPC for PANDA*. In *IEEE Nuclear Science Symposium Conference Record*, pages 2273–2279, 2009. *cited in 8.5 (p. 133)*

[150] F. Böhmer. *A High-Rate Time Projection Chamber for PANDA: Simulation Studies and GPU-based Track-Finding*. Diploma thesis, Technische Universität München, Physik Department, 2009. *cited in 8.5 (p. 133)*

[151] A. Gobbi et al. *A highly-segmented $\Delta E$-time-of-flight wall as forward detector of the $4\pi$-system for charged particles at the SIS/ESR accelerator*. Nuclear Instruments and Methods in Physics Research A **324** (1993) 156-176. *cited in 8.6 (p. 134)*

[152] M. Berger, *PhD thesis in preparation*. Technische Universiät München, Physik Department. *cited in 8.6 (p. 137)*

[153] K. Bicker and C. Höppner, *Doxygen documentation of the GFTools namespace in GENFIT*. currently available at http://genfit.sourceforge.net/doxy/namespaceGFTools.html. *cited in 8.6 (p. 137)*

[154] M. L. Benabderrahmane et al. *Measurement of the In-Medium $K^0$ Inclusive Cross Section in $\pi^-$-Induced Reactions at 1.15GeV/c*. Physical Review Letters **102 18** (2009) 182501. arXiv:0807.3361. *cited in 8.6 (p. 137)*

[155] C. Höppner and S. Neubert, *GENFIT source-code repository*. http://sourceforge.net/projects/genfit. *cited in 9 (p. 141)*

[156] T. Abe et al. (Belle II Collaboration). *Belle II Technical Design Report*. arXiv:1011.0352 (2010). *cited in 9 (p. 141)*

# Acknowledgments

First of all, I would like to thank my advisor Prof. Stephan Paul for giving me the opportunity to work on the very interesting projects presented in this thesis. He has created a unique work environment at E18, where there seems to be no limit to what an interested student can learn.
I am very grateful to my mentor Dr. Bernhard Ketzer for all his support and guidance through my entire journey of hardware development and data analysis. He has been a great teacher of the methodology of experimental physics. I very much appreciate his constructive criticism of the manuscript of this dissertation.
I would like to extend my gratitude to Prof. Werner Vogelsang for persistently helping me comprehend the concepts of perturbative QCD.
I would like to thank all members of E18 for the countless discussions on interesting topics of physics and beyond. My special thanks go to Sebastian Neubert for making the design and implementation of GENFIT a fun and educational experience. I am thankful to Quirin Weitzel for creating the first member of the GEM-TPC family. I thank him and Florian Haas for being great office mates. I am thankful to Felix Böhmer for enhancing my workumstances with his unique sense of humor. I would also like to thank all the other members of the GEM-TPC team at TUM for the interesting discussions and the eventful beam times we shared: Jia-Chii Berger-Chen, Laura Fabbietti, Markus Ball, Martin Berger, Francesco Cusanno, Sverre Dørheim, Igor Konorov, Robert Münzer, Johannes Rauch, and Maxence Vandenbroucke. Special thanks also go to Sebastian Uhl for his patient help with the software of the COMPASS experiment. I would like to thank Karin Frank for being the administrative backbone of E18.

Lastly and most importantly, I thank all my friends and family for their love and constant support.